4-22-2021 10:00 AM

The Development of Fluorine-18 Imaging Agents Targeting the GHSR

Marina D. Childs, *The University of Western Ontario*

Supervisor: Luyt, Leonard G., *The University of Western Ontario*
A thesis submitted in partial fulfillment of the requirements for the Doctor of Philosophy degree in Chemistry
© Marina D. Childs 2021

Abstract

Molecular imaging is an interdisciplinary field of study that allows for real-time visualization of biological processes in both healthy and disease states. Fluorine-18 positron emission tomography (PET) imaging is a highly sensitive technique where molecular probes containing fluorine-18 serve to specifically locate and visualize the expression of relevant disease biomarkers. The growth hormone secretagogue receptor 1a (GHSR) is differentially expressed in cancer and cardiac pathology, making it a biomarker of interest for imaging such diseases. This thesis discusses the development and optimization of GHSR-targeting ^{18}F-PET imaging probes as well as proposes a new imaging agent discovery technique.

Chapter 2 describes the radiofluorination of two bulky, aromatic prosthetic groups in high radiochemical yields using spirocyclic iodonium ylide (SCIDY) precursors. Subsequent conjugation of these prosthetic groups to a high-affinity peptide based on ghrelin, the endogenous ligand for the GHSR, provided access to two ^{18}F-labelled ghrelin(1-8) analogues. One of these probes was investigated *in vitro* and *in vivo* as a potential PET tracer for targeted GHSR imaging.

Chapter 3 investigates the serum and hepatic metabolic stability of the ghrelin(1-8) ^{18}F-PET probe. Initial *in vitro* stability studies on the peptide identified a metabolic soft-spot between Leu^5 and Ser^6. A structure-activity-stability relationship study evaluated a series of modified ghrelin(1-8) analogues, which revealed new insights into the structural importance of the residues at these positions along with a new lead candidate with improved stability and strong GHSR binding affinity.

Chapter 4 describes the effort to label a quinazolinone-based small molecule with fluorine-18 to access a new high-affinity GHSR PET imaging agent. The design and synthesis of a new quinazolinone-based SCIDY precursor for direct ^{18}F-fluorination is presented.

Chapter 5 introduces a novel chemical technology for direct discovery of molecular imaging agents through the application of the drug discovery technique, fragment-based

drug design. For the first time, a fluorine-containing fragment library was assembled where each member contains fluorine in a position readily accessible to fluorine-18. This library was screened for binding toward the GHSR resulting in the identification of two fragment hits for future optimization into GHSR-targeting PET imaging agents. The resulting candidate molecules that emerge from this research would be the first examples of using a fragment-based approach to directly discover novel molecular imaging agents.

Keywords

Summary for Lay Audience

Molecular imaging is a scientific field of study that allow scientists to non-invasively visualize what the cells in our body are doing in real-time. The pictures obtained through imaging procedures, such as PET, provide valuable insight into diagnosing and tracking diseases including cancer. Some diseases carry specific biomarkers, allowing scientists to develop molecules that bind to these biomarkers, like a key fits a lock. By using small amounts of molecules containing a radioactive atom, such as fluorine-18, PET scanners can detect radioactive decay to construct images. The incorporation of fluorine-18 into the molecular probe requires the use of specific chemical reactions. This thesis discusses the development and optimization of molecular imaging probes containing fluorine-18 targeting the biomarker, GHSR, and the methods used to make these compounds.

Chapter 2 describes the chemical synthesis and fluorine-18 labelling of two prosthetic groups, which act as carrier molecules to introduce fluorine-18 into a biomolecule of interest. These prosthetic groups were used to gain access to two GHSR-targeting biomolecules, one of which was subsequently investigated in a biological system as a potential PET imaging probe.

Molecular imaging probes need to be relatively stable in the body to successfully locate and accumulate at their biomarker. Chapter 3 discusses the stability of a peptide-based GHSR imaging probe in the presence of blood and liver enzymes, which are capable of metabolizing peptide biomolecules. The chapter also demonstrates how chemical synthesis can be applied to modify the molecular probe to improve its stability without impeding its binding to the biomarker.

Chapter 4 describes the effort to directly incorporate fluorine-18 into the chemical structure of a GHSR-binding molecule. The design and execution of a series of chemical reactions in an effort to access this potential PET probe, is presented.

Drug discovery is the process by which new potential medications are developed. One technique used for discovering drugs is fragment-based drug design, where small molecules (fragments) are tested for binding to a given biomarker. The successful

fragments are then further developed into drug candidates. Chapter 5 presents the potential of modifying fragment-based drug design, by exclusively designing fragments that may contain fluorine-18, as a chemical technology to directly discover new molecular imaging probes.

Co-Authorship Statement

Chapter 1, sections 1.5 and 1.6 were adapted from the published review: Childs, M.D and Luyt, L.G. *Mol. Imaging*. 2020, **19**, 1-15.

Chapter 2 is a manuscript in preparation. All peptides and small molecules were synthesized, purified, characterized, and radiolabelled by Marina Childs. Cells for binding assays were prepared by Rebecca McGirr and cells for *in vitro* cell uptake experiments were prepared by Dr. Tyler Lalonde. All *in vitro* competitive binding assays and cell uptake studies were performed by Marina Childs. The µPET imaging and biodistribution study was performed by Dr. Lihai Yu with assistance from Marina Childs and Lise Desjardins (animal technician).

Chapter 3 is a manuscript in preparation. Synthesis, purification, characterization, *in vitro* competitive binding assays, and *in vitro* serum stability studies for compounds **3-6**, **9-11**, and **22** were completed by Derian Hodgson. All other chemical synthesis, purification, characterization, competitive binding assays, serum stability, and all liver S9 fraction stability studies were carried out by Marina Childs. Cells for *in vitro* competitive binding assays were prepared by Peter Pham.

All work and data analysis in chapter 4 was performed by Marina Childs. [^{18}F]fluoride for all radiolabelling experiments in Chapters 2 and 4 was generously donated by Dr. Michael Kovacs at the Lawson Cyclotron & PET Radiochemistry Facility at St. Joseph's Hospital in London, Ontario, Canada.

All chemical synthesis, purification, characterization, fragment screening, and hit validation presented in chapter 5 was performed by Marina Childs. Cells for *in vitro* fragment screen and competitive binding assays were prepared by Peter Pham.

Acknowledgements

The past five years have been filled with growth, struggle, adventure, and incredibly important people. I feel I can confidently say I would not have made it through graduate school without them.

First, I want to thank my incredibly supportive husband, Jason. Whether research has made me jump for joy over a successful run of experiments or made me want to hide under the covers and never come out, he was always there to celebrate the highs and reassure me during the lows. I can't thank him enough for his unwavering love, patience, and care over the years and I look forward to what life has in store for us in the future.

The true root of all my achievements comes down to the fact that I am blessed to have two unbelievably loving and supportive parents, Michael and Deborah. From a young age, they instilled in me a strong work ethic and always encouraged me to reach my potential. They always say how proud they are of me and my accomplishments and their constant support is invaluable to me.

I have also been very fortunate to work alongside some fantastic colleagues. A huge thank you to Will Turnbull, Emily Murrell, Mark Milne, and Jordan LeSarge for teaching me so much, providing helpful research advice, and just overall being excellent company. I also want to thank all the Luyt lab members both past and present for being great friends with who I could celebrate achievements and commiserate over research frustrations. You all made graduate school so much easier.

Finally, I would like to thank my supervisor and mentor, Dr. Len Luyt, for allowing me to follow my interests, and helping me figure out what those interests are. With his support and expertise, I was able to grow my existing skills and learn so many new techniques in his lab. Whenever research projects were struggling, I could hear him say "keep fighting the good fight". His encouragement and positivity always left me feeling reassured and ready to keep moving forward. I am eternally grateful to him for helping me to develop as a scientist and for the opportunity to share the fruits of my labour at multiple conferences where I traveled to exciting new places and met many great people.

Table of Contents

List of Tables

List of Figures

List of Schemes

List of Abbreviations

4-FBA	4-fluorobenzoic acid
4'-FBC	4'-fluorobiphenyl-4-carboxyl
6-FN	6-Fluoro-2-naphthyl
β^+	Positron
β-homoL	*L*-β-homoleucine
δ	Chemical Shift
μL	Microliter
μM	Micromolar
μmol	Micromole
μPET	Micro Positron Emission Tomography
ν	Neutrino
Abu	*L*-α-aminobutyric acid
ACN	Acetonitrile
ADME	Absorption, Distribution, Metabolism, and Excretion
Alloc	Allyloxycarbonyl
ArylBPin	Aryl Boronic Pinacol Ester
AU	Arbitrary Units
AUC	Area Under Curve
Boc	*tert*-butyloxycarbonyl
Bq	Bequerel
BSA	Bovine Serum Albumin
Cha	Cyclohexylalanine
CNS	Central Nervous System
cpm	Counts per Minute
CT	Computed Tomography
CuAAC	Copper-catalyzed Azide-alkyne Cycloaddition
Da	Dalton
DAG	Desacyl Ghrelin
d.c.	Decay Corrected

DCM	Dichloromethane
DIBAL-H	Diisobutylaluminum hydride
DIPEA	*N*,*N*-diisopropylethylamine
DMAP	4-Dimethylaminopyridine
DMF	*N*,*N*-dimethylformamide
DMDO	Dimethyldioxirane
DMSO	Dimethylsulfoxide
Dpr	*L*-2,3-Diaminopropionic acid
EC$_{50}$	Half Maximal Effective Concentration
EDC	*N*-(3-Dimethylaminopropyl)-*N*′-ethylcarbodiimide hydrochloride
EDG	Electron Donating Group
EDTA:	Ethylenediaminetetraacetic acid
Eq.	Equivalents
ESI	Electrospray Ionization
Et$_2$O	Diethyl ether
Et$_3$N	Triethylamine
EtOH	Ethanol
EtOAc	Ethyl acetate
EWG	Electron Withdrawing Group
eYFP	Enhanced Yellow Fluorescent Protein
FBDD	Fragment-Based Drug Design
FBS	Fetal Bovine Serum
FDA	U.S. Food and Drug Administration
FDG	2-Fluoro-2-deoxyglucose
Fmoc	Fluorenylmethoxycarbonyl
g	Gram
GBq	Gigabequerel
GHS	Growth Hormone Secretagogue
GHSR	Growth Hormone Secretagogue Receptor 1a
GHSR-1b	Growth Hormone Secretagogue Receptor 1b
GOAT	Ghrelin *O*-acyl transferase

GPCR	G-protein Coupled Receptor
h	Hour
HATU	1-[bis(dimethylamino)methylene]-1*H*-1,2,3-triazolo[4,5-b]pyridinium 3-oxid hexafluorophosphate
HBSS	Hank's balanced salt solution
HCTU	2-(6-Chloro-1-H-benzotriazole-1-yl)-1,1,3,3-tetramethylaminium hexafluorophosphate
HEK293	Human Embryonic Kidney 293 Cells
HEPES	4-(2-hydroxyethyl)piperazine-1-ethanesulfonic acid
HPLC	High-Performance Liquid Chromatography
HRMS	High Resolution Mass Spectrometry
HAS	Human Serum Albumin
Hse	Homoserine
HTRF	Homogenous Time-resolved Fluorescence
HTS	High-Throughput Screening
IC_{50}	Half Maximal Inhibitory Concentration
ID/g	Injected Dose per Gram
Inp	Isonipecotic Acid
IP1	Inositol Phosphate
IP3	Inositol Triphosphate
k	Elimination Rate Constant
K_{222}	Kryptofix 2.2.2
K_i	Inhibitory Constant
KDa	Kilodalton
keV	Kiloelectronvolt
LC	Liquid Chromatography
LE	Ligand Efficiency
LEAP2	Liver-expressed Antimicrobial Peptide 2
LG	Leaving Group
M	Molar
MA	Molar Activity

MBHA	4-Methylbenzhydrylamine
MBq	Megabecquerel
MeOH	Methanol
mg	Milligram
MHz	Megahertz
min	Minutes
mL	Millilitre
mM	Millimolar
mmol	Millimole
MRI	Magnetic Resonance Imaging
MS	Mass Spectrometry
mV	Millivolts
m/z	Mass-to-Charge Ratio
n	Number
Nal-1	1-Naphthylalanine
NHS	*N*-hydroxysuccinimide
Nle	Norleucine
nM	Nanomolar
NMP	*N*-Methyl-2-pyrrolidone
NMR	Nuclear Magnetic Resonance
PBS	Phosphate-Buffered Saline
PC	Prohormone Convertase
PEG	Polyethylene Glycol
PET	Positron Emission Tomography
PFP	Pentafluorophenyl
PG	Prosthetic Group
p.i.	Post-injection
PTC	Phase Transfer Catalyst
RCC	Radiochemical Conversion
RCP	Radiochemical Purity
RCY	Radiochemical Yield

Ro3	Rule of Three
Rpm	Rotations per minute
RPMI 1640	Roswell Park Memorial Institute 1640 Medium
rt	Room Temperature
SAR	Structure-Activity Relationship
SASR	Structure-Activity-Stability Relationship
SCIDY	Spirocyclic Iodonium Ylide
SFB	*N*-Succinimidyl 4-fluorobenzoate
S_N2	Nucleophilic Aliphatic Substitution
S_NAr	Nucleophilic Aromatic Substitution
SPECT	Single Photon Emission Computed Tomography
SPIAd	Spiroadamantyl-1,3-dioxane-4,6-dione
SPPS	Solid-Phase Peptide Synthesis
SPR	Surface Plasmon Resonance
$t_{1/2}$	Half-life
TBAF	Tetra-*n*-butylammonium fluoride
TBME	*tert*-butyl methyl ether
t-BuOH	*tert*-butanol
TEAB	Tetraethylammonium bicarbonate
TFA	Trifluoroacetic Acid
THF	Tetrahydrofuran
THPTA	Tris-hydroxypropyltriazolylmethylamine
TIPS	Triisopropylsilane
TLC	Thin Layer Chromatography
TMAH	Tetramethylammonium hydroxide
TMEDA	*N,N,N′,N′*-tetramethylethylenediamine
TOF	Time-of-Flight
Ts	Tosyl
UHPLC	Ultra High-Performance Liquid Chromatography
UV	Ultraviolet

Chapter 1

1 Introduction

1.1 Molecular Imaging

The field of molecular imaging allows one to non-invasively visualize biological processes taking place in live cells or intact living organisms in real time. Scientists may use the data generated by the various existing imaging modalities to better understand biochemical processes at the molecular level, identify regions of pathology, and diagnose or track diseases in human patients.[1] Such imaging modalities include, but are not limited to, magnetic resonance imaging (MRI), computed tomography (CT), positron emission tomography (PET), single photon emission computed tomography (SPECT), and optical imaging. Each modality has its own inherent advantages and limitations, such as relative sensitivity and spatial resolution (Figure 1.1), all of which are taken into consideration depending on the nature of a particular study.

MRI and CT are widely available imaging modalities, which use inherent soft-tissue contrast to provide suitable images with high spatial resolution. While these modalities certainly have their advantages, they are limited by their low sensitivity ($10^{-3} – 10^{-5}$ M for MRI) and propensity for artifacts in the images.[1] To enhance contrast and improve sensitivity, molecular contrast agents are routinely employed. However, these agents are often administered in large doses, which could inadvertently cause toxic effects, and they are limited in substrate scope. Nuclear imaging modalities such as positron emission tomography (PET) and single photon emission computed tomography (SPECT) require the use of radiolabeled imaging agents, where a radioisotope is present within a molecular probe and the image is constructed by measuring and localizing the radioactive decay.[2] While these nuclear imaging modalities require the use of ionizing radiation, their unparalleled sensitivity ($10^{-10} – 10^{-12}$ M) allow for only very small amounts of the imaging probe to be administered to the subject, thus significantly reducing the probability of eliciting undesirable pharmacological effects. Despite these advantages, nuclear imaging modalities suffer from low spatial resolution and may, therefore, be combined with MRI or CT in a complementary fashion to obtain anatomical reference.

Optical imaging also offers a highly sensitive method to investigate biochemical processes, but without the use of ionizing radiation. However, it is limited by shallow depth penetration, making it impractical for many *in vivo* studies, and thus predominantly applied toward *in vitro* and *ex vivo* uses.
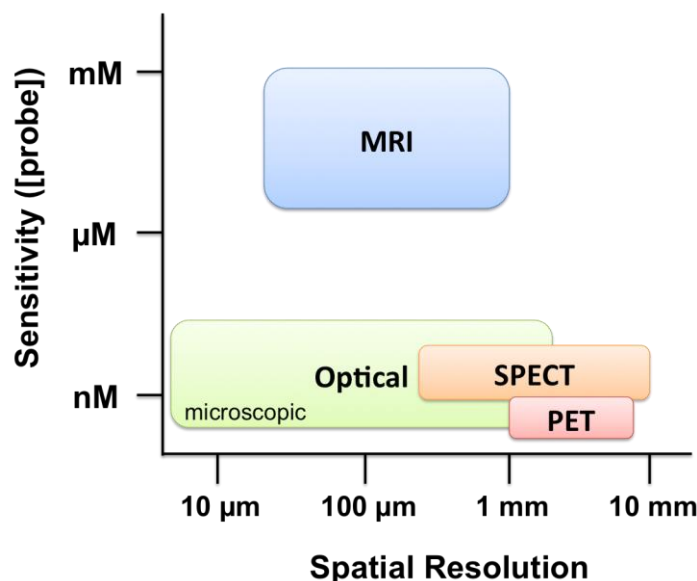
Figure 1.1. Relating sensitivity and spatial resolution of different molecular imaging modalities. Ranges represent both preclinical and clinical values.

1.2 PET Imaging

PET is a valuable imaging modality most commonly used for the diagnosis and treatment monitoring of cancer. This nuclear imaging modality allows functional imaging of biological processes in real time by targeting a pharmaceutically relevant biomarker with a target-specific imaging probe.[1] In order to do this, PET requires the incorporation of a positron-emitting radionuclide into the molecular structure of the probe, where the positron decay can be quantifiably measured and related back to the biomarker of interest. There are a number of radionuclei that are appropriate for PET imaging including carbon-11, nitrogen-13, oxygen-15, fluorine-18, copper-64 and gallium-68, each with their own merits and limitations. The most commonly used PET radionuclide today is fluorine-18 due to its facile production by cyclotron, suitable half-life for radiopharmaceuticals (109.8 min), and slightly improved spatial resolution over other PET radionuclei.[3]

Fluoride-18 is most often generated on a cyclotron through the $^{18}O(p,n)^{18}F$ reaction where an ^{18}O-enriched water target is bombarded with a proton beam to produce aqueous [^{18}F]-fluoride, which can be isolated through ion-exchange chromatography.[4] The fluoride-18 nucleus has an excess of protons causing it to become unstable leading to decay by a proton transforming into a neutron and emitting a positron and a neutrino as shown in figure 1.2.[5] The positron and neutrino are released from the nucleus where the positron will lose its kinetic energy and annihilate with an electron. This interaction produces two 511 keV gamma photons, which travel in opposite directions (180° apart). A ring of PET detectors arranged around the subject capture the photons produced by positron decay and convert them into electrical signals to be used for construction of the PET image.
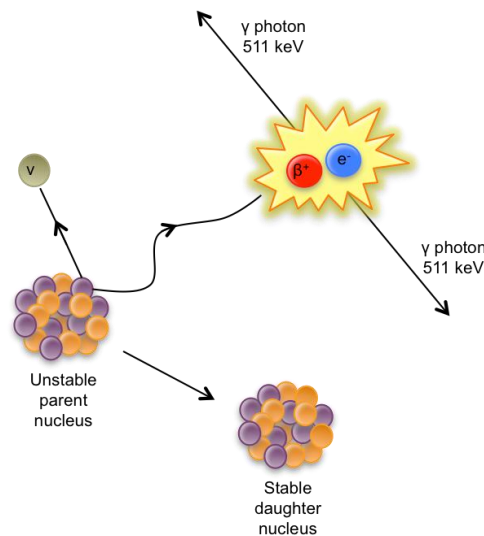
Figure 1.2. Positron (β^+) decay from the unstable, radioactive nucleus to its stable daughter nucleus by converting a proton (purple) to a neutron (orange) through emission of a positron and a neutrino (ν).

One of the primary advantages of PET over other imaging modalities is its ability to sensitively detect changes in biochemical processes before anatomical changes become apparent and are detectable by imaging modalities such as MRI or CT; this makes PET a valuable diagnostic tool in the clinic.[1] It also is able to provide an image with limitless depth penetration and unparalleled sensitivity, meaning only a very small amount of the imaging probe is required to obtained a good image with quantifiable data.[1] Conversely,

PET is among the more expensive imaging modalities, has a lower spatial resolution compared to MRI, and its use of ionizing radiation adds the need for further safety considerations. Nevertheless, it is quite flexible in terms of what types of imaging probes may be developed for binding specific molecular targets. Common types of imaging probes include small molecules, peptides, and macromolecules including antibodies and DNA/RNA aptamers.

1.3 Fluorine-18 Labelling Methods

Targeted PET imaging probes are designed to incorporate a targeting entity, which specifically binds to a biomarker of interest, and a radioactive signalling entity, the decay of which is externally detected and used to construct the PET image. The signalling entity, fluorine-18, can be chemically conjugated to the targeting entity either directly or indirectly through short, efficient syntheses. Direct labelling (Figure 1.3A) is the most straightforward approach and introduces the radionuclide to the targeting entity in a short, one-step reaction. While this method is time efficient, an advantage when working with short-lived radionuclei, there is a challenge in performing site-specific labelling without disturbing other functional groups within the molecular structure of the probe. This is particularly challenging with sensitive biomolecules such as peptides, which are not stable under the harsh labelling conditions that are often required in radiochemistry. For this reason, an indirect approach may be preferable through the use of a prosthetic group (Figure 1.3B). A prosthetic group is a small, reactive, radiolabelled molecule that is subsequently conjugated to the biomolecule under far more gentle reaction conditions. While this approach overcomes the inability to radiolabel certain compounds, it usually requires multiple reaction and purification steps to arrive at the final product, which can result in lower overall radiochemical yields (RCY) and a longer synthesis time. Regardless of the labelling method chosen, it is imperative that the link between the signalling and targeting entities is stable and remains intact *in vivo.*
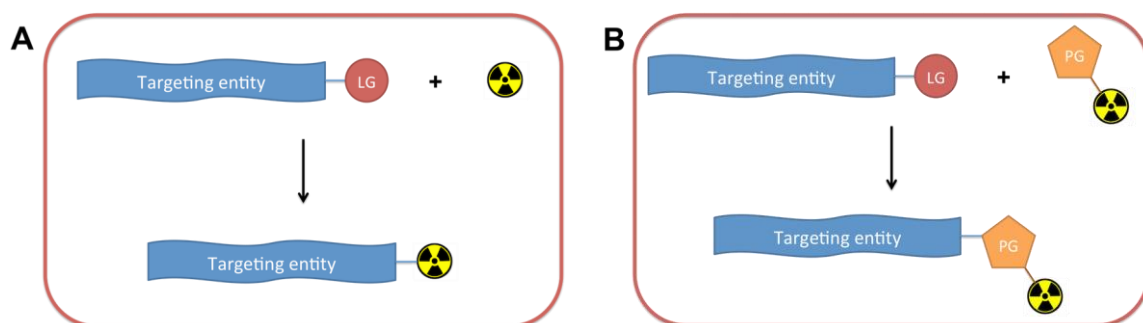
Figure 1.3. General methods for introducing a PET radionuclide to a targeting entity. A) Direct labelling; B) Indirect labelling; LG = Leaving group; PG = Prosthetic group.

In radiochemistry, nucleophilic fluoride-18 is produced with a cyclotron through bombardment of a $H_2^{18}O$ liquid target with protons. The newly formed ^{18}F-fluoride ion is extracted from its enriched water environment through ion-exchange chromatography and residual water is removed through azeotropic distillation with acetonitrile. Typically, radiofluorination reactions are carried out in the presence of base, such as carbonate or bicarbonate ions, to avoid the formation of $[^{18}F]HF$. A phase-transfer catalyst (PTC) is used to aid in the solubility and effective nucleophilicity of the fluoride ion in organic solvents. Kryptofix 222 (K_{222}) is a common PTC used in conjunction with K_2CO_3 to sequester the potassium ion. Generally, polar aprotic solvents give the best radiofluorination results, but there are instances where radiofluorination has been successful in other types of solvents.[6] Due to the limiting half-life of fluorine-18, radiofluorination reaction times must be short, usually ranging from 5-30 minutes, and, as such, typically require high temperatures (~80-150 ˚C). Some common ^{18}F-labelling techniques include, but are not limited to, nucleophilic aliphatic substitution, nucleophilic aromatic substitution, reductive elimination of hypervalent iodonium compounds, copper-mediated ^{18}F-labelling of aromatic compounds, and isotopic exchange. Simple, organic reactions such as nucleophilic substitution techniques and click chemistry are routinely employed to incorporate prosthetic groups to the targeting entity of the imaging probe.

1.3.1 ^{18}F-Fluorination by Nucleophilic Aliphatic Substitution

Nucleophilic aliphatic substitution (S_N2) has been one of the most common and reliable methods for ^{18}F-labelling. The simplicity of using nucleophilic ^{18}F-fluoride to displace a

suitable leaving group provides facile access to C_{sp3}-^{18}F bonds in high radiochemical yields and molar activities. Common leaving groups in order of reactivity include triflate > tosylate ~ mesylate > I > Br > Cl.[7] As with most ^{18}F-fluorination techniques, reaction conditions include the use of azeotropically dried [^{18}F]F$^-$ in anhydrous polar aprotic solvents, high temperatures generally between 80-130 ˚C, and short reaction times of 5-20 minutes. This method can be applied toward direct ^{18}F-labelling (Scheme 1.1A) or used for the production of [^{18}F]fluoroalkyl prosthetic groups for indirect ^{18}F-labelling (Scheme 1.1C). Perhaps the most prevalent [^{18}F]fluoroalkylation agent is 2-[^{18}F]fluoroethyl tosylate ([^{18}F]FETos), which has been applied to the preparation of countless imaging probes due to its small size, relative stability, and facile synthesis. Non-volatile and commercially available ethylene 1,2-ditosylate is easily radiofluorinated and conveniently purified by preparative HPLC to produce [^{18}F]FETos in high decay-corrected (d.c) radiochemical yields of 50-80%.[8] While [^{18}F]FETos has been branded as the workhorse prosthetic group for ^{18}F-fluoroalkylation, other reactive groups are routinely used in place of the tosylate for conjugation to biomolecules (Scheme 1.1B). One drawback of aliphatic ^{18}F-labelling is the propensity for ^{18}F-defluorination to occur *in vivo*, resulting in the signalling entity becoming disassociated from the targeting entity. Defluorination may occur *in vivo* resulting in accumulation of free ^{18}F-fluoride in the skeleton. Aromatic C-^{18}F bonds are stronger than aliphatic C-^{18}F bonds, and therefore ^{18}F-labelled aromatic systems are generally favoured over aliphatic systems when possible. However, emerging strategies to improve the stability of aliphatic C-^{18}F bonds and prevent defluorination have shown some success.[9]

Scheme 1.1. Application of nucleophilic aliphatic substitution in ^{18}F-labelling. A) Direct labelling strategy for the preparation of [^{18}F]FDG for imaging glucose metabolism;[10] B) General preparation of [^{18}F]fluoroalkylating agents; C) Using [^{18}F]FETos as a prosthetic group for ^{18}F-labelling of [^{18}F]fluoroethyl choline ([^{18}F]FECH) for cancer imaging.[8]
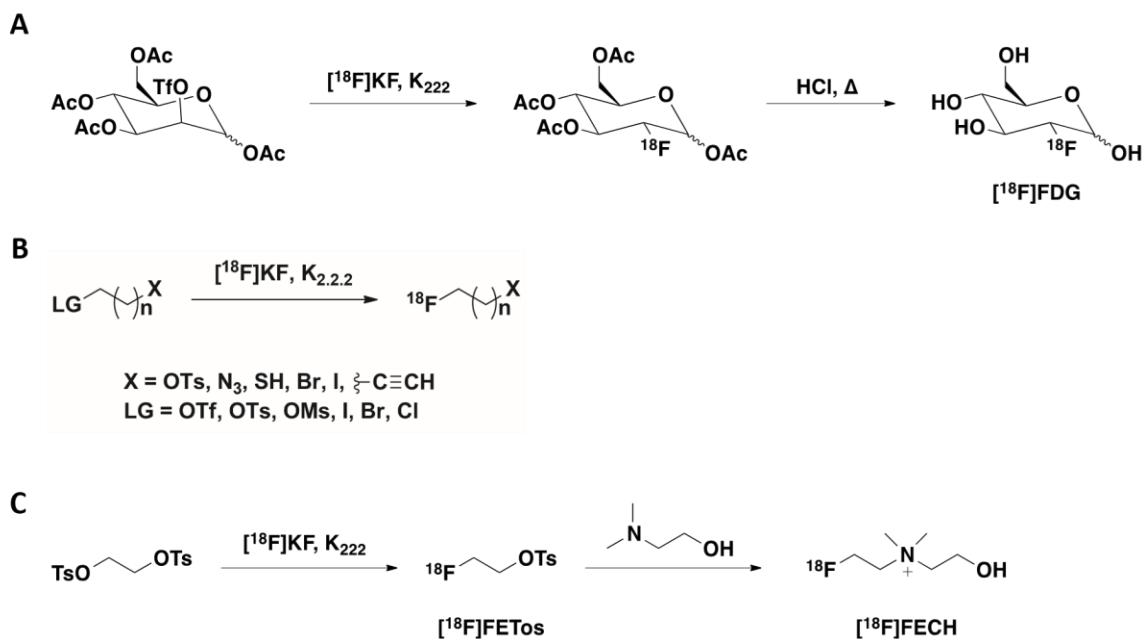
1.3.2 ^{18}F-Fluorination by Nucleophilic Aromatic Substitution

Nucleophilic aromatic substitution is a prominent method to label fluoroarenes with fluoride-18 through the formation of C_{sp2}-^{18}F bonds. Conventional ^{18}F-labelling conditions of high temperatures (80-150 °C), short reaction times (5-20 min), basic environment, and anhydrous polar aprotic solvents are most commonly applied to an appropriate precursor. An ideal precursor for this labelling technique should bear a suitable leaving group (eg. $^+NMe_3$, NO_2, OTf, OTs, halogen, etc.) and an electron-withdrawing activating group (EWG) (eg. NO_2, CN, carbonyl etc.) in the *ortho* or *para* position to the leaving group. However, the necessity of an activating group severely limits the substrate scope of this reaction resulting in low product yields or no product for non-activated (lack of EWG) or deactivated (EDG present) substrates. Probe precursors successfully designed to contain an activated ring at the fluorination site may be efficiently labelled directly (Scheme 1.2A).[11] However, the real claim to fame is the application of prosthetic groups made using this technique in labelling peptides and

proteins. Perhaps the most prominent prosthetic group in this category is *N*-succinimidyl-4-[^{18}F]fluorobenzoate ([^{18}F]SFB), the synthesis of which is shown in Scheme 1.2B.[12] The ability to synthesize ^{18}F-labelled active esters allow for facile, low temperature conjugation of the prosthetic group to a biomolecule via amide formation in a short amount of time. Unfortunately, the preparation of [^{18}F]SFB comes with the pitfall of a relatively long, multi-step radiosynthesis to achieve the final ^{18}F-labelled product. Early reports for the synthesis of [^{18}F]SFB have resulted in radiochemical yields of 30-35% (d.c) in a synthesis time of 80 minutes.[12] Since then, significant effort has successfully resulted in shorter labelling times and improved radiochemical yields of this prosthetic group (Scheme 1.2B).[12–16]

Scheme 1.2. Application of nucleophilic aromatic substitution in ^{18}F-labelling. A) Direct labelling strategy for the preparation of [^{18}F]altanserin for imaging serotonin 2A receptors;[11] B) Preparation of prosthetic group [^{18}F]SFB according to Li et al. (RCY = 80%; Synthesis time = 45 min).[15]
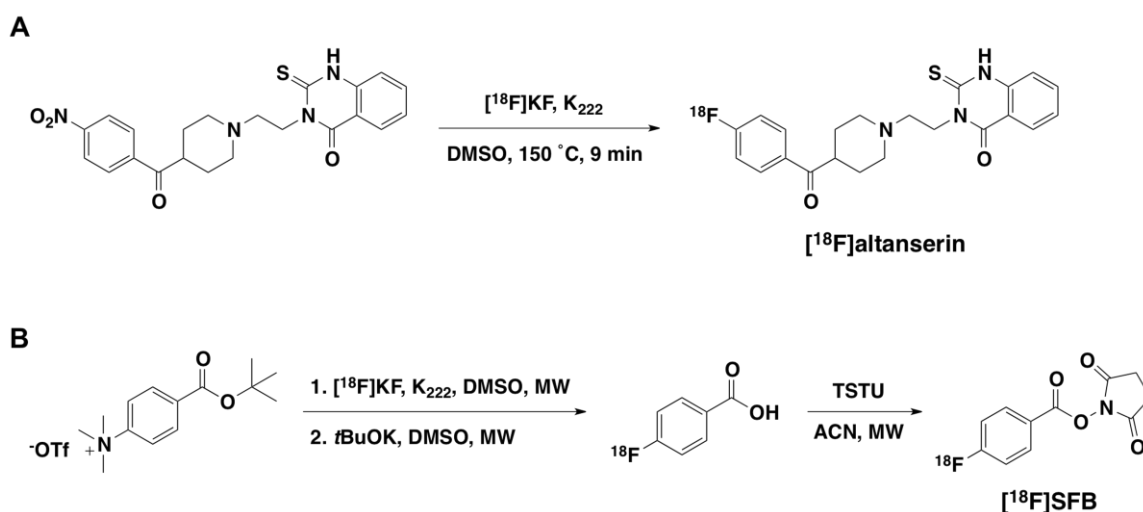
1.3.3 ^{18}F-Fluorination of Hypervalent Iodonium Compounds

Despite the widespread use of S$_N$Ar methods to label arenes with fluoride-18, the need to be able to label non-activated and deactivated arenes easily, reliably, and in high radiochemical yields remains a significant challenge. Several alternative labelling techniques have emerged to meet this demand. Among them include the use of hypervalent iodonium(III) precursors such as diaryliodonium salts and spirocyclic

iodonium ylides. Diaryliodonium salts are precursors that involve two arenes conjugated to an iodonium salt where one ring is relatively electron-deficient and the other ring is highly electron-rich (Scheme 1.3A). The relatively electron-deficient ring is the desired substrate that is preferably labelled with fluoride-18 while the electron-rich ring acts as a labelling director to influence regioselectivity. Furthermore, regioselectivity is improved with the presence of a substituent on the substrate ring *ortho* to the iodonium salt.[17] Common precursors of this nature include aryl(2-thienyl)iodonium salts and mesityl(aryl)iodonium salts, which have resulted in the successful ^{18}F-labelling of various non-activated arenes including arenes bearing electron-donating groups.[7] While conventional radiofluorination conditions are typically applied when labelling these precursors, copper-mediated fluorination has been reported on mesityl(aryl)iodonium salts with improved radiochemical yields of several electron-rich arene substrates, despite the *ortho*-substituents on the mesityl ring.[18]

Spirocyclic hypervalent iodonium(III) ylides (SCIDY) are a more recently developed class of hypervalent iodonium precursors for ^{18}F-labelling. Aryl iodide substrates are oxidized and conjugated to a bulky auxiliary group, which stabilizes the ylide allowing for storage of the precursor (Figure 1.4).[19] Most recently, spiroadamantyl-1,3-dioxane-4,6-dione (SPIAd) has been the auxiliary of choice due to its unmatched performance in stability tests, ^{18}F-labelling efficiency, and ease of synthesis (Scheme 1.3B).[20] The use of SCIDY compounds has been demonstrated to afford ^{18}F-labelled non-activated arenes in moderate to high radiochemical yields with high regioselectivity for the desired ^{18}F-labelled product.[19,20] While conventional, metal-free labelling conditions are most commonly applied with these precursors, the use of triphenylphosphine as an organocatalyst has resulted in improved radiochemical yields for several non-activated arenes.[21] Furthermore, as with iodonium salts, the presence of a substituent on the aromatic substrate *ortho* to the iodonium ylide has resulted in improved radiochemical yields due to destabilization of the transition state during ^{18}F-labelling.[20] Both the use of iodonium salts and SCIDY precursors has been successfully applied to the production of clinically relevant PET tracers including [^{18}F]fluoro-*L*-DOPA[18], [^{18}F]FPEB[22], and [^{18}F]N2B-0518[23] for neuroimaging.
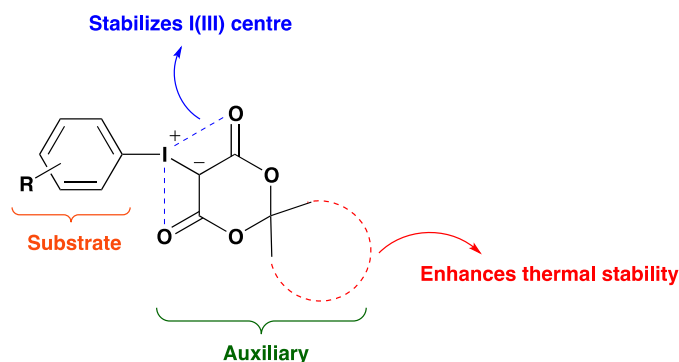
Figure 1.4. General design of SCIDY precursors.

Scheme 1.3. ^{18}F-labelling of iodonium precursors. A) Radiofluorination of aryl(2-thienyl)iodonium salts under metal-free conditions (top)[24] and radiofluorination of mesityl(aryl)iodonium salts under Cu-mediated conditions (bottom)[18]; B) Typical radiofluorination conditions for a SCIDY precursor with a SPIAd auxiliary.[20]
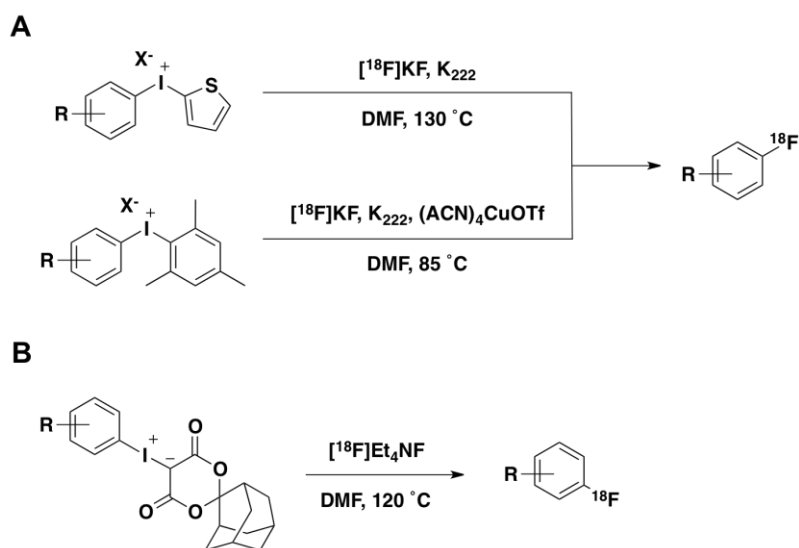
1.3.4 Copper-Mediated ^{18}F-Fluorination of Aromatic Compounds

The development of operationally simple ^{18}F-fluorination methods to access electron-rich arenes from synthetically accessible and shelf-stable precursors, has been an ambitious goal over the past several years. As a result, advancement in ^{18}F-fluorination using copper catalysts has demonstrated wide utility to access a broad scope of aromatic compounds. Aryl boronic esters derived from pinacol (ArylBPin) are shelf-stable precursors that

provide access to C_{sp2}-^{18}F bonds when reacted with nucleophilic fluoride-18. The reaction relies on copper-mediation, with $Cu(OTf)_2(py)_4$ being an effective catalyst choice in otherwise conventional ^{18}F-labelling conditions, and tolerates electron-rich rings with a variety of functional groups (Scheme 1.4A). This method is compatible in the presence of air and moisture and affords ^{18}F-arenes in moderate to high radiochemical yields for most substrates.[25] One caveat is that substrates with sufficiently nucleophilic amines, even with a protecting group, may participate in a competing Chan-Lam coupling resulting in *N*-aryl bond formation in preference to ^{18}F-fluorination.[25,26] In addition to ArylBPin precursors, the use of boronic acid precursors for aromatic ^{18}F-labelling had similar success. Like boronic esters, boronic acid precursors are often synthetically accessible and shelf stable. ^{18}F-Fluorination of boronic acids is frequently mediated by $Cu(OTf)_2$ in the presence of pyridine (Scheme 1.4B) and is tolerable to air and moisture affording moderate to high radiochemical yields of many aromatic substrates.[27]

Arylstannanes offer another opportunity to access ^{18}F-fluorinated arenes from either tributyl- or trimethylstannane derivatives (Scheme 1.4C). The stable Sn-C bond allows for preparation of pharmaceutically relevant compounds for late-stage ^{18}F-fluorination. Radiosynthetic conditions for these compounds are similar to those used with boronic ester/acid precursors where $Cu(OTf)_2$ and pyridine mediate the reaction with [^{18}F]KF in an amide-based solvent at high temperatures (110-140 ˚C) over 5-30 minutes (Scheme 1.4).[28] Electron-neutral and electron-rich arylstannanes were successfully labelled in moderate to high radiochemical yields with *ortho*-substituted arylstannanes being particularly well tolerated. This is in contrast to other metal-mediated nucleophilic fluorinations, such as from boronic acids, which afforded lower radiochemical yields of such substrates.[27,28] While transition metal-mediated radiofluorination reactions provide access to previously inaccessible precursors for late-stage fluorination, it is imperative that the catalyst be completely removed from the purified product prior to biological use due to the cytotoxic effects of the metal. Nevertheless, ArylBPin, boronic acid, and arylstannane precursors offer novel or improved access to radiofluorinated arenes and have been successfully applied toward the radiosynthesis of clinically relevant ^{18}F-PET tracers including [^{18}F]DAA1106[25], [^{18}F]FPEB[27], and [^{18}F]MPPF[28].

Scheme 1.4. Copper-mediated ^{18}F-fluorination of aromatic compounds. A) ^{18}F-labelling from boronic pinacol esters (ArylBPin);[25] B) ^{18}F-labelling from boronic acid precursors;[27] C) ^{18}F-labelling from arylstannanes.[28]
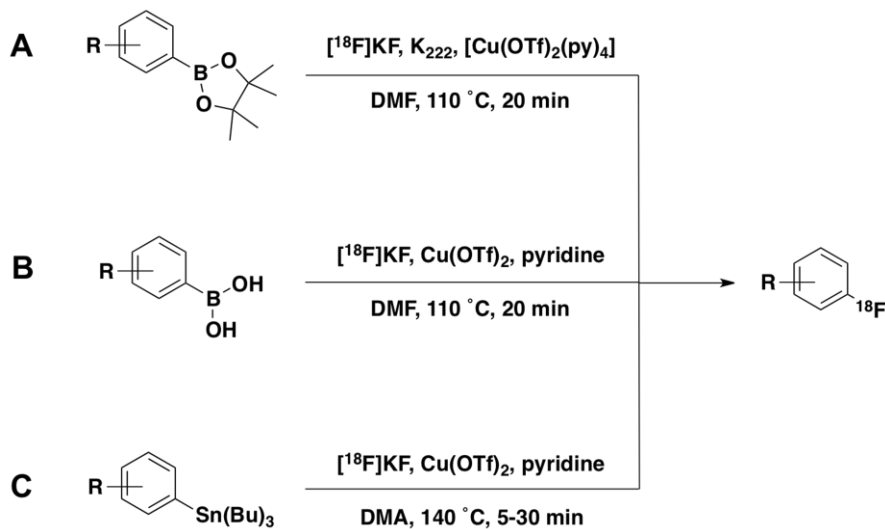
1.4   Fragment-Based Drug Design

One of the most common methods to identify small molecule chemical leads in drug discovery is high-throughput screening (HTS). HTS involves screening very large libraries of drug-like compounds, on the order of 10^6 members, against a pharmaceutically relevant target to identify binding 'hits' for further optimization into chemical leads.[29] This technology is effective at identifying hits for most targets; however, it is not without its limitations. It has been estimated that a possible $10^{60\text{-}200}$ compounds of typical HTS size (300-500 Da) exist, but a large HTS library only samples a small fraction of that chemical space.[30] This limits the degree of confidence that the initial hits obtained are sufficient candidates for subsequent hit-to-lead optimization. Additionally, even with knowledge of the binding mode, it may be unclear which structural moiety within the identified hit compound is actually participating most predominantly in target binding. This results in difficulty in deciding how best to proceed with ligand optimization in an effort to increase affinity for the receptor.
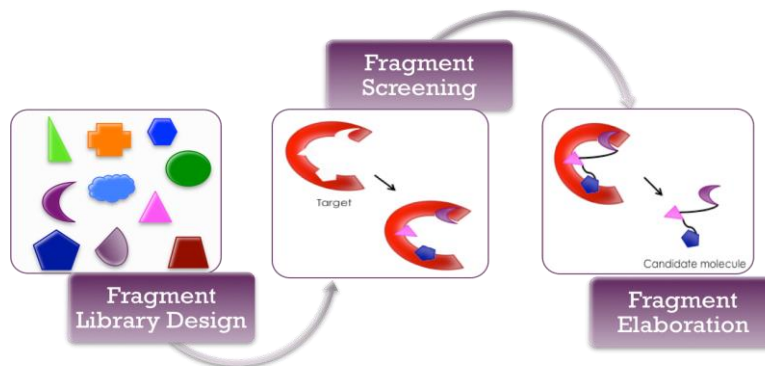
Figure 1.5. Cartoon illustration of the overall FBDD process from fragment library assembly to the generation of candidate lead molecules.

Fragment-based drug design (FBDD) is a more recent drug discovery technique that offers an alternative, or sometimes complementary, approach to HTS.[31] This method involves three stages as illustrated in figure 1.5: fragment library design, fragment screening, and fragment elaboration. Fragment library design requires the assembly of low molecular mass small molecules, called fragments, that each generally conform to the Rule of Three (Ro3) as opposed to the more widely recognized Lipinski's Rule of Five. The Rule of Three requires that each fragment meet the following requirements: (1) a molecular mass of less than 300 Da, (2) up to three hydrogen bond donors and up to three hydrogen bond acceptors, and (3) a logP (clogP) of ≤ 3.[32] With the advent of drug candidates moving beyond the Rule of Five, these rules are becoming increasingly regarded as guidelines for library assembly, rather than strict policy. Fragment libraries are typically much smaller in comparison to HTS libraries (order of 10^3 compounds), but are able to cover more chemical space than HTS campaigns since there exists a much smaller number of possible fragment-type small molecules compared to full-sized drug-like small molecules.[33] There exists a number of commercially available fragment libraries including some that are tailored to contain a specific type of functional group, or target certain classes of endogenous proteins.
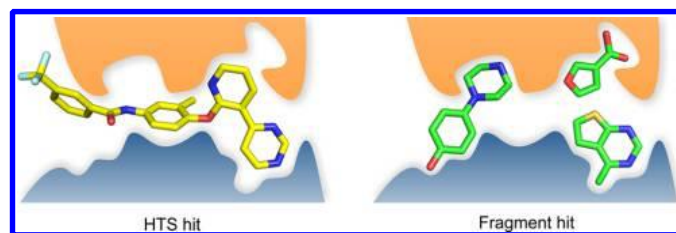
Figure 1.6. HTS hits show a better overall affinity toward the receptor but with suboptimal interactions. Fragment hits are more ligand efficient and involve fewer but higher quality interactions. Reprinted with permission from [33]. Copyright 2012 American Chemical Society.

Upon assembly or purchase of a fragment library, each compound can then be screened for binding against a chosen molecular target in a similar manner as would a HTS library. Fragments, in general, tend to have weak overall potencies toward the biological target with binding affinities in the µM to mM range, but form high-quality interactions with more atoms directly participating in binding compared to HTS hits as shown in figure 1.6.[33] This makes the fragments more "atom efficient", a concept that has been quantified as ligand efficiency (LE), which is defined as the free energy of binding ($\Delta_B G$) in kcal·mol^{-1} per non-hydrogen atom.

There are a number of biochemical and biophysical techniques used to screen fragment libraries. Some commonly employed biophysical techniques include X-ray crystallography, NMR spectroscopy, mass spectrometry, and surface plasmon resonance (SPR)[29]. X-ray crystallography is likely the most powerful biophysical approach to deliver confidence in hit identification but is not suitable for use with targets for which a crystal structure has yet to be elucidated. Additionally, all of these biophysical techniques require the molecular target to be isolated from its cellular environment. This can be particularly difficult to accomplish with membrane-bound protein targets, as many of them tend to lose their native conformation upon removal from their membrane environment.[34] Biochemical assay techniques are more compatible with such targets as they can be performed using live cells. One biochemical screening technique is the competitive radioligand-displacement binding assay, where screened compounds must inhibit a known radiolabeled ligand with high target affinity from binding to the target.

Such inhibition results in a decrease in measured radioactivity at the target thereby indicating a successful hit. Other examples of biochemical assays can include functional assays such as a calcium mobilization assay, and reporter gene assays.[34] Additionally, *in silico* screening may be used to screen fragments virtually using a known crystal structure of the molecular target or a previously validated homology model. This type of virtual screening is useful as a preliminary screen of large libraries prior to experimental screening assays.

Once screening has been completed, fragment hits may be structurally elaborated to become initial candidate leads through an iterative process of rational design and chemical synthesis. There are a few different strategies broadly applied to fragment elaboration: fragment merging, fragment linking, or fragment growing.[31] Choosing which strategy to pursue depends on knowledge of the binding mode for a fragment hit, which can be obtained through complementary screening strategies and fragment-focused structure activity relationship studies (SAR). Fragment merging involves incorporation of structural components of overlapping fragment hits into one larger molecule. Fragment linking is used to join two non-overlapping fragment hits using some optimized linker moiety. Finally, fragment growing is employed if all fragment hits are found to bind in the same binding pocket, or if the binding mode is unknown. The initial fragment hit is first optimized and then elaboration may be monitored by potency, ligand efficiency, and other general medicinal chemistry considerations.

The fragment-based technique for the discovery of novel drugs, while relatively recent, is already firmly implemented in the pharmaceutical industry with four drugs on the market today having been discovered through FBDD. The first successful drug discovered through FBDD was vemurafenib, known by its trade name, Zelboraf®. It was approved in the United States in 2011 and is used to treat metastatic melanoma by inhibiting the BRAFV600E kinase mutant.[35] The second drug, venetoclax, was approved in 2015 as a B-cell lymphoma 2 protein inhibitor in chronic lymphocytic leukemia.[36] The third drug, erdafitinib, is a FGFR inhibitor approved recently in 2019 for treatment of urothelial carcinomas.[37] Finally, pexidartinib, which targets the CSF1 receptor, was also approved in 2019 to treat tenosynovial giant-cell tumor, a group of rare tumors that form in the

joints.[38] The success of these fragment-based drugs shows promise for the technique, and while established in drug discovery, FBDD has not yet been applied toward the discovery of molecular imaging agents.

1.5 The GHSR and its Endogenous Ligands

1.5.1 The Growth Hormone Secretagogue Receptor 1a

The growth hormone secretagogue receptor (GHSR) is a member of the G protein-coupled receptor (GPCR) superfamily and was first identified in 1996 by Howard and co-workers.[39] It is also commonly referred to as the ghrelin receptor and exists in two known isoforms in humans, GHSR-1a and GHSR-1b. The GHSR-1a is made up of 366 amino acids and is the only active form of the receptor. Isoform 1b is 289 amino acids in length with 100% sequence identity to that of the GHSR-1a up to Leu265. The GHSR-1a, hereafter referred to as GHSR, was first discovered in the pituitary and hypothalamus as a receptor that bound growth hormone secretagogues (GHS), a class of synthetic therapeutics developed to stimulate endogenous growth hormone secretion. Many GHS molecules were developed prior to the discovery and identification of the GHSR or its endogenous ligands; some of the many examples include GHRP-6, GHRP-2, hexarelin, MK 0677, G-7039, and ipamorelin.[40–46] Since that time, the GHSR has been found to be expressed in tissues outside the CNS, including the pancreas, thyroid gland, spleen, adrenal gland, gastrointestinal tract, and cardiovascular system.[47,48] Intracellular signalling of this receptor is mediated by the endogenous ligand for the GHSR, ghrelin.

1.5.2 Ghrelin

Kojima and coworkers first identified ghrelin in 1999 as the endogenous ligand for the GHSR (EC_{50} = 2.5 nM).[49] Later, it was determined that the gene product is preproghrelin, which translates to a 117 amino acid polypeptide that is post-translationally cleaved after a 23 amino acid signal peptide to give the 94 amino acid peptide, proghrelin (Figure 1.7).[50] Proghrelin may then be processed by prohormone convertase (PC) 1/3 to yield a 28 amino acid ghrelin peptide, and then acylated by ghrelin *O*-acyl transferase (GOAT) to produce bioactive ghrelin.[51–53] GOAT is a membrane-bound enzyme known to specifically attach an *n*-octanoyl fatty acid side chain off the serine residue in position 3

of ghrelin.[51,52] This unique acylation is essential in order for ghrelin to bind and activate the GHSR, whereas the non-acylated form of ghrelin, desacyl ghrelin (DAG), has no affinity for the receptor ($IC_{50} > 10,000$ nM).[54] Interestingly, DAG is the predominate form of ghrelin found in circulation, but its particular function in relation to the receptor is still not fully understood. However, DAG does participate in physiological pathways independent of the GHSR including binding to the corticotropin releasing factor receptor type 2a (CRF2a), exerting beneficial actions on vascular function, and cardiac protection.[55–57] Additionally, a cyclic analogue of DAG, known as Livoletide, is currently in phase III clinical trials for the treatment of Prader-Willi syndrome.[58] The GHSR-1b isoform does not bind ghrelin or growth hormone secretagogues and, therefore, does not share the same signalling profile as the GHSR-1a.[59] The biological function of the GHSR-1b is still not well understood, though it has been shown to modulate the relatively high constitutive activity of the GHSR-1a through proposed hetero-dimerization of the two isoforms on the endoplasmic reticulum.[60–62] Therefore, the majority of the research on ligand development has been devoted exclusively to targeting the GHSR isoform 1a.
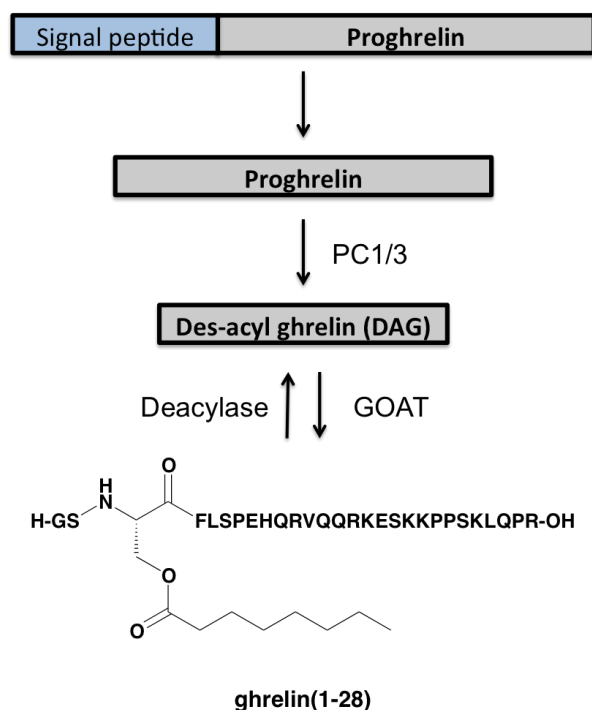
Figure 1.7. Biosynthetic processing from preproghrelin to ghrelin.

1.5.3 Liver-Expressed Antimicrobial Peptide 2

Recently in 2018, Ge et al. reported their discovery of liver-expressed antimicrobial peptide 2 (LEAP2) as a second endogenous ligand for the GHSR.[63] Mature LEAP2 is a 40 amino acid bicyclic peptide with 2 disulfide bridges, originally isolated in 2003 from human blood ultrafiltrate (Figure 1.8).[64] It was found to function as an antagonist for the receptor, causing inhibition of ghrelin-induced GHSR activation.[63,65] Later reports demonstrated that LEAP2 also behaved as an inverse agonist towards GHSR constitutive activity. M'Kadmi et al. found that LEAP2 displaces ghrelin from the orthosteric binding site of the GHSR (K_i = 1.26 nM) and substantially decreased ghrelin-independent receptor signalling (EC_{50} = 22.8 nM) in an inositol phosphate (IP1) production assay.[66] Similar to ghrelin, the full peptide sequence of LEAP2 is not necessary for the ligand to affect the receptor. Rather, the *N*-terminal region, LEAP2(1-14), which contains no disulfide bridges, is sufficient to maintain strong receptor binding (K_i = 3.66 nM) and activity as an inverse agonist (EC_{50} = 76.4 nM).[66] Furthermore, blocking endogenous LEAP2 was found to enhance ghrelin-induced GHSR activation *in vivo*.[63] The ability for LEAP2 to tune the ghrelin-GHSR system makes it an interesting therapeutic target for the treatment of metabolic diseases, such as obesity.

H-MTPFWRGVSLRPIGASCRDDSECITRLCRKRRCSLSVAQE-OH

Figure 1.8. Amino acid sequence of mature LEAP2.

1.5.4 Clinical Relevance of GHSR Expression and Ghrelin Secretion

Activation of the GHSR by ghrelin results in a variety of physiological functions including regulation of appetite, energy homeostasis, growth hormone secretion, cell proliferation and survival, glucose and lipid metabolism, blood pressure regulation, and the protection of cells in the nervous and cardiovascular systems.[67–71] Research into perturbing the expression of ghrelin for the treatment of metabolic disorders, including anorexia, cachexia, obesity, and diabetes has resulted in the rapid expansion of reports of ghrelin receptor agonists, antagonists, and inverse agonists.[72–75] Several review articles summarize many of these ligands and their journey towards the clinic.[46,76–78]

Additionally, altered GHSR and ghrelin expression has been observed in many cancers including pancreatic cancer, breast cancer, prostate cancer, ovarian cancer, gastric cancer, colon cancer, thyroid cancer, pituitary adenoma, and lung cancer.[71,79–84] Particularly, differential expression of the GHSR in prostate cancer tissues compared to benign hyperplasia was demonstrated by Lu et al, indicating a potential for use of the GHSR as a diagnostic biomarker for such cancers.[85] Therefore, targeted imaging of this receptor could provide a minimally invasive method for monitoring cancer treatment and progression. Moreover, the GHSR is abnormally expressed in cardiac pathology; increased expression has been demonstrated in the myocardium of patients with chronic heart failure and decreased expression in patients with end-stage cardiomyopathy.[79,86] Related to these findings, ghrelin administration has been shown to have several therapeutic effects in cardiac disease including improving cardiac function in models of chronic heart failure.[71] As such, there is growing interest in developing ghrelin analogues for the purpose of imaging the biological processes related to cardiac GHSR. Current research to image the GHSR is underway through the development of probes derived from ghrelin, LEAP2, growth hormone secretagogues, and small molecules.

1.6   Molecular Imaging Agents Targeting the GHSR

1.6.1 Molecular Imaging Agents Based on Ghrelin

Soon after the discovery of ghrelin, researchers were interested in elucidating the structure activity relationship (SAR) between this peptide hormone and its receptor. Early work focused on investigating the role of the aliphatic side chain of ghrelin, the biological importance of the ester linkage to this side chain, and the minimum sequence length required to maintain activation of the receptor.[54,87] These studies, reported in the early 2000s, determined that the octanoyl side chain, while crucial for binding, could tolerate various structural modifications provided that sufficient hydrophobicity is retained. The ester group linking the aliphatic side chain to the ghrelin peptide can be replaced by substituting Ser^3 with diaminopropionic acid (Dpr), which affords a more chemically robust amide linkage with no detriment to the binding affinity. Furthermore, it was found that the *N*-terminal tetrapeptide, Gly-Ser-Ser(*n*-octanoyl)-Phe-NH$_2$, was the smallest truncated analogue of ghrelin that could still activate the GHSR, albeit with low potency.

Binding affinity and activation was stronger with longer analogues, such as ghrelin(1-10) and ghrelin(1-14). An alanine scan of ghrelin(1-14) systematically confirmed the importance of a positive charge at the *N*-terminus, identified Phe[4] as a critical residue for binding, and suggested that most other amino acids in the sequence could be replaced to further optimize affinity and potency.[88]

The last decade has seen a substantial increase in the number of imaging probes targeting the GHSR with 2009 marking the first publication investigating the potential to image this receptor as a cancer target. In this preliminary investigation, Rosita et al. reported on the development of ghrelin analogues bearing PET and SPECT imaging moieties.[89] The authors utilized structure-activity knowledge reported in the early years of ghrelin research to investigate two classes of ghrelin analogues. First, peptides containing fluorine within the aliphatic side chain of ghrelin were investigated as potential probes for ^{18}F-PET imaging. Peptides were synthesized and their binding affinities towards the GHSR were assessed via an *in vitro* radioligand-displacement binding assay. The resulting best candidate was a ghrelin(1-14) analogue bearing fluorine at the end of a 12C side chain, ghrelin(1-14)-12C-F (**1**), which offered an IC_{50} value of 27.9 nM.[89] The second class of ghrelin analogues investigated the potential to incorporate a [185/187]Re/^{99m}Tc chelator into the aliphatic side chain for SPECT imaging. Most often, the imaging portion of a radiopharmaceutical is positioned far from the binding site so as not to have a negative effect on the binding affinity.[90–94] This is particularly common for radiotracers bearing metal chelators due to the relatively large size of the appended metal-complex. However, the authors chose to apply a more compact design that incorporates the imaging moiety in a position crucial for binding. Despite the added steric bulk, the relatively small and lipophilic organometallic species, cyclopentadienyl tricarbonyl ($CpM(CO)_3$), was successfully incorporated into the side chain resulting in a Re-labelled ghrelin(1-14) analogue, ghrelin(1-14)-4C-CpRe(CO)$_3$ (**2**), with an IC_{50} of 35 nM.[89] Peptides **1** and **2** (Figure 1.9) set the stage for future development of ghrelin-based GHSR imaging agents.
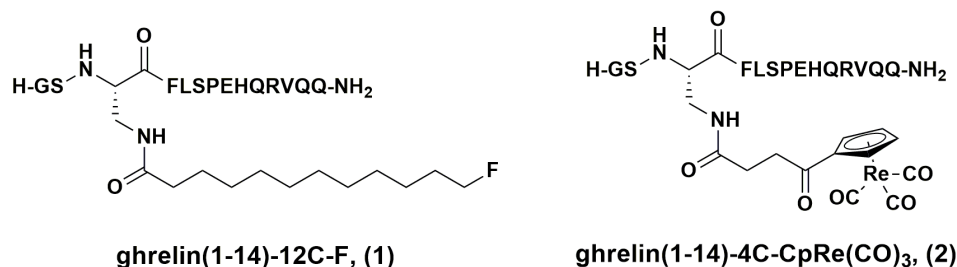
Figure 1.9. Fluorine and rhenium functionalized ghrelin analogues as potential GHSR-targeting PET and SPECT imaging probes.

Later in 2015, Koźmiński and Gniazdowska continued work on developing SPECT imaging probes for the GHSR labelled with technetium-99m (Figure 1.10).[95] The authors reported three analogues of ghrelin(1-7) conjugated to polydentate ^{99m}Tc-complexes via a bifunctional coupling agent (BFCA), isocyanobutyric acid succinimidyl ester, on a lysine residue at the *C*-terminus of the peptide. All analogues were produced in 85%-95% radiochemical yields and molar activities in the range of 20-25 GBq/µmol. First, a positively charged analogue, [Lys^7(^{99m}Tc(CO)$_3$L$_{N,O}$CN-BFCA)$^+$]ghrelin(1-7) **(3)**, was developed and labelled, but showed poor *in vitro* stability in human serum and was dismissed from further biological evaluation. A neutral analogue, [Lys^7(^{99m}Tc(CO)$_3$L$_{S,O}$CN-BFCA)]ghrelin(1-7) **(4)**, which was stable in aqueous solutions and human serum, had a K$_i$ value of 1.1 nM, but showed significant uptake in kidneys and liver (21% and 28% respectively at 30 min p.i.) when evaluated through an *in vivo* biodistribution study. In contrast, another stable, but slightly more lipophilic analogue, [Lys^7(^{99m}Tc(NS$_3$)CN-BFCA)]ghrelin(1-7) **(5)**, possessed a K$_i$ value of 2.1 nM, and showed much lower kidney uptake but similar liver uptake compared to analogue **4** (2% and 29% at 30 min p.i.). These analogues represent the first ^{99m}Tc-labelled ghrelin-based SPECT imaging agents.
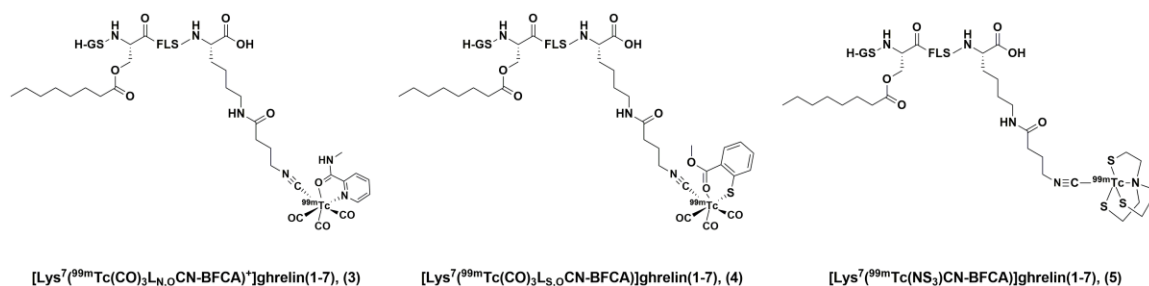
Figure 1.10. ^{99m}Tc-SPECT imaging probes for the GHSR-1a.

During the early 2000s, the development of GHSR targeted probes was also underway outside the realm of nuclear imaging modalities. The first fluorescently labelled ghrelin analogue was reported by Enderle et al. with the goal of developing a non-radioactively labelled compound that could identify the GHSR and measure the binding affinity of other test compounds in cell-based assays.[96] The resulting analogues featured ghrelin truncated to the first 18 amino acids in the peptide sequence. A variety of maleimide-conjugated fluorophores, including Texas Red, tetramethyl rhodamine, BODIPY FL, and MR121, were conjugated to an additional cysteine residue on the *C*-terminus of the peptide to give analogues of the form: [Dpr(octanoyl)[3],Cys(dye)[19]]ghrelin(1-19) amide.[96] In 2011, Leyris et al. developed a high-affinity red fluorescent ghrelin analogue, known as red-ghrelin, for use in a homogenous time-resolved fluorescence (HTRF) assay to screen ligands for the GHSR.[97] The biological properties of red-ghrelin were characterized and validated through a competitive radioligand-displacement assay and inositol phosphate (IP1) accumulation. While the precise structure of this probe was not disclosed in the article, it was reported to bind to the GHSR with a K_i value of 19 nM and induce IP1 accumulation as efficiently as ghrelin with an EC_{50} value of 88 nM, approximately half as potent as their evaluation of native ghrelin. In addition to its use in the HTRF assay, red-ghrelin has also been used as a probe to localize GHSR expression and identify GPCR heteromerization in mouse brain.[98,99]

Later that year, McGirr et al. reported another fluorescently labelled ghrelin analogue for optical imaging of the GHSR (Figure 1.12).[100] The imaging label, fluorescein isothiocyanate (FITC), was incorporated onto the peptide via amide conjugation to the *C*-terminal lysine side chain, giving [Dpr(octanoyl)[3],Lys(fluorescein)[19]]ghrelin(1–19) **(6)**.

The IC$_{50}$ value of this dye-labelled probe was 9.5 nM, which is comparable to hexarelin, a known GHSR agonist, and slightly weaker than natural ghrelin. Furthermore, this probe was used to provide the first visualization of GHSR *in situ* without the need for an antibody. GHSR expressing CHO cells were incubated with the probe and fluorescence imaging revealed distinct clustering of fluorescent signal indicative of receptor internalization. Additionally, specific binding was also observed in mouse cardiac tissue alluding to the interesting possibility of using ghrelin analogues for detecting GHSR expression in other tissues as well. Lu et al. further evaluated this probe as a tool in detecting the receptor in human prostate cancer vs. normal tissues.[85] The fluorescent signal from the probe bound to prostate cancer tissue was significantly higher when compared to normal tissue (P = 0.0093) and benign hyperplasia (P = 0.0027) following signal amplification, indicating differential receptor expression in these different tissues (Figure 1.11).

The success of the fluorescein ghrelin probe in GHSR detection prompted its use in other biological studies. Indeed, since its development, this probe has been used on numerous occasions in the identification of ghrelin binding sites in genetically engineered cells and in mouse brain tissue.[101–104] The brain areas accessible to ghrelin have been elucidated by systematically mapping the distribution of centrally or peripherally administered tracer **6** in the mouse brain, demonstrating uptake in GHSR expressing brain areas.[105–108] Further efforts utilized this probe to better illuminate the possible mechanisms by which circulating ghrelin accesses its receptor in the brain.[106,109,110] Other studies have used probe **6** to investigate the ability for ghrelin to interact with plasma proteins such as serum albumin, and the ability for GHSR to interact with other GPCRs.[111,112]
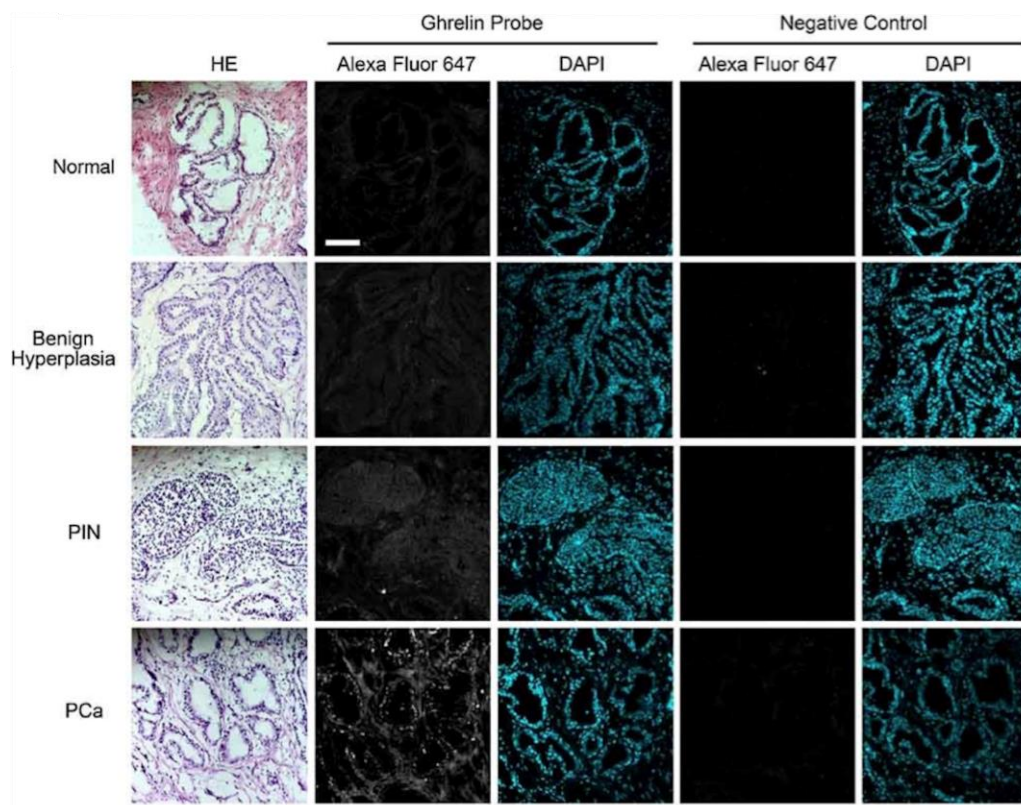
Figure 1.11. Differential ghrelin probe binding in prostate cancer *ex vivo*. Ghrelin probe binding was evaluated in benign tissue subdivided into normal and hyperplasia, prostatic intraepithelial neoplasia (PIN), and prostate cancer using the hapten amplification approach. Negative control was processed in the absence of ghrelin probe. Grayscale = ghrelin probe, Blue = DAPI. Scale bar = 10 μm.[85] Reprinted with permission from John Wiley and Sons.

However, due to interference by tissue autofluorescence and the dye's susceptibility to photobleaching, the fluorescein dye was replaced with a more stable, far-red sulfonated cyanine 5 dye (SulfoCy5) producing the ghrelin-based probe, [Dpr(octanoyl)³, Lys(SulfoCy5)¹⁹]ghrelin(1–19) **(7)**. Douglas et al. reported on the new probe (Figure 1.12), which was determined to have an IC_{50} value of 25.8 nM, a decrease in GHSR affinity compared to the fluorescein-containing peptide.[113] Nevertheless, the SulfoCy5-labelled ghrelin analogue was not only able to detect cardiac GHSR expression, but it was also able to track GHSR expression during differentiation of P19-derived cardiomyocytes. Since then, this analogue has been used to detect the dynamics of

myocardial GHSR in a mouse model of diabetic cardiomyopathy and before and after cardiac transplantation in humans, indicating the utility of fluorescent peptide analogs in mapping GHSR expression in healthy, developing, and diseased heart models, as well as human hearts.[114,115]

The increasing promise of fluorescently labelled ghrelin analogues contributed to a desire to develop ghrelin imaging probes with improved metabolic stability. Recently, ghrelin(1-20) was cyclized through a lactam bridge between Glu[12] and Lys[16] for improved stability of secondary structure, and labelled with the SulfoCy5 dye off the *C*-terminal lysine residue (Figure 1.12).[116] This stapled peptide, cyclo-12,16[Dpr (octanoyl)[3],Glu[12],Lys(SulfoCy5)[20]]ghrelin(1–20) **(8)**, was reported to have an IC$_{50}$ value of 1.0 nM, which is an improved affinity compared to any previously reported fluorescent ghrelin analogue, and was found to image receptor expression in three ovarian cancer cell lines: OvCar8 GHSR positive cells as well as parental OvCar3 and HEYA8 cells.

[Dpr(octanoyl)[3], Lys(fluorescein)[19]]ghrelin(1–19), (6)   [Dpr(octanoyl)[3], Lys(SulfoCy5)[19]]ghrelin(1–19), (7)   cyclo-12,16([Dpr(octanoyl)][3], Glu[12], Lys(SulfoCy5)[20]]ghrelin(1–20)), (8)
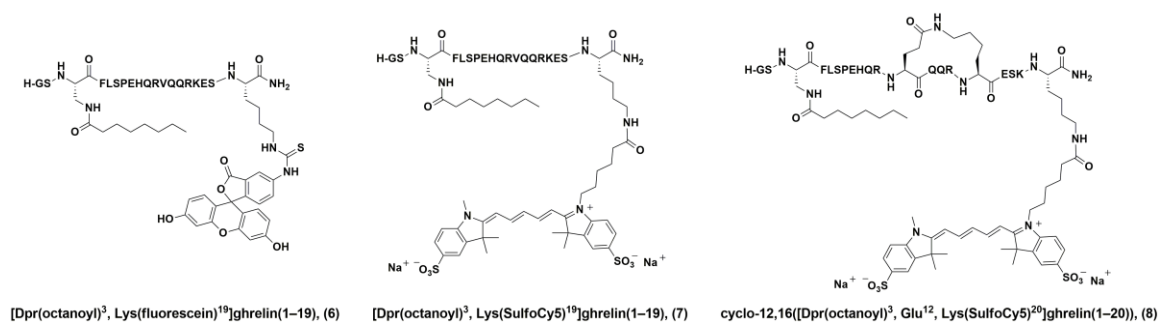
Figure 1.12. Ghrelin-derived fluorescent probes for optical imaging of the GHSR-1a.

The ability to incorporate a bulky dye off the *C*-terminus of truncated ghrelin opened up the possibility of implementing other imaging moieties such as radionuclide-containing prosthetic groups or radiometal chelators in that position, while maintaining desirable binding affinities in the low nanomolar range. Chollet et al. developed full length ghrelin(1-28) and truncated ghrelin(1-16) agonists labelled with gallium-68 via a 7-triazacyclononane,1-glutaric acid-4,7-acetic acid (NODAGA) chelator for PET imaging (Figure 1.14).[93] Highly potent [Ga]-NODAGA peptide conjugates were synthesized and their ligand-receptor interactions were characterized through an inositol triphosphate (IP3) turnover assay resulting in EC$_{50}$ values in the 0.7-2.0 nM range. Initially, the

chelator was conjugated to the peptide at the *N*-terminus, and, unsurprisingly, the modification was not well tolerated and N^α-NODAGA(Ga)-ghrelin(1−28) lost all activity toward the receptor. It is well established in the literature that an available *N*-terminus is necessary for ligand-receptor binding between ghrelin and the GHSR.[54,87] Conversely, by placing the chelator on the Lys[16] residue, away from the *N*-terminal region of the peptide (**9, 10, 11**), the agonistic activity was restored. Analogues **9** and **10** contained the full ghrelin(1-28) sequence while analogue **11** was truncated to the first 16 amino acids. No significant difference in EC_{50} value arose due to the length of the peptide. The possibility of using such radiotracers to study ghrelin signalling *in vivo* also prompted the authors to develop an inverse agonist probe in parallel with the agonist probes. N^α-NODAGA(Ga)-KwFwLL-CONH$_2$ **(12)** is based off a hexapeptide inverse agonist for the GHSR previously developed by the same group.[117] Similar to N^α-NODAGA(Ga)-ghrelin(1−28), the inverse agonist conjugate contained the chelator on the *N*-terminus resulting in a substantial, but not complete, loss in inverse agonist activity toward the receptor. All three ^{68}Ga-labelled agonists and the radiolabelled inverse agonist were evaluated *in vivo* to analyze their pharmacokinetic and non-specific biodistribution profiles. The agonists showed fast blood clearance, poor *in vivo* stability, and high kidney accumulation (Figure 1.13). In contrast, the inverse agonist was found to have slower blood clearance, higher stability, wider tissue distribution, and favoured hepatobiliary metabolism (Figure 1.13). Likely, the peptidomimetic nature of **[^{68}Ga]12** protects it from metabolic degradation, whereas the natural ghrelin sequence is easily recognizable by peptidases.
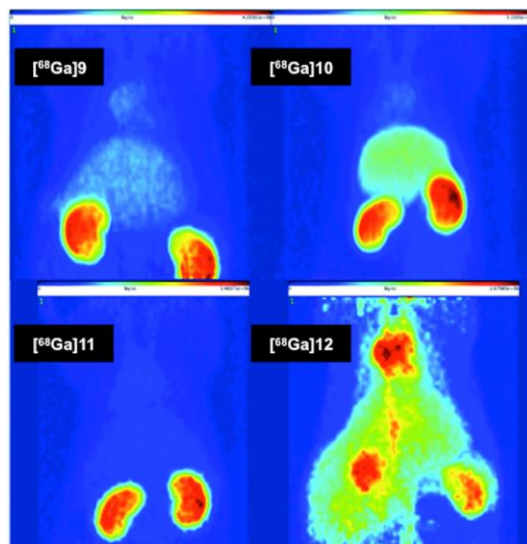
Figure 1.13. Maximum intensity projection of PET studies of ^{68}Ga-labeled compounds **[68Ga]9-12** at 5 min midframe time (duration of measurement: 6 min). The images were scaled to the maximum activity (Bq.cm^{-3}) in each image.[93] Adapted with permission from ref. [93]. Copyright 2012 American Chemical Society.

[K^{16}(NODAGA(^{68}Ga))]ghrelin(1-28), ([^{68}Ga]9)   [Dpr^3, K^{16}(NODAGA(^{68}Ga))]ghrelin(1-28), ([^{68}Ga]10)   [Dpr^3, K^{16}(NODAGA(^{68}Ga))]ghrelin(1-16), ([^{68}Ga]11)

N$^{\alpha}$-NODAGA(^{68}Ga)-KwFwLL-CONH$_2$, ([^{68}Ga]12)   [Dpr^3(octanoyl), Lys^{19}(^{68}Ga-DOTA)]ghrelin(1-19), ([^{68}Ga]14)
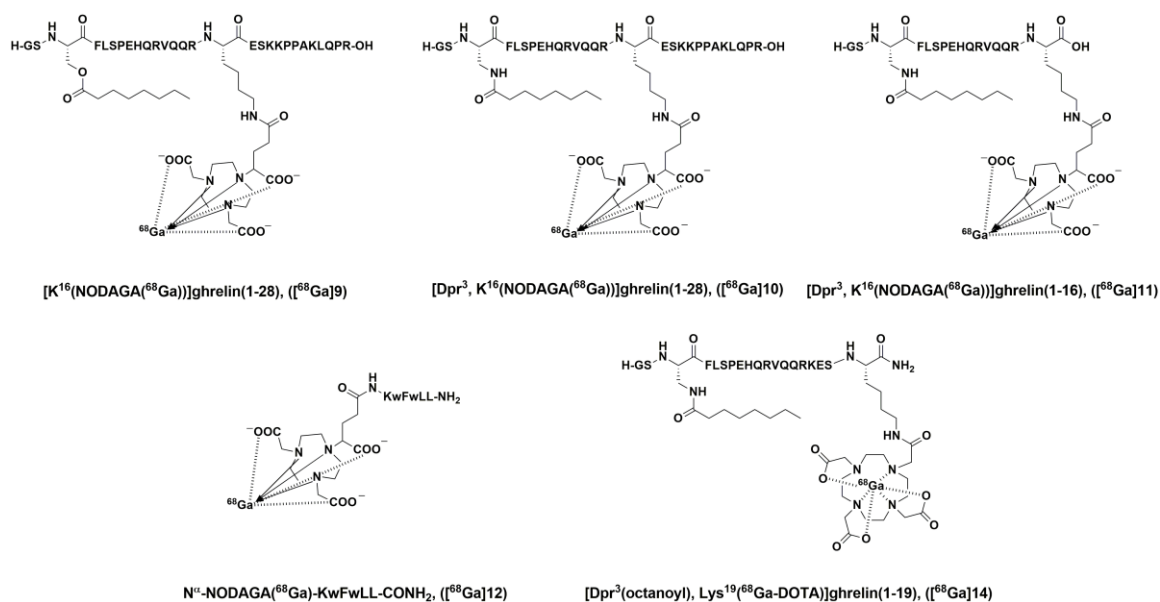
Figure 1.14. Gallium-68 labelled imaging probes for PET imaging of the GHSR-1a.

Another example of incorporating imaging moieties off the *C*-terminus of ghrelin was reported by Murrell et al.[118] The authors developed a novel ^{18}F-prosthetic group based on an azadibenzocyclooctyne (ADIBO) scaffold and demonstrated its ability to be

incorporated into biomolecules through successful conjugation to ghrelin(1-19) with minimal effects on the binding affinity (Figure 1.15). The resulting peptide analogue, [Dpr^3(octanoyl),Lys^{19}(triazole-ADIBO-F)]ghrelin(1–19) (**13**), was found to have an IC$_{50}$ value of 9.7 nM and was labelled with fluoride-18 to produce **[^{18}F]13** in radiochemical yields of 64-66% and molar activities of 0.6-0.9 GBq/µmol.[118]

Charron et al. continued with this theme and reported a probe containing a 1,4,7,10-tetraazacyclododecane-1,4,7,10-tetraacetic acid (DOTA) chelator off the *C*-terminal lysine residue (Figure 1.14), [Dpr^3(octanoyl),Lys^{19}(Ga-DOTA)]ghrelin(1-19) (**14**), which possessed an IC$_{50}$ value of 5.9 nM, comparable to natural ghrelin (IC$_{50}$ = 3.1 nM).[94] The probe was labelled with gallium-68 in radiochemical yields of 54%-83% and molar activities of 10.2-22.8 GBq/µmol. Pre-clinical PET imaging was done on NOD-SCID male mice using two cancer cells lines for xenograft studies: HT1080/GHSR and parental HT1080 cells. While **[^{68}Ga]14** did show increased uptake in the HT1080/GHSR xenografts compared to the parental HT1080 xenograft, significant accumulation in the kidneys prompted the authors to not pursue further *in vivo* evaluation, but rather to focus their efforts on developing shorter ghrelin analogues with improved pharmacokinetic profiles.

Indeed, the same group conducted an extensive structure-activity relationship campaign to develop a truncated ghrelin(1-8) analogue that maintained high affinity for the GHSR.[119] This SAR investigation on the *N*-terminal ghrelin(1-8) sequence identified favourable modifications to residues 1, 3, 4, and 8 resulting in the peptide analogue, [Inp^1,Dpr^3(6-fluoro-2-naphthoate),1-Nal^4,Thr^8]ghrelin(1−8) amide (**15**), which possessed an unprecedented IC$_{50}$ value of 0.11 nM, the strongest affinity ghrelin analogue reported to date (Figure 1.15).[119] Undoubtedly, the most intriguing modification in this analogue is the substitution of the *n*-octanoyl side chain on residue 3 for a fluorine-containing aromatic moiety. Interestingly, this is not the only instance where aromatic substituents were incorporated onto residue 3 of a ghrelin analogue. In 2015, Zhao et al. reported a new class of GOAT inhibitors containing aromatic groups conjugated to the ghrelin sequence in this position via a triazole linkage.[120] However, the residue 3 aromatic moiety in peptide **15** not only contributed to the favourable binding affinity of the compound, but

also added a fluorine atom for ^{18}F-labelling. A molecular docking study using a homology model of the GHSR suggested the naphthyl group not only occupied a hydrophobic subpocket of the receptor's orthosteric site, but also proposed an interaction between the fluorine atom and Val 205 thereby enhancing the binding affinity.[119,121] To label this compound with fluoride-18, a novel [^{18}F]6-fluoro-2-pentafluorophenyl naphthoate ([^{18}F]PFPN) prosthetic group was synthesized via nucleophilic aromatic substitution with fluoride-18, but resulted in low radiochemical yields of the radiofluorinated product **[^{18}F]15** (3.1% RCY), which presents a challenge for *in vivo* evaluation. Likely, the aromatic naphthyl moiety was not sufficiently activated to facilitate the necessary substitution reaction.

[^{18}F][Dpr[3](octanoyl),Lys[19](triazole-ADIBO-F)]ghrelin(1–19) ([^{18}F]13)   [Inp[1],Dpr[3](6-fluoro-2-naphthoate),1-Nal[4],Thr[8]]ghrelin(1-8), ([^{18}F]15)

[1-Nal[4],Lys[5](4-FB)]G-7039, ([^{18}F]16)   [Tyr[4],Lys[5](2-FP)]G-7039, (17)
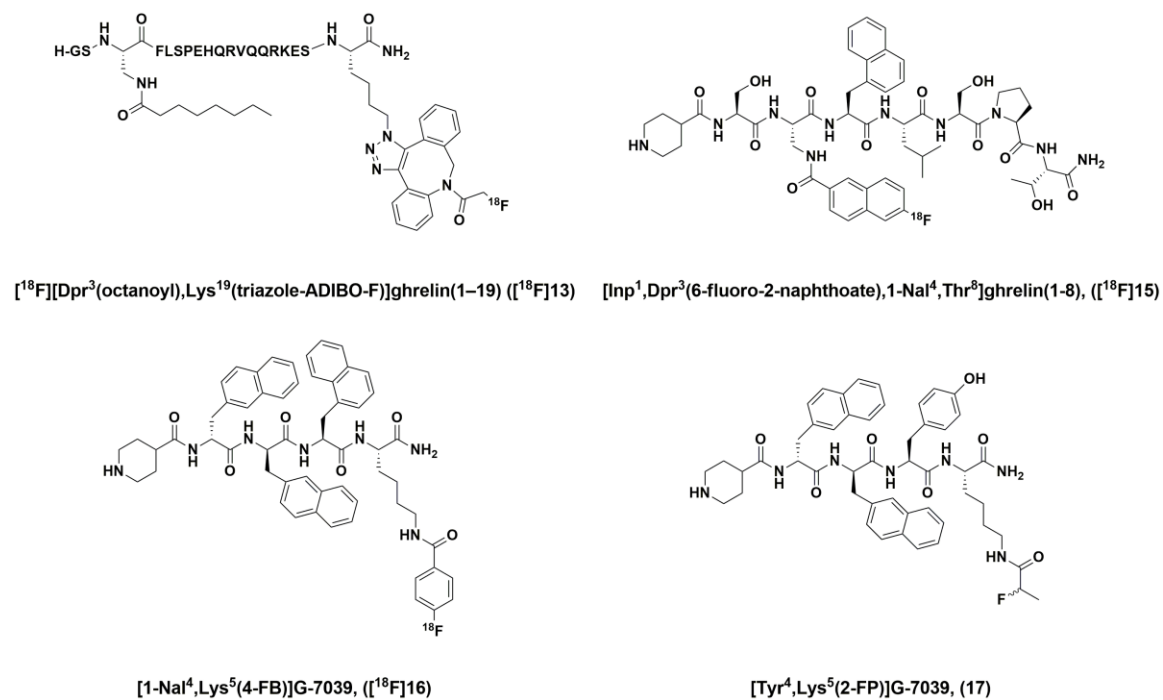
Figure 1.15. Peptidic and peptidomimetic probes for fluorine-18 PET imaging of the GHSR.

1.6.2 Molecular Imaging Agents Based on Other Peptides and Peptidomimetics

Until 2018, most reported peptidic GHSR targeted imaging probes were derived from endogenous ghrelin. Fowkes et al. sought to develop a growth hormone secretagogue-based probe for PET imaging of the GHSR.[122] The authors studied an extensive number of growth hormone secretagogues including GHRP-1, GHRP-2, GHRP-6, ipamorelin, and G-7039 as potential ^{18}F-PET imaging agents. The fluorine-modified secretagogue derivative with the strongest binding affinity for the GHSR was [1-Nal^4,Lys^5(4-fluorobenzoate)]G-7039 (**16**) (Figure 1.15), with an IC_{50} value of 69 nM and an EC_{50} value of 1.1 nM based on Ca^{2+}-mobilization. Conjugation of a N-succinimidyl-4-[^{18}F]fluorobenzoate ([^{18}F]SFB) prosthetic group to [1-Nal^4]G7039 afforded **[^{18}F]16** in an average, overall radiochemical yield of 48% (n=3) and molar activity >34 GBq/μmol. This probe was further analyzed through *in vivo* PET imaging of cardiac GHSR.[123] *Ex vivo* biodistribution revealed that tracer distribution was independent of circulating levels of endogenous ghrelin. However, no significant correlation between tracer uptake and GHSR expression in the heart was observed and there was significant uptake in off target tissues, such as the liver, spleen, lungs, and kidneys. Some of the issues that may have led to the tracer's poor performance *in vivo* include the relatively weak binding affinity for a PET imaging agent and the high cLogP value of 8.76. To address these challenges, Lalonde et al. replaced the 4-fluorobenzoyl prosthetic group off the Lys^5 side chain with a 2-fluoropropionyl (2-FP) group and performed a focused SAR study at the fourth position of ligand **16**.[124] A single amino acid replacement of 1-Nal^4 with tyrosine was identified producing a new ligand for the GHSR, [Tyr^4,Lys^5(2-FP)]G-7039 (**17**) with improved properties (Figure 1.15). Compound **17** was determined to have a 70-fold increase in binding toward the receptor (IC_{50} = 0.28 nM) and a significantly lower cLogP value of 2.77. However, radiosynthesis and *in vivo* evaluation of this new ligand has yet to be reported.

The recent identification of LEAP2 as a second endogenous ligand for the GHSR prompted a desire to develop a fluorescent analogue of LEAP2 suitable for studying the pharmacological behaviour of GHSR:LEAP2 complexes compared to those of GHSR:ghrelin.[63,65,66] Barrile et al. recently reported the resulting fluorescent ligand,

LEAP2(1-17)-DY-647P1 (**18**), also referred to as F-LEAP2, which is based on the first 17 amino acids of the mature peptide sequence (Figure 1.16).[125] By taking advantage of Cys^{17}, which traditionally forms an intramolecular disulfide bridge with Cys^{28} in the endogenous sequence, the authors were able to conjugate a DY-647P1 fluorophore to the *C*-terminus of the ligand. Compound **18** was confirmed to bind strongly to the GHSR with a K_i value of 3.9 nM, which is similar to that of native LEAP2 (K_i = 1.26 nM) and LEAP2(1-14) (K_i = 3.66 nM).[66] Furthermore, analogue **18** caused a decrease in constitutive GHSR activity in a GPTγS functional assay, indicating that the inverse agonist properties of the peptide were not affected by the addition of the fluorophore. An *in vivo* bioactivity assessment study revealed that pre-treatment of mice with intracerebroventricular (ICV) injected **18** inhibited ghrelin-induced food intake by ~40%, similar to native LEAP2. Additionally, cell imaging studies of the new probe showed that the fluorescent signal was limited to the cell surface indicating that the fluorescently-labelled peptide does not induce receptor internalization, which is consistent with previous reports.[65] Finally, *ex vivo* imaging of mouse brain tissue indicated the strongest intensity of **18** was located in the hypothalamus, consistent with the high receptor expression reported for this brain region. LEAP2(1-17)-DY-647P1 represents the first probe based on an antagonist/inverse agonist for fluorescence imaging of the GHSR and could be a valuable tool for further pharmacological analyses of this receptor.

LEAP2(1-17)-DY-647P1, (18)
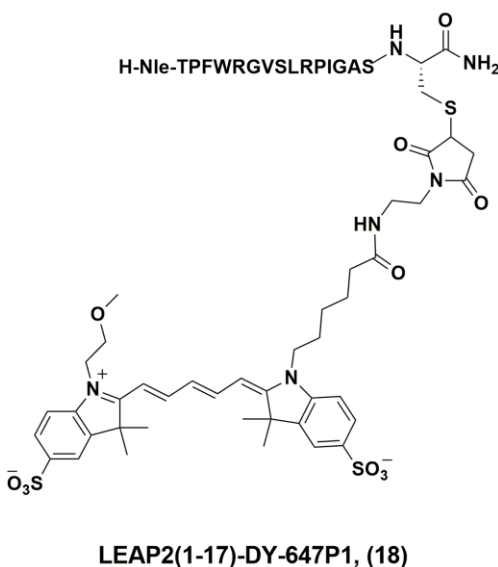
Figure 1.16. Fluorescently labelled LEAP-2 derivative for optical imaging of the GHSR.

Table 1.1: Properties and radiosynthetic results of peptidic GHSR imaging probes.

Compound No.	IC$_{50}$	EC$_{50}$	RCY	clogD	Imaging Modality	Ref.
1 (fig. 1.9)	27.9 nM	N.R.	N.R.	N.R.	^{18}F-PET	[89]
2 (fig. 1.9)	35 nM	N.R.	N.R.	N.R.	^{99m}Tc-SPECT	[89]
3 (fig. 1.10)	N.R.	N.R.	> 85%	0.73[b]	^{99m}Tc-SPECT	[95]
4 (fig. 1.10)	1.1 nM[a]	N.R.	> 85%	0.88[b]	^{99m}Tc-SPECT	[95]
5 (fig. 1.10)	2.1 nM[a]	N.R.	> 95%	1.10[b]	^{99m}Tc-SPECT	[95]
red-ghrelin	19 nM[a]	88 nM	N/A	N.R.	Optical	[97]
6 (fig. 1.12)	9.5 nM	N.R.	N/A	N.R.	Optical	[100]
7 (fig. 1.12)	25.8 nM	N.R.	N/A	N.R.	Optical	[113]
8 (fig. 1.12)	1.0 nM	N.R.	N/A	N.R.	Optical	[116]
9 (fig. 1.14)	N.R.	0.72 nM	N.R.	N.R.	^{68}Ga-PET	[93]
10 (fig. 1.14)	N.R.	1.91 nM	N.R.	N.R.	^{68}Ga-PET	[93]
11 (fig. 1.14)	N.R.	1.41 nM	N.R.	N.R.	^{68}Ga-PET	[93]
12 (fig. 1.14)	N.R.	643.2 nM	N.R.	N.R.	^{68}Ga-PET	[93]
13 (fig. 1.15)	9.7 nM	N.R.	64-66%	N.R.	^{18}F-PET	[118]
14 (fig. 1.14)	5.9 nM	N.R.	54-83%	N.R.	^{68}Ga-PET	[94]
15 (fig. 1.15)	0.11 nM	N.R.	3.1%	N.R.	^{18}F-PET	[119]
16 (fig. 1.15)	69 nM	1.1 nM	48%	8.76	^{18}F-PET	[122]
17 (fig. 1.15)	0.28 nM	0.121 nM	N.R.	2.77	^{18}F-PET	[124]
18 (fig. 1.16)	3.9 nM[a]	N.R.	N.R.	N.R.	Optical	[125]

N.R. – not reported; [a] Reported as K$_i$; [b] Lipophilicity determined experimentally

1.6.3 Molecular Imaging Agents Based on Small Molecules

In 2007, Bayer pharmaceuticals reported a number of quinazolinone derivatives as a new class of small molecule GHSR antagonists for the treatment of obesity and diabetes.[126] The piperidine-substituted quinazolinone scaffold (Figure 1.17) showed inherently nanomolar affinity for the receptor, while alkylating the piperidine ring nitrogen (R$_1$) gave rise to the functionally antagonistic activity.
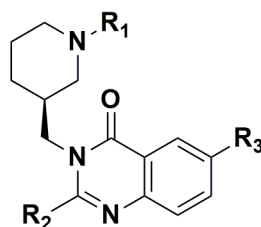
Figure 1.17. General scaffold for quinazolinone-derived small molecule GHSR-1a imaging probes.

In 2011, Potter et al. sought to utilize this class of high-affinity small molecules to develop GHSR targeting PET radioligands.[127] One of the molecules reported by Bayer, racemic 6-(4-fluorophenoxy)-3-(piperidin-3-yl)methyl)-2-o-tolylquniazolin-4(3H)-one (**19**), possessed a binding affinity of $K_i = 0.9$ nM toward the GHSR (Figure 1.18).[126] The authors modified this compound to incorporate a carbon-11 radionuclide off the piperidine nitrogen (R_1). The resulting imaging probe, (**20**), was synthesized and found to bind to the GHSR with a K_i value of 22 nM (Figure 1.18). Compound **[^{11}C]20** was labelled in a non decay-corrected radiochemical yield of 25%, a molar activity of 8300 mCi/μmol, and a radiochemical purity of 99%. Due to the high density of the receptor in the hypothalamus and pituitary, the authors sought to evaluate their probe as a potential radiotracer for brain PET imaging of the GHSR. *In vivo* PET imaging in mice revealed low tracer accumulation in the hypothalamus with a gradual increase in uptake to 0.86% ID/g over the 90-minute imaging period. Signal in the hypothalamus was significantly blocked with **19**, indicating receptor-mediated uptake. However, some tracer uptake in the rest of the brain, made up of tissues with low GHSR density, indicated non-specific tracer uptake, which was confirmed in a blocking study. The authors postulated that the lipophilicity of the tracer (clogD = 4.1) may be too high to be an effective CNS radioligand and recommended that future GHSR radioligands for brain PET imaging have picomolar binding affinities and lower lipophilicities. Of note, this was the first report of a radiolabelled imaging probe for PET imaging of the GHSR and the first report of *in vivo* GHSR imaging data.
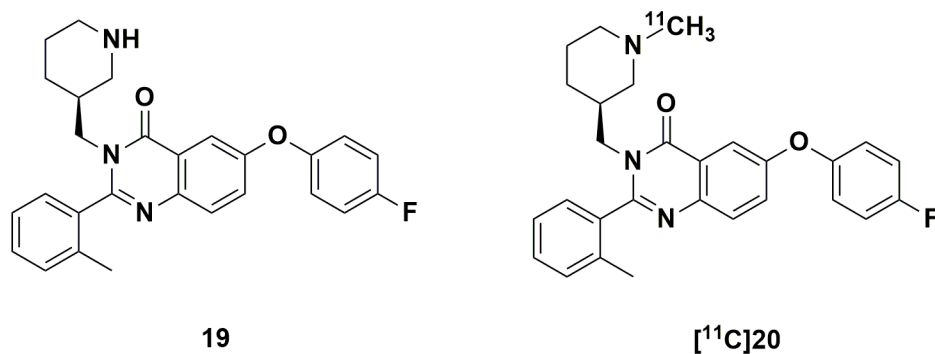
Figure 1.18. Quinazolinone derivative reported by Bayer pharmaceuticals (**19**) and resulting ^{11}C-labelled probe **([11C]20)** from Potter et al.[126,127]

Later in 2017, Kawamura et al. continued the endeavour of labelling small molecule GHSR antagonists with PET radionuclides and reported three new radioligands: **21, 22, and 23** (Figure 1.19) with low nanomolar binding affinities (K_i = 16 nM, 4.0 nM, 7.0 nM respectively).[128] Compound **21** was labelled with fluoride-18 in a low radiochemical yield of 2.5% and a high molar activity of 300 GBq/µmol. Compounds **22** and **23** were labelled with carbon-11 in radiochemical yields of 1.7% and 16%, respectively and molar activities of 240 GBq/µmol and 100 GBq/µmol, respectively. *In vivo* biodistribution studies showed relatively low levels of tracer uptake in the mouse brain for all three radioligands, likely due to their relatively high lipophilicities (Table 1.2). Compound **[18F]21** exhibited increased bone uptake over 60 min post-injection (p.i.), indicative of ^{18}F-defluorination. Interestingly, compound **[11C]23** exhibited relatively high tracer uptake in the pancreas (6.5% ID/g) at 60 min p.i. Pre-treatment of the mouse with 10 mg/kg of a high-affinity GHSR antagonist, YIL781 (K_i = 17 nM)[129], resulted in significantly less uptake of **[11C]23** in the pancreas at 60 min p.i. However, this change in radioactive signal was found to be dependent on the tracer administered. Compound **[11C]23** showed the largest decrease in signal (20%) with pre-treatment of YIL781 compared to **[11C]22** and **[18F]21**, which showed little to no change in signal compared to the control. Figure 1.20 shows a representative PET image of **[11C]23** uptake with and without pre-treatment with the antagonist.
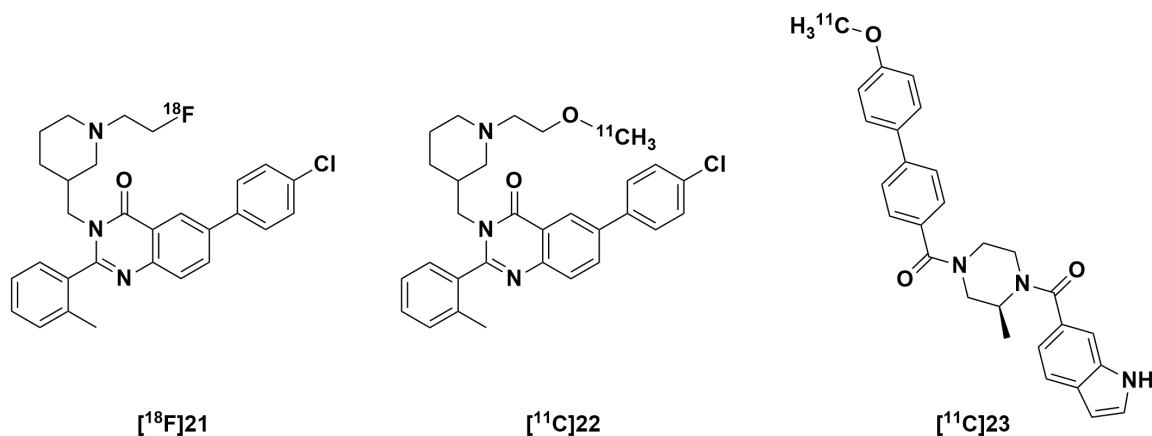
Figure 1.19. Structures of small molecule GHSR-1a antagonists for ^{18}F-PET and ^{11}C-PET imaging reported by Kawamura et al.[128]
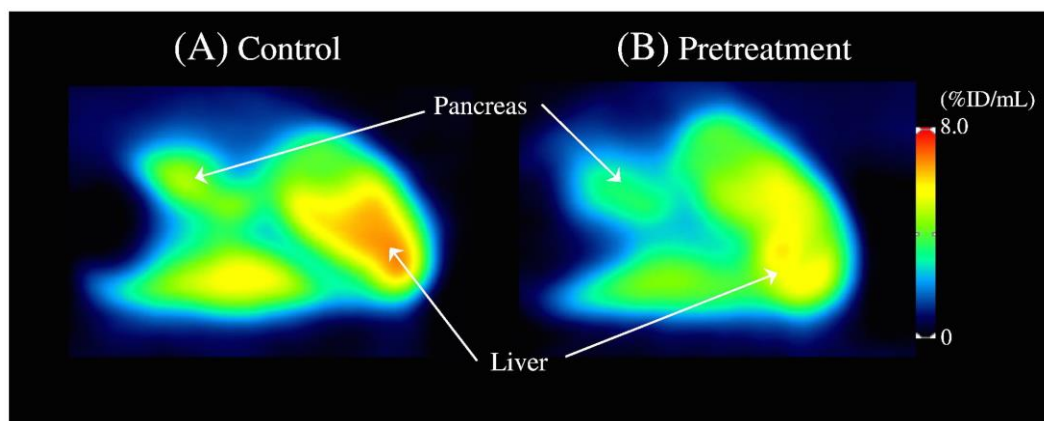
Figure 1.20. Representative PET images of mice using **[11C]23** (20–50 MBq/140–520 pmol) in the control (A) and pretreatment with YIL781 (10 mg/kg b.w.) conditions.[128] Reprinted with permission from Elsevier.

Another group seeking to generate compounds suitable for GHSR imaging in the brain reported a SAR study on fluorinated quinazolinone derivatives with low nanomolar affinities.[130] Substitution at the piperidine nitrogen is known to have an effect on binding to the receptor; therefore, the authors chose a known, high affinity, quinazolinone derivative as a starting point for SAR studies, compound **24**.[131] Results from the study revealed that both enantiomers of the original lead candidate, **(S)-24** and **(R)-24**, and a new derivative, **(S)-25** had the strongest binding affinities (IC$_{50}$ = 2.2 nM, 3.9 nM, and 2.7 nM, respectively). Further *in vitro* evaluation of **(S)-24, (R)-24, and (S)-25** confirmed

all three molecules to be potent partial agonists with EC_{50} values of 0.7 nM, 0.6 nM, and 1.0 nM, respectively. Furthermore, the calculated $logD_{7.4}$ values for these compounds were lower than previously reported quinazolinone derivatives ($clogD_{7.4}$ = 2.1 for (**R/S**)-**24** and $clogD_{7.4}$ = 2.9 for (**S**)-**25**), which are expected to be favourable for brain imaging. However, the difficulty with these compounds lies in their ability to be translated into radiolabelled imaging agents. While each molecule possesses a fluorine atom, the position of the aromatic fluorine is challenging for ^{18}F-labelling due to the weakly activated nature of the aromatic ring for conventional substitution techniques. The use of relatively mild ^{18}F-fluorination methodologies for such difficult aromatic molecules is becoming more commonplace; however, radiolabelling of these molecules has yet to be reported.

(S)-24   **(R)-24**   **25**
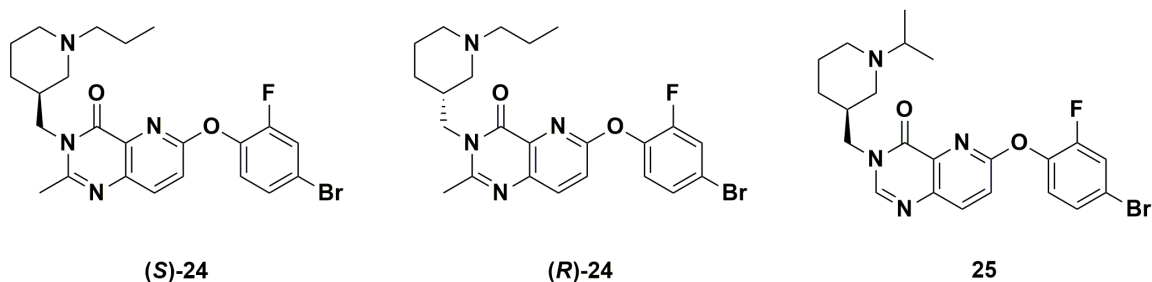
Figure 1.21. High affinity quinazolinone-derived partial agonists for the GHSR-1a reported by Moldovan et al.[130]

The most recent attempt to develop quinazolinone derivatives for ^{18}F-fluorine PET imaging of the GHSR was reported in 2018 by Hou et al.[132] The authors also used the compound initially reported by Bayer (**19**) as their starting point for SAR studies. The study identified three small molecule derivatives with low nanomolar to sub-nanomolar binding affinities toward the receptor. One key structural modification was the replacement of the fluorophenyl group with a benzothiazolyl group, which resulted in improved binding affinities. Additionally, modifying the alkyl substituent on the piperidine nitrogen to a fluoroethyl group allowed incorporation of fluorine in a position readily accessible for radiosynthetic incorporation of fluorine-18. Two derivatives bearing fluorine substituents, **26** and **27**, possessed low nanomolar affinity toward the receptor with IC_{50} values of 9.3 nM and 20.6 nM, respectively. Both compounds were successfully radiolabelled with fluoride-18 through nucleophilic aliphatic substitution of a

tosylate precursor with fluoride-18 in radiochemical yields of 10.3% and 7.0% respectively. An additional fluorine-bearing derivative identified in this work, **28**, retained the isopropyl group off the piperidine nitrogen, but rather incorporated fluorine in place of the methyl group on the tolyl portion of the molecule. The resulting lead candidate showed sub-nanomolar binding affinity with an IC_{50} of 0.02 nM, which represents the strongest binding affinity of any GHSR ligand reported to date. In order to better comprehend the binding mode of quinazolinone derivatives toward the GHSR, the authors performed molecular docking studies with several of their developed derivatives, including compound **28**, utilizing a previously validated homology model of the GHSR (Figure 1.23A).[121] The docked poses placed the piperidine amine in close proximity to Glu124 on the receptor, which is regarded as an anchoring point for binding via an ionic interaction. Significant π-π stacking interactions between the aromatic substituents on the small molecules and Phe279 and Tyr106 in the receptor were established. Interestingly, the fluorine in compound **28** was involved in the π-π stacking interaction with Phe279 resulting in an additional binding interaction, not observed in derivatives bearing the methylphenyl group, that may contribute to its unprecedented binding affinity (Figure 1.23B). Radiolabelling of **28** with fluoride-18 was attempted through nucleophilic aromatic substitution of a nitro-bearing precursor. However, the labelling attempts were unsuccessful possibly due to the insufficient activation of the aromatic ring. Further development of the radiosynthesis for this molecule has yet to be reported.
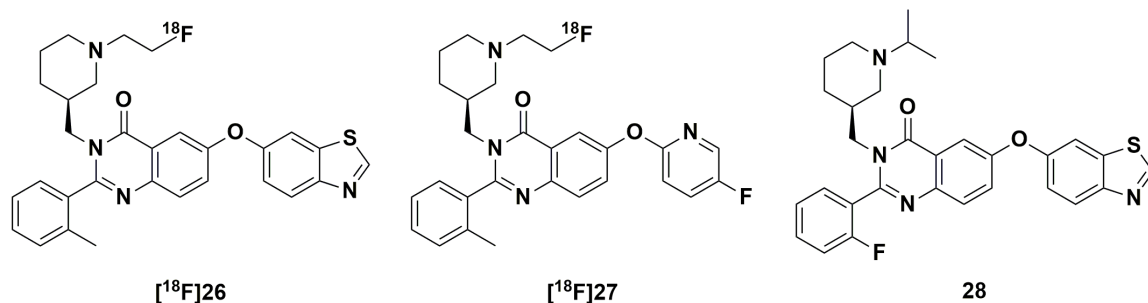
Figure 1.22. Small molecule quinazolinone analogues reported by Hou et al. for ^{18}F-PET imaging of the GHSR.[132]
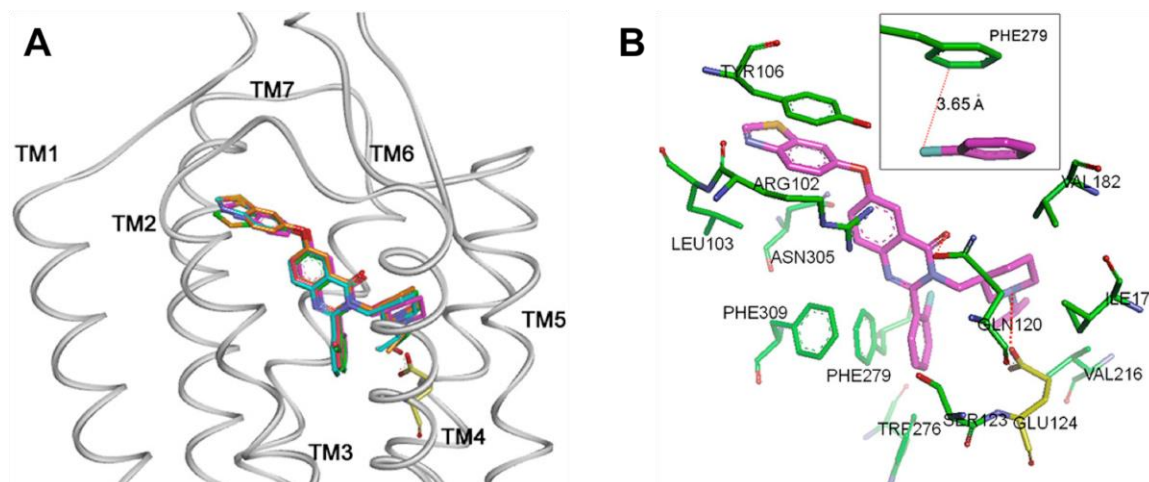
Figure 1.23. The complex structures from molecular docking studies using a homology model of GHS-R1a. (A) Side view of quinazolinone derivatives superimposed in the GHS-R1a; (B) A view from extracellular side; 3D depiction of the binding mode and surrounding residues for compound **28**. Ligands are shown in purple sticks; the residues are shown in green sticks except for Glu124 that is shown in yellow. The insert figures show the closest distances between the fluorine of quinazolinone derivative **28** and phenyl ring in Phe279 on the receptor. Adapted with permission from ref. [132]. Copyright 2018 American Chemical Society.

Table 1.2. Properties and radiosynthetic results of small molecule GHSR imaging probes.

Compound No.	IC$_{50}$	EC$_{50}$	RCY	clogD	Imaging Modality	Ref.
20 (fig. 1.18)	22 nM[a]	N.R.	25%	4.1	^{11}C-PET	[127]
21 (fig. 1.19)	16 nM[a]	N.R.	2.5%	5.4	^{18}F-PET	[128]
22 (fig. 1.19)	4.0 nM[a]	N.R.	1.7%	5.1	^{11}C-PET	[128]
23 (fig. 1.19)	7.0 nM[a]	N.R.	16%	3.9	^{11}C-PET	[128]
(*S*)-24 (fig. 1.21)	2.2 nM	0.7 nM	N.R.	2.1	^{18}F-PET	[130]
(*R*)-24 (fig. 1.21)	3.9 nM	0.6 nM	N.R.	2.1	^{18}F-PET	[130]
25 (fig. 1.21)	2.7 nM	1.0 nM	N.R.	2.9	^{18}F-PET	[130]
26 (fig. 1.22)	9.3 nM	N.R.	7.0%	4.25	^{18}F-PET	[132]
27 (fig. 1.22)	20.6 nM	N.R.	10.3%	3.40	^{18}F-PET	[132]
28 (fig. 1.22)	0.02 nM	N.R.	N.R.	2.39	^{18}F-PET	[132]

N.R. – not reported; [a] Reported as K$_i$

Since the discovery of the GHSR, there has been a growing interest in advancing our understanding of this receptor's dynamic processes and exploring the therapeutic potential of pharmaceuticals for this target. Molecular imaging provides a minimally invasive window into investigating GHSR expression in normal and disease states. In the last decade, the number of molecular imaging agents targeting this receptor has steadily grown resulting in probes for nuclear imaging modalities (SPECT/PET) using ^{11}C, ^{18}F, ^{68}Ga and ^{99m}Tc radioisotopes, and optical imaging through fluorescent dyes. This development has resulted in novel ligands with high affinity for the GHSR based on ghrelin, growth hormone secretagogues, and small molecules previously discovered for therapeutic applications. These probes continue to evolve as researchers seek to optimize their physical and biological properties and proceed to *in vivo* evaluation. The optical imaging probes have been used for cellular and tissue imaging to investigate the GHSR as a potential biomarker for cardiac disease, and PET imaging probes are being developed for potential cancer and brain imaging. In addition to the incorporation of imaging moieties onto known GHSR compounds, novel ligands with imaging in mind have resulted from structure-activity relationship studies. The acquisition of knowledge regarding the dynamic function of this receptor and ghrelin is continuing to unfold, revealing numerous therapeutic possibilities. The integration of GHSR targeted imaging probes with ligands currently under investigation as potential therapeutics could be a step toward a more harmonized approach in drug research providing valuable information on biodistribution, kinetics, and metabolic behaviour of such drug molecules and the treatment monitoring of receptor-influenced disorders.

1.7   Metabolic Stability of Peptides

A key part of the process to bring an imaging agent from the bench to the clinic is in evaluating its pharmacokinetic behaviour *in vivo*. Pharmacokinetics is defined as the branch of pharmacology that describes the movement of drug molecules within the body.[133] Upon identification of a targeting entity and successful conjugation of a signalling moiety for imaging, the imaging probe undergoes pre-clinical *in vivo* evaluation to observe its pharmacokinetic behaviour.

Peptide-based drug candidates have demonstrated wide versatility in both structure and function making them highly active toward specific biological targets, such as G protein-coupled receptors (GPCR). They also feature a low molecular weight relative to larger biomolecules such as antibodies, which enables rapid penetration and accumulation in target tissues.[134] Additionally, many radiolabelling and bioconjugation techniques have been applied to peptides in the development of peptide-based imaging agents.[8,135,136] Despite these promising advantages of peptides, there are obstacles that limit their utility, particularly in their pharmacokinetic profile. Proteolysis is the predominant reason why natural peptides may demonstrate low metabolic stability resulting in a low plasma half-life, indicating rapid clearance from the bloodstream.[137] While the presence of proteases is ubiquitous throughout the body, degradation of peptides primarily occurs in tissues including the blood, liver, kidneys, and gastrointestinal tract.[138] The metabolic rate of peptides is highly dependent on factors that stem from the nature of its chemical structure including size, charge, and lipophilicity.[133] Most natural peptides tend to be highly hydrophilic and therefore have a tendency toward high kidney uptake and a strong preference for renal clearance. However, it is possible for smaller (<1 kDa), more lipophilic peptides to be passively taken up in the liver, metabolized, and excreted through hepatobiliary elimination.[133]

1.7.1 Improving the Metabolic Stability of Peptides

To combat these limitations, several chemical modifications to the peptide structure have been described as strategies to improve the pharmacokinetic profile. Simple modifications to the *N*- and *C*-termini, such as *N*-acetylation and *C*-amidation, aid to disguise the peptide from exopeptidases, which hydrolyze peptides inward from the termini regions. Head-to-tail cyclization of a peptide also accomplishes this goal by covalently joining the *N*- and *C*-termini while introducing increased structural rigidity, which may inhibit protease binding and, therefore, increase metabolic stability. Cyclization of peptides not only affords an increase in proteolytic stability, but also an increase in conformational rigidity, which may increase target specificity. In addition to head-to-tail cyclization, internal cyclization between side chains is also a method to increase rigidity and give rise to secondary structure. Some examples of internal cyclization include, but are not limited

to, the formation of a disulphide bridge, lactam formation, ring-closing metathesis, Diels-Alder cycloaddition, and copper-catalyzed azide-alkyne cycloaddition (CuAAC).[139] Synthetic side chain to side chain cyclization is also termed 'peptide stapling'.

Other methods to improve the metabolic stability of peptides include substituting the natural *L*-amino acids for unnatural *D*-amino acids or other non-canonical amino acids. The use of unnatural amino acids renders that region of the molecule unrecognizable to proteases and thus improves stability. Additionally, amide bond surrogates may be implemented with the same idea of providing an unrecognizable environment to proteases. Amide bonds that are particularly susceptible to protease cleavage may be replaced with a transition-state mimic, which is a functional group that resembles the tetrahedral intermediate observed during the transition state of amide bond hydrolysis, but is not itself hydrolyzed.[140] Other peptide backbone alterations may include the use of beta amino acids, *N*-alkylation of the amide nitrogen, aza-peptides, α-aminoxy acids, and thioamides, heterocycles, alkenes, and fluoroalkenes as amide bond surrogates (Figure 1.24).[140–144] Another technique to overcome the barriers that limit peptides as drugs and imaging agents are the use of peptoids. Peptoids are a class of peptidomimetics wherein the amino acid side chain is positioned on the amide nitrogen as opposed to the α-carbon.[145] This structural modification provides stability of the amide bond toward protease degradation and, furthermore, eliminates the presence of stereocentres on the peptoid backbone. As a result, peptoids, and more specifically macrocylic peptoids, are also highly rigid, which could increase their target selectivity provided they maintain strong binding affinity and activity toward their intended target.

The techniques outlined thus far are predominantly used to improve the metabolic stability of peptides. Other techniques, such as PEGylation and glycosylation, may be used to tune the distribution and excretion of the ligand. PEGylation involves the conjugation of a polyethylene glycol (PEG) chain to the peptide while glycosylation involves conjugating a carbohydrate through the formation of a glycosidic linkage. Both techniques are strategies designed to increase the hydrophilicity and molecular weight of the peptide resulting in decreased hepatic and renal clearance ultimately elongating the plasma half-life of the compound.[138,146,147] Another technique to increase plasma half-life

includes the use of long-lived proteins such as human serum albumin (HSA). HSA may be directly conjugated to the target peptide or indirectly tethered through an albumin-binding molecule such as phenol red.[147] While the toolbox of chemical modifications for peptides to improve their pharmacokinetic profile is large and continuously growing, there is always a balance between making structural modifications to improve metabolic stability and maintaining the biological affinity and activity of the ligand toward its target.
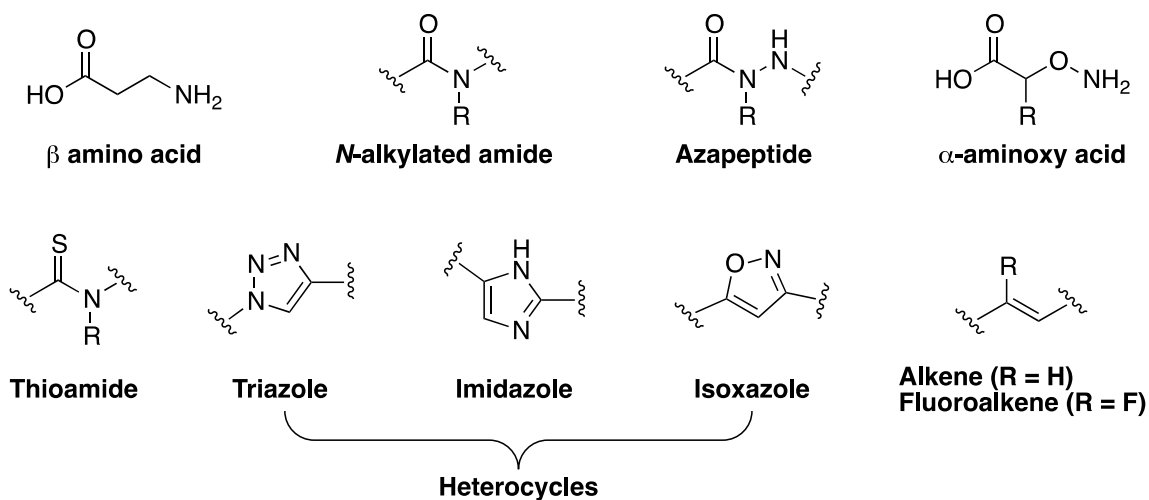
Figure 1.24. Examples of peptide backbone modifications to improve metabolic stability.

1.8 Summary

This thesis documents the development of ^{18}F-labelled, high-affinity GHSR imaging probes. The methods and compounds discussed here may be used toward ^{18}F-PET imaging of the GHSR in cancer and cardiac disease states. Chapter 2 describes the radiosynthesis of two ghrelin(1-8) analogues bearing non-activated aromatic groups using a prosthetic group approach from hypervalent iodonium ylide precursors. One of these analogues is also evaluated *in vitro* and through initial preclinical studies. Chapter 3 investigates the metabolic stability of this ghrelin(1-8) analogue including a targeted structure-activity-stability relationship study to address identified metabolic soft-spots and develop a more robust, high-affinity ghrelin analogue for imaging the GHSR. Chapter 4 discusses the synthesis of a spirocyclic iodonium ylide on a quinazolinone scaffold as an ^{18}F-labelling precursor toward a high-affinity small molecule GHSR

radiotracer. Chapter 5 presents the application of fragment-based drug design as a novel strategy toward the development of molecular imaging probes by identifying new targeting scaffolds that inherently contain fluorine for ^{18}F-PET imaging. Finally, chapter 6 will recapitulate the main findings of this thesis and summarize the future prospects of this work in the field of molecular imaging.

1.9   References

1   M. L. James and S. S. Gambhir, *Physiol. Rev.*, 2012, **92**, 897–965.

2   S. . Meikle, P. Kench, M. Kassiou and R. B. Banati, *Phys. Med. Biol.*, 2005, **50**, R45–R61.

3   F. Wuest, in *PET Chemistry*, eds. P. A. Schubiger, L. Lehmann and M. Friebe, Springer, 2007.

4   P. A. Schubiger, L. Lehmann and M. Friebe, *PET Chemistry*, 2007.

5   O. Jacobson, D. O. Kiesewetter and X. Chen, *Bioconjug. Chem.*, 2015, **26**, 1–18.

6   D. W. Kim, D. Ahn, Y. Oh, S. Lee and H. S. Kil, *J. Am. Chem. Soc.*, 2006, **128**, 16394–16397.

7   X. Deng, J. Rong, L. Wang, N. Vasdev, L. Zhang, L. Josephson and S. H. Liang, *Angew. Chemie - Int. Ed.*, 2019, **58**, 2580–2605.

8   R. Schirrmacher, B. Wängler, J. Bailey, V. Bernard-Gauthier, E. Schirrmacher and C. Wängler, *Semin. Nucl. Med.*, 2017, **47**, 474–492.

9   M. Kuchar and C. Mamat, *Molecules*, 2015, **20**, 16186–16220.

10   G. S. K. Hamacher, H.H. Coenen, *J. Nucl. Med.*, 1986, **27**, 235–238.

11   F. Hasler, O. F. Kuznetsova, R. N. Krasikova, T. Cservenyak, B. B. Quednow, F. X. Vollenweider, S. M. Ametamey and G. Westera, *Appl. Radiat. Isot.*, 2009, **67**, 598–601.

12   G. Vaidyanathan and M. R. Zalutsky, *Nat. Protoc.*, 2006, **1**, 1655–1661.

13   D. Thonon, D. Goblet, E. Goukens, G. Kaisin, J. Paris, J. Aerts, S. Lignon, X. Franci, R. Hustinx and A. Luxen, *Mol. Imaging Biol.*, 2011, **13**, 1088–1095.

14   U. Ackermann, S. D. Yeoh, J. I. Sachinidis, S. S. Poniger, A. M. Scott and H. J. Tochon-Danguy, *J. Label. Compd. Radiopharm.*, 2011, **54**, 671–673.

15   K. P. Li, M. K. Hu, C. Kwang-Fu Shen, W. Y. Lin, S. Hou, L. B. Zhao, C. Y.

Cheng and D. H. Shen, *Appl. Radiat. Isot.*, 2014, **94**, 113–117.

16   I. N. Petersen, J. Madsen, C. Bernard, M. Poulie, A. Kjær and M. M. Herth, *Molecules*, 2019, **24**, 3436.

17   J.-H. Chun, S. Liu, Y.-S. Lee and V. W. Pike, *J. Org. Chem.*, 2010, **75**, 3332–3338.

18   N. Ichiishi, A. F. Brooks, J. J. Topczewski, M. E. Rodnick, M. S. Sanford and P. J. H. Scott, *Org. Lett.*, 2014, **16**, 3224–3227.

19   B. H. Rotstein, N. a Stephenson, N. Vasdev and S. H. Liang, *Nat. Commun.*, 2014, **5**, 4365.

20   B. H. Rotstein, L. Wang, R. Y. Liu, J. Patteson, E. E. Kwan, N. Vasdev and S. H. Liang, *Chem. Sci.*, 2016, **7**, 4407–4417.

21   J. E. Jakobsson, G. Grønnevik and P. J. Riss, *Chem. Commun.*, 2017, **53**, 12906–12909.

22   S. H. Liang, L. Wang, N. A. Stephenson, B. H. Rotstein and N. Vasdev, *Nat. Protoc.*, 2019, **14**, 1530–1545.

23   H. Fu, W. Tang, Z. Chen, V. V. Belov, G. Zhang, T. Shao, X. Zhang, Q. Yu, J. Rong, X. Deng, W. Han, S. J. Myers, P. Giffenig, L. Wang, L. Josephson, Y. Shao, A. T. Davenport, J. B. Daunais, M. Papisov, H. Yuan, Z. Li, S. F. Traynelis and S. H. Liang, *ACS Chem. Neurosci.*, 2019, **10**, 2263–2275.

24   T. L. Ross, J. Ermert, C. Hocke and H. H. Coenen, *J. Am. Chem. Soc.*, 2007, **129**, 8018–8025.

25   M. Tredwell, S. M. Preshlock, N. J. Taylor, S. Gruber, M. Huiban, J. Passchier, J. Mercier, C. Génicot and V. Gouverneur, *Angew. Chemie - Int. Ed.*, 2014, **53**, 7751–7755.

26   N. J. Taylor, E. Emer, S. Preshlock, M. Schedler, M. Tredwell, S. Verhoog, J. Mercier, C. Genicot and V. Gouverneur, *J. Am. Chem. Soc.*, 2017, **139**, 8267–8276.

27   A. V. Mossine, A. F. Brooks, K. J. Makaravage, J. M. Miller, N. Ichiishi, M. S. Sanford and P. J. H. Scott, *Org. Lett.*, 2015, **17**, 5780–5783.

28   K. J. Makaravage, A. F. Brooks, A. V. Mossine, M. S. Sanford and P. J. H. Scott, *Org. Lett.*, 2016, **18**, 5440–5443.

29   C. W. Murray and D. C. Rees, *Nat. Chem.*, 2009, **1**, 187–192.

30   A.-D. Gorse, *Curr. Top. Med. Chem.*, 2006, **6**, 3–18.

31   D. Joseph-McCarthy, A. J. Campbell, G. Kern and D. Moustakas, *J. Chem. Inf. Model.*, 2014, **54**, 693–704.

32   M. Congreve, R. Carr, C. Murray and H. Jhoti, *Drug Discov. Today*, 2003, **8**, 876–877.

33   D. E. Scott, A. G. Coyne, S. A. Hudson and C. Abell, *Biochemistry*, 2012, **51**, 4990–5003.

34   A. Lawson, *Curr. Top. Med. Chem.*, 2015, **15**, 2523–2527.

35   G. Bollag, J. Tsai, J. Zhang, C. Zhang, P. Ibrahim, K. Nolop and P. Hirth, *Nat. Rev. Drug Discov.*, 2012, **11**, 873–886.

36   S. Cang, C. Iragavarapu, J. Savooji, Y. Song and D. Liu, *J. Hematol. Oncol.*, 2015, **8**, 1–8.

37   C. W. Murray, D. R. Newell and P. Angibaud, *Medchemcomm*, 2019, **10**, 1509–1511.

38   W. D. Tap, Z. A. Wainberg, S. P. Anthony, P. N. Ibrahim, C. Zhang, J. H. Healey, B. Chmielowski, A. P. Staddon, A. L. Cohn, G. I. Shapiro, V. L. Keedy, A. S. Singh, I. Puzanov, E. L. Kwak, A. J. Wagner, D. D. Von Hoff, G. J. Weiss, R. K. Ramanathan, J. Zhang, G. Habets, Y. Zhang, E. A. Burton, G. Visor, L. Sanftner, P. Severson, H. Nguyen, M. J. Kim, A. Marimuthu, G. Tsang, R. Shellooe, C. Gee, B. L. West, P. Hirth, K. Nolop, M. van de Rijn, H. H. Hsu, C. Peterfy, P. S. Lin, S. Tong-Starksen and G. Bollag, *N. Engl. J. Med.*, 2015, **373**, 428–437.

39   A. D. Howard, S. D. Feighner, D. F. Cully, J. P. Arena, P. A. Liberator, C. Rosenblum, M. Hamelin, D. L. Hreniuk, O. C. Palyha, J. Anderson, P. S. Paress, C. Diaz, M. Chou, K. K. Liu, K. K. Mckee, S. Pong, L. Chaung, A. Elbrecht, M. Dashkevicz, R. Heavens, M. Rigby, D. J. S. Sirinathsinghji, D. C. Dean, D. G. Melillo, A. A. Patchett, R. Nargund, P. R. Griffin, J. A. Demartino, S. K. Gupta, J. M. Schaeffer, R. G. Smith and L. H. T. Van Der Ploegt, *Science (80-.).*, 1996, **273**, 974–977.

40   C. Y. Bowers, F. A. Momany, G. A. Reynolds and A. Hong, *Endocrinology*, 1984, **114**, 1537–1545.

41   C. Y. Bowers, *J. Pediatr. Endocrinol. Metab.*, 1993, **6**, 21–31.

42   R. Deghenghi, M. M. Cananzi, A. Torsello, C. Battisti, E. E. Muller and V. Locatelli, *Life Sci.*, 1994, **54**, 1321–1328.

43   A. A. Patchett, R. P. Nargund, J. R. Tata, M. H. Chen, K. J. Barakat, D. R. Johnston, K. Cheng, W. S. Chan, B. Butler, G. Hickey, T. Jacks, K. Schleim, S. S. Pong, L. P. Chaung, H. Y. Chen, E. Fraziert, K. H. Leung, S. L. Chiu and R. G. Smith, *Proc. Natl. Acad. Sci. U. S. A.*, 1995, **92**, 7001–7005.

44   K. A. Elias, G. S. Ingle, J. P. Burnier, R. G. Hammonds, R. S. McDowell, T. E. Rawson, T. C. Somers, M. S. Stanley and M. J. Cronin, *Endocrinology*, 1995, **136**, 5694–5699.

45   K. Raun, B. S. Hansen, N. L. Johansen, H. Thogersen, K. Madsen, M. Ankersen and P. H. Andersen, *Eur. J. Endocrinol.*, 1998, **139**, 552–561.

46   A. Moulin, J. Ryan, J. Martinez and J. A. Fehrentz, *ChemMedChem*, 2007, **2**, 1242–1259.

47   B. Ueberberg, N. Unger, W. Saeger, K. Mann and S. Petersenn, *Horm. Metab. Res.*, 2009, **41**, 814–821.

48   S. Gnanapavan, B. Kola, S. Bustin, D. Morris, P. McGee, P. Fairclough, S. Bhattacharya, R. Carpenter, A. Grossman and M. Korbonits, *J. Clin. Endocrinol. Metab.*, 2002, **87**, 2988–2991.

49   M. Kojima, H. Hosoda, Y. Date, M. Nakazato, H. Matsuo and K. Kangawa, *Nature*, 1999, **402**, 656–660.

50   X. Zhu, Y. Cao, K. Voodg and D. F. Steiner, *J. Biol. Chem.*, 2006, **281**, 38867–38870.

51   J. Yang, M. S. Brown, G. Liang, N. V. Grishin and J. L. Goldstein, *Cell*, 2008, **132**, 387–396.

52   J. A. Gutierrez, P. J. Solenberg, D. R. Perkins, J. A. Willency, M. D. Knierman, Z. Jin, D. R. Witcher, S. Luo, J. E. Onyia and J. E. Hale, *Proc. Natl. Acad. Sci. U. S. A.*, 2008, **105**, 6320–6325.

53   C. T. Lim, B. Kola, A. Grossman and M. Korbonits, *Endocr. J.*, 2011, **58**, 707–710.

54   M. A. Bednarek, S. D. Feighner, S. S. Pong, K. K. McKee, D. L. Hreniuk, M. V.

Silva, V. A. Warren, A. D. Howard, L. H. Y. Van der Ploeg and J. V. Heck, *J. Med. Chem.*, 2000, **43**, 4370–4376.

55   C. Y. Chen, A. Inui, A. Asakawa, K. Fujino, I. Kato, C. C. Chen, N. Ueno and M. Fujimiya, *Gastroenterology*, 2005, **129**, 8–25.

56   M. Zanetti, G. G. Cappellari, A. Graziani and R. Barazzoni, *Int. J. Mol. Sci.*, 2019, **20**, 1–10.

57   D. N. Huynh, H. Elimam, V. L. Bessi, L. Ménard, Y. Burelle, R. Granata, A. C. Carpentier, H. Ong and S. Marleau, *Front. Endocrinol. (Lausanne).*, 2019, **9**, 1–9.

58   S. Allas, A. Caixàs, C. Poitou, M. Coupaye, D. Thuilleaux, F. Lorenzini, G. Diene, A. Crinò, F. Illouz, G. Grugni, D. Potvin, S. Bocchini, T. Delale, T. Abribat and M. Tauber, *PLoS One*, 2018, **13**, 1–19.

59   Y. Yin, Y. Li and W. Zhang, *Int. J. Mol. Sci.*, 2014, **15**, 4837–4855.

60   K. B. S. Chow, J. Sun, K. Man Chu, W. Tai Cheung, C. H. K. Cheng and H. Wise, *Mol. Cell. Endocrinol.*, 2012, **348**, 247–254.

61   Y. Mear, A. Enjalbert and S. Thirion, *Front. Neurosci.*, 2013, **7**, 1–7.

62   B. Holst, A. Cygankiewicz, T. H. Jensen, M. Ankersen and T. W. Schwartz, *Mol. Endocrinol.*, 2003, **17**, 2201–2210.

63   X. Ge, H. Yang, M. A. Bednarek, H. Galon-Tilleman, P. Chen, M. Chen, J. S. Lichtman, Y. Wang, O. Dalmas, Y. Yin, H. Tian, L. Jermutus, J. Grimsby, C. M. Rondinone, A. Konkar and D. D. Kaplan, *Cell Metab.*, 2018, **27**, 461–469.

64   A. Krause, R. Sillard, B. Kleemeier, E. Kluver, E. Maronde, J. R. Conejo-Garcia, W. G. Forssmann, P. Schulz-Knappe, M. C. Nehls, F. Wattler, S. Wattler and K. Adermann, *Protein Sci.*, 2003, **12**, 143–152.

65   J. H. Wang, H. Z. Li, X. X. Shao, W. H. Nie, Y. L. Liu, Z. G. Xu and Z. Y. Guo, *FEBS J.*, 2019, **286**, 1332–1345.

66   C. M'Kadmi, A. Cabral, F. Barrile, J. Giribaldi, S. Cantel, M. Damian, S. Mary, S. Denoyelle, S. Dutertre, S. Péraldi-Roux, J. Neasta, C. Oiry, J. L. Banères, J. Marie, M. Perello and J. A. Fehrentz, *J. Med. Chem.*, 2019, **62**, 965–973.

67   Y. Lv, T. Liang, G. Wang and Z. Li, *Biosci. Rep.*, 2018, **38**, 1–13.

68   L. Mihalache, A. Gherasim, O. Niță, M. C. Ungureanu, S. S. Pădureanu, R. S. Gavril and L. I. Arhire, *Hormones*, 2016, **15**, 186–196.

69   P. Kurowska, E. Mlyczynska and A. Rak, *J. Physiol. Pharmacol.*, 2019, **70**, 3–13.

70   Y. Mao, T. Tokudome and I. Kishimoto, *Curr. Hypertens. Rep.*, 2016, **18**, 1–6.

71   T. Tokudome, K. Otani, M. Miyazato and K. Kangawa, *Peptides*, 2019, **111**, 42–46.

72   W. Chen and P. J. Enriori, *Transl. Gastrointest. Cancer*, 2015, **4**, 14–27.

73   G. Colldén, M. H. Tschöp and T. D. Müller, *Int. J. Mol. Sci.*, 2017, **18**, 798.

74   J. A. da Silva Pereira, F. C. da Silva and P. M. M. de Moraes-Vieira, *J. Diabetes Res.*, 2017, **2017**, 1–15.

75   J. B. Soares, R. Roncon-Albuquerque and A. Leite-Moreira, *Expert Opin. Ther. Targets*, 2008, **12**, 1177–1189.

76   L. Costantino and D. Barlocco, *Expert Opin. Ther. Pat.*, 2014, **24**, 1007–1019.

77   K. O. Cameron, S. K. Bhattacharya and A. K. Loomis, *J. Med. Chem.*, 2014, **57**, 8671–8691.

78   M. Vodnik, B. Štrukelj and M. Lunder, *Horm. Metab. Res.*, 2016, **48**, 1–15.

79   A. Beiras-Fernandez, S. Kreth, F. Weis, C. Ledderose, T. Pöttinger, C. Dieguez, A. Beiras and B. Reichart, *Peptides*, 2010, **31**, 2222–2228.

80   T. C. Lin and M. Hsiao, *Biochim. Biophys. Acta*, 2017, **1868**, 51–57.

81   W. Wang, Z. X. Chen, D. Y. Guo and Y. X. Tao, *Pharmacol. Ther.*, 2018, **191**, 135–147.

82   M. Grönberg, C. Nilsson, I. Markholm, I. Hedenfalk, C. Blomqvist, L. Holmberg, E. Tiensuu Janson and M. L. Fjällskog, *Sci. Rep.*, 2018, **8**, 1–10.

83   L. K. Chopin, I. Seim, C. M. Walpole and A. C. Herington, *Endocr. Rev.*, 2012, **33**, 849–891.

84   D. Nikolopoulos, S. Theocharis and G. Kouraklis, *Surg. Oncol.*, 2010, **19**, e2–e10.

85   C. Lu, M. S. McFarland, R. L. Nesbitt, A. K. Williams, S. Chan, J. Gomez-Lemus, A. M. Autran-Gomez, A. Al-Zahrani, J. L. Chin, J. I. Izawa, L. G. Luyt and J. D. Lewis, *Prostate*, 2012, **72**, 825–833.

86   Aleksova, Beltrami, Bevilacqua, Padoan, Santon, Biondi, Barbati, Stenner, Gortan Cappellari, Barazzoni, Ziberna, Zwas, Avraham, Agostoni, Not, Livi and Sinagra, *J. Clin. Med.*, 2019, **8**, 1152.

87   M. Matsumoto, H. Hosoda, Y. Kitajima, N. Morozumi, Y. Minamitake, S. Tanaka,

H. Matsuo, M. Kojima, Y. Hayashi and K. Kangawa, *Biochem. Biophys. Res. Commun.*, 2001, **287**, 142–146.

88   M. Van Craenenbroeck, F. Gregoire, P. De Neef, P. Robberecht and J. Perret, *Peptides*, 2004, **25**, 959–965.

89   D. Rosita, M. A. Dewit and L. G. Luyt, *J. Med. Chem.*, 2009, **52**, 2196–2203.

90   A. L. Tornesello, L. Buonaguro, M. L. Tornesello and F. M. Buonaguro, *Molecules*, 2017, **22**, 1282.

91   A. Boschi, L. Uccelli and P. Martini, *Appl. Sci.*, 2019, **9**, 2526.

92   P. F. J. Lipiński, P. Garnuszek, M. Maurin, R. Stoll, N. Metzler-Nolte, A. Wodyński, J. C. Dobrowolski, M. K. Dudek, M. Orzełowska and R. Mikołajczak, *EJNMMI Res.*, 2018, **8**, 33.

93   C. Chollet, R. Bergmann, J. Pietzsch and A. G. Beck-Sickinger, *Bioconjug. Chem.*, 2012, **23**, 771–784.

94   C. L. Charron, M. S. McFarland, S. Dhanvantari and L. G. Luyt, *MedChemCommun*, 2018, **9**, 1761–1767.

95   P. Koźmiński and E. Gniazdowska, *Nucl. Med. Biol.*, 2015, **42**, 28–37.

96   Patent 7173109B2, 2007.

97   J. P. Leyris, T. Roux, E. Trinquet, P. Verdié, J. A. Fehrentz, N. Oueslati, S. Douzon, E. Bourrier, L. Lamarque, D. Gagne, J. C. Galleyrand, C. M'kadmi, J. Martinez, S. Mary, J. L. Banères and J. Marie, *Anal. Biochem.*, 2011, **408**, 253–262.

98   A. Kern, R. Albarran-Zeckler, H. E. Walsh and R. G. Smith, *Neuron*, 2012, **73**, 317–332.

99   M. Schaeffer, F. Langlet, C. Lafont, F. Molino, D. J. Hodson, T. Roux, L. Lamarque, P. Verdié, E. Bourrier, B. Dehouck, J. L. Banéres, J. Martinez, P. F. Méry, J. Marie, E. Trinquet, J. A. Fehrentz, V. Prévot and P. Mollard, *Proc. Natl. Acad. Sci. U. S. A.*, 2013, **110**, 1512–1517.

100   R. McGirr, M. S. McFarland, J. McTavish, L. G. Luyt and S. Dhanvantari, *Regul. Pept.*, 2011, **172**, 69–76.

101   E. J. L. Soto, F. Agosti, A. Cabral, E. R. Mustafa, V. M. Damonte, M. A. Gandini, S. Rodríguez, D. Castrogiovanni, R. Felix, M. Perelló and J. Raingo, *J. Gen.*

Physiol., 2015, **146**, 205–219.

102   A. Cabral, E. Portiansky, E. Sánchez-Jaramillo, J. M. Zigman and M. Perello, *Psychoneuroendocrinology*, 2016, **67**, 27–39.

103   L. Berrout and M. Isokawa, *Brain Res.*, 2018, **1678**, 20–26.

104   M. P. Cornejo, F. Barrile, P. N. De Francesco, E. L. Portiansky, M. Reynaldo and M. Perello, *Neuroscience*, 2018, **392**, 107–120.

105   A. Cabral, G. Fernandez and M. Perello, *Neuroscience*, 2013, **253**, 406–415.

106   A. Cabral, S. Valdivia, G. Fernandez, M. Reynaldo and M. Perello, *J. Neuroendocrinol.*, 2014, **26**, 542–554.

107   G. Fernandez, A. Cabral, M. F. Andreoli, A. Labarthe, C. M'Kadmi, J. G. Ramos, J. Marie, J. A. Fehrentz, J. Epelbaum, V. Tolle and M. Perello, *Endocrinology*, 2018, **159**, 1021–1034.

108   M. P. Cornejo, P. N. De Francesco, G. García Romero, E. L. Portiansky, J. M. Zigman, M. Reynaldo and M. Perello, *Brain Struct. Funct.*, 2018, **223**, 3133–3147.

109   A. Cabral, M. P. Cornejo, G. Fernandez, P. N. De Francesco, G. Garcia-Romero, M. Uriarte, J. M. Zigman, E. Portiansky, M. Reynaldo and M. Perello, *Endocrinology*, 2017, **158**, 1436–1449.

110   M. Uriarte, P. N. De Francesco, G. Fernandez, A. Cabral, D. Castrogiovanni, T. Lalonde, L. G. Luyt, S. Trejo and M. Perello, *Mol. Neurobiol.*, 2019, **56**, 4120–4134.

111   D. Lufrano, S. A. Trejo, R. E. Llovera, M. Salgueiro, G. Fernandez, V. Martínez Damonte, F. L. González Flecha, J. Raingo, M. R. Ermácora and M. Perelló, *Mol. Cell. Endocrinol.*, 2016, **436**, 130–140.

112   H. Schellekens, P. N. De Francesco, D. Kandil, W. F. Theeuwes, T. McCarthy, W. E. P. A. Van Oeffelen, M. Perelló, L. Giblin, T. G. Dinan and J. F. Cryan, *ACS Chem. Neurosci.*, 2015, **6**, 1186–1197.

113   G. A. F. Douglas, R. McGirr, C. L. Charlton, D. B. Kagan, L. M. Hoffman, L. G. Luyt and S. Dhanvantari, *Peptides*, 2014, **54**, 81–88.

114   R. Sullivan, R. McGirr, S. Hu, A. Tan, D. Wu, C. Charron, T. Lalonde, E. Arany, S. Chakrabarti, L. Luyt and S. Dhanvantari, *J. Endocr. Soc.*, 2018, **2**, 178–189.

115   R. Sullivan, V. K. Randhawa, A. Stokes, D. Wu, T. Lalonde, B. Kiaii, L. Luyt, G.

Wisenberg and S. Dhanvantari, *J. Endocr. Soc.*, 2019, **3**, 748–762.

116   T. Lalonde, T. G. Shepherd, S. Dhanvantari and L. G. Luyt, *Pept. Sci.*, 2018, **111**, e24055.

117   B. Holst, M. Lang, E. Brandt, A. Bach, A. Howard, T. M. Frimurer, A. Beck-Sickinger and T. W. Schwartz, *Mol. Pharmacol.*, 2006, **70**, 936–946.

118   E. Murrell, M. S. Kovacs and L. G. Luyt, *ChemMedChem*, 2018, **13**, 1625–1628.

119   C. L. Charron, J. Hou, M. S. McFarland, S. Dhanvantari, M. S. Kovacs and L. G. Luyt, *J. Med. Chem.*, 2017, **60**, 7256–7266.

120   F. Zhao, J. E. Darling, R. A. Gibbs and J. L. Hougland, *Bioorganic Med. Chem. Lett.*, 2015, **25**, 2800–2803.

121   J. Hou, C. L. Charron, M. M. Fowkes and L. G. Luyt, *Eur. J. Med. Chem.*, 2016, **123**, 822–833.

122   M. M. Fowkes, T. Lalonde, L. Yu, S. Dhanvantari, M. S. Kovacs and L. G. Luyt, *Eur. J. Med. Chem.*, 2018, **157**, 1500–1511.

123   A. Abbas, L. Yu, T. Lalonde, D. Wu, J. D. Thiessen, L. G. Luyt and S. Dhanvantari, *Mol. Imaging*, 2018, **17**, 1–11.

124   T. Lalonde, M. M. Fowkes, J. Hou, P. E. Thibeault, M. Milne, S. Dhanvantari, R. Ramachandran and L. G. Luyt, *ChemMedChem*, 2019, **14**, 1762–1766.

125   F. Barrile, C. M'Kadmi, P. N. De Francesco, A. Cabral, G. García Romero, E. R. Mustafá, S. Cantel, M. Damian, S. Mary, S. Denoyelle, J.-L. Banères, J. Marie, J. Raingo, J.-A. Fehrentz and M. Perelló, *Mol. Cell. Endocrinol.*, 2019, **498**, 110573.

126   J. Rudolph, W. P. Esler, S. O'Connor, P. D. G. Coish, P. L. Wickens, M. Brands, D. E. Bierer, B. T. Bloomquist, G. Bondar, L. Chen, C.-Y. Chuang, T. H. Claus, Z. Fathi, W. Fu, U. R. Khire, J. A. Kristie, X.-G. Liu, D. B. Lowe, A. McClure, M. Michels, A. A. Ortiz, P. D. Ramsden, R. W. Schoenleber, T. E. Shelekhin, A. Vakalopoulos, W. Tang, L. Wang, L. Yi, S. J. Gardell, J. N. Livingston, L. J. Sweet and W. H. Bullock, *J. Med. Chem.*, 2007, **50**, 5202–5216.

127   R. Potter, A. G. Horti, H. T. Ravert, D. P. Holt, P. Finley, U. Scheffel, R. F. Dannals and R. L. Wahl, *Bioorganic Med. Chem.*, 2011, **19**, 2368–2372.

128   K. Kawamura, M. Fujinaga, Y. Shimoda, T. Yamasaki, Y. Zhang, A. Hatori, L. Xie, H. Wakizaka, K. Kumata, T. Ohkubo, Y. Kurihara, M. Ogawa, N. Nengaki

and M. R. Zhang, *Nucl. Med. Biol.*, 2017, **52**, 49–56.

129 W. P. Esler, J. Rudolph, T. H. Claus, W. Tang, N. Barucci, S. E. Brown, W. Bullock, M. Daly, L. DeCarr, Y. Li, L. Milardo, D. Molstad, J. Zhu, S. J. Gardell, J. N. Livingston and L. J. Sweet, *Endocrinology*, 2007, **148**, 5175–5185.

130 R. P. Moldovan, S. Els-Heindl, D. J. Worm, T. Kniess, M. Kluge, A. G. Beck-Sickinger, W. Deuther-Conrad, U. Krügel and P. Brust, *Int. J. Mol. Sci.*, 2017, **18**, 1–16.

131 P. Hanrahan, J. Bell, G. Bottomley, S. Bradley, P. Clarke, E. Curtis, S. Davis, G. Dawson, J. Horswill, J. Keily, G. Moore, C. Rasamison and J. Bloxham, *Bioorganic Med. Chem. Lett.*, 2012, **22**, 2271–2278.

132 J. Hou, M. S. Kovacs, S. Dhanvantari and L. G. Luyt, *J. Med. Chem.*, 2018, **61**, 1261–1275.

133 B. Meibohm, in *Pharmaceutical Biotechnology*, eds. D. J. A. Crommelin, R. D. Sindelar and B. Meibohm, Springer, 2013, pp. 101–132.

134 N. Abbasi Gharibkandi, J. M. Conlon and S. J. Hosseinimehr, *Peptides*, 2020, **133**, 170385.

135 C. L. Charron, J. L. Hickey, T. K. Nsiama, D. R. Cruickshank, W. L. Turnbull and L. G. Luyt, *Nat. Prod. Rep.*, 2016, **33**, 761–800.

136 O. Morris, M. Fairclough, J. Grigg, C. Prenant and A. McMahon, *J. Label. Compd. Radiopharm.*, 2019, **62**, 4–23.

137 L. Diao and B. Meibohm, *Clin. Pharmacokinet.*, 2013, **52**, 855–868.

138 J.-F. Yao, H. Yang, Y.-Z. Zhao and M. Xue, *Curr. Drug Metab.*, 2018, **19**, 892–901.

139 Y. H. Lau, P. De Andrade, Y. Wu and D. R. Spring, *Chem. Soc. Rev.*, 2015, **44**, 91–102.

140 S. Sun, Q. Jia and Z. Zhang, *Bioorganic Med. Chem. Lett.*, 2019, **29**, 2535–2550.

141 A. Choudhary and R. T. Raines, *ChemBioChem*, 2011, **12**, 1801–1807.

142 Y. Ma, D. Yang, Y. Ma and Y. H. Zhang, *ChemBioChem*, 2012, **13**, 73–79.

143 I. E. Valverde and T. L. Mindt, *Chimia (Aarau).*, 2013, **67**, 262–266.

144 R. Chingle, C. Proulx and W. D. Lubell, *Acc. Chem. Res.*, 2017, **50**, 1541–1556.

145 A. M. Webster and S. L. Cobb, *Chem. - A Eur. J.*, 2018, **24**, 7560–7573.

146   H. Wu and J. Huang, *Curr. Protein Pept. Sci.*, 2016, **17**, 582–595.

147   X. Sun, Y. Li, T. Liu, Z. Li, X. Zhang and X. Chen, *Adv. Drug Deliv. Rev.*, 2017, **110**–**111**, 38–51.

Chapter 2

2 Radiofluorination of Non-activated Aromatic Prosthetic Groups for Synthesis and Evaluation of Fluorine-18 Labelled Ghrelin(1-8) Analogues

2.1 Introduction

The growing field of molecular imaging has made way for minimally invasive approaches to disease diagnosis and treatment monitoring. Nuclear imaging modalities such as positron emission tomography (PET) and single-photon emission computed tomography (SPECT) afford real-time visualization of biological processes at the molecular and cellular levels. The development of imaging probes that target specific disease-relevant biomarkers provides a window into specific biochemical pathways via these imaging techniques. The growth hormone secretagogue receptor 1a (GHSR) is a G-protein coupled receptor (GPCR) known to play a predominant role in regulating various physiological pathways such as growth hormone secretion, appetite, and cell proliferation.[1–4] This receptor has also been linked to a number of diseases including obesity, various types of cancer, and heart disease, making it a potential biomarker for molecular imaging.[5–11] The development of targeted probes for the GHSR could offer a deeper insight into the mechanism of behaviour of this receptor as well as monitor its expression in various disease states, such as cancer.

The endogenous ligand for the GHSR is ghrelin, a 28 amino acid peptide that, when acylated by ghrelin *O*-acyl transferase (GOAT) on the serine-3 residue, is capable of regulating food intake, glucose metabolism, and body weight.[12–15] The binding affinity of acylated ghrelin toward the GHSR is $IC_{50} = 3.1$ nM[16], while the unacylated version of the peptide (desacyl ghrelin) displays no affinity for the receptor ($IC_{50} > 10,000$ nM)[17], demonstrating the necessity of this post-translational modification. Early structure-activity analysis revealed that, in addition to a free *N*-terminal amine, only the first ten *N*-terminal amino acids are required to maintain strong binding affinity of ghrelin to the GHSR, while the first four amino acids are most essential for biological activation.[17] Over the last decade, significant effort has been made to develop ghrelin into a targeted

imaging agent for the GHSR resulting in over ten unique potential probes for various imaging modalities including PET, SPECT, and optical imaging.[18]

In 2017, Charron et al. developed a probe for ^{18}F-PET imaging of the GHSR derived from ghrelin(1-8).[16] A structure-activity relationship study to develop a truncated ghrelin analogue with strong affinity toward the receptor while also incorporating fluorine for fluorine-18 labelling allowed several amino acid substitutions to be identified in addition to confirming the tolerance of fluorine-containing aromatic groups in place of the native octanoyl side chain. Furthermore, a molecular docking study offered insight into the potential binding mode of these hydrophobic moieties and revealed that bulkier, polycyclic aromatic groups were better suited for binding compared to a single phenyl ring.[16] In particular, a 6-fluoro-2-naphthyl (6-FN) group showed a significant improvement in binding affinity over its octanoyl counterpart. The resulting lead candidate from this study was [Inp^1,Dpr^3(6-FN),1Nal^4,Thr^8]ghrelin(1-8) amide (**1**) (Figure 2.1) and this peptide possessed an IC$_{50}$ value of 0.11 nM, making it the highest affinity ghrelin analogue reported to date.[16]

Initial attempts to radiolabel peptide **1** with fluoride-18 through conventional nucleophilic aromatic substitution (S$_N$Ar) methods resulted in low radiochemical yields (RCY) of 6.5% for the fluorinated prosthetic group and 3.1% for the final probe, **[^{18}F]1**.[16] The bulky nature of the 6-FN prosthetic group likely renders the fluorination site insufficiently activated for fluoride-18 substitution to be efficient. Practical methodologies for simple and efficient radiofluorination of non-activated arenes have been a significant challenge in the past. Several labelling techniques have emerged in an attempt to meet this demand. Transition-metal-mediated strategies from boronic acid, boronic ester, and arylstannane precursors have been developed using readily available copper catalysts achieving radiofluorinated arenes in good radiochemical yields and regioselectivity.[19–21] Diaryliodonium salts have also provided access to a wide range of electron-rich fluoroarenes, but can suffer from issues with regioselectivity, non-trivial synthesis, and limited shelf-life.[22,23] In recent years, the use of spirocyclic hypervalent iodonium(III) ylides (SCIDY) as precursors for fluoride-18 labelling of aromatic compounds has also been demonstrated as an attractive method to access non-activated

arenes. Several advantages of this method include high reactivity and regioselectivity toward the radiofluorinated arene, metal-free radiofluorination, a broad substrate scope, and thermally stable precursors under appropriate storage conditions.[24,25] As a result, non-activated and electron-rich arenes have been labelled with fluorine-18 providing access to several clinically relevant PET tracers.[26–31]

Herein, we describe the radiosynthesis of the previously reported ghrelin(1-8) analogue, **[18F]1**, from a SCIDY precursor as well as initial *in vitro* and *in vivo* evaluation of this potential imaging probe. Since aromatic groups appear to be of value for incorporating fluorine-18 while maintaining receptor binding affinity, we also expanded this chemical space by synthesizing the optimized ghrelin(1-8) sequence with a another non-activated aromatic group, 4'-fluorobiphenyl-4-carboxyl (4'-FBC), to give [Inp[1],Dpr[3](4'-FBC),1Nal[4],Thr[8]]ghrelin(1-8) amide (**2**) (Figure 2.1). The SCIDY radiolabelling approach was also successfully applied to this analogue further solidifying this method as an approach to gain synthetic access to these ghrelin(1-8) analogues with high affinity toward the GHSR.
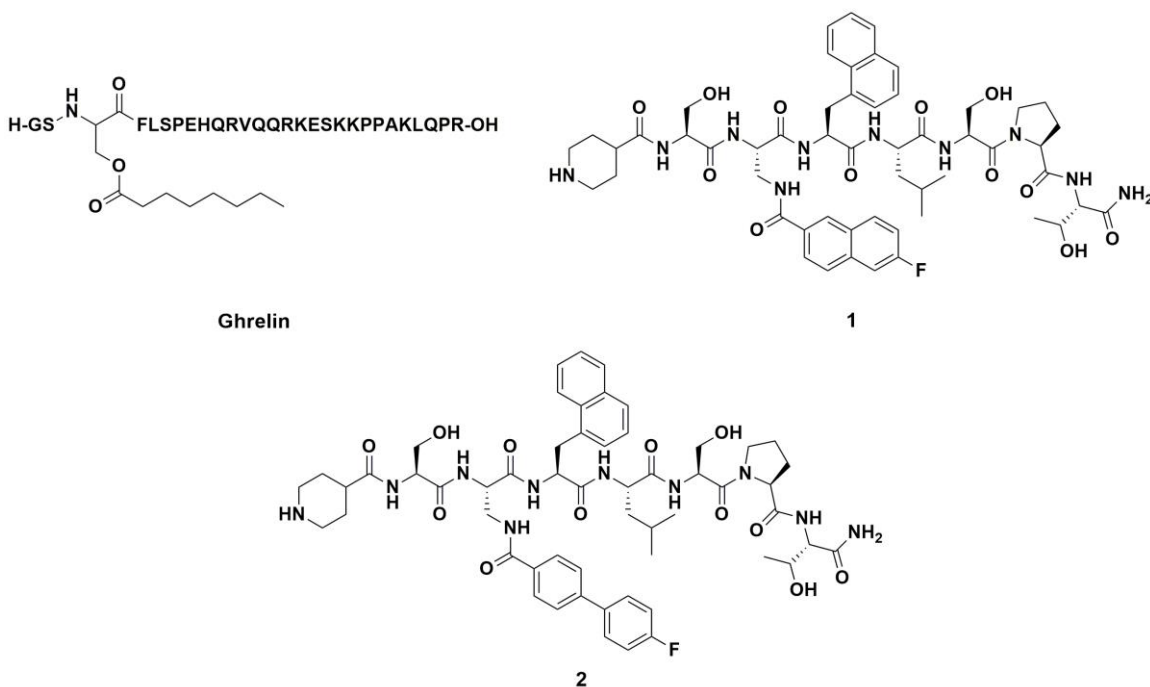
Figure 2.1. Structures of natural human ghrelin(1-28) and ghrelin(1-8) analogues **1** and **2**.

2.2 Results and Discussion

2.2.1 Design and Synthesis

Peptides **1** and **2** were synthesized via standard Fmoc solid-phase peptide synthesis on Rink Amide MBHA resin using standard Fmoc-protected amino acids with acid-labile side chain protecting groups. An orthogonal Alloc protecting group was used on the Dpr[3] side chain to ensure specific conjugation of the 6-FN or 4'-FBC groups to this position. The synthesized peptides were cleaved under strongly acidic conditions, purified, and characterized by reversed-phase HPLC and HRMS. A competitive radioligand-displacement binding assay was used to determine the peptide binding affinities toward the GHSR, which are reported as IC_{50} values. The binding affinity of **1** was 0.094 nM, which is in agreement with the previously reported IC_{50} value of 0.11 nM.[16] The binding affinity of **2** was 2.23 ± 0.93 nM, which is comparable to that of natural ghrelin.

The synthesis of SCIDY precursors for the [^{18}F]6-FN and [^{18}F]4'-FBC prosthetic groups is shown in scheme 2.1. Commercially available, 6-amino-2-naphthoic acid (**3**) was protected with a methyl ester (**4**) and the aryl amine was then converted to an aryl iodide (**5**) via a diazonium salt intermediate under mildly acidic conditions. The iodonium ylide **6** was prepared by oxidizing **5** with dimethyldioxirane (DMDO) in acetone to produce a diacetoxyiodoarene intermediate, which was then converted to the ylide under basic conditions using the spiroadamantyl-1,3-dioxane-4,6-dione (SPIAd) auxiliary.[32] The SPIAd auxiliary was chosen due to reports on its improved thermal stability compared to other SCIDY precursors, improved stability under radiofluorination reaction conditions, and ease of synthesis.[25] Preparation of the 4'-FBC prosthetic group was accomplished through selective iodination of biphenyl-4-carboxylic acid (**7**) to give aryl iodide **8** in excellent yields followed by protection with a methyl ester (**9**). A similar attempt to selectively iodinate 6-fluoro-2-napthoic acid to access compound **5** was unsuccessful and resulted in low yields due to the formation of several by-products. Compound **9** was then oxidized and converted to the iodonium ylide **10** under the same conditions described for obtaining **6**. The radiolabelling precursor, **6**, was stable at -20 ˚C while precursor **10** was only stable when stored at -80 ˚C.

Scheme 2.1. Synthesis of SCIDY precursors **6** and **10** for [^{18}F]6-FN and [^{18}F]4'-FBC prosthetic groups. Isolated reaction yields are shown in brackets below compound numbers.
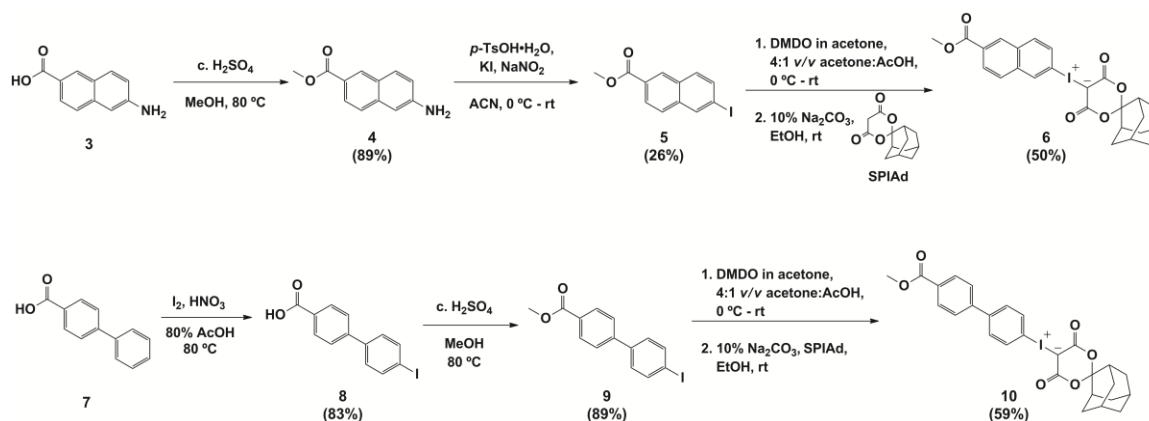
2.2.2 Radiochemistry

Optimization of the radiofluorination protocol was done manually with naphthyl precursor **6** using nucleophilic fluoride-18 (200-300 MBq) and is summarized in table 2.1. The initial radiofluorination attempt employed the preferred ^{18}F-labelling conditions reported by Rotstein et al. (Table 2.1, entry 1) using tetraethylammonium bicarbonate (TEAB) as the fluoride-18 counter ion source, anhydrous DMF (0.4 mL), 2 mg of **6**, and reaction conditions of 120 °C for 10 min.[25] The transformation of free fluoride-18 to product, reported as the non-isolated radiochemical conversion (RCC) of the reaction, was determined by analytical radio-HPLC of the reaction mixture. Under the aforementioned literature conditions, the RCC of entry 1 was a respectable 69%. However, using potassium carbonate and Kryptofix 222 as the base and phase transfer catalyst resulted in an improved RCC of 87% (entry 2).

Recently, Riss et al. reported the use of PPh$_3$ as an organocatalyst that assists radiofluorination reactions resulting in increased radiochemical yields and reaction rate.[33] The use of PPh$_3$ as an additive in this reaction along with a change in solvent to DMSO maintained a high product formation (entry 3). However, the emergence of radioactive by-products was observed, which, fortunately, could be prevented by lowering the temperature to 95 °C resulting in an excellent RCC of 91% (entry 4). The positive effect

of PPh$_3$ became more apparent when compared to the same reaction conditions without the additive, which resulted in a significantly lower yield (entry 5). Thus, a temperature of 95 ˚C was used for all subsequent trials. The reaction time was evaluated at 5, 10, and 20 minutes and the RCC ceased to increase after a 10-minute reaction time remaining stable without the emergence of by-products for up to 20 minutes (entries 4, 6-7). Notably, the use of PPh$_3$ was not as effective when TEAB was used (entry 8), indicating a possible link between PPh$_3$ and K$^+$/K$_{[2.2.2]}$ in facilitating effective radiofluorination of **6**. Upon the use of a Cu(ACN)$_4$PF$_6$ as a catalyst to investigate possible copper-mediated radiofluorination, little to no product was observed (entries 9-10), further supporting metal-free radiofluorination conditions for SCIDY precursors.

The reaction solvent was also evaluated by initially changing the solvent back to DMF (0.4 mL). Intriguingly, this resulted in significant formation of radioactive by-products and the RCC decreased from 71% after 10 minutes to 39% after 20 minutes (entries 11-12), indicating the product was unstable over time in the presence of DMF and PPh$_3$. Furthermore, the reaction proceeded with a low RCC in a 12:1 ACN:DMSO mixture (0.4 mL) (entry 13), however, the yield substantially improved when the proportion of DMSO was increased to 50% (entry 14). Over the course of these trials, it became clear that the optimal conditions for this ^{18}F-labelling reaction were K$_2$CO$_3$/K$_{[2.2.2]}$ (2 mg/7 mg), 2 mg of **6** and 2 mg of PPh$_3$ in anhydrous DMSO (0.4 mL), and reaction conditions of 95 ˚C for 10 minutes (Scheme 2.2).

Table 2.1. Optimization of radiofluorination protocol to product **[^{18}F]11** from SCIDY precursor **6**.

Entry	Base/PTC	Catalyst	Solvent	Temp. (°C)	Time (min)	RCC*
1	TEAB	-	DMF	120	10	69%
2	K$^+$/K$_{[2.2.2]}$	-	DMF	120	10	87%
3	K$^+$/K$_{[2.2.2]}$	PPh$_3$	DMSO	120	10	79%
4	K$^+$/K$_{[2.2.2]}$	PPh$_3$	DMSO	95	10	91%
5	K$^+$/K$_{[2.2.2]}$	-	DMSO	95	10	73%
6	K$^+$/K$_{[2.2.2]}$	PPh$_3$	DMSO	95	5	66%
7	K$^+$/K$_{[2.2.2]}$	PPh$_3$	DMSO	95	20	91%
8	TEAB	PPh$_3$	DMSO	95	10	52%
9	K$^+$/K$_{[2.2.2]}$	Cu(ACN)$_4$PF$_6$	DMSO	95	10	< 5%
10	K$^+$/K$_{[2.2.2]}$	Cu(ACN)$_4$PF$_6$	DMSO	95	20	< 5%
11	K$^+$/K$_{[2.2.2]}$	PPh$_3$	DMF	95	10	71%
12	K$^+$/K$_{[2.2.2]}$	PPh$_3$	DMF	95	20	39%
13	K$^+$/K$_{[2.2.2]}$	PPh$_3$	12:1 ACN:DMSO	95	10	45%
14	K$^+$/K$_{[2.2.2]}$	PPh$_3$	1:1 ACN:DMSO	95	10	85%

*non-isolated, radiochemical conversions were determined by analytical radio-HPLC. *Note.* Reactions were performed using 2 mg of precursor **6** in 0.4 mL of solvent, with TEAB (7 mg) or K$_2$CO$_3$/K$_{[2.2.2]}$ (2 mg/7 mg). K$_{[2.2.2]}$ = Kryptofix 222.

Scheme 2.2. Optimized radiofluorination of precursors **6** and **10** to produce **[^{18}F]11** and **[^{18}F]12**.
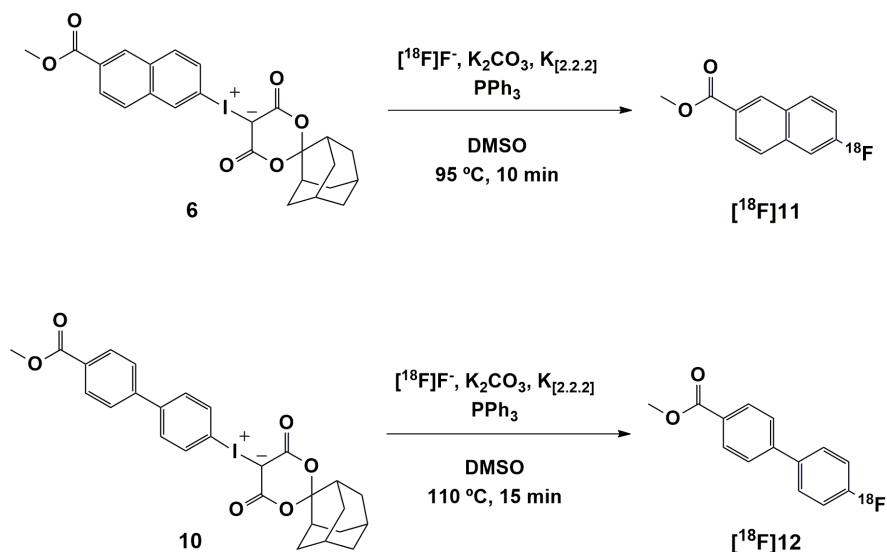
Separation of **[^{18}F]11** from unreacted fluoride-18 was accomplished through normal phase separation on a silica Sep-Pak. The biphenyl precursor **10** was labelled with fluoride-18 under similar conditions, however, it was observed that a slightly higher temperature of 110 ˚C and reaction time of 15 minutes was optimal for producing **[^{18}F]12** (Scheme 2.2). Preparation of the final prosthetic groups prior to peptide conjugation was carried out according to scheme 2.3 for both **[^{18}F]11** and **[^{18}F]12** as previously described.[16] Methyl ester deprotection followed by formation of a pentafluorophenyl (PFP) activated ester was achieved in two steps in high isolated radiochemical yields for both prosthetic groups. Compound **[^{18}F]15** was prepared in an overall decay-corrected radiochemical yield of 47 ± 10%, which is significantly improved over the RCY of 6.5% reported using the S_NAr approach. Prosthetic group **[^{18}F]16** was produced in a moderate overall RCY of 31% ± 2% supporting the applicability of the SCIDY method to label non-activated arenes for prosthetic group bioconjugation. The PFP ester prosthetic groups were then conjugated to the peptide precursor, [Inp[1],Dpr[3],1Nal[4],Thr[8]]ghrelin(1-8) amide (**17**), producing **[^{18}F]1** and **[^{18}F]2** in overall decay-corrected radiochemical yields of 24 ± 2% and 17 ± 3%, respectively. Isolated overall radiochemical yields and purities for radiolabelled products are described in table 2.2. Automated synthesis of **[^{18}F]11** followed by manual preparation of **[^{18}F]1** resulted in a molar activity of 19.3 GBq/μmol.

Manual radiosynthesis of **[¹⁸F]2** using less activity resulted in a molar activity of 5.3 GBq/µmol. To confirm the identity of radiolabelled products, independent injections of the analytical radio-HPLC trace of the isolated product was compared to the UV-HPLC chromatogram of the non-radioactive standard (Figure 2.2). The average, overall reaction and purification time for all steps to produce **[¹⁸F]1** or **[¹⁸F]2** was 150 minutes. Due to the higher binding affinity and comparable radiofluorination yields, further *in vitro* and *in vivo* evaluation was performed for **[¹⁸F]1** only.

Scheme 2.3. Preparation of ^{18}F-labelled ghrelin(1-8) analogues from **[¹⁸F]11** and **[¹⁸F]12**.
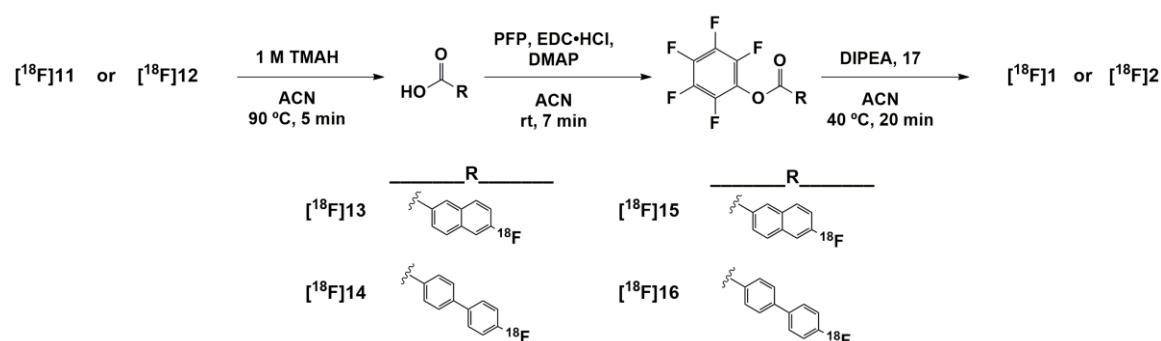
Table 2.2. Overall radiochemical yields and radiochemical purities of radioactive reaction steps to produce **[¹⁸F]1** and **[¹⁸F]2.**

	Overall RCY (%)	RCP (%)
[¹⁸F]11	58 ± 11	98
[¹⁸F]15	47 ± 10	98
[¹⁸F]1	24 ± 2	98
[¹⁸F]12	41 ± 5	98
[¹⁸F]16	31 ± 2	98
[¹⁸F]2	17 ± 3	98

Note. Radiochemical yields were isolated and decay-corrected. Radiochemical purities were determined by analytical radio-HPLC of the purified product.
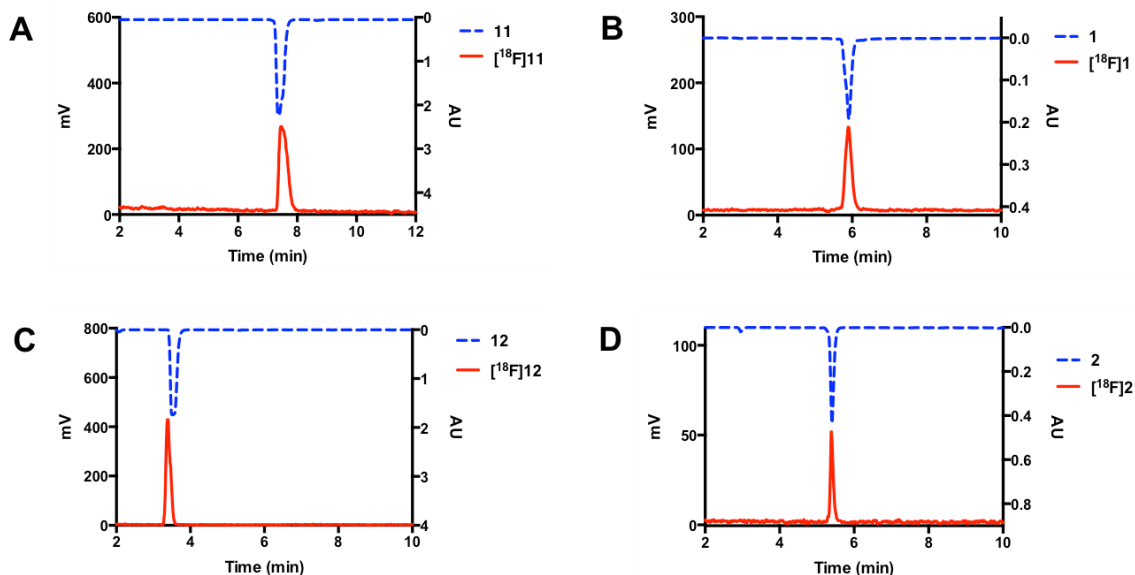
Figure 2.2. Analytical (Radio)HPLC traces. Independent injections of the radio-HPLC trace of the radiolabelled product is shown in red (mV) and the UV-HPLC trace of the non-radioactive standard is shown in blue (AU). (A) **[$^{18/19}$F]11**; (B) **[$^{18/19}$F]1**; (C) **[$^{18/19}$F]12**; (D) **[$^{18/19}$F]2**.

2.2.3 *In Vitro* Cell Uptake of **[^{18}F]1**

Cellular uptake of the **[^{18}F]1** probe was carried out in LNCaP cells transfected to overexpress the GHSR as well as in wild type LNCaP cells, which express the GHSR to a lesser extent (Figure 2.3).[34] After a 60-minute incubation, uptake of **[^{18}F]1** in the LNCaP GHSR$^+$ cells was significantly higher compared to the uptake observed in the wild type cell line (2.9 ± 0.4% vs. 2.1 ± 0.2%, respectively). To confirm specificity of binding, blocking of cellular uptake was performed with 20 µM of unlabelled peptide **1** in both cell lines. Blocking reduced uptake of **[^{18}F]1** to 1.3 ± 0.2% in the overexpressed LNCaP GHSR$^+$ cells and 1.1 ± 0.2% in the wild type cells. While blocking did significantly reduce cell uptake of the probe, there remained some radioactivity in both cell lines indicating some non-specific interactions. It is possible that the hydrophobic nature of a few amino acid residues within the peptide and the ^{18}F-labelled prosthetic group, which are necessary for binding to the GHSR, may contribute to these non-specific interactions. Nevertheless, these data indicate receptor-mediated binding of the ^{18}F-labelled probe to the cells.
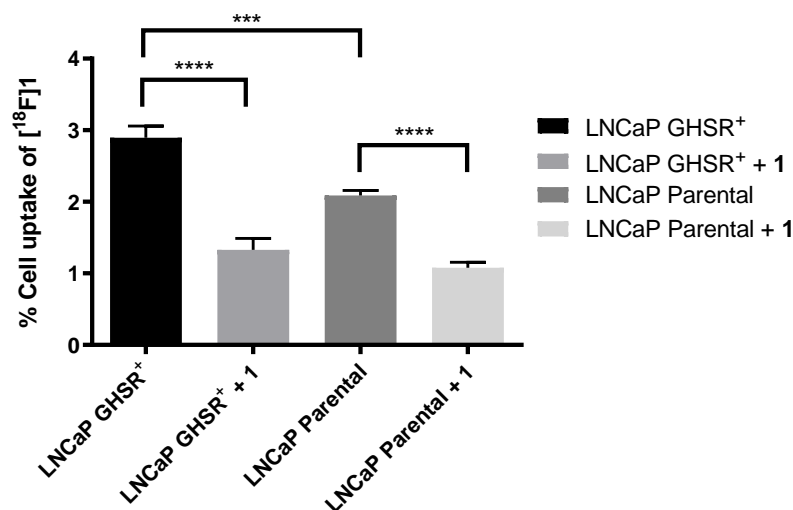
Figure 2.3. *In vitro* cell uptake of **[^{18}F]1** in LNCaP GHSR$^+$ cells (n = 5), LNCaP Parental cells (n = 5), LNCaP GHSR$^+$ cells blocked with 20 µM **1** (n = 5), and LNCaP Parental cells blocked with 20 µM of **1** (n = 5). ($^{***}P = 0.0002$; $^{****}P < 0.0001$).

2.2.4 *Ex Vivo* Biodistribution of **[^{18}F]1**

Ex vivo biodistribution studies were performed with **[^{18}F]1** in normal mice (Figure 2.4). Each mouse (n = 4) was injected with 3-5 MBq of **[^{18}F]1** prior to being sacrificed at 60 minutes post-injection (p.i.) and the amount of radioactivity was determined in the organs of interest. A blocking study was also performed in normal mice (n = 4) by administering 2 mg/mL of **1** prior to probe injection. Animals were sacrificed at 60 minutes p.i. and the amount of radioactivity was determined in the organs of interest. The majority of activity was found in the intestines (28.67 ± 7.49% ID/g). This, coupled with the significant uptake remaining in the liver (5.94 ± 0.65% ID/g), suggests a preference for hepatic clearance. A small amount of activity was observed in the kidneys and the stomach (1.11 ± 0.05 and 1.19 ± 0.26% ID/g respectively). No significant differences in activity were observed in any organs in the blocking study.
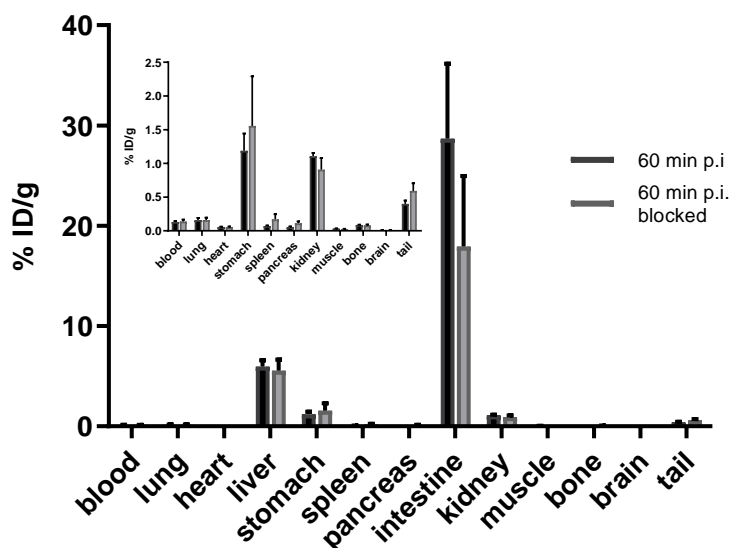
Figure 2.4. *Ex vivo* biodistribution of [^{18}F]1 in normal mice at 60 minutes post-injection (n = 4) and with blocking using 2 mg/mL of **1** (n = 4). No statistical significance in probe uptake observed in blocking study ($P < 0.05$).

2.2.5 *In Vivo* PET Imaging of [^{18}F]1

In vivo PET imaging was obtained in normal mice (n = 1) by injecting 3-5 MBq of [^{18}F]1 and immediately performing dynamic PET imaging over the course of 60 minutes. The dynamic scans were processed in 3-minute intervals at 3-6 minutes p.i. and 57-60 minutes p.i. to monitor the distribution and clearance of the probe. A coronal PET image at 3-6 minutes p.i. showed substantial blood clearance and strong accumulation of activity in the kidneys and the liver (Figure 2.5A-B). The activity later transitioned largely out of the kidneys and liver and into the intestines at 57-60 minutes p.i. (Figure 2.5C-D), which is consistent with the biodistribution results. While most peptides are highly hydrophilic and tend to prefer a renal clearance pathway, the relatively small size, and hydrophobic modifications in the peptide backbone of [^{18}F]1 may explain its increased liver and intestinal localization and favour toward hepatobiliary elimination. Since parenterally administered peptides must pass through the organs primarily responsible for enzymatic degradation, the blood, liver, and kidneys, it is possible that the tracer is too metabolically unstable to circulate through these organs leading to the observed rapid blood

clearance.[35,36] The poor pharmacokinetics observed for [**18F]1** indicates that it will likely be ineffective at reaching its target tumor tissue, which is why further *in vivo* evaluation was not carried out. Instead, further studies will investigate the stability of peptide **1** and identify enzymatic cleavage sites within the peptide sequence. Alterations to the peptide structure may be necessary to improve its metabolic stability while aiming to not compromise the binding affinity of this ghrelin analogue.
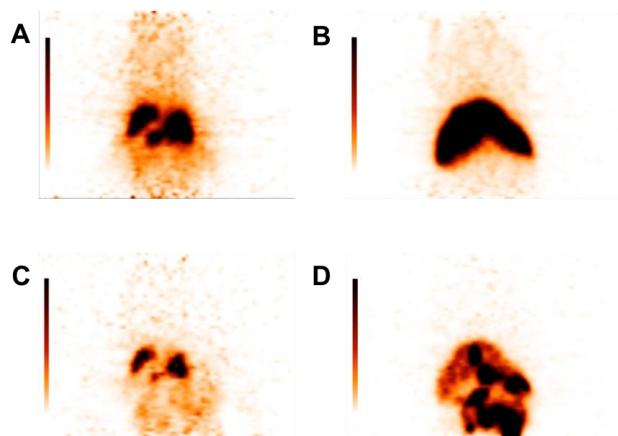
Figure 2.5. A 60-minute dynamic PET scan showing distribution of [**18F]1** in a normal mouse. Coronal image at 3-6 min p.i. at the kidney (A) and liver (B) levels. Coronal image at 57-60 min p.i. the kidney (C) and liver (D) levels.

2.3 Conclusions

Accessing ^{18}F-labelled non-activated and electron rich arenes has long been a synthetic challenge. Conventional S$_N$Ar approaches have resulted in low radiochemical yields of desired products. One of the newer strategies addressing this issue is the use of hypervalent iodonium ylides as radiofluorination precursors. The high regioselectivity, high radiochemical yields, and relatively mild labelling conditions from these precursors have afforded access to several clinically relevant PET tracers. In this study, we have successfully applied this strategy to label two bulky, non-activated aromatic prosthetic groups, [**18F]15** and [**18F]16**, with fluoride-18 in overall, decay-corrected, radiochemical yields of $47 \pm 10\%$ and $31\% \pm 2\%$, respectively. High affinity ghrelin(1-8) analogues were achieved by replacing the octanoyl side chain on residue 3 in the ghrelin sequence, which is critical for GHSR binding, with either of the non-radioactive aromatic groups.

Therefore, conjugation of these prosthetic groups to the optimized ghrelin(1-8) peptide sequence provided access to two high affinity ^{18}F-labelled ghrelin(1-8) analogues in overall radiochemical yields of 24 ± 2% and 17 ± 3%, respectively. This successful labelling approach presents the opportunity to apply these unique aromatic prosthetic groups as imaging moieties to label other targeting entities. Receptor-mediated uptake of **[^{18}F]1** was demonstrated *in vitro* in LNCaP GHSR$^+$ cells with successfully blocking using an excess of the non-radioactive standard, **1**. *Ex vivo* biodistribution data in normal mice revealed high radiotracer uptake in the liver and intestines at 60 min p.i. *In vivo* PET imaging in normal mice showed rapid blood clearance with high kidney and liver uptake at 3-6 min p.i., which transitioned to high intestinal uptake at 57-60 min p.i. consistent with the biodistribution data. Further investigation into the relationship between the peptide structure and its metabolic stability are of interest in an effort to improve its pharmacokinetic profile. Alterations to the peptide sequence may be necessary in order to improve metabolic stability while being cautious to maintain the strong binding affinity of this peptide. Nevertheless, our work demonstrates the ability to incorporate non-activated ^{18}F-labelled arenes into ghrelin analogues, providing new synthetic access to radiotracers able to detect the GHSR.

2.4 Experimental

2.4.1 Materials and Methods

All common solvents were obtained from Fisher Scientific. Amino acids, resins, and coupling agents were obtained from Chem-Impex and Aapptec. All other reagents were purchased from Sigma-Aldrich, Fisher Scientific, or Oakwood Chemicals and were used as received. Analytical and preparative reverse-phase HPLC-MS was performed on a system consisting of a Waters 600 controller, Waters prep degasser, and Waters MassLynx software. The UV absorbance was detected using a Waters 2998 Photodiode array detector. A preparative (Agilent Zorbax PrepHT SB-C18 Column 21.2 x 150 mm, 5 µm) or analytical column (Agilent Zorbax SB-C18 column 4.6 x 150 mm, 5 µm) was used. The solvent system runs gradients of 0.1% trifluoroacetic acid (TFA) in ACN and 0.1% TFA in MilliQ (18.2 mΩ·cm conductivity) water at a flow rate of 20 mL/min over 10 minutes with a 5 minute wash. Analytical UHPLC-MS was performed using a Waters

Inc. Acquity UPLC H-class instrument in combination with a Xevo QToF mass spectrometer. A Waters Acquity analytical column (UPLC BEH C18 2.1 x 50 mm, 1.7 μm) was used and the UV absorbance was detected using a Waters Acquity PDA detector. The solvent system ran gradients of 0.1% formic acid in acetonitrile (ACN, Optima grade, Fisher Scientific) and 0.1% formic acid in MilliQ water (18.2 mΩ •cm conductivity) at a flow rate of 0.6 mL/min over 3 minutes followed by a wash over 1 minute. Solution phase reactions were monitored by thin layer chromatography (TLC) using plastic-backed silica gel plates. Flash chromatography was performed using a Biotage® Isolera™ Prime advanced automated flash purification instrument. Biotage SNAP KP-Sil 10 g, 25 g, or 50 g cartridges (50 μm irregular silica) were used with solvent flow rates of 12, 25, or 50 mL/min for each cartridge type respectively along with the gradient solvent system specified. All fractions were monitored and collected by UV absorbance using the internal UV detector set at 254 nm and 280 nm. NMR spectra were obtained using either an Inova 400 MHz, or a Bruker 400 MHz spectrometer. Chemical shifts are referenced to the residual solvent peaks and recorded in parts per million. High-resolution mass spectra were determined in positive ion mode using an electrospray ionization (ESI) ion source on either a Waters Xevo QToF or a Bruker micrOToF II mass spectrometer.

2.4.2 General Fmoc Solid-Phase Peptide Synthesis

Peptides **1** and **2** were synthesized by standard Fmoc solid-phase peptide synthesis on a Biotage® Syrowave™ automated peptide synthesizer. Briefly, peptides were synthesized at a 0.1 mmol scale on Rink amide MBHA resin (0.39 mmol/g). The resin was initially swelled in DCM (4 mL) followed by Fmoc deprotection using 40% piperidine in N,N'-dimethylformamide (DMF) (1.2 mL) for two cycles (3 min, 12 min). Amino acid coupling was completed by adding the appropriate fmoc-protected amino acid (4 eq.) in DMF, HCTU (4 eq.) in DMF, and N,N'-diisopropylethylamine (DIPEA) (8 eq.) in NMP to the resin and reacting for 40 min. The cycle of Fmoc deprotection followed by amino acid coupling was repeated for until all eight amino acids were coupled to the resin. All further synthetic modifications were done manually according to scheme 2.4.

Allyloxycarbonyl (Alloc) deprotection was performed manually under an inert N_2

atmosphere by mixing the peptide resin with phenylsilane (296 µL, 2.40 mmol) in DCM (4 mL) for 5 minutes followed by the addition of tetrakis(triphenylphosphine) palladium(0) (Pd(PPh$_3$)$_4$) (17 mg, 0.015 mmol) and reacting for 10 minutes. Coupling of the 6-FN or 4'-FBC aromatic groups was then performed manually by pre-activating either 6-fluoro-2-naphthoic acid (3 eq.) or 4'-fluoro-4-carboxylic acid (**14**) with HCTU (3 eq.) and DIPEA (6 eq.) in DMF (2 mL) and subsequently adding the mixture to the peptide resin and reacting for 16 h.

Global deprotection and resin cleavage of the peptides were performed by reacting the peptide resin in a 2 mL mixture of 95% TFA, 2.5% TIPS, and 2.5% H$_2$O for 5 h. The cleaved peptide was precipitated from ice-cold *tert*-butyl methyl ether (TBME) and centrifuged at 3000 rpm for 10 minutes. The supernatant was decanted and the resulting peptide pellet was re-dissolved in 20% ACN in H$_2$O, frozen, and lyophilized to dryness. The crude peptides were purified using preparative HPLC-MS and collected fractions were combined, frozen, and lyophilized to dryness. Purity was determined using analytical UHPLC-MS and is summarized in Table 2.3.

Table 2.3. Analytical data for ghrelin(1-8) analogues.

	Sequence	[M+H]$^+$ Calculated	[M+H]$^+$ Observed	Purity	Yield
1	Inp-S-Dpr(6-FN)-1Nal-LSPT	1069.5159	1069.5227	98%	33%
2	Inp-S-Dpr(4'-FBC)-1Nal-LSPT	1095.5315	1095.5320	98%	29%

Scheme 2.4. Synthesis of ghrelin(1-8) analogues **1** and **2**.
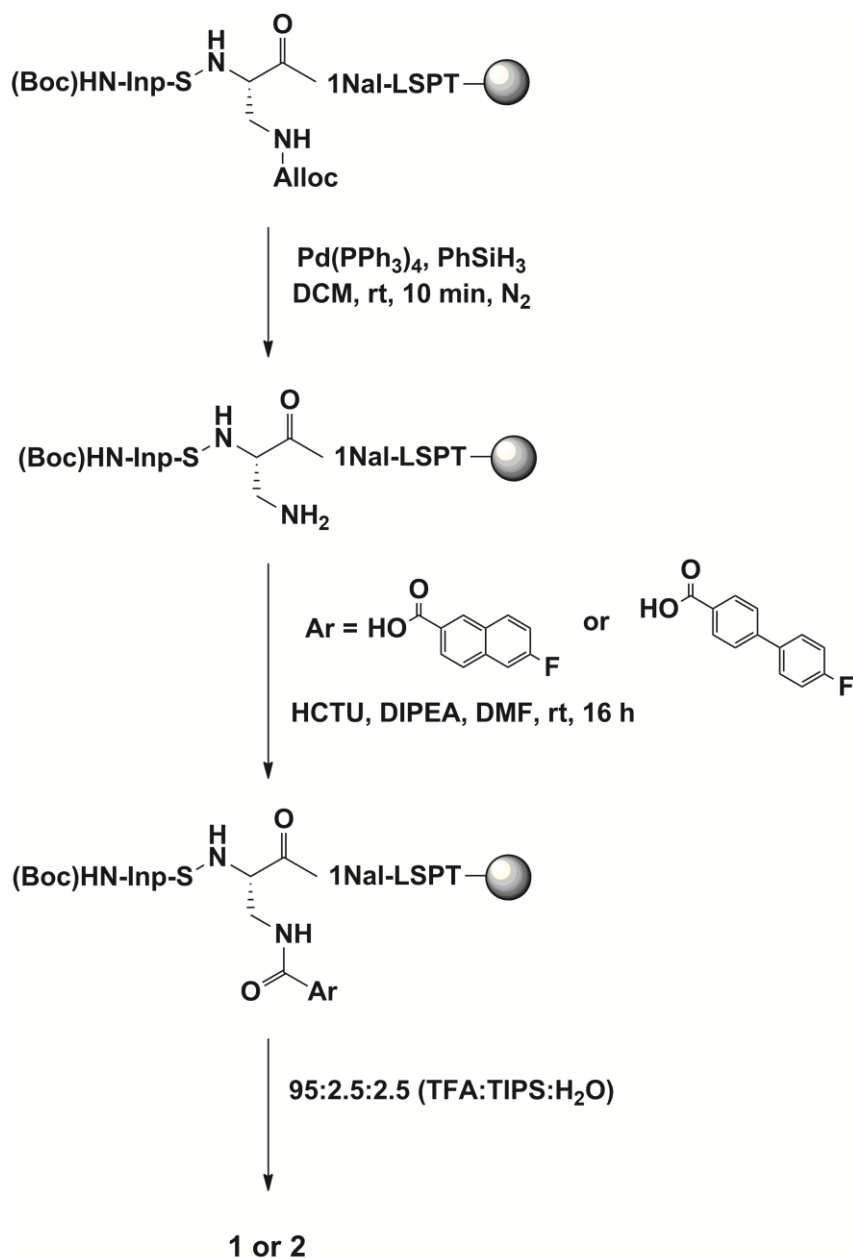
2.4.3 Small Molecule Synthesis

Spiroadamantyl-1,3-dioxane-4,6-dione (SPIAd). CAS: 455329-56-3. Synthesized according to Rotstein *et al.*[25] Briefly, malonic acid (0.501 g, 4.82 mmol) was suspended in acetic anhydride (1 mL) and conc. H_2SO_4 (20 µL) heated to 60 ˚C for 15 minutes. The reaction mixture was then cooled to room temperature and 2-adamantanone (0.735 g, 4.89 mmol) was added portion wise. The mixture stirred for an additional 1.5 h prior to being

diluted with DCM and washed three times with water. The organic extracts were washed with brine, dried over $MgSO_4$, and concentrated under reduced pressure. The crude product was recrystallized from Et_2O and hexanes to afford a white, crystalline solid (0.826 g, 72%). ^{1}H NMR (400 MHz, $CDCl_3$): δ 3.61 (s, 2H), 2.20-2.12, (m, 6H), 1.94 (s, 2H), 1.81-1.75 (m, 6H). ^{13}C NMR (100 MHz, $CDCl_3$): δ 163.2, 109.8, 37.8, 36.8, 36.7, 33.6, 26.2.

Methyl 6-amino-2-naphthoate (4). CAS: 5159-59-1. Synthesized according to Bordeau et al.[37] Briefly, 6-amino-2-naphthoic acid (1.152 g, 6.15 mmol) was dissolved in MeOH (50 mL). Concentrated sulphuric acid (2.75 mL) was added dropwise and the mixture refluxed for 16 h. The solvent was removed under reduced pressure and resulting the residue was re-suspended in H_2O and 2 M NaOH was then added until a pH of 11 was reached. The product was extracted into DCM three times and organic extracts were washed with brine, dried over $MgSO_4$, and concentrated under reduced pressure to afford a light orange solid (1.115 g, 89%). ^{1}H NMR (400 MHz, $CDCl_3$): δ 8.45 (s, 1H), 7.94 (d, ^3J = 8.2 Hz, 1H), 7.75 (d, ^3J = 8.5 Hz, 1H), 7.58 (d, ^3J = 8.3 Hz, 1H), 6.98 (s, 2H), 3.94 (s, 3H). ^{13}C NMR (100 MHz, $CDCl_3$): δ 167.7, 146.6, 137.6, 131.2, 131.0, 126.7, 126.0, 125.8, 123.9, 118.8, 107.9, 52.1.

Methyl 6-iodo-2-naphthoate (5). CAS: 5042-98-8. Synthesized according to Krasnokutskaya et al.[38] Briefly, compound **4** (1.113 g, 5.53 mmol) was added portion-wise to a solution of *p*-TsOH (3.162 g, 16.6 mmol) in ACN (20 mL). The resulting solution was cooled to 10 ˚C and a pre-made solution of $NaNO_2$ (0.790 g, 11.5 mmol) and KI (2.299 g, 13.8 mmol) in H_2O was added dropwise (4 mL). The reaction stirred at room temperature for 2 h prior to being quenched with saturated $NaHCO_3$(aq) and saturated $Na_2S_2O_3$(aq). The resulting precipitate was extracted into EtOAc three times, dried over $MgSO_4$, and concentrated under reduced pressure. The crude product was purified by flash column chromatography (1:1 DCM:EtOAc) resulting in a pale yellow solid (0.444 g, 26%). ^{1}H NMR (400 MHz, $CDCl_3$): δ 8.55 (s, 1H), 8.29 (s, 1H), 8.07 (dd $^{3,4}J$ = 8.6, 1.6 Hz, 1H), 7.80 - 7.75 (m, 2H), 7.67 (d, ^3J = 8.6 Hz, 1H), 3.98 (s, 3H). ^{13}C NMR (100 MHz, $CDCl_3$): δ 167.0, 136.8, 136.7, 135.5, 131.3, 131.0, 130.7, 128.1, 127.1, 126.3, 94.8, 52.4.

Methyl (1r,3r,5r,7r)-spiro[adamantane-2,2'-[1,3]dioxane]-4',6'-dion-[6-iodonium-2-naphthoate] ylide (6). Aryl iodide **5** (0.250 g, 0.801 mmol) was suspended in a solution of 4:1 acetone:acetic acid (7 mL) and cooled to 0 ˚C. Freshly prepared DMDO in acetone was added and the reaction stirred for 1 h at 0 ˚C and then was allowed to warm to room temperature over 3 h. The solvent was removed *in vacuo* and the resulting solid was re-suspended in EtOH (4 mL). SPIAd (0.194 g, 0.819 mmol) was pre-dissolved in 10% Na_2CO_3(aq) (3 mL) and added dropwise to the reaction mixture. The pH was adjusted to 9-10 with 10% Na_2CO_3(aq) and the reaction stirred at room temperature for 3 h. The mixture was diluted with H_2O, extracted into DCM three times, and washed with brine. The organic extracts were dried over $MgSO_4$ and concentrated under reduced pressure. The crude product was purified by flash column chromatography (17%-100% EtOAc in DCM) to produce a white solid (0.219 g, 50%). ^{1}H NMR (400 MHz, CDCl$_3$): δ 8.60 (s, 1H), 8.40 (s, 1H), 8.17 (dd, $^{3,4}J$ = 8.6, 1.6 Hz, 1H), 7.95 (d, ^3J = 8.9 Hz, 1H), 7.90 – 7.87 (m, 2H), 4.00 (s, 3H), 2.44 (br s, 2H), 2.18 – 2.15 (m, 4H), 1.86 (br s, 2H), 1.72 – 1.69 (m, 5H), 1.60 (m, 1H). ^{13}C NMR (100 MHz, CDCl$_3$): δ 166.3, 163.5, 136.3, 133.6, 133.4, 133.2, 131.0, 130.3, 128.9, 128.6, 127.4, 113.4, 107.9, 55.8, 52.7, 37.2, 35.7, 33.8, 26.6. HRMS (ESI$^+$): [M+Na]$^+$ calculated = 569.0437; [M+Na]$^+$ observed = 569.0412.

Methyl 6-fluoro-2-naphthoate (11). CAS: 5043-00-5. Synthesized according to Bordeau et al.[37] Briefly, 6-fluoro-2-naphthoic acid (0.303 g, 1.60 mmol) was dissolved in MeOH (15 mL). Concentrated sulphuric acid (0.70 mL) was added dropwise and the mixture refluxed for 16 h. The solvent was removed under reduced pressure and resulting the residue was re-dissolved in EtOAc and washed with saturated NaHCO$_3$ (aq) three times. The organic extracts were then washed with brine, dried over MgSO$_4$, and concentrated under reduced pressure to afford a white solid (0.288 g, 88%). ^{1}H NMR (400 MHz, CDCl$_3$): δ 8.59 (s, 1H), 8.08 (d, ^3J = 8.4 Hz, 1H), 7.96-7.92 (m, 1H), 7.82 (d, ^3J = 8.5 Hz, 1H), 7.48 (d, ^3J = 9 Hz, 1H), 7.34 – 7.30 (m, 1H), 3.98 (s, 3H). ^{13}C NMR (100 MHz, CDCl$_3$): δ 167.1, 162.1 9 (d, J_{CF} = 248 Hz), 136.7, 132.0, 131.0, 129.6, 127.6, 126.9, 126.4, 117.3 (d, $^2J_{CF}$ = 25 Hz), 111.1 (d, $^2J_{CF}$ = 21 Hz), 52.3.

Pentafluorophenyl 6-fluoro-2-naphthoate (15). Synthesized according to Charron et al.[16] Briefly, to a solution of 6-fluoro-2-naphthoic acid (0.203 g, 1.06 mmol) and

pentafluorophenol (0.218 g, 1.18 mmol) dissolved in DCM (50 mL) at 0 ˚C was added EDC•HCl (0.310 g, 1.62 mmol) and DMAP (0.034 g, 0.277 mmol). The mixture stirred at 0 ˚C for 1 h prior to being quenched with saturated NH_4Cl (aq). The product was extracted into DCM three times prior to being dried over $MgSO_4$ and concentrated under reduced pressure to afford a beige solid. The crude product was passed through a silica plug washing with 5% EtOAc in hexanes to obtain the purified product as a white solid (0.359 g, 95%). ^{1}H NMR (400 MHz, $CDCl_3$): δ 8.79 (s, 1H), 8.18 (dd, $^{3,4}J$ = 8.6, 1.0 Hz, 1H), 8.02 (dd, $^{3,4}J$ = 9.0, 5.6 Hz, 1H), 7.92 (d, ^3J = 8.7 Hz, 1H), 7.55 (dd, $^{3,4}J$ = 9.5, 2.4 Hz, 1H), 7.39 (dt, $^{3,4}J$ = 8.6, 2.5 Hz, 1H). ^{13}C NMR (100 MHz, $CDCl_3$): δ 162.7 (d, J_{CF} = 250 Hz), 162.6, 142.6, 140.9, 140.1, 139.3, 138.3, 137.4, 136.7, 132.9, 132.3, 129.4, 128.1, 126.4, 123.6, 117.9 (d, $^2J_{CF}$ = 25 Hz), 111.4 (d, $^2J_{CF}$ = 21 Hz). ^{19}F NMR (376 MHz, $CDCl_3$): δ -162.2, -157.8, -152.4, -108.5. HRMS (ESI$^+$): [M+Na]$^+$ calculated = 356.0272; [M+Na]$^+$ observed = 356.0274.

4'-Iodobiphenyl-4-carboxylic acid (8). CAS: 1399583. 4-Biphenylcarboxylic acid (1.016 g, 5.12 mmol), iodine (2.733 g, 10.8 mmol), and conc. nitric acid (10 mL) were suspended in 80% acetic acid (aq) and heated to 85 ˚C for 16 h. The reaction mixture was then cooled to room temperature and the resulting precipitate was filtered and washed with acetic acid followed by water, sat. $Na_2S_2O_3$(aq), and water once again to give an off-white solid (1.381 g, 83%). ^{1}H NMR (400 MHz, DMSO-d_6): δ 8.01 (d, ^3J = 8.4 Hz, 2H), 7.84 (d, ^3J = 8.4 Hz, 2H), 7.77 (d, ^3J = 8.4 Hz, 2H), 7.53 (d, ^3J = 8.4 Hz, 2H). ^{13}C NMR (100 MHz, DMSO-d_6): δ 167.2, 142.9, 138.6, 137.8, 130.6, 130.0, 129.1, 126.6, 94.9. HRMS (ESI$^+$): M$^+$ calculated = 216.0587; M$^+$ observed = 216.0581.

Methyl 4'-iodobiphenyl-4-carboxylate (9). CAS: 158407-15-9. Synthesized according to Bordeau et al.[37] Briefly, compound **8** (0.245, 0.755 mmol) was dissolved in MeOH (15 mL). Concentrated sulphuric acid (1 mL) was added dropwise and the mixture refluxed for 16 h. The solvent was removed under reduced pressure and resulting the residue was re-suspended in 2 M NaOH and extracted with DCM three times. The organic extracts were washed with brine, dried over $MgSO_4$, and concentrated under reduced pressure to afford a white solid (0.226 g, 89%). ^{1}H NMR (400 MHz, $CDCl_3$): δ 8.10 (d, ^3J = 8.4 Hz, 2H), 7.79 (d, ^3J = 8.4 Hz, 2H), 7.61 (d, ^3J = 8.4 Hz, 2H), 7.35 (d, ^3J = 8.4 Hz, 2H), 3.94

(s, 3H). ^{13}C NMR (100 MHz, CDCl$_3$) δ 167.0, 144.6, 139.6, 138.2, 130.4, 129.4, 129.2, 126.9, 94.3, 52.3.

Methyl (1r,3r,5r,7r)-spiro[adamantane-2,2'-[1,3]dioxane]-4',6'-dion-[4'-iodonium biphenyl-4-carboxylate]ylide (10). Aryl iodide **9** (0.329 g, 0.973 mmol) was suspended in a solution of 4:1 acetone:acetic acid (5 mL) and cooled to 0 ˚C. Freshly prepared DMDO in acetone was added and the reaction stirred for 1 h at 0 ˚C and then was allowed to warm to room temperature over 3 h. The solvent was removed *in vacuo* and the resulting solid was re-suspended in EtOH (2 mL). SPIAd (0.340 g, 1.44 mmol) was pre-dissolved in 10% Na$_2$CO$_3$(aq) (3 mL) and added dropwise to the reaction mixture. The pH was adjusted to 9-10 with 10% Na$_2$CO$_3$(aq) and the reaction stirred at room temperature for 4 h. The mixture was diluted with H$_2$O, extracted into DCM three times, and washed with brine. The organic extracts were dried over MgSO$_4$ and concentrated under reduced pressure. The crude product was purified by flash column chromatography (17%-100% EtOAc in DCM) to produce a yellow solid (0.329 g, 59%). ^{1}H NMR (400 MHz, CDCl$_3$): δ 8.13 (d, ^3J = 7.8 Hz, 2H), 7.96 (d, ^3J = 8.0 Hz, 2H), 7.62 (m, 4H), 3.95 (s, 3H), 2.44 (br s, 2H), 2.18 – 2.15 (m, 4H), 1.86 (br s, 2H), 1.72 – 1.69 (m, 5H), 1.60 – 1.58 (m, 1H). ^{13}C NMR (100 MHz, CDCl$_3$): δ 166.7, 163.5, 143.1, 138.1, 134.1, 130.8, 130.5, 130.4, 127.4, 113.3, 107.8, 56.1, 52.5, 37.3, 35.8, 33.6, 26.7. HRMS (ESI$^+$): [M+H]$^+$ calculated = 573.0769; [M+H]$^+$ observed = 573.0137.

4'-Fluorobiphenyl-4-carboxylic acid (14). CAS: 1399520. To a solution of K$_2$CO$_3$ (1.123 g, 8.13 mmol) in 8:8:1 toluene:EtOH:H$_2$O (17 mL) was added 1-fluoro-4-iodobenzene (0.42 mL, 3.64 mmol), 4-carboxybenzeneboronic acid (0.502 g, 3.03 mmol), and tetrakis(triphenylphosphine)-palladium(0) (71 mg, 0.061 mmol). The reaction stirred at 80 ˚C for 16 h prior to being cooled to room temperature and volatiles removed under reduced pressure. The residue was re-suspended in 2N HCl(aq) and extracted three times into EtOAc prior to being washed with brine, dried over MgSO$_4$, and concentrated under reduced pressure. The crude product was then recrystallized from hot MeOH and water to give an off-white solid (0.394 g, 60%). ^{1}H NMR (400 MHz, DMSO-d_6): δ 12.98 (br s, 1H), 8.01 (d, ^3J = 8.5 Hz, 2H), 7.80 – 7.77 (m, 4H), 7.33 (t, ^3J = 8.9 Hz, 2H). ^{13}C NMR (100 MHz, DMSO-d_6): δ 167.1, 162.3 (d, J_{CF} = 244 Hz), 143.2, 135.5, 130.0, 129.6,

129.1, 129.0, 126.8, 115.9 (d, $^2J_{CF}$ = 21 Hz). HRMS (ESI$^+$): M$^+$ calculated = 323.9647; M$^+$ observed = 323.9648.

Methyl 4'-fluorobiphenyl-4-carboxylate (12). CAS: 80254-87-1. Synthesized according to Bordeau et al.[37] Briefly, compound **14** (0.079, 0.363 mmol) was dissolved in MeOH (10 mL). Concentrated sulphuric acid (1 mL) was added dropwise and the mixture refluxed for 16 h. The solvent was removed under reduced pressure and resulting the residue was re-suspended in 2 M NaOH and extracted with DCM three times. The organic extracts were washed with brine, dried over MgSO$_4$, and concentrated under reduced pressure to afford a white solid (0.073 g, 87%). ^{1}H NMR (400 MHz, CDCl$_3$): δ 8.10 (d, ^3J = 8.6 Hz, 2H), 7.62 – 7.57 (m, 4H), 7.15 (t, ^3J = 8.6 Hz, 2H), 3.94 (s, 3H). ^{13}C NMR (100 MHz, CDCl$_3$) δ 167.1, 163.1 (d, J_{CF} = 246 Hz), 144.7, 136.3, 130.3, 129.1, 129.0, 127.0, 116.0 (d, $^2J_{CF}$ = 21 Hz), 52.3.

Pentafluorophenyl 4'-fluorobiphenyl-4-carboxylate (16). Compound **14** (0.083, 0.383 mmol) was suspended in DCM and cooled to 0°C prior to adding pentafluorophenol (0.090 g, 0.489 mmol), EDC•HCl (0.112 g, 0.589 mmol), and DMAP (0.0098 g, 0.080 mmol). The reaction mixture stirred for 1 h at 0 °C and was then quenched with sat. NH$_4$Cl (aq). The product was extracted into DCM three times prior to being washed with brine, dried over MgSO$_4$, and concentrated under reduced pressure to afford a white solid. The crude product was passed through a silica plug washing with 5-40% EtOAc in hexanes to obtain the purified product as a white solid (0.121 g, 83%). ^{1}H NMR (400 MHz, CDCl$_3$): δ 8.27 (d, ^3J = 8.6 Hz, 2H), 7.72 (d, ^3J = 8.6 Hz, 2H), 7.63 (dd, $^{3,4}J$ = 8.9, 5.2 Hz, 2H), 7.19 (t, ^3J = 8.7 Hz, 2H). ^{13}C NMR (100 MHz, CDCl$_3$): δ 163.4 (d, J_{CF} = 248 Hz), 162.6, 146.6, 142.9, 141.0, 140.3, 139.3, 138.5, 136.9, 131.5, 129.3, 129.2, 127.5, 125.7, 116.2 (d, $^2J_{CF}$ = 21 Hz). ^{19}F NMR (376 MHz, CDCl$_3$): δ -162.3, -157.9, -152.4, -113.3. HRMS (ESI$^+$): M$^+$ calculated = 382.0428; M$^+$ observed = 382.0426.

2.4.4 Radiosynthesis

All anhydrous solvents were purchased from Sigma-Aldrich and used as received. Fluoride-18 was obtained as [^{18}F]H$_2$^{18}O by cyclotron. QMA carbonate SPE, C18 Sep-Pak, and Silica Sep-Pak cartridges were purchased from Waters. Analytical radio-RP-

HPLC (Agilent RP-C18 column 4.6 x 150 mm, 5 µm) and semi-preparative RP-HPLC (Agilent RP-C18 column 19 x 150 mm, 5µm) were performed using a Waters 1525 Binary HPLC Pump, a Waters 2487 dual λ absorbance detector (292 and 220 nm), Waters InLine degasser, a gamma detector, and data was recorded using Breeze software. The solvent system runs gradients of 0.1% trifluoroacetic acid (TFA) in ACN and 0.1% TFA in MilliQ water at a flow rate of 1.5 mL/min for analytical and 4.0 mL/min for preparative HPLC over 10 minutes with a 5 minute wash. Fractions were collected and solvent was evaporated using a Biotage® V10 Evaporator. All radiochemical yields (RCY) were determined for the isolated product and are decay-corrected. All radiochemical purities (RCP) were determined by radio-HPLC on the isolated product. All reactions were performed manually unless otherwise indicated.

Fluoride-18 was trapped on a QMA carbonate SPE cartridge and eluted into a 20 mL glass vial with a solution of K_2CO_3 (2 mg) and kryptofix 222 (7 mg) in 1 mL of 3:7 H_2O:ACN. The solution was evaporated to dryness on a Biotage V10 Evaporator and further dried azeotropically with 1 mL of anhydrous ACN, repeated twice.

Methyl [^{18}F]6-fluoro-2-naphthoate ([^{18}F]11): A solution of precursor **6** (2 mg) and PPh$_3$ (2 mg) in anhydrous DMSO (400 µL) was added to dried [^{18}F]F$^-$ (1 GBq) and allowed to react at 95 ˚C for 10 min. The reaction mixture was then diluted with *tert*-butyl methyl ether (TBME) and loaded onto a silica Sep-Pak cartridge, which was pre-conditioned with hexanes (10 mL). The product was eluted into a clean reaction vial using 9:1 hexanes: EtOAc (3 mL) and evaporated to dryness on a Biotage V10 Evaporator. The purified product was isolated in a 58 ± 11% RCY and >98% RCP. The identity of **[^{18}F]11** was confirmed by co-injection with the non-radioactive standard, **11**, showing a consistent retention time of 7.4 minutes (40-90% gradient).

Methyl [^{18}F]6-fluoro-2-naphthoate ([^{18}F]11) (Automated Synthesis): A Tracerlab FX$_{FN}$ (GE Healthcare) was used. Vial 1 contained K_2CO_3 (2.0 mg) and K$_{[2.2.2]}$ (7.0 mg) in H_2O (200 µL) and ACN (800 µL). Vials 2 and 3 each contained ACN (1 mL). Vial 4 contained a solution of precursor **6** (2 mg) in anhydrous DMSO (0.4 mL). Vial 5 contained 1:1 ACN:H_2O (4 mL). Fluorine-18 (86 GBq) was produced on a GE Healthcare PETtrace 880 cyclotron (16.5 MeV) via a ^{18}O(p,n) nuclear reaction. Fluoride-18 was

delivered to a QMA carbonate Sep-Pak to isolate the $[^{18}O]H_2O$ from fluoride-18. The fluoride was then eluted into the reaction vial using the $K_2CO_3/K_{[2.2.2]}$ solution in vial 1. The $[^{18}F]F^-$ was azeotropically dried by heating the reaction vial to 75 °C under full vacuum for 5 min. This was repeated 2 more times using anhydrous ACN from vials 2 and 3. Once dried, the solution containing precursor **6** in vial 4 was added to the reaction vessel, heated to 95 °C and allowed to react for 10 min. Following this reaction, the contents of vial 5 were added to quench the reaction. The reaction mixture was then purified by HPLC (Isocratic 50% ACN in H_2O). The product was collected into 20 mL scintillation vial in the side chamber and removed for manual synthesis.

Pentafluorophenyl [^{18}F]6-fluoro-2-naphthoate ([^{18}F]15): Anhydrous ACN (1 mL) was added to re-dissolve **[^{18}F]11** followed by 20 µL of 1 M tetramethylammonium hydroxide (TMAH). The reaction mixture was heated to 90 ˚C for 5 min prior to being diluted with 0.1% TFA in water (7 mL) and loaded onto a C18 Sep Pak pre-conditioned with ethanol (10 mL) and water (10 mL). The product was then eluted into a reaction vial containing pentafluorophenol (20 mg), EDC•HCl (10 mg), and DMAP (1 mg) using anhydrous ACN (1 mL). The mixture reacted at room temperature for 7 min prior to being quenched with H_2O (1 mL) and purified by preparative radio-HPLC (55-95% gradient). The purified product was isolated in an overall RCY across all 3 steps of 47 ± 10% and >98% RCP. The identity of **[^{18}F]15** was confirmed by co-injection with the non-radioactive standard, **15**, showing a consistent retention time of 9.3 minutes (55-95% gradient).

H-Inp-S-Dpr([^{18}F]6-FN)-1Nal-LSPT-NH$_2$ ([^{18}F]1): A solution of peptide precursor (H-Inp-S-Dpr-1Nal-LSPT-NH$_2$, 2 mg) dissolved in anhydrous ACN (1 mL) was added to dried **[^{18}F]15** followed by DIPEA (30 µL). The mixture reacted for 20 min at 40 ˚C prior to being quenched with H_2O (1 mL) and purified by preparative radio-HPLC (20-80% gradient). The purified product was isolated in a 50 ± 7% RCY and >98% RCP for this step. The overall RCY across all 4 steps was 24 ± 2%. The identity of **[^{18}F]1** was confirmed by co-injection with the non-radioactive standard, **1**, showing a consistent retention time of 5.9 minutes (20-80% gradient).

Methyl [^{18}F]4'-fluorobiphenyl-4-carboxylate ([^{18}F]12): A solution of precursor **10** (2 mg) and PPh$_3$ (2 mg) in anhydrous DMSO (400 µL) was added to dried $[^{18}F]F^-$ (1 GBq)

and allowed to react at 110 ˚C for 15 min. The reaction mixture was then diluted with *tert*-butyl methyl ether (TBME) and loaded onto a silica Sep-Pak cartridge, which was pre-conditioned with hexanes (10 mL). The product was eluted into a clean reaction vial using 9:1 hexanes: EtOAc (3 mL) and evaporated to dryness on a Biotage V10 Evaporator. The purified product was isolated in a 41 ± 5% RCY and >98% RCP. The identity of **[^{18}F]12** was confirmed by co-injection with the non-radioactive standard, **12**, showing a consistent retention time of 3.4 minutes (55-95% gradient).

Pentafluorophenyl [^{18}F]4'-fluorobiphenyl-4-carboxylate ([^{18}F]16): Anhydrous ACN (1 mL) was added to re-dissolve **[^{18}F]12** followed by 20 µL of 1 M tetramethylammonium hydroxide (TMAH). The reaction mixture was heated to 90 ˚C for 5 min prior to being diluted with 0.1% TFA in water (7 mL) and loaded onto a C18 Sep Pak pre-conditioned with ethanol (10 mL) and water (10 mL). The product was then eluted into a reaction vial containing pentafluorophenol (20 mg), EDC•HCl (10 mg), and DMAP (1 mg) using anhydrous ACN (1 mL). The mixture reacted at room temperature for 7 min prior to being quenched with H_2O (1 mL) and purified by preparative radio-HPLC (70-95% gradient). The purified product was isolated in an overall RCY across all 3 steps of 31 ± 2% and >98% RCP. The identity of **[^{18}F]16** was confirmed by co-injection with the non-radioactive standard, **16**, showing a consistent retention time of 6.5 minutes (70-95% gradient).

H-Inp-S-Dpr([^{18}F]4'-FBC)-1Nal-LSPT-NH$_2$ ([^{18}F]2): A solution of peptide precursor **17** (H-Inp-S-Dpr-1Nal-LSPT-NH$_2$, 2 mg) dissolved in anhydrous ACN (1 mL) was added to dried **[^{18}F]16** followed by DIPEA (30 µL). The mixture reacted for 20 min at 40 ˚C prior to being quenched with H_2O (1 mL) and purified by preparative radio-HPLC (20-80% gradient). The purified product was isolated in a 54 ± 8% RCY and >98% RCP for this step. The overall RCY across all 4 steps was 17 ± 3%. The identity of **[^{18}F]2** was confirmed by co-injection with the non-radioactive standard, **2**, showing a consistent retention time of 5.4 minutes (20-80% gradient).

2.4.5 Competitive Radioligand-Displacement Binding Assay

The affinity of ghrelin(1-8) analogues for the GHSR was determined through a competitive radioligand-displacement binding assay using human [^{125}I]-ghrelin(1-28) as the radioligand (PerkinElmer, NEX388010UC). The assay was performed on ice using HEK293 cells transiently transfected with GHSR1a-eYFP by means of calcium phosphate transfection for 48 hours prior to being harvested and frozen to 2 million cells per vial in 10% DMSO in FBS. A 1 mM stock solution of the test peptide was initially prepared in binding buffer (25 mM HEPES, 5 mM MgCl$_2$, 1 mM CaCl$_2$, 2.5 mM EDTA, and 0.4% BSA, pH 7.4). A frozen aliquot of cells was thawed, centrifuged (3,000 rpm, 10 min, room temperature), and the resulting cell pellet was resuspended in binding buffer. The radioligand (15 pM) and cells (100 000 cells/assay tube) were added to each assay tube containing varying concentrations of test peptide (10^{-6} M, 10^{-7} M, 10^{-8} M, 10^{-9} M, 10^{-10} M, 10^{-11} M, 10^{-12} M) and incubated at 37 °C with agitation for 20 minutes. The assay tubes were then centrifuged at 13,000 g for 5 min and the supernatant was subsequently removed. The cell pellet was washed with ice-cold Tris-HCl buffer (50 mM, pH 7.4) and centrifuged again at 13,000 g for 5 min. The supernatant was removed and the amount of [^{125}I]-ghrelin(1-28) remaining in the tubes was counted using a γ counter. IC$_{50}$ values were determined by non-linear regression analysis to fit a four-parameter dose-response curve using GraphPad Prism® 6 version 6.0c. All binding assays were performed in triplicate.

2.4.6 Cell uptake

The LNCaP GHSR$^+$ cells were maintained in RPMI-1640 medium (Wisent) supplemented with 10% fetal bovine serum (FBS; Wisent) and 1% Penicillin Streptomycin. Cells were seeded into 6-well tissue culture plates (Sarstedt) at a density of 4.0 x 10^5 cells per 35-mm well. Cells were allowed to seed for 48 hours before the cell uptake experiment was performed. Serum media was removed and plates were rinsed with HBSS (1 mL) followed by incubation with 2% BSA in HBSS for 30 min to reduce non-specific binding to the plates. The BSA solution was removed and cells were washed with 0.1% BSA in HBSS. Cells were incubated with 0.1 - 0.5 MBq of [^{18}F]1 in HBSS (1 mL) for 60 min at 37 ºC. For blocking experiments, wells were incubated with 0.1 - 0.5

MBq of [^{18}F]1 and 20 µM of unlabelled probe (**1**) in HBSS (1 mL) for 60 min at 37 °C. At the end of the incubation time, plates were washed with cold HBSS three times to remove any unbound probe. Cells were then removed from the plate by scraping and wells were washed with cold PBS three times. Cell suspensions and wash solutions from each well were counted for activity on a γ counter. Data was then normalized based on the amount of activity added to the well and decay corrected. The percent uptake of [^{18}F]1 was calculated for each experiment and a one-way ANOVA with Tukey's multiple comparisons test was used to determine significance between cell lines and blocking studies ($^{***}P = 0.0002$; $^{****}P < 0.0001$).

2.4.7 Animal Studies

The Animal Use Subcommittee of the Canadian Council on Animal Care (CCAC) at Western University approved the protocols for all mouse handling and treatment procedures described in this study (AUP-2017-137). The CCAC is the national organization responsible for setting and maintaining standards for the ethical use and care of animals in science in Canada.

2.4.8 Biodistribution

A group of male C57BL/6 mice (n = 4) were anaesthetized with 2% isofluorane by inhalation prior to being injected with 3-5 MBq of [^{18}F]1 via intravenous tail vein administration. A second group of male C57BL/6 mice (n = 4) were anaesthetized with 2% isofluorane by inhalation prior to being injected with 100 µL of blocking agent **1** (2 mg/mL) in saline followed by 3-5 MBq of [^{18}F]1 via intravenous tail vein administration 5 minutes later. The animals were sacrificed at 60-minutes post radiotracer injection. The tissues and organs of interest were removed and weighed prior to being counted for radioactivity in a gamma counter. Data was then normalized based on the amount of activity injected and decay corrected. The percent injected dose per gram of tissue (% ID/g) was calculated for each organ and a paired t-test was used to determine significance between the two groups for each organ ($P < 0.05$).

2.4.9 µPET Imaging

In vivo imaging studies were carried out in male C57BL/6 mice (n = 1). Prior to the imaging session, animals were warmed using a heat lamp and anaesthetized with 1.5% isofluorane by inhalation. The mouse head and body were positioned on the scanning bed using medical tape and a catheter was placed in the lateral tail vein for administration of [¹⁸F]1. The mouse was injected with 3-5 MBq of [¹⁸F]1 and a 60- minute dynamic scan was performed using a Siemens Inveon prelinical PET scanner. Small animal PET scans were reconstructed using Explore Vista software.

2.5   References

1   A. D. Howard, S. D. Feighner, D. F. Cully, J. P. Arena, A. Paul, C. I. Rosenblum, M. Hamelin, D. L. Hreniuk, O. C. Palyha, M. Hamelin, D. L. Hreniuk, O. C. Palyha, J. Anderson, P. S. Paress, C. Diaz, M. Chou, K. K. Liu, K. K. Mckee, S. Pong, A. Elbrecht, M. Dashkevicz, R. Heavens, M. Rigby, J. S. Dalip, A. D. Howard, S. D. Feighner, D. F. Cully, J. P. Arena, P. A. Liberator, C. Rosenblum, M. Hamelin, D. L. Hreniuk, O. C. Palyha, J. Anderson, P. S. Paress, C. Diaz, M. Chou, K. K. Liu, K. K. Mckee, S. Pong, L. Chaung, A. Elbrecht, M. Dashkevicz, R. Heavens, M. Rigby, D. J. S. Sirinathsinghji, D. C. Dean, D. G. Melillo, A. A. Patchett, R. Nargund, P. R. Griffin, J. A. Demartino, S. K. Gupta, J. M. Schaeffer, R. G. Smith and L. H. T. Van Der Ploegt, *Science (80-.).*, 1996, **273**, 974–977.

2   L. Mihalache, A. Gherasim, O. Niță, M. C. Ungureanu, S. S. Pădureanu, R. S. Gavril and L. I. Arhire, *Hormones*, 2016, **15**, 186–196.

3   Y. Mao, T. Tokudome and I. Kishimoto, *Curr. Hypertens. Rep.*, 2016, **18**, 1–6.

4   Y. Lv, T. Liang, G. Wang and Z. Li, *Biosci. Rep.*, 2018, **38**, 1–13.

5   T. Tokudome, K. Otani, M. Miyazato and K. Kangawa, *Peptides*, 2019, **111**, 42–46.

6   Y. Mear, A. Enjalbert and S. Thirion, *Front. Neurosci.*, 2013, **7**, 1–7.

7   W. Chen and P. J. Enriori, *Transl. Gastrointest. Cancer*, 2015, **4**, 14–27.

8   G. Colldén, M. H. Tschöp and T. D. Müller, *Int. J. Mol. Sci.*, 2017, **18**, 798.

9   A. Beiras-Fernandez, S. Kreth, F. Weis, C. Ledderose, T. Pöttinger, C. Dieguez, A. Beiras and B. Reichart, *Peptides*, 2010, **31**, 2222–2228.

10   T. C. Lin and M. Hsiao, *Biochim. Biophys. Acta*, 2017, **1868**, 51–57.

11   L. K. Chopin, I. Seim, C. M. Walpole and A. C. Herington, *Endocr. Rev.*, 2012, **33**, 849–891.

12   M. Kojima, H. Hosoda, Y. Date, M. Nakazato, H. Matsuo and K. Kangawa, *Nature*, 1999, **402**, 656–660.

13   T. D. Müller, R. Nogueiras, M. L. Andermann, Z. B. Andrews, S. D. Anker, J. Argente, R. L. Batterham, S. C. Benoit, C. Y. Bowers, F. Broglio, F. F. Casanueva, D. D'Alessio, I. Depoortere, A. Geliebter, E. Ghigo, P. A. Cole, M. Cowley, D. E. Cummings, A. Dagher, S. Diano, S. L. Dickson, C. Diéguez, R. Granata, H. J. Grill, K. Grove, K. M. Habegger, K. Heppner, M. L. Heiman, L. Holsen, B. Holst, A. Inui, J. O. Jansson, H. Kirchner, M. Korbonits, B. Laferrère, C. W. LeRoux, M. Lopez, S. Morin, M. Nakazato, R. Nass, D. Perez-Tilve, P. T. Pfluger, T. W. Schwartz, R. J. Seeley, M. Sleeman, Y. Sun, L. Sussel, J. Tong, M. O. Thorner, A. J. van der Lely, L. H. T. van der Ploeg, J. M. Zigman, M. Kojima, K. Kangawa, R. G. Smith, T. Horvath and M. H. Tschöp, *Mol. Metab.*, 2015, **4**, 437–460.

14   J. Yang, M. S. Brown, G. Liang, N. V. Grishin and J. L. Goldstein, *Cell*, 2008, **132**, 387–396.

15   J. A. Gutierrez, P. J. Solenberg, D. R. Perkins, J. A. Willency, M. D. Knierman, Z. Jin, D. R. Witcher, S. Luo, J. E. Onyia and J. E. Hale, *Proc. Natl. Acad. Sci. U. S. A.*, 2008, **105**, 6320–6325.

16   C. L. Charron, J. Hou, M. S. McFarland, S. Dhanvantari, M. S. Kovacs and L. G. Luyt, *J. Med. Chem.*, 2017, **60**, 7256–7266.

17   M. A. Bednarek, S. D. Feighner, S. S. Pong, K. K. McKee, D. L. Hreniuk, M. V. Silva, V. A. Warren, A. D. Howard, L. H. Y. Van der Ploeg and J. V. Heck, *J. Med. Chem.*, 2000, **43**, 4370–4376.

18   M. D. Childs and L. G. Luyt, *Mol. Imaging*, 2020, **19**, 1–15.

19   A. V. Mossine, A. F. Brooks, K. J. Makaravage, J. M. Miller, N. Ichiishi, M. S. Sanford and P. J. H. Scott, *Org. Lett.*, 2015, **17**, 5780–5783.

20   S. Preshlock, S. Calderwood, S. Verhoog, M. Tredwell, M. Huiban, A. Hienzsch, S. Gruber, T. C. Wilson, N. J. Taylor, T. Cailly, M. Schedler, T. L. Collier, J. Passschier, R. Smits, J. Mollitor, A. Hoepping, M. Mueller, C. Genicot, J. Mercier

and V. Gouverneur, *Chem. Commun.*, 2016, **52**, 8361–8364.

21   K. J. Makaravage, A. F. Brooks, A. V. Mossine, M. S. Sanford and P. J. H. Scott, *Org. Lett.*, 2016, **18**, 5440–5443.

22   N. Ichiishi, A. F. Brooks, J. J. Topczewski, M. E. Rodnick, M. S. Sanford and P. J. H. Scott, *Org. Lett.*, 2014, **16**, 3224–3227.

23   V. W. Pike, *J. Label. Compd. Radiopharm.*, 2018, **61**, 196–227.

24   B. H. Rotstein, N. a Stephenson, N. Vasdev and S. H. Liang, *Nat. Commun.*, 2014, **5**, 4365.

25   B. H. Rotstein, L. Wang, R. Y. Liu, J. Patteson, E. E. Kwan, N. Vasdev and S. H. Liang, *Chem. Sci.*, 2016, **7**, 4407–4417.

26   C. Varlow, E. Murrell, J. P. Holland, A. Kassenbrock, W. Shannon, S. H. Liang, N. Vasdev and N. A. Stephenson, *Molecules*, 2020, **25**, 982.

27   L. Wang, S. Yao, R. Tang, H. Zhu, L. Zhang, J. Gong, Q. Chen, T. L. Collier, H. Xu and S. H. Liang, *J. Label. Compd. Radiopharm.*, 2020, **63**, 119–128.

28   H. Jia, Z. Cai, D. Holden, Y. He, S. F. Lin, S. Li, E. Baum, A. Shirali, M. Kapinos, H. Gao, J. Ropchan and Y. Huang, *ACS Chem. Neurosci.*, 2020, **11**, 1673–1681.

29   Y. W. Jung, G. Gu and D. M. Raffel, *J. Label. Compd. Radiopharm.*, 2019, **62**, 835–842.

30   K. Kumata, Y. Zhang, M. Fujinaga, T. Ohkubo, W. Mori, T. Yamasaki, M. Hanyu, L. Xie, A. Hatori and M. R. Zhang, *Bioorganic Med. Chem.*, 2018, **26**, 4817–4822.

31   T. L. Collier, M. D. Normandin, N. A. Stephenson, E. Livni, S. H. Liang, D. W. Wooten, S. A. Esfahani, M. G. Stabin, U. Mahmood, J. Chen, W. Wang, K. Maresca, R. N. Waterhouse, G. El Fakhri, P. Richardson and N. Vasdev, *Nat. Commun.*, 2017, **8**, 15761.

32   D. F. Taber, P. W. DeMatteo and R. A. Hassan, *Org. Synth.*, 2013, **90**, 350–357.

33   J. E. Jakobsson, G. Grønnevik and P. J. Riss, *Chem. Commun.*, 2017, **53**, 12906–12909.

34   P. L. Jeffery, A. C. Herington and L. K. Chopin, *J. Endocrinol.*, 2002, **172**, R7–R11.

35   J.-F. Yao, H. Yang, Y.-Z. Zhao and M. Xue, *Curr. Drug Metab.*, 2018, **19**, 892–901.

36   M. Werle and A. Bernkop-Schnürch, *Amino Acids*, 2006, **30**, 351–367.

37   G. Bordeau, R. Lartia, G. Metge, C. Fiorini-Debuisschert, F. Charra and M. P. Teulade-Fichou, *J. Am. Chem. Soc.*, 2008, **130**, 16836–16837.

38   E. A. Krasnokutskaya, N. I. Semenischeva, V. D. Filimonov and P. Knochel, *Synthesis (Stuttg).*, 2007, **1**, 81–84.

Chapter 3

3 Investigating the *In Vitro* Metabolic Stability of Ghrelin(1-8) Analogues

3.1 Introduction

Peptides have been established as medicinally relevant biomolecules owing to their moderate molecular mass, which lies between that of small molecules and larger macromolecules, such as proteins and antibodies. Other favourable attributes of peptides include their high target affinity and selectivity, sufficiently rapid clearance from blood and non-target tissues, and ease of synthesis.[1] As such, peptides have been involved in the treatment and tracking of various diseases including a multitude of cancer types.[2–4] Molecular imaging affords the ability to visualize and track disease states in a minimally invasive manner. Over the past 20 years, peptides have been developed into imaging agents through installation of radionuclei for imaging and therapeutic purposes. The high target affinity and specificity of peptides as radiopharmaceuticals, which allows for rapid accumulation of the tracer at the target site, provides particular utility towards the imaging and treatment of cancer tumors that highly express peptide receptors.[5] However, the biological half-life of natural peptides is often quite short ($t_{1/2}$ ~ 2-30 min) due to proteolysis leading to exceedingly rapid blood clearance, which is detrimental to the pharmacokinetic profile of peptide-based radiopharmaceuticals.[1,5]

The growth hormone secretagogue receptor 1a (GHSR) is one of several G-protein coupled receptors found to be overexpressed in multiple types of cancer.[2,6] Its endogenous ligand, ghrelin, is a 28 amino acid peptide with ties to several physiological processes, including appetite regulation and energy homeostasis.[7,8] The ghrelin-GHSR axis has been linked to various disease states including cancer and various metabolic disorders, such as obesity, diabetes, and cachexia.[9–11] The high affinity and specificity of ghrelin for its target made it a valuable starting point for the development of imaging probes targeting the GHSR. Therefore, efforts to image the GHSR have resulted in the development of several ghrelin mimetics for optical and nuclear imaging of this receptor target.[12] However, like many natural peptides, ghrelin suffers from poor metabolic

stability when administered *in vivo*.[13] Therefore, the development of ghrelin-based GHSR imaging agents not only need to modify ghrelin to include a traceable imaging moiety, but also needs to modify the peptide to improve its pharmacokinetic behaviour. As such, it is prudent to investigate how structural modifications affect metabolic stability in addition to target affinity. Several early reports studied the structure-activity relationship (SAR) between ghrelin and the GHSR laying the groundwork for the development of ghrelin analogues as imaging probes.[14–16] One recent study reported a high-affinity fluorine-containing ghrelin analogue, truncated to only the first eight amino acids for ^{18}F-PET imaging. The peptide [Inp^1,Dpr^3(6-FN),1Nal^4,Thr^8]ghrelin(1-8) amide (**1**) (Figure 3.1) showed sub-nanomolar receptor affinity (IC$_{50}$ = 0.11 nM) toward the GHSR making it the highest affinity ghrelin analogue reported to date.[17]

The study that resulted in the peptide **1** focused its efforts on investigating the SAR of ghrelin(1-8) at positions 1, 4, and 8, as well as the side chain modification at position 3. Other positions in the ghrelin(1-8) analogue sequence remained untouched. The authors employed common strategies known to improve metabolic stability without hindering receptor affinity including amidation of the *C*-terminus and of the linkage between Ser^3 and the acyl side chain.[14,15] Positions 1 and 4 were modified to include unnatural amino acids, isonipecotic acid (Inp) and 1-naphthylalanine (Nal-1), likely improving the stability further, particularly at the *N*-terminus, which would otherwise be exposed to enzymatic degradation from exopeptidases. Embedded in the hydrophobic side chain at position 3, a key location for receptor binding, is a fluorine which may be incorporated as fluorine-18 for PET imaging.

A recent *in vivo* biodistribution study of **[18F]1** in normal mice revealed high radiotracer uptake in the liver and intestines at 60 min post-injection (p.i) (figure 2.4). *In vivo* PET imaging in normal mice showed fast blood clearance with high kidney and liver uptake at 3-6 min p.i., which transitioned to high intestinal uptake at 57-60 min p.i., consistent with the biodistribution data (figure 2.5). A possible explanation for this observation is poor metabolic stability of the imaging probe. While peptide **1** offers substantially improved binding affinity over natural ghrelin, there has been little investigation into the metabolic stability of this analogue. Despite the presence of multiple unnatural amino acids in

peptide **1**, other areas of the molecule remain susceptible to proteolytic cleavage. Such areas are referred to as metabolic soft-spots, and they can be addressed through targeted structural modification to improve metabolic stability.

The aim of the present study is to explore the *in vitro* metabolic stability of ghrelin analogue **1** and identify the metabolites formed in the presence of blood and liver metabolic enzymes. Metabolic stability of other peptidic GHSR ligands have been studied *in vitro* through incubations in various human media including serum, liver/kidney microsomes, and liver/kidney S9 fraction for the purpose of sport drug testing applications.[18,19] Due to the rapid blood clearance observed for this probe and its propensity to be taken up in the liver, examining its metabolic stability in serum and liver media was of interest. As a result of this study, a metabolic soft-spot between Leu[5] and Ser[6] was identified and served as the basis for the development of a library of novel ghrelin(1-8) analogues based on **1** for targeted improvement of proteolytic stability while maintaining a strong binding affinity toward the GHSR.

3.2   Results and Discussion

3.2.1 *In Vitro* Metabolic Stability of Ghrelin(1-8) Analogue **1**

One of the drawbacks to peptides as pharmaceutical agents is their tendency toward rapid blood clearance due to low proteolytic stability.[20] To investigate the stability of **1** and identify any metabolic soft spots, an *in vitro* stability assay in human serum was carried out. The amount of intact peptide was measured by UHPLC-MS at various time points over the course of 24 hours. As an additional comparison, a control sequence of ghrelin(1-8), with minimal modification compared to the native sequence, was also evaluated by the same method. The peptide [Dpr[3](*n*-octanoyl)]ghrelin(1-8) (**2**) (Figure 3.1) was synthesized and its serum stability analyzed to evaluate and compare how modifications at positions 1, 4, and 8 influenced *in vitro* stability. The use of an amide linkage at position 3 was maintained since it is well known that cleavage of the natural ester at this position occurs rapidly in the presence of proteases, which would complicate the analysis of observing metabolites resulting from peptide backbone fragmentation.[13] As a control, the chemical stability of both peptides **1** and **2** were evaluated and found to

be chemically stable when incubated in buffer at 37 ˚C over 24 hours, indicating that all degradation in the serum experiments was enzyme-mediated.
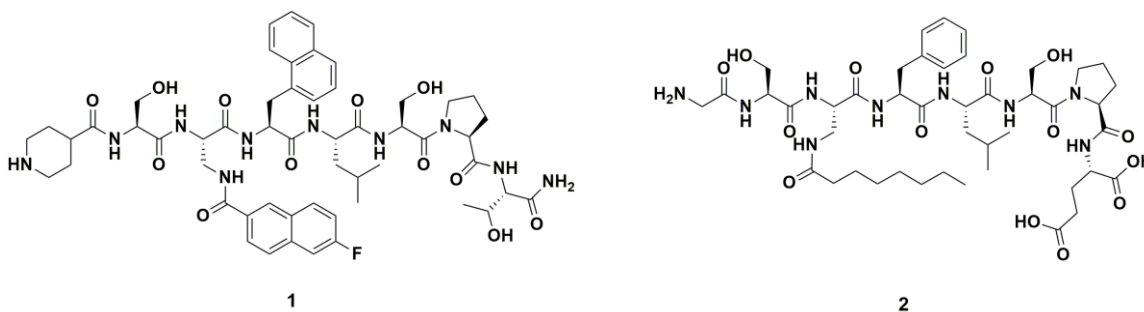
Figure 3.1. Structures of ghrelin(1-8) analogues **1** and **2**.

Following the 24-hour incubation of peptide **1** in human serum, 8% of the parent peptide remained intact (Figure 3.2A) and four peaks corresponding to metabolites were observed by UHPLC-MS (Figure 3.3A). Mass-to-charge ratio (m/z) values corresponding to each peak allowed for the identification of each metabolite to be proposed (Figure 3.4). Over the course of the assay, formation of the four metabolites (**3**-**6**) was asynchronous as illustrated in figure 3.3. Metabolite **3** was observed after only 30 minutes and steadily increased over the next 5.5 hours, after which its growth slowed. The rate of formation of the other three metabolites started to increase later in the experiment with metabolite **6** only observed in substantial quantities after 24 hours. The pattern in which the metabolites arose suggests the possibility that metabolites **4-6** were formed from further degradation of metabolite **3** instead of from the parent peptide **1**. Analysis of the metabolites formed from peptide **2** observed cleavage at the same position as in peptide **1**, however, additional degradation from the *N*-terminus of the peptide inward was also observed. Peptide **2** was completely degraded after 6 hours of incubation with a half-life of 1.8 h, which is less than half of peptide **1**, which had a half-life of 4.7 h (Figure 3.2).
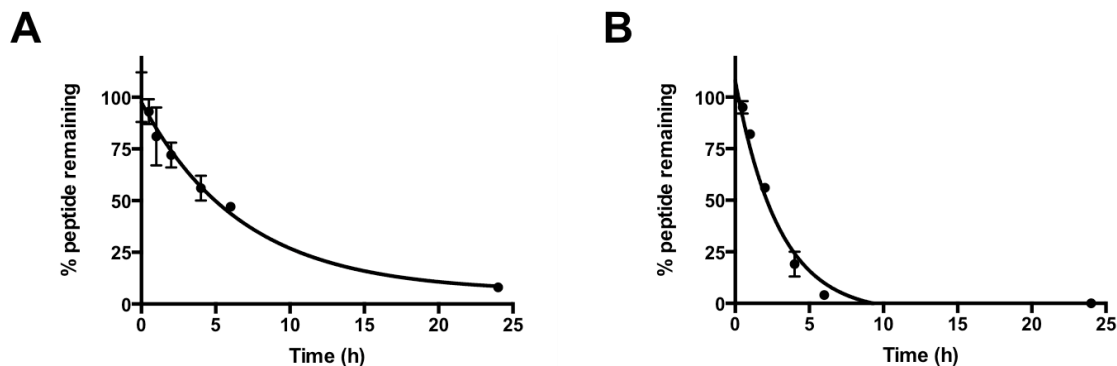
Figure 3.2. (A) Stability of peptide **1** in human serum over 24 h resulting in a half-life of 4.7 h; (B) Stability of peptide **2** in human serum over 24 h resulting in a half-life of 1.8 h.

To confirm the identity of metabolites **3-6,** each metabolite was independently synthesized and characterized via UHPLC-MS. The retention time for each synthesized metabolite matched that of the observed metabolites from the assay data. Additionally, the mass and UV absorbance data were also a match in all cases. This thereby confirms the identity of the serum assay metabolites and confirms the amide bond between Leu[5] and Ser[6] as a metabolic soft spot of **1**. This assessment of peptides **1** and **2** provides a contextual comparison of the two sequences and clearly indicates that the modifications to ghrelin(1-8) resulting in peptide **1** served to not only improve the binding affinity, but also its serum stability. In particular, the substitution of glycine for isonipecotic acid (Inp) at the *N*-terminus in peptide **1** afforded improved stability likely due to the unnatural nature of Inp. However, despite these improvements, the peptide remains insufficiently stable in the serum media and its metabolic profile indicates the presence of a metabolic soft-spot that merits further investigation.
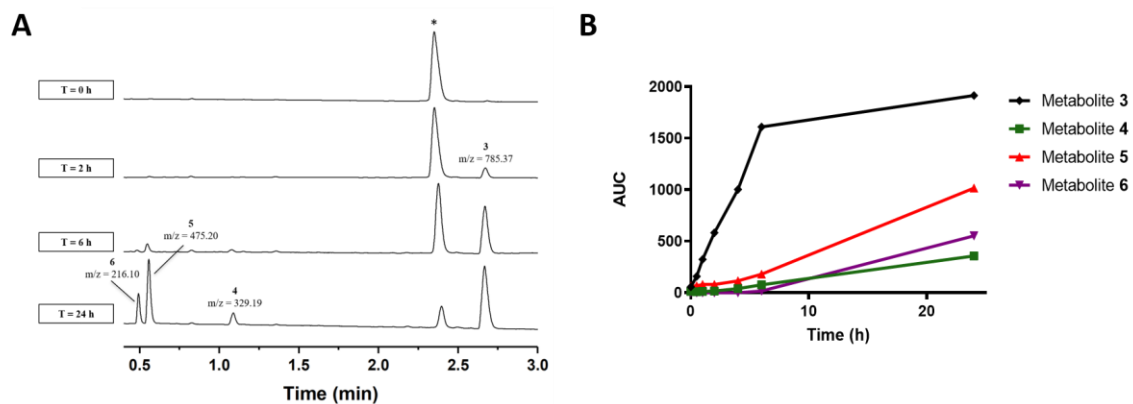
Figure 3.3. (A) Stacked UHPLC-UV chromatograms of peptide **1** metabolism in human serum at select time points. * indicates parent peptide **1**. UV peaks for metabolites **3-6** identified by their m/z values. (B) Quantification of metabolites **3-6** over time. AUC = Area under curve from selected ion chromatogram.
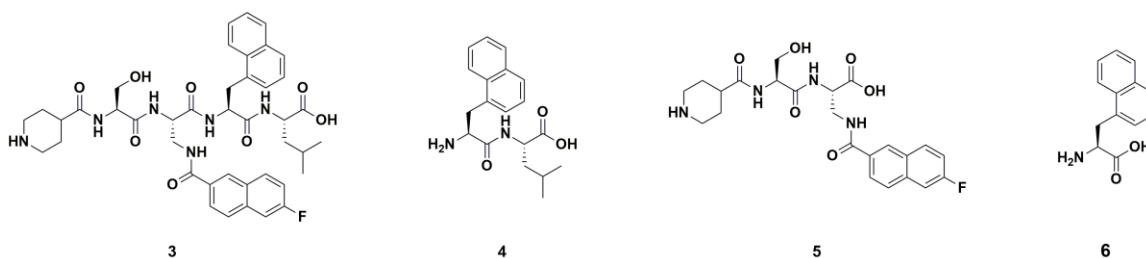
Figure 3.4. Structures of identified metabolites produced from peptide **1** in human serum.

In order to investigate the hepatic stability of peptide **1**, a stability assay in human liver S9 fraction was performed. The S9 fraction is a subcellular fraction of liver hepatocytes and contains the full complement of liver enzymes, some of which may be responsible for peptide metabolism in this organ. Samples of both peptides **1** and **2** were incubated with S9 fraction media at a low concentration over the course of 4 hours and the amount of intact peptide was measured by UHPLC-MS at various time points. Due to the low peptide concentration (3 µM), the rate of metabolism is directly proportional to peptide concentration allowing for analysis according to first-order kinetics.[21] As such, the *in vitro* half-life ($t_{1/2}$) of each peptide was determined according to equation 3.1, where the elimination rate constant (*k*) is obtained from the slope of the linear relationship between $Ln(\%T_0)$ and time (Figure 3.5).

$$t_{1/2} = \frac{ln(2)}{k} \qquad (3.1)$$

Peptide **1** was completely degraded after 4 hours with a half-life of 1.1 h, which is near double the half-life of 0.57 h for peptide **2** (Figure 3.5A). Three proposed metabolites identified based on their m/z values indicate degradation from the *C*-terminus of peptide **1** with cleavage of amino acids Thr[8], Pro[7], and Ser[6] (Figure 3.6). The amount present of metabolites **7** and **8** appeared to decrease after the first hour of incubation indicating that these metabolites were themselves being metabolized. Interestingly, one of these metabolites, which was present in the largest quantity by the end of the experiment (Figure 3.5B), was metabolite **3,** also observed as a product of serum metabolism. This further supports the presence of a metabolic soft spot between Leu[5] and Ser[6] and that the enzymes that metabolize this peptide are not solely expressed in one specific organ.
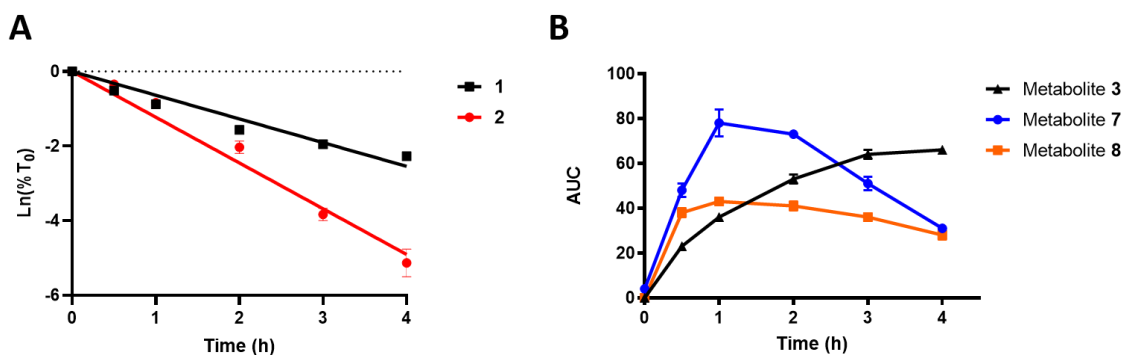
Figure 3.5. (A) Stability of peptides **1** and **2** in human liver S9 fraction over 4 hours. (B) Quantification of metabolites **3**, **7**, and **8** over time from peptide **1**. AUC = Area under curve from selected ion chromatogram.
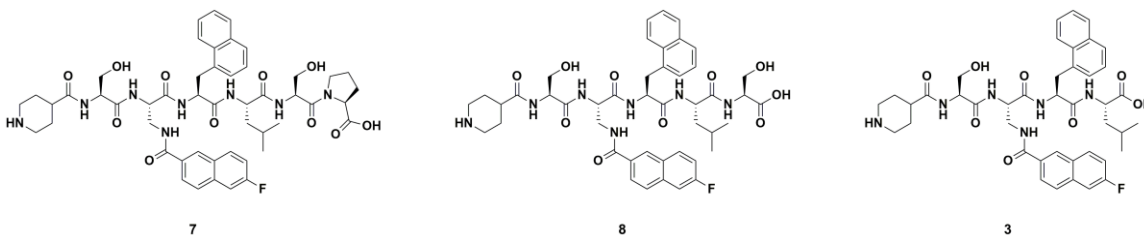
Figure 3.6. Structures of identified metabolites produced from peptide **1** in human liver S9 fraction.

Another consideration is the fact that an amide bond was used to conjugate the fluorine-bearing aryl group to the peptide backbone. Since this amide bond is also susceptible to hydrolysis in the same manner as peptide bonds, it is worthwhile to note that no cleavage of the fluorine-containing aromatic group was observed in our *in vitro* stability studies.[5] This suggests that the ^{18}F-labelled prosthetic group would likely not be lost during *in vivo* PET imaging.

3.2.2 Structure-Activity-Stability Study of Ghrelin(1-8) Analogues

Following identification of Leu[5] and Ser[6] in peptide **1** as a metabolic soft-spot through both serum and hepatic stability investigation, a targeted library of ghrelin(1-8) analogues was developed in an effort to improve the *in vitro* stability while maintaining the strong binding affinity of this peptide. There is limited information describing the SAR between positions 5 and 6 in ghrelin and the receptor. An alanine scan of ghrelin(1-14) showed negligible changes in IC_{50} when alanine was substituted for Leu[5] or Ser[6] compared to the unmodified peptide sequence.[16] This suggests that modifications at these two positions may be well tolerated. Therefore, analogues of peptide **1** were synthesized via standard Fmoc solid-phase peptide synthesis, purified by reverse-phase HPLC-MS, and characterized by UHPLC-MS.

The binding affinities of all analogues toward the GHSR were evaluated in a competitive radioligand-displacement binding assay against [^{125}I]-ghrelin(1-28) using HEK293 cells transiently transfected with GHSR-eYFP (Table 3.1). As controls, acylated human ghrelin(1-28) and peptide **1** were evaluated to confirm the integrity of the assay. Human ghrelin and peptide **1** were found to possess binding affinity values of 2.48 nM and 0.09 nM, respectively, which are in agreement with published literature values.[17] Additionally, all analogues were evaluated *in vitro* for metabolic stability in human serum and human liver S9 fraction, the results of which are summarized in table 3.1.

Table 3.1. *In vitro* binding affinity and metabolic stability of ghrelin(1-8) analogues based on peptide **1**.

#	Sequence	IC$_{50}$ (nM)	Serum t$_{1/2}$ (h)	S9 t$_{1/2}$ (h)
	Human ghrelin(1-28)	2.48	n.d	n.d
1	Inp-S-Dpr(6-FNA)-Nal-1-LSPT-NH$_2$	0.09	4.7	1.08
2	GS-Dpr(n-octanoyl)-FLSPE-OH	n.d	2.0	0.57
9	Inp-S-Dpr(6-FNA)-Nal-1-**l**SPT-NH$_2$	56.5 ± 6.5	>24	>4
10	Inp-S-Dpr(6-FNA)-Nal-1-L**s**PT-NH$_2$	3.55 ± 0.25	>24	>4
11	Inp-S-Dpr(6-FNA)-Nal-1-**ls**PT-NH$_2$	11.5 ± 0.3	>24	>4
12	Inp-S-Dpr(6-FNA)-Nal-1-L**t**PT-NH$_2$	2.52 ± 0.32	>24	>4
13	Inp-S-Dpr(6-FNA)-Nal-1-**Nle**-SPT-NH$_2$	1.50 ± 0.27	1.7	0.55
14	Inp-S-Dpr(6-FNA)-Nal-1-**Cha**-SPT-NH$_2$	1.88 ± 0.67	2.4	1.18
15	Inp-S-Dpr(6-FNA)-Nal-1-L**C**PT-NH$_2$	7.15 ± 0.18	<0.5	0.95
16	Inp-S-Dpr(6-FNA)-Nal-1-L**T**PT-NH$_2$	0.62 ± 0.10	>24	1.25
17	Inp-S-Dpr(6-FNA)-Nal-1-L-**Hse**-PT-NH$_2$	1.43 ± 0.08	>24	1.40
18	Inp-S-Dpr(6-FNA)-Nal-1-L**N**PT-NH$_2$	1.90 ± 0.56	>24	>4
19	Inp-S-Dpr(6-FNA)-Nal-1-L**Q**PT-NH$_2$	1.21 ± 0.12	>24	2.03
20	Inp-S-Dpr(6-FNA)-Nal-1-L-**Abu**-PT-NH$_2$	2.54 ± 0.65	>24	0.46
21	Inp-S-Dpr(6-FNA)-Nal-1-L-**Dpr**-PT-NH$_2$	0.32 ± 0.03	>24	>4
22	Inp-S-Dpr(6-FNA)-Nal-1-L-**S(*N*-Me)**-PT-NH$_2$	1.32 ± 0.58	>24	>4
23	Inp-S-Dpr(6-FNA)-Nal-1-**β-homoL**-SPT-NH$_2$	2.11 ± 0.21	>24	1.48
24	Inp-S-Dpr(6-FNA)-Nal-1-**L*ψ*[Tz]S**PT-NH$_2$	1.79 ± 0.11	n.d	n.d

n.d – not determined

A common practice in seeking to improve metabolic stability of peptides through structural modification is by inverting the stereochemistry at specific sites within the peptide sequence. The use of *D*-amino acids in place of *L*-amino acids serves as an effective method to disrupt the ability for enzymes to recognize and bind the ligand in order to facilitate peptide hydrolysis. Analogue **9** substituted Leu[5] for *D*-Leu and, while the ligand was completely stable to both stability media, this modification led to a dramatically negative impact on binding affinity reducing the IC_{50} to 56.5 nM. This indicates that the stereochemistry at position 5 is critical for favourable binding toward the GHSR. Interestingly, recent work investigating the binding mode of ghrelin toward the GHSR used NMR studies and molecular modelling to suggest that Phe[4], Leu[5], and the Dpr[3]-linked *n*-octanoyl side chain in ghrelin come together to form a rigid hydrophobic core when in the GHSR-bound state.[22] It would not be unreasonable to then suggest that appropriate stereochemistry at these positions may indeed be necessary for such a core to form during a binding event. In contrast, substitution of Ser[6] for *D*-Ser (**10**) did not cause such a drastic reduction in binding affinity indicating that stereochemistry at this position is not as vital. Rather, compound **10** resulted in an IC_{50} value of 3.55 nM, which is comparable to that of natural ghrelin(1-28). Predictably, an amalgamation of the alterations made in analogues **9** and **10** resulted in analogue **11** with a binding affinity value between those two compounds (IC_{50} = 11.5 nM). Furthermore, the use of *D*-Thr[6] in place of serine (**12**) also resulted in a reduction in binding affinity similar to that of compound **10**, indicating that stereochemistry at positions 5 and 6 within this peptide sequence should remain in the *L* configuration to preserve binding affinity despite the improved *in vitro* metabolic stability. Interestingly, modification at positions 5 and/or 6 with *D*-amino acids also resulted in the suppression of metabolites **7** and **8**, which form during incubation with liver S9 fraction. This indicates that structural modification at one position in the molecule may lead to enhanced stability of other nearby areas.

In maintaining appropriate *L* stereochemistry at position 5, two non-canonical amino acids, norleucine (Nle) and cyclohexylalanine (Cha), which both possess hydrophobic alkyl side chains, were substituted in place of Leu[5] in an effort to maintain similar physicochemical properties. Both analogues **13** and **14** led to a mild reduction in binding affinity with IC_{50} values of 1.50 nM and 1.88 nM, respectively. However, the surprising

result was that these analogues also both led to a reduction in both serum and hepatic metabolic stability despite their unnatural nature. It is possible that the side chains of Nle and Cha were similar enough to Leu allowing for sufficient, or likely improved recognition by metabolizing proteases. Therefore, the focus of further optimization was focused at position 6 and the peptide backbone.

To explore the structure-activity-stability relationship at position 6, Ser^6 was substituted with other polar, uncharged amino acids including cysteine (**15**), threonine (**16**), homoserine (Hse) (**17**), asparagine (**18**), and glutamine (**19**). Due to the propensity for cysteine to be oxidized in a biological environment, analogue **15** was found to possess a half-life in human serum of less than 30 minutes. Analogues **16-19** explored the chemical space occupied by the residue in position 6. Peptides **17-19** demonstrated IC_{50} values in the low nanomolar range, which is still a reduction in binding affinity compared to the parent peptide **1**. However, analogue **16** with Thr^6 was found to possess subnanomolar affinity with an IC_{50} value of 0.62 nM, which is only a slight reduction compared to peptide **1**. Interestingly, all four analogues **16-19** resulted in substantial improvement in serum stability with half-lives over 24 hours. This was surprising since modifications in these analogues involved natural amino acids, with the exception of **17**. However, metabolic stability in liver S9 fraction was not substantially improved in peptides **16** and **17**. Analogue **19** was nearly twice as stable as peptide **1** in the liver S9 fraction media and analogue **18** was confirmed to have a half-life of over 4 hours. Unlike modifications using *D*-amino acids, some of these modifications at position 6 were unable to also suppress hydrolysis at the *C*-terminus in order to improve hepatic stability.

In addition to evaluating the impact of expanding the local chemical space at position 6, we also sought to explore the necessity of the serine hydroxyl in this position. As such, analogue **20** substituted Ser^6 with *L*-α-aminobutyric acid (Abu), which replaces the polar hydroxyl group with a non-polar methyl group. Removal of polarity on the position 6 residue resulted in a reduction in binding affinity with an IC_{50} value of 2.54 nM, indicating that the serine hydroxyl plays at least a minor role in binding to the GHSR. In contrast to removing polarity from this position, analogue **21** converted Ser^6 to Dpr^6, which places a formal positive charge on this residue under physiological conditions.

Remarkably, the binding affinity of this analogue was very similar to the parent peptide with an IC_{50} value of 0.32 nM. Additionally, analogue **21** also demonstrated full stability over 24 hours in human serum signifying that hydrolysis of peptide **1** in human serum is likely dependent on the presence of serine in position 6. Furthermore, the half-life of over 4 hours in human liver S9 fraction demonstrates the ability for this single modification at position 6 to also suppress metabolism at the *C*-terminus to a large extent.
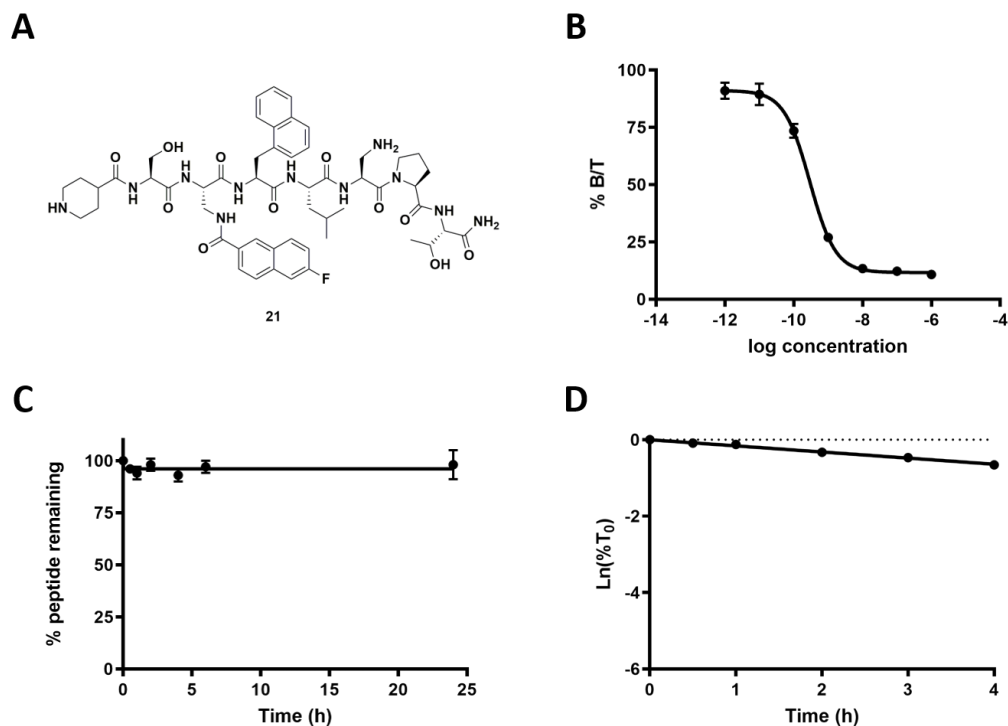
Figure 3.7. Structure and *in vitro* data for ghrelin(1-8) analogue **21**. (A) Structure; (B) IC_{50} curve ($IC_{50} = 0.32 \pm 0.03$ nM) (n = 2); (C) Human serum stability ($t_{1/2} > 24$ h); (D) Human liver S9 fraction ($t_{1/2} > 4$ h).

In addition to modifying the side chain residues of peptides, modification to the peptide backbone can also result in improved metabolic stability. To that end, *N*-methylation of the amide nitrogen between positions 5 and 6 resulted in analogue **22**. While a reduction in binding affinity was observed, this analogue was also stable in both serum and liver S9 fraction media. A recent report suggested a weak interaction between this amide proton and the GHSR backbone, which may explain the reduction in affinity in analogue **22** due to its removal.[22] Substitution of Leu[5] for *L*-β-homoleucine (**23**) expanded the peptide

backbone by an additional carbon thus adding additional flexibility to the peptide. However, this negatively impacted the binding affinity and, while serum stability was improved substantially, liver S9 fraction stability was only improved marginally.

Finally, the amide bond bridging positions 5 and 6 was replaced with a 1,4-triazole to give analogue **24**. Such triazoles show similar planarity and size compared to amide bonds and have been identified as suitable metabolically stable bioisosteres of *trans* amide bonds.[23] While the synthesis of such triazole-containing analogues is compatible with solid-phase peptide synthesis (SPPS) through copper-catalyzed click chemistry, the appropriate amino acid-derived alkyne and azide building blocks must be first prepared individually. Scheme 3.1 outlines the synthesis of azido serine (**27**) and the leucine-alkyne (**31**) derivative, which led to peptide **24** through SPPS. Fmoc-*L*-Ser(*t*Bu)-OH (**25**) was Fmoc-deprotected to produce the free amino acid (**26**), which then underwent a diazo transfer with imidazole-1-sulfonyl azide hydrogen sulfate to produce azide **27**. Preparation of **31** involved reduction of commercially available Weinreb amide **28** to α-amino aldehyde **29**, which subsequently underwent a Seyferth-Gilbert homologation with the Bestmann-Ohira reagent to produce alkyne **30**. The Boc protecting group was then removed and replaced with Fmoc to make the alkyne building blocking compatible with Fmoc SPPS. To confirm enantiomeric purity of the leucine-alkyne building block, a small sample of alkyne **31** was coupled to Fmoc-*L*-Ala-OH and the diastereoisomeric purity of the resulting dipeptide was analyzed by HPLC and NMR spectroscopy. Gratifyingly, no racemization of the leucine chiral center was observed, which is in accordance with the literature.[23] Peptide **24** was ultimately obtained through SPPS as outlined in scheme 3.1C and evaluated for binding toward the GHSR. The resulting binding affinity of **24** was reduced to an IC_{50} value of 1.79 nM, a moderate reduction compared to the parent peptide **1**. It is possible that the reduction in binding affinity may be due to the removal of the amide proton from that position resulting in a similar affinity value to that of analogue **22**.

Scheme 3.1. (A) Synthesis of azido serine **27**; (B) Synthesis of amino alkyne **31**; (C) General synthetic outline for the synthesis of triazole-containing peptide **24**.
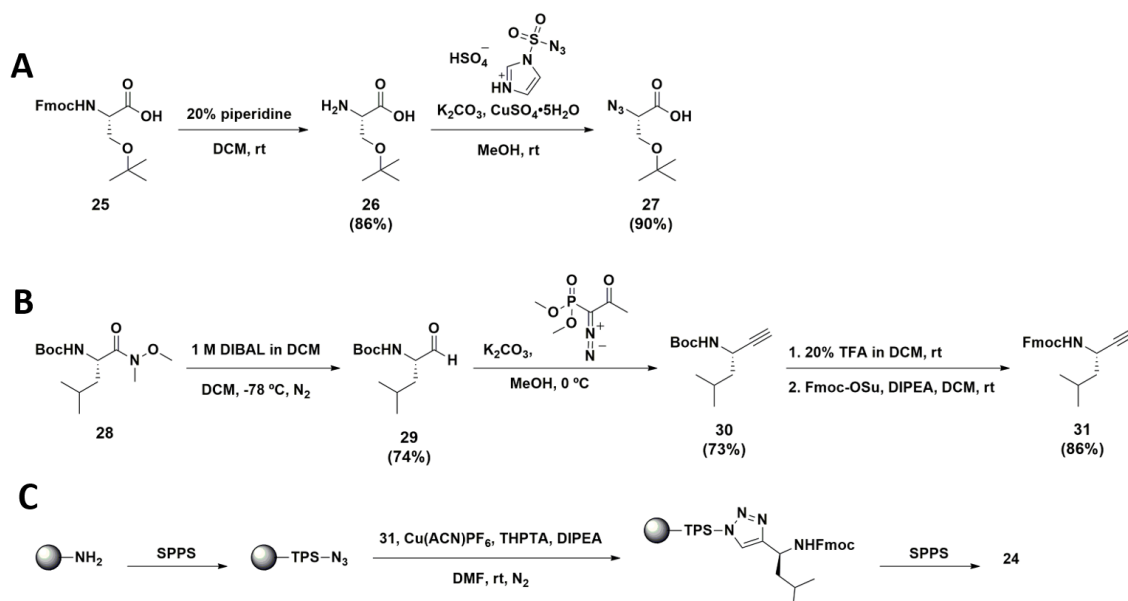
3.3 Conclusions

The GHSR has been implicated as a potential biomarker for disease states including several types of cancer and cardiac pathology. In the interest of imaging GHSR expression, several molecular probes based on the endogenous ligand for the GHSR, ghrelin, have been developed.[12] However, one of the key barriers to peptides as pharmaceutical agents is their propensity to undergo rapid enzymatic degradation through proteolysis. In an effort to better understand and improve the stability of a high-affinity GHSR ligand, peptide **1**, we evaluated the *in vitro* stability of this ligand in human serum and human liver S9 fraction. The metabolites identified through these experiments revealed a metabolic soft-spot between Leu[5] and Ser[6] in this peptide sequence.

To address this metabolic weak point, a focused library of ghrelin(1-8) analogues was created and evaluated for stability and affinity toward the GHSR. The analogues contained within this library possessed modifications to residues 5 and 6, as well as to the peptide backbone. Little work investigating the structure-activity relationship of ghrelin analogues at positions 5 and 6 exist. As such, this library also serves to provide additional insight into the structural importance of the residues at these positions. It is well

established in the literature that the *N*-terminal region of ghrelin is most important for its binding toward the GHSR.[14,15] This work further demonstrate this importance through modifications at positions 5 and 6. In particular, the critical nature of *L*-stereochemistry at position 5 and, to a lesser extent, position 6 was revealed. As a result simple substitution of *D*-amino acids could not be applied in this molecular context. Additional exploration of the local chemical space at residue 6 concluded that this residue needed to remain small in size in order to preserve the subnanomolar binding affinity. Additionally, probing the necessity of the hydroxyl group on Ser^6 for GHSR binding concluded that a polar group is required, but does not necessarily need to be uncharged. The influence of these modifications at residue 6 on functional GHSR activation has not yet been elucidated. As such, investigation into the functional structure-activity relationship with compounds **1**, **20**, **21**, and **22** to determine the importance of this residue in GHSR activation is currently underway.

Overall, of the 16 ghrelin(1-8) analogues evaluated in this study, only two maintained subnanomolar binding affinity. However, of these two analogues, peptide **21**, which substituted Ser^6 with Dpr, also demonstrated substantial improvement in metabolic stability in both human serum and human liver S9 fraction compared to parent peptide **1**. This peptide further demonstrates the capability of a modification at position 6 to influence metabolic stability at the *C*-terminus. Future efforts to develop an efficient method to label peptide **21** with fluoride-18 are required prior to preclinical PET imaging *in vivo*. Nevertheless, the improved *in vitro* stability and strong binding affinity make this peptide a viable lead candidate for further evaluation as a GHSR imaging agent.

3.4 Experimental

3.4.1 Materials and Methods

All common solvents were obtained from Fisher Scientific. Amino acids, resins, and coupling agents were obtained from Chem-Impex and Aapptec. Human [^{125}I]-ghrelin (NEX388010UC) was purchased from Perkin Elmer. All other reagents were purchased from Sigma-Aldrich, Fisher Scientific, or Oakwood Chemicals and were used as received. Analytical and preparative reverse-phase HPLC-MS was performed on a system

consisting of a Waters 600 controller, Waters prep degasser, and Waters MassLynx software. The UV absorbance was detected using a Waters 2998 Photodiode array detector. A preparative (Agilent Zorbax PrepHT SB-C18 Column 21.2 x 150 mm, 5 µm) or analytical column (Agilent Zorbax SB-C18 column 4.6 x 150 mm, 5 µm) was used. The solvent system ran gradients of solvent A, 0.1% trifluoroacetic acid (TFA) in ACN, and solvent B, 0.1% TFA in MilliQ (18.2 mΩ·cm conductivity) water, over 10 minutes with a 5 minute wash. A flow rate of 20 mL/min or 1.50 mL/min was used for preparative and analytical runs, respectively. Analytical UHPLC-MS was performed using a Waters Inc. Acquity UPLC H-class instrument in combination with a Xevo QToF mass spectrometer. A Waters Acquity analytical column (UPLC BEH C18 2.1 x 50 mm, 1.7 µm) was used and the UV absorbance was detected using a Waters Acquity PDA detector. The solvent system ran gradients of solvent A, 0.1% formic acid in acetonitrile (ACN, Optima grade, Fisher Scientific), and solvent B, 0.1% formic acid in MilliQ water (18.2 mΩ •cm conductivity), at a flow rate of 0.6 mL/min over 3 minutes followed by a wash over 1 minute. Solution phase reactions were monitored by thin layer chromatography (TLC) using aluminum-backed silica gel TLC plates. Flash chromatography was performed using a Biotage® Isolera™ Prime advanced automated flash purification instrument. Biotage SNAP KP-Sil 10 g, 25 g, or 50 g cartridges (50 µm irregular silica) were used with solvent flow rates of 12, 25, or 50 mL/min for each cartridge type respectively along with the gradient solvent system specified. NMR spectra were obtained using a Bruker 400 MHz spectrometer. Chemical shifts are referenced to the residual solvent peaks and recorded in parts per million. High-resolution mass spectra were determined in positive ion mode using an electrospray ionization (ESI) ion source on either a Waters Xevo QToF or a Bruker micrOToF II mass spectrometer.

3.4.2 General Fmoc Solid Phase Peptide Synthesis

Peptides were synthesized by standard Fmoc solid-phase peptide synthesis on a Biotage® Syrowave™ automated peptide synthesizer. Briefly, peptides were synthesized at a 0.1 mmol scale on Rink amide MBHA resin (0.39 mmol/g). The resin was initially swelled in DCM (4 mL) followed by Fmoc deprotection using 40% piperidine in *N*,*N'*-dimethylformamide (DMF) (1.2 mL) for two cycles (3 min, 12 min). Amino acid

coupling was completed by adding the appropriate Fmoc-protected amino acid (4 eq.) in DMF, HCTU (4 eq.) in DMF, and *N*,*N*'-diisopropylethylamine (DIPEA) (8 eq.) in NMP to the resin and reacting for 40 min. The cycle of Fmoc deprotection followed by amino acid coupling was repeated for until all amino acids were coupled to the resin. All further synthetic modifications were performed manually.

Allyloxycarbonyl deprotection of the Dpr[3] side chain was performed manually under an inert N_2 atmosphere by mixing the peptide resin with phenylsilane (296 µL, mmol) in DCM (4 mL) for 5 minutes followed by the addition of tetrakis(triphenylphosphine)palladium(0) (Pd(PPh$_3$)$_4$) (17 mg, mmol) and reacting for 10 minutes. Coupling of 6-fluoro-2-naphthoic acid to the free side chain amine on Dpr[3] was then performed manually by reacting the resin with a solution of 6-fluoro-2-naphthoic acid (3 eq.), HCTU (3 eq.), and DIPEA (6 eq.) in DMF (2 mL) twice (2 h, 16 h).

Global deprotection and resin cleavage of the peptides were performed by reacting the peptide resin in a solution of 95% TFA, 2.5% TIPS, and 2.5% H_2O (2 mL) for 5 h. The cleaved peptide was precipitated from ice-cold *tert*-butyl methyl ether (TBME) and centrifuged at 3000 rpm for 10 minutes. The supernatant was then decanted and the resulting peptide pellet was re-dissolved in 20% ACN in H_2O, frozen, and lyophilized until dry. The crude peptides were purified using preparative HPLC-MS and collected fractions were combined, frozen, and lyophilized until dry. Purity was determined using analytical UHPLC-MS and is summarized in table 3.2.

Table 3.2. Characterization of peptides including synthesized peptide metabolites.

#	Sequence	$[M+H]^+$ calculated	$[M+H]^+$ found	Yield	Purity
1	Inp-S-Dpr(6-FNA)-Nal-1-LSPT-NH$_2$	1069.5159	1069.5227	33%	99%
2	GS-Dpr(n-octanoyl)-FLSPE-OH	948.5042	948.5121	29%	96%
3	Inp-S-Dpr(6-FNA)-Nal-1-L-OH	785.3669	785.3503	1%	95%
4	Nal-1-L-OH	329.1860	329.1737	43%	95%
5	Inp-S-Dpr(6-FNA)-OH	475.1987	475.2006	1%	99%
6	Nal-1-OH	216.1019	216.1051	27%	95%
9	Inp-S-Dpr(6-FNA)-Nal-1-**l**SPT-NH$_2$	1069.5159	1069. 3982	3%	98%
10	Inp-S-Dpr(6-FNA)-Nal-1-L**s**PT-NH$_2$	1069.5159	1069.4397	12%	96%
11	Inp-S-Dpr(6-FNA)-Nal-1-**ls**PT-NH$_2$	1069.5159	1069.4397	13%	99%
12	Inp-S-Dpr(6-FNA)-Nal-1-L**t**PT-NH$_2$	1083.5315	1083.5210	15%	95%
13	Inp-S-Dpr(6-FNA)-Nal-1-**Nle**-SPT-NH$_2$	1069.5159	1069.5227	15%	99%
14	Inp-S-Dpr(6-FNA)-Nal-1-**Cha**-SPT-NH$_2$	1109.5472	1109.5300	13%	97%
15	Inp-S-Dpr(6-FNA)-Nal-1-L**C**PT-NH$_2$	1085.4930	1085.5042	31%	99%
16	Inp-S-Dpr(6-FNA)-Nal-1-L**T**PT-NH$_2$	1083.5315	1083.5210	21%	95%
17	Inp-S-Dpr(6-FNA)-Nal-1-L-**Hse**-PT-NH$_2$	1083.5315	1083.5417	22%	97%
18	Inp-S-Dpr(6-FNA)-Nal-1-L**N**PT-NH$_2$	1096.5268	1096.4343	35%	95%
19	Inp-S-Dpr(6-FNA)-Nal-1-L**Q**PT-NH$_2$	1110.5424	1110.5437	29%	96%
20	Inp-S-Dpr(6-FNA)-Nal-1-L-**Abu**-PT-NH$_2$	1067.5366	1067.5332	25%	99%
21	Inp-S-Dpr(6-FNA)-Nal-1-L-**Dpr**-PT-NH$_2$	1068.5319	1068.5486	23%	99%
22	Inp-S-Dpr(6-FNA)-Nal-1-L-**S(*N*-Me)**-PT-NH$_2$	1083.5315	1069.4792	10%	99%
23	Inp-S-Dpr(6-FNA)-Nal-1-**β-homoL**-SPT-NH$_2$	1083.5315	1083.5417	17%	96%
24	Inp-S-Dpr(6-FNA)-Nal-1-**L*ψ*[Tz]S**PT-NH$_2$	1093.5266	1093.5284	14%	98%

3.4.3 Small Molecule Synthesis

3-(1-naphthyl)-*L*-alanine 6. CAS: 55516-54-6 . Fmoc-3-(1-naphthyl)-*L*-alanine (0.0781 g, 0.1 mmol) was suspended in DCM (3 mL). Piperidine was added dropwise until the white, opaque solution turned transparent. The mixture was then stirred for 20 minutes at room temperature before removal of excess solvent under reduced pressure to obtain a fine, white, crude powder. Trituration of the crude product with a small amount of cold DCM yielded pure metabolite **6** (0.010 g, 27%). UHPLC−MS method: 05−95% acetonitrile (0.1% TFA) in water (0.1% TFA), 3 min run; t_R (min) 0.92. HRMS (ESI$^+$): $[M+H]^+$ calculated = 216.1019; $[M+H]^+$ observed = 216.1051.

Imidazole-1-sulfonyl azide hydrogen sulfate. CAS: 1357503-23-1. This diazo transfer agent was synthesized according to Potter et al.[24] Briefly, A mixture of NaN_3 (2.11 g, 32.4 mmol) in anhydrous EtOAc (30 mL) was cooled to 0 ºC under a nitrogen atmosphere. Dropwise, sulfuryl chloride (2.6 mL, 32 mmol) was added and the reaction mixture was allowed to warm to room temperature overnight under N_2. The mixture was again cooled 0 ºC and imidazole (4.22 g, 62.0 mmol) was added portionwise. The reaction stirred at 0 ºC for 3 hours prior to being quenched by the addition of saturated $NaHCO_3$(aq) (100 mL). The organic layer was separated and washed with H_2O (100 mL), dried over $MgSO_4$, and filtered into a new reaction vessel. The organic mixture was cooled to 0 ºC and placed under a nitrogen atmosphere prior to the dropwise addition of concentrated H_2SO_4 (1.8 mL). After stirring for 1 hour at 0 ºC, the resulting white precipitate was filtered washing with a small amount of ice-cold EtOAc (1.56 g, 18%). UHPLC−MS method: 05−95% acetonitrile (0.1% TFA) in water (0.1% TFA), 3 min run; t_R (min) 1.07. HRMS (ESI$^+$): $[M+H]^+$ calculated = 174.0080; $[M+H]^+$ observed = 174.0050.

(*S*)-2-amino-3-(*tert*-butoxy)propanoic acid (26). CAS: 18822-58-7. A solution of Fmoc-*L*-Ser(*t*Bu)-OH (1.003 g, 2.61 mmol) in 20% piperidine in DCM (15 mL) stirred at room temperature for 30 minutes. The solvent was removed under reduced pressure co-evaporating with DCM (x3). The residue was then re-suspended in Et_2O and the resulting solid filtered to give pure **26** as a white powder (0.361 g, 86%). ^1H NMR (400 MHz, D_2O): δ 3.83-3.87 (m, 2H), 3.75-3.79 (m, 1H), 1.23 (s, 9H). ^{13}C NMR (100 MHz, D_2O): δ

172.27, 74.85, 60.14, 55.16, 26.37. HRMS (ESI$^+$): [M+H]$^+$ calculated = 162.1125; [M+H]$^+$ observed = 162.1150.

(*S*)-2-azido-3-(*tert*-butoxy)propanoic acid (27). CAS: 333366-25-9. Adapted from Goddard-Borger and Stick.[25] Briefly, to a solution of compound **26** (0.239 g, 1.48 mmol) in anhydrous MeOH (7 mL) was added K_2CO_3 (0.558 g, 4.04 mmol), $CuSO_4 \cdot 5H_2O$ (0.007 g, 0.028 mmol). Imidazole-1-sulfonyl azide hydrogen sulfate (0.490 g, 1.80 mmol) was added and the reaction mixture stirred overnight at room temperature. The solvent was removed under reduced pressure and the residue was re-suspended in DCM and H_2O. The mixture was acidified to a pH of 1 using 1 M HCl(aq) and product extracted into DCM (x3). The organic extracts were combined, washed with brine (80 mL), dried over $MgSO_4$, and concentrated under reduced pressure to reveal pure **27** as a colourless oil (0.249 g, 90%). ^{1}H NMR (400 MHz, CDCl$_3$): δ 9.80 (s, br, 1H), 3.95 (t, *J* = 4 Hz , 1H), 3.81 (d, *J* = 4 Hz, 2H), 1.20 (s, 9H). ^{13}C NMR (100 MHz, CDCl$_3$): δ 173.9, 74.5, 62.8, 61.6, 27.2.

(*S*)-*tert*-butyl (4-methyl-1-oxopentan-2-yl)carbamate (29). CAS: 58521-45-2. Adapted from Valverde et al.[23] Briefly, Boc-*L*-leucine *N*,*O*-dimethylhydroxamide (0.764 g, 2.79 mmol) was dissolved in anhydrous DCM (40 mL) and cooled to -78 ºC under a nitrogen atmosphere. DIBAL-H (1 M in DCM, 3 mL) was added dropwise and the reaction mixture was allowed to stir for 1 h at -78 ºC. A second addition of DIBAL-H (1 M in DCM, 3 mL) was added dropwise and the reaction mixture was allowed to stir for 2 h at -78 ºC. The reaction mixture was then diluted with DCM and quenched with saturated aqueous Rochelle salt. The product was extracted into DCM, dried over $MgSO_4$, and concentrated under reduced pressure. The crude aldehyde was purified by silica flash chromatography with 10-20% EtOAc in hexanes to reveal compound **29** as a colourless oil (0.445 g, 74%). ^{1}H NMR (400 MHz, CDCl$_3$): δ 9.52 (s, 1H), 5.05 (s, br, 1H), 4.16 (s, br, 1H), 1.75-1.66 (m, 1H), 1.63-1.55 (m, 2H), 1.39 (s, 9H), 0.91 (d, *J* = 6.6 Hz, 6H). ^{13}C NMR (100 MHz, CDCl$_3$): δ 200.6, 155.7, 80.0, 58.4, 38.1, 28.3, 24.7, 23.1, 21.9.

(*S*)-*tert*-butyl (5-methylhex-1-yn-3-yl)carbamate (30). CAS: 143327-83-7. Adapted from Valverde et al.[23] Briefly, to a solution of aldehyde **29** (0.287 g, 1.34 mmol) in anhydrous MeOH (10 mL) at 0 ºC was added K_2CO_3 (0.565 g, 4.09 mmol) and the

Bestmann-Ohira reagent (0.402 mL, 2.68 mmol). The reaction mixture was allowed to warm to room temperature overnight. The solvent was removed under reduced pressure and the resulting residue was re-suspended in DCM and H_2O. The product was extracted into DCM (x3) and the organic extracts were then washed with H_2O followed by brine. The organic solution was dried over $MgSO_4$ and concentrated under reduced pressure. The crude alkyne was purified by a silica plug with 10% EtOAc in hexanes to reveal compound **30** as a colourless oil (0.21 g, 73%). ^{1}H NMR (400 MHz, CDCl$_3$): δ 4.64 (s, br, 1H), 4.43 (s, br, 1H), 2.25 (d, J = 2.2 Hz, 1H), 1.80 (m, 1H), 1.52 (m, 2H), 1.45 (s, 9H), 0.93 (dd, J = 6.6, 3.7 Hz, 6H). ^{13}C NMR (100 MHz, CDCl$_3$): δ 154.9, 84.0, 80.0, 70.9, 45.3, 41.4, 28.5, 25.1, 22.8, 22.0.

(*S*)-(9*H*-fluoren-9-yl)methyl (5-methylhex-1-yn-3-yl)carbamate (31). CAS: 1179990-64-7. Alkyne **30** (0.256 g, 1.21 mmol) was dissolved in a solution of 20% TFA in DCM (10 mL) and reacted at room temperature for 1 hour. The solvent was removed under reduced pressure co-evaporating with DCM (x3). The residue was re-suspended in DCM (15 mL) prior to the addition of Fmoc-OSu (0.818 g, 2.43 mmol) and DIPEA (0.634 mL, 3.64 mmol). The mixture stirred overnight at room temperature. The solution was diluted with DCM and washed with 1 M HCl(aq) (x2), saturated NaHCO$_3$(aq) (x2), and brine (x1). The organic layer was then dried over $MgSO_4$ and concentrated under reduced pressure to give a yellow oil. The crude product was purified by silica flash chromatography using 2-20% EtOAc in hexanes to reveal compound **31** as a white powder (0.346 g, 86%). UHPLC−MS method: 40−80% acetonitrile (0.1% TFA) in water (0.1% TFA), 3 min run; t$_R$ (min) 2.56. ^{1}H NMR (400 MHz, CDCl$_3$): δ 7.77 (d, J = 7.5 Hz, 2H), 7.60 (d, J = 7.1 Hz, 2H), 7.41 (t, J = 7.4 Hz, 2H), 7.32 (td, J = 7.1, 1 Hz, 2H), 4.90 (d, J = 7.5 Hz, 1H), 4.53-4.43 (m, 3H), 4.23 (t, J = 6.4 Hz, 1H), 2.29 (d, J = 2.3 Hz, 1H), 1.80 (m, 1H), 1.57 (m, 2H), 0.96 (d, J = 4.8 Hz, 6H). ^{13}C NMR (100 MHz, CDCl$_3$): δ 155.5, 143.9, 141.5, 127.8, 127.2, 125.2, 120.1, 83.6, 71.3, 67.0, 47.4, 45.2, 42.0, 25.1, 22.7, 22.1. HRMS (ESI$^+$): [M+H]$^+$ calculated = 334.1802; [M+H]$^+$ observed = 334.1844.

Solid-phase copper-catalyzed cycloaddition. The peptide resin was swelled in DCM (4 mL) and then washed with degassed DMF (x4). A solution of alkyne **31** (2 eq.) and DIPEA (1 eq.) in degassed DMF (0.5 mL) was added to the resin followed by a solution

of Cu(ACN)₄PF₆ (0.5 eq.) and THPTA (0.5 eq.) in DMF (0.5 mL). The mixture was vigorously shaken overnight at room temperature. The reaction mixture was then drained and the resin washed with DMF (x4), a solution of 0.5% sodium diethyldithiocarbamate in DMF (x3), and DCM (x4).

Determination of the optical purity of leucine alkyne 31. CAS: 1472653-71-6. Compound **30** (0.0502 g, 0.238 mmol) was dissolved in a solution of 20% TFA in DCM (2 mL) and stirred at room temperature for 1 hour. The solvent was then removed under reduced pressure co-evaporating with DCM (x3). The resulting residue was re-dissolved in DCM and Fmoc-*L*-Ala-OH (0.0994 g, 0.319 mmol), HCTU (0.118 g, 0.285 mmol), and DIPEA (0.130 mL, 0.746 mmol) were added. The mixture stirred at room temperature for 30 minutes prior to being concentrated under reduced pressure. The crude dipeptide was purified by silica flash chromatography using 7-50% EtOAc in hexanes to give a white solid (0.0739 g, 77%). The dipeptide was then characterized by UHPLC and NMR spectroscopy, which detected no presence of the *D*-enantiomer of compound **31**. UHPLC−MS method: 50−75% acetonitrile (0.1% TFA) in water (0.1% TFA), 3 min run; t_R (min) 1.59. ^{1}H NMR (400 MHz, CDCl₃): δ 7.77 (d, *J* = 7.5 Hz, 2H), 7.58 (d, *J* = 7.4 Hz, 2H), 7.40 (t, *J* = 7.4 Hz, 2H), 7.32 (t, *J* = 7.0 Hz, 2H), 6.34 (s, br, 1H), 5.42 (s, br, 1H), 4.74 (qd, *J* = 8.2, 2.2 Hz, 1H), 4.40 (d, *J* = 6.7 Hz, 2H), 4.23-4.20 (m, 2H), 2.20 (d, *J* = 2.2 Hz, 1H), 1.74 (m, 1H), 1.54-1.50 (m, 2H), 1.40 (d, *J* = 6.4 Hz, 3H), 0.91 (d, *J* = 6.6 Hz, 6H). ^{13}C NMR (100 MHz, CDCl₃): δ 171.2, 156.2, 143.8, 141.4, 127.9, 127.2, 125.2, 120.2, 83.1, 71.3, 67.4, 50.5, 47.2, 44.8, 40.1, 25.2, 22.8, 22.0, 18.6. HRMS (ESI⁺): [M+H]⁺ calculated = 405.2173; [M+H]⁺ observed = 405.2138.

3.4.4 Competitive Binding Assay (IC₅₀)

The binding affinities of ghrelin analogues toward the GHSR were determined using a competitive radioligand-displacement binding assay using human [^{125}I]-ghrelin(1-28) (PerkinElmer Inc., cat. NEX388010UC) as the radioligand. HEK293 cells were transiently transfected with GHSR-eYFP using XtremeGENE™ 9 DNA transfection agent (Sigma-Aldrich, cat. 06365787001) according to the manufacturer's protocol over 48 hours prior to being frozen at 2 million cells per vial in 10% DMSO in FBS. Human

ghrelin(1-28) (Cedarlane Labs, cat. HOR-297) was tested as a reference to ensure the integrity of the results. A frozen aliquot of cells were thawed, centrifuged (3,000 rpm, 10 min, room temperature), and the cell pellet was resuspended in binding buffer (25 mM HEPES, 5 mM magnesium chloride, 2.5 mM EDTA, 1 mM calcium chloride, and 0.4% BSA, pH = 7.4). The radioligand (15 pM) and cells (100,000 cells per assay tube) were added to solutions of the individual ghrelin(1-8) analogues in binding buffer (in triplicate at concentrations of 10^{-6} M, 10^{-7} M, 10^{-8} M, 10^{-9} M, 10^{-10} M, 10^{-11} M, and 10^{-12} M) at a final volume of 300 µL, and incubated at 37 °C for 20 minutes with agitation. The tubes were then centrifuged at 13,000 g for 5 min and unbound [^{125}I]-ghrelin was removed in the supernatant. The cell pellets were then washed with 500 µL of ice-cold TRIS-HCl buffer (50 mM, pH = 7.4) and centrifuged again at 13,000 g for 5 min. The quantity of [^{125}I]-ghrelin bound to the cell membranes was measured by gamma counter. Non-linear regression analysis to fit a 4-parameter dose response curve using GraphPad Prism (version 6.0c) provided IC_{50} values.

3.4.5 Metabolic Stability of Ghrelin(1-8) Analogues

Chemical Stability

The chemical stabilities of peptides **1** and **2** were assessed by incubating each peptide (1 mM) in PBS (pH = 7.4) at 37 °C. The peptide was allowed to equilibrate in solution for 10 minutes prior to the collection of sample aliquots. Aliquots (15 µL) of the peptide solution were removed in triplicate at 0, 0.5, 1, 2, 4, 6, and 24 h and mixed with 0.1% TFA in ACN (60 µL). The samples were then analyzed by UHPLC-MS (5 µL volume injected). The selected ion chromatogram corresponding to the m/z value of the peptide was obtained and the resulting peak was integrated to quantify the amount of intact peptide remaining at each time-point. Both peptides were 100% intact after 24 hours.

Human Serum Stability

The stability of ghrelin(1-8) analogues in human serum (Sigma-Aldrich, cat. H4522) was assessed by incubating each peptide (1 mM) at 37 °C in a 25% serum solution containing PBS at pH 7.4. The peptide was allowed to equilibrate in solution for 10 minutes prior to

the collection of sample aliquots. Aliquots (15 µL) of the peptide solution were removed in triplicate at 0, 0.5, 1, 2, 4, 6, and 24 h. The reaction was quenched with 4% NH_4OH(aq) (60 µL) and salts and proteins were removed using a Waters Oasis HLB microextraction plate (30 µm) (Waters, cat. 186001828BA). The cartridge was first activated with MeOH (200 µL) followed by water (200 µL). The sample was loaded onto the cartridge and the column was washed with 5% MeOH in water (200 µL). The peptide was then eluted using 2% formic acid in MeOH (2 x 30 µL). An aliquot (20 µL) of the eluted peptide was diluted with a solution of 0.1% TFA in H_2O (80 µL) and subsequently analyzed by UHPLC-MS (5 µL volume injected). The selected ion chromatogram corresponding to the m/z value of the peptide was obtained and the resulting peak was integrated to quantify the amount of intact peptide remaining at each time-point.

Human Liver S9 Fraction Stability

The stability of ghrelin(1-8) analogues in human liver S9 fraction (Fisher Scientific, cat. HMS9PL) was assessed by incubating each peptide (3 µM) with liver S9 fraction (1 mg/mL), $MgCl_2\cdot6H_2O$ (3 mM), and 0.1 M potassium phosphate buffer (pH = 7.4) at 37 °C with gentle agitation at 300 rpm. Aliquots (50 µL) of the reaction mixture were removed in triplicate at 0, 0.5, 1, 2, 3, and 4 h. The reaction was quenched with ice-cold 25% MeOH in ACN (200 µL), vortexed, and placed on ice for 20 minutes, which caused the S9 fraction material to precipitate. The mixture was then centrifuged at 14,000 g for 10 minutes. An aliquot (100 µL) of the supernatant was then mixed with H_2O (100 µL) and subsequently analyzed by UHPLC-MS (10 µL volume injected). The selected ion chromatogram corresponding to the m/z value of the peptide was obtained and the resulting peak was integrated to quantify the amount of intact peptide remaining at each time-point.

3.5 References

1   N. Abbasi Gharibkandi, J. M. Conlon and S. J. Hosseinimehr, *Peptides*, 2020, **133**, 170385.

2   C. L. Charron, J. L. Hickey, T. K. Nsiama, D. R. Cruickshank, W. L. Turnbull and

L. G. Luyt, *Nat. Prod. Rep.*, 2016, **33**, 761–800.

3   X. Sun, Y. Li, T. Liu, Z. Li, X. Zhang and X. Chen, *Adv. Drug Deliv. Rev.*, 2017, **110**–**111**, 38–51.

4   A. P. Davenport, C. C. G. Scully, C. de Graaf, A. J. H. Brown and J. J. Maguire, *Nat. Rev. Drug Discov.*, 2020, **19**, 389–413.

5   B. J. Evans, A. T. King, A. Katsifis, L. Matesic and J. F. Jamie, *Molecules*, 2020, **25**, 2314.

6   C. Lu, M. S. McFarland, R. L. Nesbitt, A. K. Williams, S. Chan, J. Gomez-Lemus, A. M. Autran-Gomez, A. Al-Zahrani, J. L. Chin, J. I. Izawa, L. G. Luyt and J. D. Lewis, *Prostate*, 2012, **72**, 825–833.

7   L. Mihalache, A. Gherasim, O. Niță, M. C. Ungureanu, S. S. Pădureanu, R. S. Gavril and L. I. Arhire, *Hormones*, 2016, **15**, 186–196.

8   Y. Lv, T. Liang, G. Wang and Z. Li, *Biosci. Rep.*, 2018, **38**, 1–13.

9   J. B. Soares, R. Roncon-Albuquerque and A. Leite-Moreira, *Expert Opin. Ther. Targets*, 2008, **12**, 1177–1189.

10   G. Colldén, M. H. Tschöp and T. D. Müller, *Int. J. Mol. Sci.*, 2017, **18**, 798.

11   T. C. Lin and M. Hsiao, *Biochim. Biophys. Acta*, 2017, **1868**, 51–57.

12   M. D. Childs and L. G. Luyt, *Mol. Imaging*, 2020, **19**, 1–15.

13   J. Tong, N. Dave, G. M. Mugundu, H. W. Davis, B. D. Gaylinn, M. O. Thorner, M. H. Tschöp, D. D'Alessio and P. B. Desai, *Eur. J. Endocrinol.*, 2013, **168**, 821–828.

14   M. A. Bednarek, S. D. Feighner, S. S. Pong, K. K. McKee, D. L. Hreniuk, M. V. Silva, V. A. Warren, A. D. Howard, L. H. Y. Van der Ploeg and J. V. Heck, *J. Med. Chem.*, 2000, **43**, 4370–4376.

15   M. Matsumoto, H. Hosoda, Y. Kitajima, N. Morozumi, Y. Minamitake, S. Tanaka, H. Matsuo, M. Kojima, Y. Hayashi and K. Kangawa, *Biochem. Biophys. Res. Commun.*, 2001, **287**, 142–146.

16   M. Van Craenenbroeck, F. Gregoire, P. De Neef, P. Robberecht and J. Perret, *Peptides*, 2004, **25**, 959–965.

17   C. L. Charron, J. Hou, M. S. McFarland, S. Dhanvantari, M. S. Kovacs and L. G. Luyt, *J. Med. Chem.*, 2017, **60**, 7256–7266.

18   S. Esposito, K. Deventer, L. Geldof and P. Van Eenoo, *J. Pept. Sci.*, 2015, **21**, 1–9.

19   T. Lange, A. Thomas, C. Görgens, M. Bidlingmaier, K. Schilbach, E. Fichant, P. Delahaut and M. Thevis, *Biomed. Chromatogr.*, 2021, **e5075**, 1–18.

20   B. Meibohm, in *Pharmaceutical Biotechnology*, eds. D. J. A. Crommelin, R. D. Sindelar and B. Meibohm, Springer, 2013, pp. 101–132.

21   K. J. Coe and T. Koudriakova, in *Optimization in Drug Discovery*, eds. G. W. Caldwell and Z. Yan, Humana Press, 2004, pp. 87–100.

22   G. Ferré, M. Louet, O. Saurel, B. Delort, G. Czaplicki, C. M'Kadmi, M. Damian, P. Renault, S. Cantel, L. Gavara, P. Demange, J. Marie, J. A. Fehrentz, N. Floquet, A. Milon and J. L. Banères, *Proc. Natl. Acad. Sci. U. S. A.*, 2019, **116**, 17525–17530.

23   I. E. Valverde, A. Bauman, C. A. Kluba, S. Vomstein, M. A. Walter and T. L. Mindt, *Angew. Chemie - Int. Ed.*, 2013, **52**, 8957–8960.

24   G. T. Potter, G. C. Jayson, G. J. Miller and J. M. Gardiner, *J. Org. Chem.*, 2016, **81**, 3443–3446.

25   E. D. Goddard-Borger and R. V. Stick, *Org. Lett.*, 2007, **9**, 3797–3800.

Chapter 4

4 Synthesis of a Spirocyclic Iodonium Ylide on a Quinazolinone Scaffold for ^{18}F-PET Imaging of the GHSR

4.1 Introduction

Molecular imaging is a growing interdisciplinary field that provides a window into the inner workings of the human body. Imaging modalities such as PET and SPECT allow for the minimally invasive visualization of biological processes in real time. In particular, ^{18}F-PET is among the most commonly used methods for imaging due to its unparalleled sensitivity, high specificity, and unlimited depth penetration.[1] The fluorine-18 radioisotope is often an ideal choice for the development of PET radiotracers due to its suitable half-life for radiopharmaceutical synthesis (109.8 min), facile production by cyclotron, and slightly improved spatial resolution over other PET radionuclei.[2] Due to the similar size of fluorine compared to hydrogen and the similar bond energy to C-H bonds, C-F bonds are, at times, able to be substituted for C-H bonds during pharmaceutical drug development resulting in similar or improved pharmacological activity.[3] Additionally, organic radionuclei, such as fluorine-18, do not require the use of a bulky chelator to be conjugated to a biologically relevant targeting entity, unlike radiometals, such as gallium-68 and copper-64. This makes them more favourable for use in small molecule imaging probe development since their small size is less likely to interfere with the ability for a small targeting entity to bind to its biological target. Furthermore, the ability to position the fluorine atom directly onto the targeting entity would then present the opportunity for direct, late-stage labelling of the imaging precursor with fluorine-18.

The growth hormone secretagogue receptor 1a (GHSR) is a G protein-coupled receptor (GPCR) that is predominantly expressed in the pituitary and the hypothalamus.[4] Since its discovery in 1996, expression of this receptor has also been identified in tissues outside the CNS including the pancreas, thyroid gland, spleen, adrenal gland, gastrointestinal tract, and cardiac tissue.[5,6] A variety of physiological functions may be regulated when

the GHSR is activated by its endogenous ligand, ghrelin, including appetite, energy homeostasis, growth hormone secretion, and cell proliferation.[7–10] Furthermore, the GHSR is known to possess unusually high constitutive activity, which presents the opportunity to develop agonists, antagonists, and inverse agonists targeting this receptor for treatment of multiple metabolic disorders including anorexia, cachexia, obesity, and diabetes.[11] Targeted molecular imaging of the GHSR could provide insights into its role in biological processes related to these and other disease states.

Most imaging probes that target the GHSR are derived from its endogenous ligand, ghrelin, which is a 28 amino acid peptide with a unique octanoyl side chain modification on the serine in the third position. However, in 2000, Merck reported the development of a new class of non-peptidic quinazolinone-derived GHSR agonists from a directed screening hit.[12] Later in 2007, Bayer pharmaceuticals reported the results of a high-throughput screening campaign, which identified a series of piperidine-substituted quinazolinone derivatives as GHSR antagonists.[13] N-Alkylation of the piperidine nitrogen was able to tune the functional activity of these compounds to form GHSR antagonists with the goal of developing novel therapeutics to treat obesity and diabetes. The first instance of these derivatives as GHSR imaging probes was reported in 2011 when Potter et al. described a ^{11}C-labelled quinazolinone derivative (**1**) for PET imaging of GHSR expression in the brain (Figure 4.1).[14] The derivative had nanomolar binding affinity with a K_i value of 22 nM. However, *in vivo* PET imaging revealed low tracer accumulation in the pituitary and hypothalamus, which are regions of high GHSR expression, and non-specific uptake in other brain tissues. The authors postulated that the lipophilicity of the tracer ($clogD_{7.4} = 4.1$) may be too high to be an effective CNS radioligand and recommended that future GHSR radioligands for brain PET imaging have picomolar binding affinities and lower lipophilicities.[14] Since that time, other ^{11}C-labelled and, subsequently, ^{18}F-labelled quinazolinone derivatives have been reported as potential GHSR imaging probes.[15–17] However, *in vivo* evaluation of these probes, which have yet to meet the proposed affinity and lipophilicity criteria, showed low uptake in the mouse brain.[15]

Recently, Hou et al. reported three new quinazolinone derivatives for ^{18}F-PET imaging of the GHSR (Figure 4.1).[17] Compounds **2** and **3** were *N*-alkylated with a fluoroethyl group on the piperidine nitrogen, which provided facile synthetic access to the ^{18}F-labelled versions of these compounds via a [^{18}F]fluoroethyl tosylate prosthetic group. The other fluorine-bearing compound, **4**, was found to have picomolar binding affinity (IC$_{50}$ = 20 pM), the strongest binding affinity for any GHSR-targeting compound reported to date, and a clogD$_{7.4}$ of 2.39, hypothesized to be suitable for penetration of the blood-brain-barrier. However, labelling compound **4** with fluorine-18 through conventional nucleophilic aromatic substitution methods (S$_N$Ar) from a nitro precursor was unsuccessful, possibly due to the quinazolinone scaffold not being sufficiently electron withdrawing.[17]
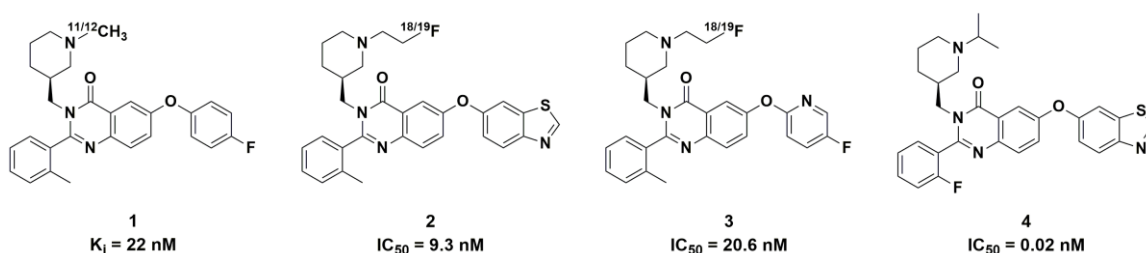
Figure 4.1. Structures of select previously reported quinazolinone derivatives and their binding affinities toward the GHSR.[14,17]

Recently, the use of spirocyclic iodonium(III) ylides (SCIDY) as precursors for ^{18}F-labelling has been successfully applied toward the synthesis of non-activated ^{18}F-labelled arenes.[18] Aryl iodide substrates, which are oxidized and conjugated to a bulky auxiliary group, have been shown to be reactive and regioselective for the ^{18}F-labelled aromatic product. Several pharmaceutically relevant substrates have been labelled through this method including electron-deficient and electron-rich arenes in moderate to high radiochemical yields.[19–22] Most recently, spiroadamantyl-1,3-dioxane-4,6-dione (SPIAd) has been the auxiliary of choice due to its unmatched performance in stability tests, ^{18}F-labelling efficiency, and ease of synthesis.[23] Furthermore, the presence of a substituent on the aromatic substrate *ortho* to the iodonium ylide, has resulted in improved radiochemical yields due to destabilization of the transition state during ^{18}F-labelling.[23] Due to the non-activated nature of the fluorine-bearing aromatic ring in compound **4** and

the position of quinazolinone scaffold being *ortho* to the fluorine atom, we sought to apply the SCIDY labelling method toward producing [**^{18}F**]**4** for ^{18}F-PET imaging of the GHSR.

4.2   Results and Discussion

4.2.1 Design and Synthesis of SCIDY Precursor

Synthesis of the non-radioactive standard, compound **4**, was carried out as previously described in similar or improved yields (Scheme 4.1).[17] Regrettably, the SCIDY precursor (**14**) could not be accessed using the same synthetic pathway with the simple replacement of 2-fluorobenzoyl chloride with 2-iodobenzoyl chloride in the first step of synthesis. The reactive nature of the aryl iodide outcompetes that of the aryl bromide to conjugate 6-hydroxybenzothiazole to the quinazolinone scaffold via an Ullmann coupling in step 4 of the synthesis. Unsurprisingly, instead of obtaining only the desired bromo-substituted product, mono-substitution of the iodine and di-substitution at both reactive sites were also observed. Furthermore, the undesirable by-products were inseparable from the bromo-substituted product. Therefore, a new synthetic pathway was proposed to access the SCIDY precursor **14**.

Scheme 4.1. Synthesis of non-radioactive compound **4** adapted from Hou et al.[17] and the initial synthetic pathway to prepare SCIDY precursor **14**. (n.d. = not determined).
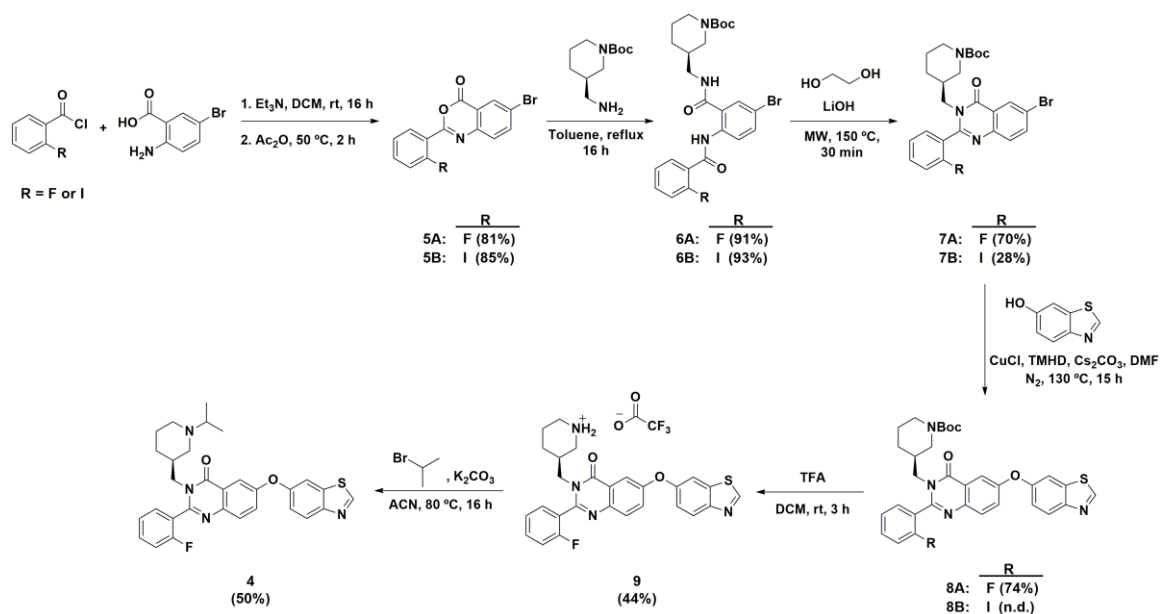
Scheme 4.2 shows a new synthetic pathway for the purpose of accessing SCIDY precursor **14**. Commercially available 5-bromoisatoic anhydride was first ring-opened with (*R*)-1-Boc-3-(aminomethyl)piperidine under basic conditions. The Ullmann coupling step was then carried out prior to introducing the aryl iodide moiety to prevent the presence of competing reactive sites. Fortunately, this reaction proceeded without the need for a protecting group on the aniline nitrogen. Following incorporation of the aryl iodide moiety, cyclization of compound **12** was initially carried out using the same conditions as outlined in the third step of scheme 4.1. However, in addition to the desired product, **8B**, significant loss of the Boc protecting group was also observed. Since the subsequent reaction step was to remove the Boc group, the reaction from step 4 was directly subjected to trifluoroacetic acid (TFA) in dichloromethane for complete Boc removal. Still, purification of the resulting reaction mixture resulted in very low yields of the desired product due to the presence of small amounts of many inseparable by-products. Therefore, further optimization of this step was carried out to minimize the presence of undesired by-products and prevent the loss of the Boc group for a more controlled, higher yielding reaction.

Scheme 4.2. Synthetic pathway to produce SCIDY precursor **14**.
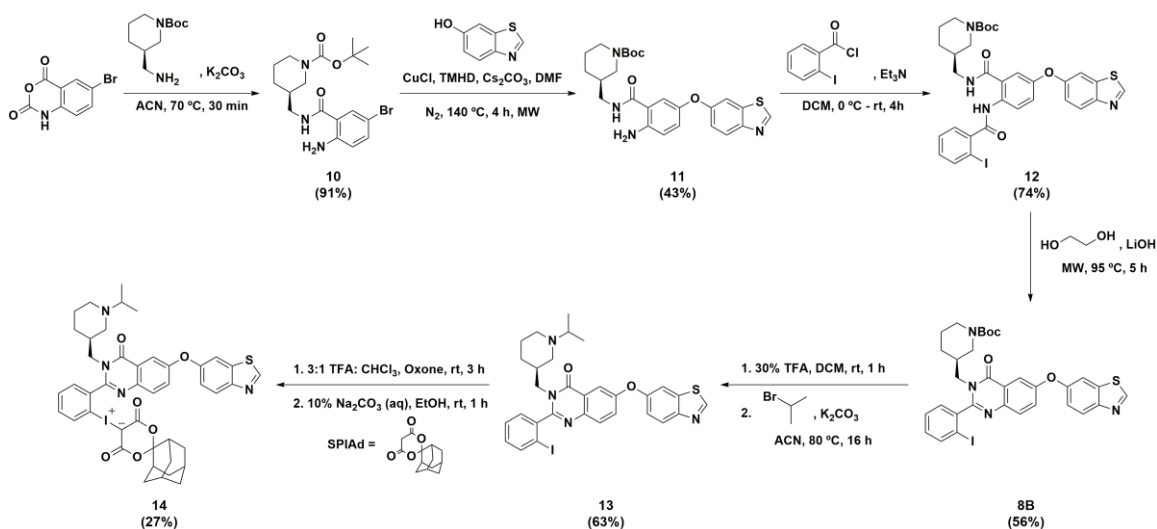
The ring-closing reaction shown in step 4 of scheme 4.2 was carried out on a small-scale (0.04 mmol) of over increasing temperature via microwave irradiation, and product formation was monitored over multiple time points by UHPLC-MS (Table 4.1). At temperatures below 95 ˚C, no side reactions were detected (Table 4.1, entries 1-3), but, at a temperature of 95 ˚C, very small amounts of various by-products began to be observable (Table 4.1, entries 4-6). These by-products were inferred by mass spectrometry and their proposed structures are shown in figure 4.2. Based on this data, all further cyclization reactions for compound **12** were carried out at 95 ˚C for 5 hours under microwave irradiation. Of note, cyclization of compound **6A** in scheme 4.1 was carried out in the presence of 2 equivalents of LiOH according to Hou et al.[17] Upon increasing the scale of reaction for cyclization of compound **12** under the newly optimized conditions with 2-6 equivalents of LiOH, a significant amount of by-product **17**, which corresponds to substitution of iodine with ethylene glycol on compound **12**, was observed (~45%). Increasing the proportion of LiOH to 9-12 equivalents without altering the concentration of starting material suppressed the formation of this by-product almost entirely.

Table 4.1. Optimization of temperature and time for cyclization of compound **12**.

Entry	Time (h)	Temperature (°C)	Product Yield[a]	Residual Starting Material[a]
1	0.5	50	0%	100%
2	1.0	75	10%	90%
3	1.5	90	30%	70%
4	2.5	95	60%	30%[b]
5	4.0	95	75%	12%[b]
6	5.0	95	87%	8%[b]

Reaction conditions: 0.04 mmol **12**, LiOH (9 eq), ethylene glycol (0.5 mL), MW. Reaction monitored by UHPLC-MS. [a]Non-isolated yields determined by UV integration of the UHPLC chromatogram. [b]By-products observed at this time point.
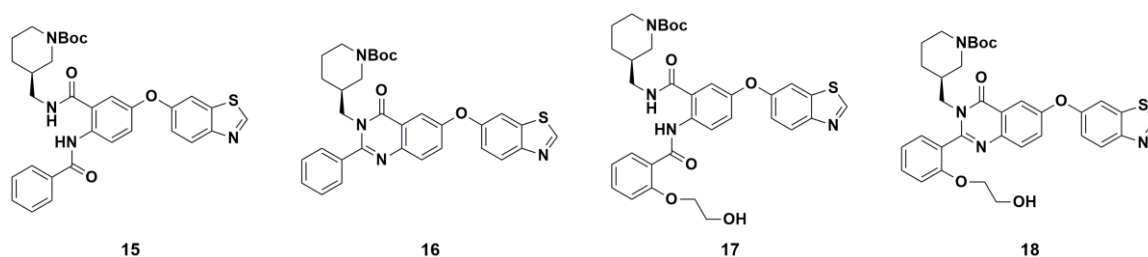
Figure 4.2. Observable by-products during the cyclization of compound **12**.

The remaining steps in scheme 4.2 involved removal of the Boc protecting group, which was accomplished without need for purification and could be used directly for *N*-alkylation of the piperidine nitrogen with bromopropane according to literature procedures.[17] To prepare the iodonium ylide, aryl iodide **13** was initially oxidized to the diacetoxyiodoarene intermediate using dimethyldioxirane (DMDO), a relatively mild oxidizing agent, and 20% acetic acid in acetone. Following oxidation, the addition of SPIAd and an increase in pH allowed for the formation of the iodonium ylide. However, according to the mass spectrum, rather than forming the desired SCIDY precursor, the observed mass associated with the newly formed product was 16 mass units higher than expected, indicating possible oxidation elsewhere in the molecule. It has been reported that heterocycles may be sensitive to oxidation under such reaction conditions; however, this can be circumvented in sufficiently acidic environments.[23,24] Another mild oxidizing

agent, oxone monopersulfate, and 75% trifluoroacetic acid in chloroform was able to sufficiently oxidize aryl iodide **13** to form a [bis(trifluoroacetoxy)iodo]arene intermediate, which could then be directly converted to the desired iodonium ylide **14** without non-specific oxidation. Ultimately, the novel synthetic pathway outlined in scheme 4.2 was successful in producing a SCIDY quinazolinone derivative as a precursor for ^{18}F-fluorination.

4.2.2 Radiochemistry

Nucleophilic fluoride-18 was produced by cyclotron through bombardment of a $H_2{}^{18}O$ liquid target with protons. The general radiofluorination reaction is shown in scheme 4.3. Most literature reports for producing ^{18}F-labelled molecules from iodonium ylides use tetraethylammonium bicarbonate (TEAB) as the base, but several have also shown success using the K_2CO_3/K_{222} complex.[25–28] Typically, polar aprotic solvents such as DMF or DMSO show the highest success in this type of radiofluorination and high temperatures of 120 °C are most common. Initially, SCIDY precursor **14** was subjected to ^{18}F-labelling conditions reported by Rotstein et al., which have been successful for a wide scope of different aryl substrates (Table 4.2, entries 1-2).[18,23] However, these conditions did not yield any radiolabelled product.

Scheme 4.3. General scheme for ^{18}F-fluorination of SCIDY precursor **14**.
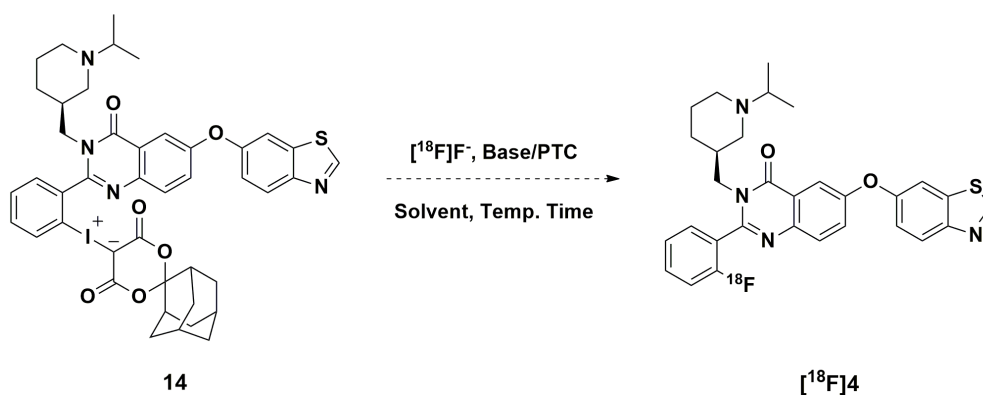
Attempts to identify suitable conditions to label compound **14** with fluoride-18 are summarized in table 4.2. While triphenylphosphine as an additive to radiofluorination reactions with iodonium ylides has been reported to increase reaction yields, the use of

K_2CO_3/K_{222} as the base/PTC with and without triphenylphosphine was unsuccessful in producing any labelled product (Table 4.2, entries 3-4).[27] While no radiolabelled products were detected in the radiofluorination reactions, many new UV peaks were observed indicating decomposition of the precursor. In an attempt to mitigate the loss of intact precursor, the reaction temperature was lowered to 80-100 ˚C (Table 4.2, entries 4-8) and the amount of base included in the reaction was also reduced. However, despite these efforts, no radiolabelled product was observed.

Table 4.2. Attempts to label SCIDY precursor **14** with fluoride-18.

Entry	Base/PTC	Amount 14	Solvent	Temp. (˚C)	Time (min)
1	9 mg TEAB	2 mg	DMF	120	10
2	9 mg TEAB	2 mg	DMF	120	20
3[a]	2 mg K_2CO_3/7 mg K_{222}	2 mg	DMSO	120	10
4	4 mg K_2CO_3/14 mg K_{222}	2 mg	DMSO	100	10
5	3.5 mg TEAB	2 mg	DMF	80	10
6	3.5 mg TEAB	2 mg	DMF	95	10
7	2.5 mg TEAB	4 mg	DMF	95	10
8	2.5 mg TEAB	4 mg	DMF	95	20
9	1.5 mg TEAB	4 mg	DMF	50	10
10	1.5 mg TEAB	4 mg	DMF	70	10
11	1.5 mg TEAB	4 mg	DMF	90	10
12	1 mg K_2CO_3/4 mg K_{222}	4 mg	DMF	50	10
13	1 mg K_2CO_3/4 mg K_{222}	4 mg	DMF	70	10

N.B. Each reaction batch used 200-400 MBq $[^{18}F]F^-$. All solvents were anhydrous and used as received. Reactions were monitored by radio-HPLC. [a] Included 2 mg of PPh_3.

A thermal stability investigation of precursor **14** in the presence of low amounts of base at varying temperatures was carried out to observe its tolerance of radiofluorination conditions. Solutions of the iodonium ylide **14** (5 mM) in DMF in the presence of either TEAB (13 mM), K_2CO_3 (18 mM) and K_{222} (20 mM), or no base were heated at

temperatures ranging from room temperature (22 ˚C) to 110 ˚C for 10 minutes at each temperature. Aliquots of the reaction mixture were analyzed by UHPLC-MS to determine the amount of intact precursor remaining relative to the amount at the beginning of the experiment (T_0). As shown in figure 4.3, in the presence of no base added, compound **14** was stable at 22 ˚C and 50 ˚C, and only a 19% loss of precursor was evident after heating at 70 ˚C. In the presence of TEAB, 20% of precursor was lost after heating at 50 ˚C and complete degradation was evident at 70 ˚C, indicating that base has a negative effect on precursor stability. In the presence of K_2CO_3 and K_{222}, the precursor was stable up to 70 ˚C, however, rapid degradation at higher temperatures resulted in complete degradation by 110 ˚C. With a better understanding of the thermal stability of compound **14**, radiofluorination was attempted at low base concentrations and at increasing temperature beginning at 50 ˚C (Table 4.2, entries 9-13). Unfortunately, no radiolabelled products could be detected and complete precursor degradation was still observed.
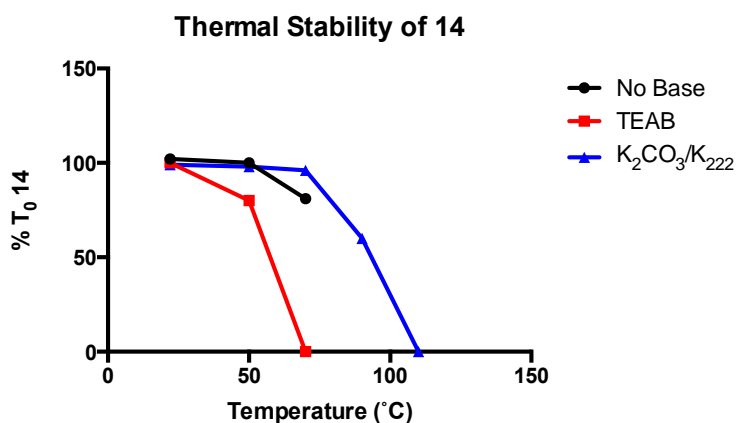
Figure 4.3. Thermal stability of iodonium ylide **14** over increasing temperature. Closed circles: No base added. Closed squares: 1 mg of TEAB added. Closed triangles: 1 mg K_2CO_3 and 3 mg K_{222} added. Conditions: 2 µmol of iodonium ylide **14**, 1 mg of base (where applicable), 3 mg K_{222} (where applicable), DMF (400 µL), heated for 10 minutes at each temperature. Data presented as a percentage of intact precursor at T_0.

4.3 Conclusions

The use of SCIDY precursors has been successfully applied to a multitude of highly functionalized molecules and existing PET radiotracers.[23,29–31] The value of this labelling

method stems from its demonstrated ability to be used in the radiofluorination of non-activated and electron-rich arenes. Due to the non-activated nature of the fluorinated aromatic ring moiety in **4** and the unsuccessful attempt to label this molecule via S_NAr, we sought to approach ^{18}F-fluorination of **4** using the iodonium ylide approach. Therefore, we designed a novel synthetic pathway, which produced precursor **14** in moderate to high yields at each synthetic step. Numerous attempts to label compound **14** with fluoride-18 were carried out under several reaction conditions by modifying variables including, base, base quantity, precursor quantity, temperature, and time. However, despite our best efforts, radiofluorination of SCIDY precursor **14** to produce **[^{18}F]4** could not be achieved. Several peaks observed in the HPLC-UV chromatogram throughout radiolabelling reactions indicate that this is likely due to the high instability of this precursor under radiolabelling conditions, which requires heat and the presence of base. In future investigations, milder bases may be warranted as a means to balance the stability of the precursor with the efficiency of producing the desired radiolabelled product.[19] Additionally, other ^{18}F-labelling techniques for non-activated arenes, such as boronic esters, boronic acids, and arystannanes, are available as alternative precursors, which may demonstrate increased stability to the necessarily harsh ^{18}F-labelling conditions for radiosynthesis of **[^{18}F]4**.[32] Ligand **4** demonstrates the strongest binding affinity toward the GHSR with an IC_{50} value of 20 pM. Its moderate lipophilicity (clogD = 2.39) may be suitable for blood-brain barrier penetration allowing for brain imaging. It is therefore essential that an effective radiosynthetic strategy for this compound be developed.

4.4 Experimental

4.4.1 Materials and Methods

All common solvents were obtained from Fisher Scientific. All other reagents were purchased from Sigma-Aldrich, Fisher Scientific, Oakwood Chemicals, or Ark Pharm Inc. and were used as received. Analytical UHPLC-MS was performed using a Waters Inc. Acquity UPLC H-class instrument in combination with a Xevo QToF mass spectrometer. A Waters Acquity analytical column (UPLC BEH C18 2.1 x 50 mm, 1.7 μm) was used and the UV absorbance was detected using a Waters Acquity PDA

detector. The solvent system ran gradients of 0.1% formic acid in ACN (ACN, Optima grade, Fisher Scientific) and 0.1% formic acid in MilliQ water (18.2 mΩ·cm conductivity) at a flow rate of 0.6 mL/min over 3 minutes followed by a wash over 1 minute. Solution phase reactions were monitored by thin layer chromatography (TLC) using plastic-backed silica gel plates. Flash chromatography was performed using a Biotage® Isolera™ Prime advanced automated flash purification instrument. Biotage SNAP KP-Sil 10 g, 25 g, or 50 g cartridges (50 μm irregular silica) were used for normal-phase chromatography with solvent flow rates of 12, 25, or 50 mL/min for each cartridge type respectively along with the gradient solvent system specified. Biotage C18 28 g cartridges were used for reverse-phase chromatography with a solvent flow rate of 25 mL/min along with the gradient solvent system specified. All fractions were monitored and collected by UV absorbance using the internal UV detector set at 254 nm and 280 nm. NMR spectra were obtained using either an Inova 400 MHz, or a Bruker 400 MHz spectrometer. Chemical shifts are referenced to the residual solvent peaks and recorded in parts per million. High-resolution mass spectra were determined in positive ion mode using an electrospray ionization (ESI) ion source on either a Waters Xevo QToF or a Bruker micrOToF II mass spectrometer.

4.4.2 Chemical Synthesis

6-Bromo-2-(2-fluorophenyl)-4H-benzo[d][1,3]oxazin-4-one (5A): CAS: 899054-19-4. Synthesized according to Hou et al.[17] Briefly, to a suspension of 5-bromoanthranilic acid (1.068 g, 4.94 mmol) and Et_3N (2.07 mL, 14.8 mmol) in DCM (10 mL) was added 2-fluorobenzoyl chloride (0.708 mL, 5.93 mmol) dropwise at 0 ˚C. The reaction mixture stirred at room temperature over 16 h followed by removal of the solvent under reduced pressure. The residue was taken up in acetic anhydride (10 mL) and heated gently to 50 ˚C for 2 hours. The reaction mixture was cooled at 0 ˚C for 30 min and the resulting precipitate was collected by vacuum filtration washing with EtOH to give an off-white powder (1.29 g, 81%). UHPLC−MS method: 5−95% ACN (0.1% TFA) in water (0.1% TFA), 3 min run; t_R (min) 2.40; HRMS (ESI$^+$): [M+H$^+$] calculated = 319.9717, [M+H$^+$] observed = 320.0026.

6-Bromo-2-(2-iodophenyl)-4H-benzo[d][1,3]oxazin-4-one (5B): CAS: 351890-69-2. The method similar for the preparation of compound **5A** was used except replacing 2-fluorobenzoyl chloride with 2-iodobenzoyl chloride. A yellow powder was obtained in an 85% yield. UHPLC−MS method: 40−95% ACN (0.1% TFA) in water (0.1% TFA), 3 min run; t_R (min) 1.97; HRMS (ESI$^+$): [M+H$^+$] calculated = 427.8778, [M+H$^+$] observed = 427.8930.

(*R*)-tert-Butyl 3-((5-Bromo-2-(2-fluorobenzamido)-benzamido)methyl)piperidine-1-carboxylate (6A). CAS: 2172830-17-8. Synthesized according to Hou et al.[17] Briefly, to a suspension of **5A** (0.555 g, 1.73 mmol) in toluene (10 mL) was added (*R*)-1-boc-3-(aminomethyl)piperidine (0.410 mL, 1.91 mmol). The reaction mixture stirred at 110 ˚C over 16 h following by cooling to room temperature and removal of the solvent to yield a white powder (0.903 g, 98%). UHPLC−MS method: 5−95% ACN (0.1% TFA) in water (0.1% TFA), 3 min run; t_R (min) 2.65; HRMS (ESI$^+$): [M+H$^+$] calculated = 534.1398, [M+H$^+$] observed = 534.0470.

(*R*)-tert-Butyl 3-((5-Bromo-2-(2-iodobenzamido)-benzamido)methyl)piperidine-1-carboxylate (6B). The method similar for the preparation of compound **6A** was used except replacing **5A** with **5B**. An off-white powder was obtained in a 93% yield. UHPLC−MS method: 5−95% ACN (0.1% TFA) in water (0.1% TFA), 3 min run; t_R (min) 2.83; HRMS (ESI$^+$): [M+H$^+$] calculated = 642.0459, [M+H$^+$] observed = 642.0026.

(*R*)-tert-Butyl 3-((6-Bromo-2-(2-fluorophenyl)-4-oxoquinazolin-3(4H)-yl)methyl) piperidine-1-carboxylate (7A). CAS: 2172830-18-9. Synthesized according to Hou et al.[17] Briefly, in a microwave vessel, **6A** (2.115 g, 3.96 mmol) and LiOH (0.191 g, 7.97 mmol) was dissolved in ethylene glycol (15 mL) and subjected to microwave irradiation at 150 ˚C for 30 minutes. The reaction mixture was cooled, diluted with DCM and washed thrice with water followed by brine. The combined organic layers were dried over MgSO$_4$ and concentrated under reduced pressure. The crude product was purified by silica gel chromatography using 10%-80% EtOAc in hexanes to reveal an off-white solid (1.411 g, 70%). UHPLC−MS method: 5−95% ACN (0.1% TFA) in water (0.1% TFA), 3 min run; t_R (min) 2.72; HRMS (ESI$^+$): [M+H$^+$] calculated = 516.1293, [M+H$^+$] observed = 516.0786.

(**R**)-tert-Butyl 3-((6-Bromo-2-(2-iodophenyl)-4-oxoquinazolin-3(4H)-yl)methyl) piperidine-1-carboxylate (7B). The method similar for the preparation of compound **7A** was used except replacing **6A** with **6B**. An off-white powder was obtained in a 28% yield. UHPLC−MS method: 5−95% ACN (0.1% TFA) in water (0.1% TFA), 3 min run; t_R (min) 2.92; HRMS (ESI$^+$): [M+H$^+$] calculated = 624.0353, [M+H$^+$] observed = 623.9957.

(**S**)-6-(Benzo[d]thiazol-6-yloxy)-2-(2-fluorophenyl)-3-(piperidin-3-ylmethyl) quinazolin-4(3H)-one (8A). CAS: 2179062-00-9. Synthesized according to Hou et al.[17] Briefly, a suspension of **7A** (0.460 g, 0.891 mmol), 6-hydroxybenzothiazole (0.205 g, 1.36 mmol), copper(I) chloride (0.048 g, 0.487 mmol), 2,2,6,6-tetramethyl-3,5-heptanedione (TMHD) (103 µL, 0.490 mmol), and CsCO$_3$ (0.583 g, 1.79 mmol) in anhydrous DMF (5 mL) was purged with N$_2$(g) and stirred at 130 ˚C for 15 h. The resulting mixture was filtered over celite washing with EtOAc. The organic mixture was then washed with water twice followed by brine and dried over MgSO$_4$ prior to being concentrated under reduced pressure. The crude product was purified by silica gel chromatography using 10%-80% EtOAc in hexanes to reveal an off-white solid (0.389 g, 74%). UHPLC−MS method: 5−95% ACN (0.1% TFA) in water (0.1% TFA), 3 min run; t_R (min) 2.60; HRMS (ESI$^+$): [M+H$^+$] calculated = 587.2123, [M+H$^+$] observed = 587.1674.

(**S**)-2-(2-Fluorophenyl)-6-((5-fluoropyridin-2-yl)oxy)-3-((1-isopropylpiperidin-3-yl)methyl)quinazolin-4(3H)-one (9). CAS: 2172830-20-3. Synthesized according to Hou et al.[17] Briefly, to a solution of **8A** (0.740 g, 1.26 mmol) in DCM (10 mL) was added TFA (2 mL). The reaction mixture stirred for 3 h at room temperature followed by removal of solvent and excess TFA. The resulting residue was re-suspended in sat. NaHCO$_3$(aq) and extracted into EtOAc thrice. The organic layer was washed with brine, dried over MgSO$_4$, and concentrated under reduced pressure. The crude product was purified by reverse-phase flash chromatography using 0%-100% MeOH in H$_2$O. The pure fractions were collected and lyophilized to a white powder (0.330 g, 44%). UHPLC−MS method: 5−95% ACN (0.1% TFA) in water (0.1% TFA), 3 min run; t_R (min) 1.41; HRMS (ESI$^+$): [M+H$^+$] calculated = 487.1599, [M+H$^+$] observed = 487.1456.

(*S*)-6-(Benzo[d]thiazol-6-yloxy)-2-(2-fluorophenyl)-3-((1-isopropylpiperidin-3-yl)methyl)quinazolin-4(3H)-one (4). CAS: 2172830-03-2. Synthesized according to Hou et al.[17] Briefly, to a solution of **9** (0.358 g, 0.596 mmol) and K_2CO_3 (1.00 g, 7.24 mmol) in ACN (10 mL) was added 2-bromopropane (1.00 mL, 10.6 mmol). The reaction mixture stirred for 16 h at 80 ˚C. The solvent was removed and the product was re-suspended in sat. $NaHCO_3$(aq) and extracted into EtOAc thrice. The organic layer was washed with brine, dried over $MgSO_4$, and concentrated under reduced pressure. The crude product was purified by reverse-phase flash chromatography using 2%-100% MeOH in H_2O. The pure fractions were collected and lyophilized to a white powder (0.191 g, 50%). UHPLC−MS method: 20−95% ACN (0.1% TFA) in water (0.1% TFA), 3 min run; t_R (min) 1.18; HRMS (ESI+): [M+H+] calculated = 529.2068, [M+H+] observed = 529.1797.

Spiroadamantyl-1,3-dioxane-4,6-dione (SPIAd). CAS: 455329-56-3. Synthesized according to Rotstein et al.[23] Briefly, malonic acid (0.501 g, 4.82 mmol) was suspended in acetic anhydride (1 mL) and conc. H_2SO_4 (20 µL) heated to 60 ˚C for 15 minutes. The reaction mixture was then cooled to room temperature and 2-adamantanone (0.735 g, 4.89 mmol) was added portion wise. The mixture stirred for an additional 1.5 h prior to being diluted with DCM and washed three times with water. The organic extracts were washed with brine, dried over $MgSO_4$, and concentrated under reduced pressure. The crude product was recrystallized from Et_2O and hexanes to afford a white, crystalline solid (0.826 g, 72%). ^{1}H NMR (400 MHz, $CDCl_3$): δ 3.61 (s, 2H), 2.20-2.12, (m, 6H), 1.94 (s, 2H), 1.81-1.75 (m, 6H). ^{13}C NMR (100 MHz, $CDCl_3$): δ 163.2, 109.8, 37.8, 36.8, 36.7, 33.6, 26.2.

(*R*)-*tert*-butyl 3-((2-amino-5-bromobenzamido)methyl)piperidine-1-carboxylate (10): CAS: 875269-73-1. To a suspension of 5-bromoisatoic anhydride (1.073 g, 4.43 mmol) in ACN was added K_2CO_3 (1.245 g, 9.01 mmol) and (*R*)-1-Boc-3-(aminomethyl)piperidine (0.952 mL, 4.43 mmol). The reaction mixture stirred for 1 h at 70 ˚C prior to being cooled to room temperature and the solvent removed under reduced pressure. The residue was suspended with H_2O and filtered to obtain the desired product as an off-white solid (1.664 g, 91%). The product was used without further purification. ^{1}H NMR (400 MHz, $CDCl_3$) δ 7.46 (s, br, 1H), 7.25 (dd, *J* = 8.7, 2.2 Hz, 1H), 6.74 (s, br, 1H), 6.55 (d, *J* = 8.7 Hz, 1H),

5.49 (s, br, 2H), 3.72 – 2.95 (m, 7H), 1.83-1.81 (m, 2H), 1.67-1.64 (m, 1H), 1.45 (s, 9H), 1.33-1.29 (m, 1H). ^{13}C NMR (100 MHz, CDCl$_3$) δ 168.2, 155.7, 147.6, 134.8, 129.7, 118.9, 117.7, 107.7, 79.7, 46.7, 45.0, 41.6, 35.3, 28.5, 28.3, 23.7. UHPLC−MS method: 5−95% ACN (0.1% TFA) in water (0.1% TFA), 3 min run; t$_R$ (min) 2.20. HRMS (ESI$^+$): [M+H]$^+$ calculated = 412.1230; [M+H]$^+$ observed = 412.1213.

(**R**)-***tert***-**butyl 3-((2-amino-5-(benzo[d]thiazol-6-yloxy)benzamido)methyl)piperidine-1-carboxylate (11):** A suspension of **10** (0.507 g, 1.23 mmol), 6-hydroxybenzothiazole (0.283 g, 1.87 mmol), Copper(I) chloride (0.070 g, 0.707 mmol), 2,2,6,6-tetramethyl-3,5-heptanedione (TMHD) (150 µL, 0.719 mmol), and CsCO$_3$ (0.809 g, 2.48 mmol) in anhydrous DMF (13 mL) was purged with N$_2$(g) and subjected to microwave irradiation with stirring at 140 ˚C for 4 h. The resulting mixture was filtered over celite washing with EtOAc. The product was washed with sat. NaHCO$_3$(aq) twice followed by brine and dried over MgSO$_4$ prior to being concentrated under reduced pressure. The crude product was purified by silica gel chromatography using 12%-100% EtOAc in hexanes to reveal an off-white solid (0.281 g, 47%). ^{1}H NMR (400 MHz, CDCl$_3$) δ 8.83 (s, 1H), 7.98 (d, J = 8.8 Hz, 1H), 7.30 (s, 1H), 7.15 (m, 2H), 6.96 (dd, J = 8.6, 2 Hz, 1H), 6.86 (s, br, 1H), 6.69 (d, J = 8.7 Hz, 1H), 5.45 (s, 2H), 3.69-2.91 (m, 6H), 1.77 (s, br, 2H), 1.60 (s, br, 1H), 1.35-1.25 (m, 11H). ^{13}C NMR (100 MHz, CDCl$_3$) δ 168.7, 157.3, 155.0, 152.5, 148.7, 146.2, 145.7, 135.0, 125.1, 124.2, 119.2, 118.7, 117.3, 116.9, 108.4, 79.6, 46.8, 45.1, 41.4, 35.4, 28.4, 28.1, 23.7. UHPLC−MS method: 5−95% ACN (0.1% TFA) in water (0.1% TFA), 3 min run; t$_R$ (min) 2.10. HRMS (ESI$^+$): [M+H]$^+$ calculated = 483.2066; [M+H]$^+$ observed = 483.2078.

(**R**)-***tert***-**butyl-3-((5-(benzo[d]thiazol-6-yloxy)-2-(2-iodobenzamido)benzamido)methyl)piperidine-1-carboxylate (12):** A solution of **11** (0.425 g, 0.880 g) and Et$_3$N (400 µL, 2.88 mmol) in DCM was cooled to 0 ˚C prior to the addition of 2-iodobenzoyl chloride (0.295 g, 1.10 mmol) slowly dropwise. The reaction was allowed to warm to room temperature over 3 h prior to being diluted with DCM and washed with 5% HCl(aq) thrice followed by brine. The organic layer was dried over MgSO$_4$ and concentrated under reduced pressure. The crude product was purified by silica gel chromatography using 12%-100% EtOAc in hexanes to reveal an off-white solid (0.462 g, 74%). ^{1}H NMR

(400 MHz, CDCl$_3$) δ 11.52 (s, br, 1H), 8.87 (s, 1H), 8.70 (d, J = 8.4 Hz, 1H), 7.99 (d, J = 8.8 Hz, 1H), 7.86 (d, J = 7.9 Hz, 1H), 7.63 (s, br, 1H), 7.50 (d, J = 7.9 Hz, 1H), 7.39 -7.35 (m, 3H), 7.16 (d, J = 8.6 Hz, 2H), 7.08 (t, J = 7.5 Hz, 1H), 3.64 - 2.95 (m, 6H), 1.79 – 1.73 (m, 2H), 1.57 (s, br, 1H), 1.33 – 1.24 (m, 11H). ^{13}C NMR (100 MHz, CDCl$_3$) δ 168.2, 167.6, 155.8, 155.3, 153.1, 151.9, 149.3, 141.9, 140.4, 135.5, 135.1, 131.5, 128.4, 128.2, 124.4, 123.5, 123.4, 122.5, 118.4, 118.1, 109.9, 92.9, 79.7, 46.8, 45.2, 41.6, 35.1, 28.4, 28.1, 23.5. UHPLC−MS method: 40−95% ACN (0.1% TFA) in water (0.1% TFA), 3 min run; t$_R$ (min) 2.11. HRMS (ESI$^+$): [M+H]$^+$ calculated = 713.1289; [M+H]$^+$ observed = 713.0483.

(*R*)-*tert*-butyl-3-((6-(benzo[d]thiazol-6-yloxy)-2-(2-iodophenyl)-4-oxoquinazolin-3(4H)-yl)methyl)piperidine-1-carboxylate (8B): In a microwave vessel, **12** (0.436 g, 0.612 mmol) and LiOH (0.177 g, 7.40 mmol) was dissolved in ethylene glycol (20 mL) and subjected to microwave irradiation at 95 ˚C for 5 h. The resulting precipitate was filtered washing with H$_2$O and purified by silica gel chromatography using 12%-100% EtOAc in hexanes to reveal an off-white solid (0.232 g, 56%). ^{1}H NMR (400 MHz, CDCl$_3$) δ 8.94 (s, 1H), 8.12 (d, J = 8.4 Hz, 1H), 7.92 (d, J = 6.8 Hz, 1H), 7.79 – 7.75 (m, 2H), 7.62 (s, 1H), 7.51 (m, 3H), 7.30 – 7.20 (m, 2H), 4.20 (s, br, 1H), 3.85 - 3.81 (m, 2H), 3.36 - 3.32 (m, 1H), 2.60 – 2.16 (m, 2H), 1.83 -1.55 (m, 2H), 1.36 (m, 11H), 1.00 (s, br, 1H). ^{13}C NMR (100 MHz, CDCl$_3$) δ 161.9, 157.0, 155.0, 154.7, 154.4, 153.6, 150.26, 143.3, 140.0, 139.5, 135.3, 131.3, 130.0, 128.7, 128.5, 126.4, 124.9, 122.1, 119.4, 113.8, 112.2, 96.9, 79.5, 48.4, 47.9, 44.3, 36.4, 28.7, 28.4, 24.6. UHPLC−MS method: 50−95% ACN (0.1% TFA) in water (0.1% TFA), 3 min run; t$_R$ (min) 1.82. HRMS (ESI$^+$): [M+H]$^+$ calculated = 695.1183; [M+H]$^+$ observed = 695.0670.

(*S*)-6-(benzo[d]thiazol-6-yloxy)-2-(2-iodophenyl)-3-((1-isopropylpiperidin-3-yl)methyl)quinazolin-4(3H)-one (13): A solution of **8B** (0.182 g, 0.263 mmol) dissolved in 10% TFA in DCM (20 mL) was stirred at room temperature for 1.5 h. The solvent and excess TFA was removed under reduced pressure co-evaporating with DCM. The resulting TFA salt was re-dissolved in ACN (15 mL) and K$_2$CO$_3$ (0.281 g, 2.03 mmol) and 2-bromopropane (400 µL, 4.26 mmol) were added. The mixture stirred at 70 ˚C for 16 h prior to the solvent being removed under reduced pressure. The resulting residue was

suspended in H_2O and extracted into EtOAc three times followed by the organic layer being washed with brine. The organic layer was dried over $MgSO_4$ and concentrated under reduced pressure. The crude product was purified by silica gel chromatography using 2%-20% MeOH in DCM revealing a white solid (0.127 g, 76%). ^{1}H NMR (400 MHz, $CDCl_3$) δ 9.39 (s, 1H), 8.17 (d, J = 8.6 Hz, 1H), 8.03 - 8.01 (m, 2H), 7.81 (d, J = 8.9 Hz, 1H), 7.73 – 7.68 (m, 2H), 7.61 – 7.57 (m, 2H), 7.41 – 7.31 (m, 2H), 4.15 – 4.12 (m, 1H), 3.35-3.06 (m, 3H), 2.60-2.31 (m, 2H), 1.63 (s, br, 1H), 1.22 -1.08 (m, 10H). ^{13}C NMR (100 MHz, $CDCl_3$) δ 161.0, 156.5, 156.2, 154.9, 153.5, 150.0, 142.9, 139.2, 138.6, 135.2, 131.3, 130.3, 129.9, 128.3, 126.4, 124.3, 121.5, 119.2, 113.0, 112.5, 97.8, 67.4, 48.0, 29.8, 28.3, 23.2, 22.4, 16.0, 13.9, 10.8. UHPLC−MS method: 20−95% ACN (0.1% TFA) in water (0.1% TFA), 3 min run; t_R (min) 1.33. HRMS (ESI[+]): [M+H][+] calculated = 637.1129; [M+H][+] observed = 637.1128.

Methyl (1r,3r,5r,7r)-spiro[adamantane-2,2'-[1,3]dioxane]-4',6'-dion-[(*S*)-6-(benzo[d] thiazol-6-yloxy)-2-(2-iodoniumphenyl)-3-((1-isopropylpiperidin-3-yl)methyl) quinazolin-4(3H)-one] ylide (14): To a solution of **13** (0.063 g, 0.099 mmol) in 3:1 TFA: $CHCl_3$ (3 mL) was added Oxone® monopersulfate (0.063 g, 0.204 mmol). The reaction mixture stirred at room temperature for 2 h prior to the solvent being removed under reduced pressure. The residue was suspended in $CHCl_3$ (10 mL) and filtered to remove inorganic salts. The filtrated was concentrated again to remove the solvent and the residue was re-dissolved in EtOH (1 mL) followed by the addition of SPIAd (0.031 g, 0.130 mmol) pre-dissolved in 10% Na_2CO_3(aq) (2 mL). A colour change of the reaction mixture from orange to green was noted upon the addition of the SPIAd solution. The reaction mixture (pH = 10) stirred 30 min at room temperature prior to being concentrated under reduced pressure. The residue was diluted with H_2O and extracted into DCM three times followed by being washed with brine. The organic layer was dried over $MgSO_4$ and concentrated under reduced pressure. The crude product was purified by silica gel chromatography using 2%-20% MeOH in DCM revealing a white solid (0.024 g, 27%). ^{1}H NMR (400 MHz, Methanol-*d4*) δ 9.22 (s, 1H), 8.10 (d, J = 8.7 Hz, 1H), 7.99 (d, J = 7.6 Hz, 1H), 7.89 – 7.84 (m, 3H), 7.78 – 7.75 (m, 1H), 7.70 - 7.64 (m, 3 H), 7.36 (dd, J = 8.8, 2.2 Hz, 1H), 4.48 (dd, J = 14.2, 6.3 Hz, 1H), 4.23 (dd, J = 14.1, 7.5 Hz, 1H), 3.20 – 3.17 (m, 1H), 3.12 – 3.09 (m, 1H), 3.01 – 2.98 (m, 1H), 2.60 – 2.47 (m, 4H), 2.13 – 2.06

(m, 5H), 1.84 (m, 2H), 1.78 (m, 6H), 1.72 – 1.68 (m, 1H), 1.53 – 1.40 (m, 2H), 1.15 (dd, J = 14.2, 6.6 Hz, 6H), 0.99 - 0.97 (m, 1H). ^{13}C NMR (100 MHz, Methanol-d_4) δ 166.3, 163.0, 159.5, 157.0, 155.3, 154.6, 151.3, 142.1, 136.7, 135.4, 134.7, 132.6, 132.0, 130.6, 128.0, 25.3, 123.1, 120.7, 118.6, 114.3, 114.0, 108.9, 106.6, 58.9, 58.5, 58.2, 53.1, 38.0, 36.9, 36.4, 36.1, 34.7, 28.0, 27.8, 23.8, 17.7, 16.8. UHPLC−MS method: 20−95% ACN (0.1% TFA) in water (0.1% TFA), 3 min run; t_R (min) 1.54. HRMS (ESI$^+$): [M+H]$^+$ calculated = 871.2021; [M+H]$^+$ observed = 871.1996.

4.4.3 Radiochemistry

All anhydrous solvents were purchased from Sigma-Aldrich and used as received. Fluoride-18 was obtained as [^{18}F]H$_2$^{18}O by cyclotron. QMA carbonate SPE cartridges were purchased from Waters. Analytical radio-RP-HPLC (Agilent RP-C18 column 4.6 x 150 mm, 5 µm) was performed using a Waters 1525 Binary HPLC Pump, a Waters 2487 dual λ absorbance detector (292 and 220 nm), Waters InLine degasser, a gamma detector, and data was recorded using Breeze software. The solvent system runs gradients of 0.1% trifluoroacetic acid (TFA) in ACN and 0.1% TFA in MilliQ water at a flow rate of 1.5 mL/min over 10 minutes with a 5 minute wash.

Fluoride-18 (200-400 MBq) was trapped on a QMA carbonate SPE cartridge and eluted into a 20 mL glass vial with a solution of the base/PTC (Table 4.2) in 1 mL of 3:7 H$_2$O:ACN. The solution was evaporated to dryness on a Biotage V10 Evaporator and further dried azeotropically with 1 mL of anhydrous ACN, repeated twice. A solution of precursor **14** (2-4 mg) pre-dissolved in anhydrous solvent (400 µL) was added to the dried fluoride-18 mixture and heated at a specified temperature for 5-20 minutes (Table 4.2). An aliquot of the reaction mixture was then analyzed by analytical HPLC (20-80% ACN in water) to observe any product conversion.

4.4.4 Investigating the thermal stability of precursor **14**

The stability of precursor **14** was investigated under various conditions similar to those used in radiofluorination but in the absence of fluoride-18. Precursor **14** (2 mg) was dissolved DMF (400 µL) and an aliquot (15 µL) of the mixture was taken and diluted with 1:1 ACN:H$_2$O (500 µL) to obtain a baseline measurement of intact precursor. The

amount of intact precursor was analyzed by analytical UHPLC-MS (20-95% ACN in water, 3 µL injection volume). The reaction mixture was then incubated at temperatures of 22 ˚C, 50 ˚C, 70 ˚C, 90˚C, and 110 ˚C for 10 minutes each and the amount of intact precursor remaining was analyzed and reported as a percentage of the baseline measurement.

4.5 References

1   M. L. James and S. S. Gambhir, *Physiol. Rev.*, 2012, **92**, 897–965.

2   F. Wuest, in *PET Chemistry*, eds. P. A. Schubiger, L. Lehmann and M. Friebe, Springer, 2007.

3   E. P. Gillis, K. J. Eastman, M. D. Hill, D. J. Donnelly and N. A. Meanwell, *J. Med. Chem.*, 2015, **58**, 8315–8359.

4   A. D. Howard, S. D. Feighner, D. F. Cully, J. P. Arena, A. Paul, C. I. Rosenblum, M. Hamelin, D. L. Hreniuk, O. C. Palyha, M. Hamelin, D. L. Hreniuk, O. C. Palyha, J. Anderson, P. S. Paress, C. Diaz, M. Chou, K. K. Liu, K. K. Mckee, S. Pong, A. Elbrecht, M. Dashkevicz, R. Heavens, M. Rigby, J. S. Dalip, A. D. Howard, S. D. Feighner, D. F. Cully, J. P. Arena, P. A. Liberator, C. Rosenblum, M. Hamelin, D. L. Hreniuk, O. C. Palyha, J. Anderson, P. S. Paress, C. Diaz, M. Chou, K. K. Liu, K. K. Mckee, S. Pong, L. Chaung, A. Elbrecht, M. Dashkevicz, R. Heavens, M. Rigby, D. J. S. Sirinathsinghji, D. C. Dean, D. G. Melillo, A. A. Patchett, R. Nargund, P. R. Griffin, J. A. Demartino, S. K. Gupta, J. M. Schaeffer, R. G. Smith and L. H. T. Van Der Ploegt, *Science (80-.).*, 1996, **273**, 974–977.

5   S. Gnanapavan, B. Kola, S. Bustin, D. Morris, P. McGee, P. Fairclough, S. Bhattacharya, R. Carpenter, A. Grossman and M. Korbonits, *J. Clin. Endocrinol. Metab.*, 2002, **87**, 2988–2991.

6   B. Ueberberg, N. Unger, W. Saeger, K. Mann and S. Petersenn, *Horm. Metab. Res.*, 2009, **41**, 814–821.

7   M. Kojima, H. Hosoda, Y. Date, M. Nakazato, H. Matsuo and K. Kangawa, *Nature*, 1999, **402**, 656–660.

8   K. Howick, B. T. Griffin, J. F. Cryan and H. Schellekens, *Int. J. Mol. Sci.*, 2017, **18**, 273.

9   Y. Lv, T. Liang, G. Wang and Z. Li, *Biosci. Rep.*, 2018, **38**, 1–13.

10   P. Kurowska, E. Mlyczynska and A. Rak, *J. Physiol. Pharmacol.*, 2019, **70**, 3–13.

11   B. Holst, A. Cygankiewicz, T. H. Jensen, M. Ankersen and T. W. Schwartz, *Mol. Endocrinol.*, 2003, **17**, 2201–2210.

12   Z. Ye, Y. Gao, R. K. Bakshi, M. H. Chen, S. P. Rohrer, S. D. Feighner, S. S. Pong, A. D. Howard, A. Blake, E. T. Birzin, L. Locco, R. M. Parmar, W. W. S. Chan, J. M. Schaeffer, R. G. Smith, A. A. Patchett and R. P. Nargund, *Bioorganic Med. Chem. Lett.*, 2000, **10**, 5–8.

13   J. Rudolph, W. P. Esler, S. O'Connor, P. D. G. Coish, P. L. Wickens, M. Brands, D. E. Bierer, B. T. Bloomquist, G. Bondar, L. Chen, C.-Y. Chuang, T. H. Claus, Z. Fathi, W. Fu, U. R. Khire, J. A. Kristie, X.-G. Liu, D. B. Lowe, A. McClure, M. Michels, A. A. Ortiz, P. D. Ramsden, R. W. Schoenleber, T. E. Shelekhin, A. Vakalopoulos, W. Tang, L. Wang, L. Yi, S. J. Gardell, J. N. Livingston, L. J. Sweet and W. H. Bullock, *J. Med. Chem.*, 2007, **50**, 5202–5216.

14   R. Potter, A. G. Horti, H. T. Ravert, D. P. Holt, P. Finley, U. Scheffel, R. F. Dannals and R. L. Wahl, *Bioorganic Med. Chem.*, 2011, **19**, 2368–2372.

15   K. Kawamura, M. Fujinaga, Y. Shimoda, T. Yamasaki, Y. Zhang, A. Hatori, L. Xie, H. Wakizaka, K. Kumata, T. Ohkubo, Y. Kurihara, M. Ogawa, N. Nengaki and M. R. Zhang, *Nucl. Med. Biol.*, 2017, **52**, 49–56.

16   R. P. Moldovan, S. Els-Heindl, D. J. Worm, T. Kniess, M. Kluge, A. G. Beck-Sickinger, W. Deuther-Conrad, U. Krügel and P. Brust, *Int. J. Mol. Sci.*, 2017, **18**, 1–16.

17   J. Hou, M. S. Kovacs, S. Dhanvantari and L. G. Luyt, *J. Med. Chem.*, 2018, **61**, 1261–1275.

18   B. H. Rotstein, N. a Stephenson, N. Vasdev and S. H. Liang, *Nat. Commun.*, 2014, **5**, 4365.

19   L. Wang, R. Cheng, M. Fujinaga, J. Yang, Y. Zhang, A. Hatori, K. Kumata, J. Yang, N. Vasdev, Y. Du, C. Ran, M. R. Zhang and S. H. Liang, *J. Med. Chem.*, 2017, **60**, 5222–5227.

20   K. Kumata, Y. Zhang, M. Fujinaga, T. Ohkubo, W. Mori, T. Yamasaki, M. Hanyu, L. Xie, A. Hatori and M. R. Zhang, *Bioorganic Med. Chem.*, 2018, **26**, 4817–4822.

21   H. Fu, W. Tang, Z. Chen, V. V. Belov, G. Zhang, T. Shao, X. Zhang, Q. Yu, J. Rong, X. Deng, W. Han, S. J. Myers, P. Giffenig, L. Wang, L. Josephson, Y. Shao, A. T. Davenport, J. B. Daunais, M. Papisov, H. Yuan, Z. Li, S. F. Traynelis and S. H. Liang, *ACS Chem. Neurosci.*, 2019, **10**, 2263–2275.

22   C. Varlow, E. Murrell, J. P. Holland, A. Kassenbrock, W. Shannon, S. H. Liang, N. Vasdev and N. A. Stephenson, *Molecules*, 2020, **25**, 982.

23   B. H. Rotstein, L. Wang, R. Y. Liu, J. Patteson, E. E. Kwan, N. Vasdev and S. H. Liang, *Chem. Sci.*, 2016, **7**, 4407–4417.

24   A. A. Zagulyaeva, M. S. Yusubov and V. V. Zhdankin, *J. Org. Chem.*, 2010, **75**, 2119–2122.

25   C. Drerup, J. Ermert and H. H. Coenen, *Molecules*, 2016, **21**, 1160.

26   I. N. Petersen, J. Villadsen, H. D. Hansen, J. Madsen, A. A. Jensen, N. Gillings, S. Lehel, M. M. Herth, G. M. Knudsen and J. L. Kristensen, *Org. Biomol. Chem.*, 2017, **15**, 4351–4358.

27   J. E. Jakobsson, G. Grønnevik and P. J. Riss, *Chem. Commun.*, 2017, **53**, 12906–12909.

28   S. Li, Z. Cai, M. Q. Zheng, D. Holden, M. Naganawa, S. F. Lin, J. Ropchan, D. Labaree, M. Kapinos, T. Lara-Jaime, A. Navarro and Y. Huang, *J. Nucl. Med.*, 2018, **59**, 140–146.

29   H. Jia, Z. Cai, D. Holden, Y. He, S. F. Lin, S. Li, E. Baum, A. Shirali, M. Kapinos, H. Gao, J. Ropchan and Y. Huang, *ACS Chem. Neurosci.*, 2020, **11**, 1673–1681.

30   S. H. Liang, L. Wang, N. A. Stephenson, B. H. Rotstein and N. Vasdev, *Nat. Protoc.*, 2019, **14**, 1530–1545.

31   Y. W. Jung, G. Gu and D. M. Raffel, *J. Label. Compd. Radiopharm.*, 2019, **62**, 835–842.

32   X. Deng, J. Rong, L. Wang, N. Vasdev, L. Zhang, L. Josephson and S. H. Liang, *Angew. Chemie - Int. Ed.*, 2019, **58**, 2580–2605.

Chapter 5

5 Fragment-Based Imaging Agent Discovery

5.1 Introduction

Fragment-based drug design (FBDD) is one of several target-based approaches utilized in the development of new candidate drugs in the field of medicinal chemistry.[1] Uniquely, this technology identifies chemical starting points toward the discovery of novel ligands for biological targets. These chemical starting points, referred to as fragment hits, may then be strategically optimized into full-size drug-like molecules and subsequently evaluated as clinical candidates. The FBDD strategy begins with the assembly of a library of low molecular weight molecules, known as fragments, which typically adhere to Rule of Three (Ro3) guidelines: (1) molecular mass $\leq$ 300 Da; (2) up to 3 hydrogen bond donors and up to 3 hydrogen bond acceptors; (3) logP $\leq$ 3.[2] This library is then screened for binding toward a biological target-of-interest, most commonly through biophysical techniques such as NMR spectroscopy, X-ray crystallography, or surface plasmon resonance (SPR), or through biochemical techniques such as cell-based affinity assays.[3] Fragment hits serve as chemical starting points, which undergo fragment elaboration, guided by parameters such as ligand efficiency (LE), to become drug-like leads with novel ligand scaffolds. Over the last twenty years, FBDD has been successfully applied in the pharmaceutical and biotechnology industry toward the development of viable pharmaceutical entities including four drugs brought to market to date.[4–7] The success of these fragment-based drugs shows promise for the technique, and while established in drug discovery, FBDD has not yet been applied toward the discovery of molecular imaging agents.

The field of molecular imaging allows for minimally invasive visualization of biological processes taking place in living systems in real time. Targeted molecular imaging requires the use of a molecular probe, which carries a traceable signalling entity within its structure in order to facilitate visualization of a given biological target-of-interest, known as a biomarker. In many cases, known ligands for a biomarker are structurally modified to include a signalling entity at some distance from the probe's target-binding domain,

resulting in a candidate molecular imaging agent (Figure 5.1A). However, incorporation of the signalling entity to a previously optimized ligand can cause a reduction in affinity toward the biomarker as well as negatively alter other physicochemical properties of the ligand. Therefore, it would be advantageous to design an imaging probe with the imaging moiety inherently embedded within the molecule from inception (Figure 5.1B-C).
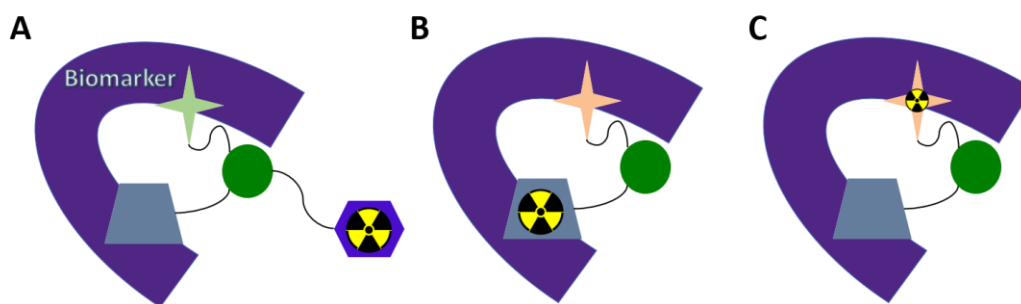
Figure 5.1. Illustration of (A) a molecular imaging probe with the signalling entity conjugated to the molecule at some distance from the target binding domain or (B) & (C) a molecular imaging probe with the signalling entity embedded in the target binding domain. Radiation symbol represents traceable signal.

Fragment screening has been successfully applied to a variety of target classes, most commonly including soluble proteins due to their amenability for biophysical screening methods, through which in-depth binding mode information may be obtained. However, FBDD campaigns for membrane-bound targets remain more of a challenge due to poor protein isolation yields and inherent instability when purified from the membrane environment.[8] G-protein coupled receptors (GPCR) are a superfamily of membrane-bound proteins and make up a large class of relevant biological targets for pharmaceutical drug development. While FBDD toward GPCR targets has been a challenge relative to soluble proteins, significant success in this area have been reported.[9,10] Several potent chemotypes were identified for the adrenergic α_{2C} receptor through cell-based and virtual fragment screens demonstrating the utility of conventional biochemical screening strategies for membrane-bound targets.[9] Additionally, stabilization techniques such as thermostabilized StaR proteins have advanced the ability for fragment-based approaches to target GPCRs, such as the adenosine A_{2A} receptor, using biophysical techniques.[10–12]

The growth hormone secretagogue receptor 1a (GHSR) is a GPCR predominantly expressed in the hypothalamus, pituitary and, to a lesser extent, in peripheral tissues such as the stomach and pancreas.[13,14] Upon binding of its endogenous ligand, ghrelin, the GHSR is able to participate in regulating a number of physiological processes including appetite, energy homeostasis, and growth hormone secretion.[15,16] Additionally, the GHSR is differentially expressed in a number of cancer types compared to healthy tissues making this receptor a potential biomarker for targeted molecular imaging of cancer.[17–19] Several efforts to develop GHSR-targeting imaging agents have focused on the modification of ghrelin to include a traceable signalling moiety for optical or nuclear imaging modalities.[20] Most candidate probes involve having this signalling moiety conjugated to the *C*-terminus of the peptide and often result in a reduction in binding affinity compared to native ghrelin. However, a few examples of incorporating the imaging moiety into the binding domain of ghrelin have been reported.[21,22] One such example substituted the unique octanoyl side chain in truncated ghrelin(1-8) with a fluorine-containing aromatic group resulting in a significantly improved receptor affinity when combined with other peptide sequence alterations.[22] While the endogenous ligands for the GHSR are peptides, it is well established that a variety of small molecules can bind to the GHSR with high affinity.[23] In fact, some small molecule ligands for the GHSR were initially discovered through screening campaigns.[23,24] A series of quinazolinone derivatives stemming from high-throughput screening (HTS) hits have been reported as GHSR antagonists and have been adopted toward the development of GHSR imaging agents for ^{11}C and ^{18}F-PET imaging.[20] Due to the membrane-bound nature of the GHSR, obtaining structural information on ligand-receptor binding has been a challenge. However, in recent years, structural models of ligand-bound GHSR have been reported, beginning to shed light on the mechanism of ligand binding and receptor activation.[25–27]

The goal of this project is to merge the established and promising technique of fragment-based drug design with the development of targeted probes for non-invasive PET imaging. First, a novel fragment library was created where fragments contain fluorine in a position that may be readily radiolabeled with fluoride-18 from a suitable precursor for ^{18}F-PET imaging. The library utilizes several known, well-established radiolabeling strategies including nucleophilic substitution reactions as well as fluorination by

reductive elimination of non-activated arenes. Other synthetic strategies to diversify the library fragments include coupling reactions as well as copper-catalyzed click chemistry. As a proof of concept, the newly synthesized fragment library was then screened *in vitro* for binding against the GHSR via a radioligand-displacement binding assay. The success of obtaining viable fragment hits for imaging agent development for the GHSR could then support further application of this methodology toward other imaging targets of interest.

5.2   Results and Discussion

5.2.1 Fluorine-containing Fragment Library

For the first time, a fluorine-containing fragment library was designed on the basis that each fragment contained fluorine in a position that could be accessed with fluorine-18 through known radiofluorination techniques including nucleophilic aromatic and aliphatic substitution reactions, as well as reductive elimination of non-activated arenes. Fluorine-containing fragments were organized into three classes based on these ^{18}F-labelling strategies (Figure 5.2). Within each fragment class, some fragments are of a certain structural subtype where each fragment in the subtype contains the same fluorine-containing moiety conjugated to a diversifying R group by either an amide-forming coupling reaction or click chemistry. All fragments were synthesized using non-radioactive fluorine-19, with the fluorine atom strategically placed in a position that may be readily radiolabeled from an appropriate precursor.
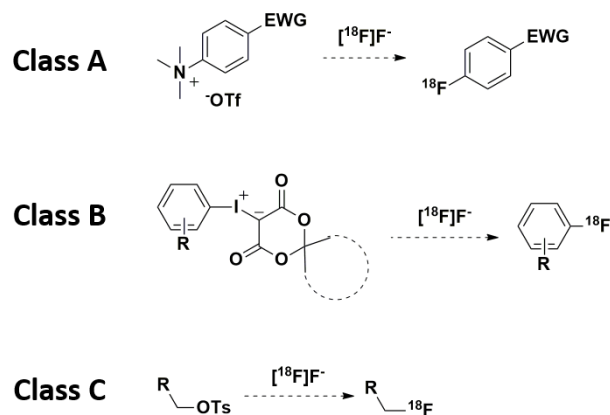
Figure 5.2. The three classes of fluorine-containing fragments classified based on radiofluorination strategy.

Class A encompasses fragments which may be radiolabelled through conventional nucleophilic aromatic substitution (S_NAr) techniques as represented in scheme 5.1. These fragments contain the fluorine atom in either the *ortho* or *para* position of an aromatic ring activated by an electron withdrawing group (EWG). A total of 23 fragments were synthesized or obtained commercially for this class with 15 belonging to a particular subtype derived from the prosthetic group, *N*-succinimidyl 4-[^{18}F]fluorobenzoate, which is often used to conjugate fluorine-18 to biomolecules for PET imaging.[28] In fluorine-18 radiochemistry, the synthesis of this prosthetic group involves nucleophilic aromatic substitution of a trimethylammonium triflate salt with nucleophilic [^{18}F]fluoride. The electron-withdrawing group (EWG) *para* to the leaving group on the aromatic ring activates the ring and favours a successful fluorination reaction. The ^{19}F-containing fragments of this subtype were synthesized from commercially available 4-fluorobenzoic acid as shown in scheme 5.1. Acid **1** was first converted to the *N*-succinimidyl activated ester **2** in a yield of 85% using EDC hydrochloride and *N*-hydroxysuccinimide (NHS). The activated ester **2** was then reacted under basic conditions with a series of diverse primary or secondary amines, which were selected at random to produce fragments **3a-o** in moderate to excellent yields.

Scheme 5.1. Synthesis of a subtype of class A fragments **[¹⁹F]3a-o** from 4-fluorobenzoic acid **1** and proposed radiosynthetic strategy of amides **[¹⁸F]3a-o** from precursor **4**.
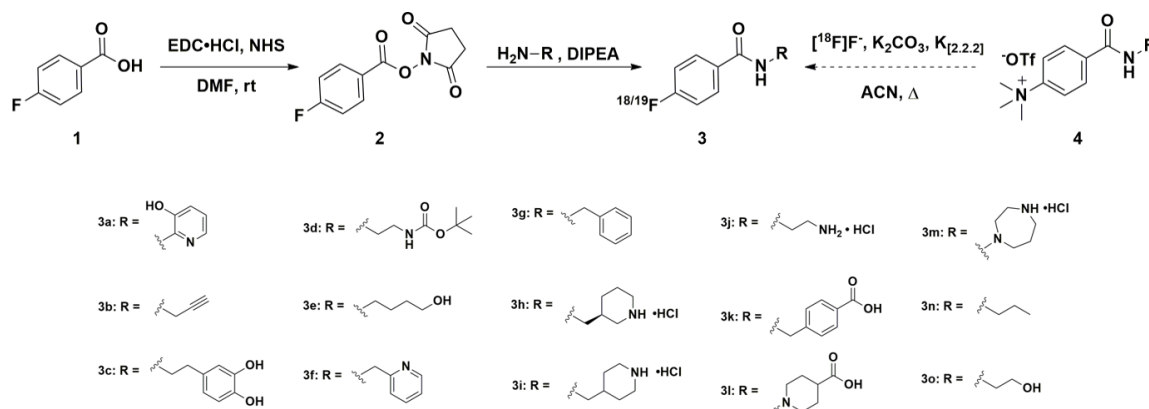
Class B also contains aromatic fragments, however, with the distinction that they lack the necessary EWG needed to facilitate S_NAr labelling with fluoride-18. Such non-activated arenes have been a great challenge for ¹⁸F-labelling in the past. Fortunately, in recent years the advent of several successful radiolabelling techniques have allowed for access to these fluoro-arenes.[29] The use of spirocyclic hypervalent iodonium ylides (SCIDY) as precursors for ¹⁸F-arenes have demonstrated high reactivity and regioselectivity toward the radiofluorinated arene, metal-free radiofluorination conditions, a broad substrate scope, and thermally stable precursors under appropriate storage conditions.[30,31] Additionally, copper-mediated ¹⁸F-labelling of boronic acid, boronic ester, and arylstannane precursors have also had significant success in the labelling of non-activated arenes and could serve as alternative labelling strategies for fragments of this class. A total of 32 fragments were synthesized or obtained commercially for this class with two subtypes accounting for half of the fragment count.

The fragments corresponding to the first subtype of class B closely resemble those from the subtype within class A with the primary difference being that the amide direction was reversed. This small yet distinct structural alteration results in removal of the EWG thereby rendering ¹⁸F-labelling via S_NAr likely unsuccessful. The ¹⁹F-containing fragments of this subtype were synthesized from commercially available 4-fluorobenzylamine (**5**), which was coupled to a diverse series of free carboxylic acids using either HATU/DIPEA or EDC/DMAP/DIPEA coupling conditions to produce

amides **6a-k** (Scheme 5.2). In early reports, these types of molecules were labelled with fluoride-18 via S$_N$Ar by synthesizing a suitable trimethylammonium triflate salt precursor with a cyano EWG in the appropriate position.[32] The cyano group could then be reduced to a primary amine and subsequently coupled to the rest of the molecule. However, as this would add several steps to the radiolabelling procedure, it is advantageous to pursue a more direct labelling method, such as the ones discussed for this fragment class, which is why this subtype was stratified into class B.

Scheme 5.2. Synthesis of subtype 1 of class B fragments **[^{19}F]6a-l** from 4-fluorobenzylamine **5** and proposed radiosynthesis of identical fragments **[^{18}F]6a-l** from precursor **7**.
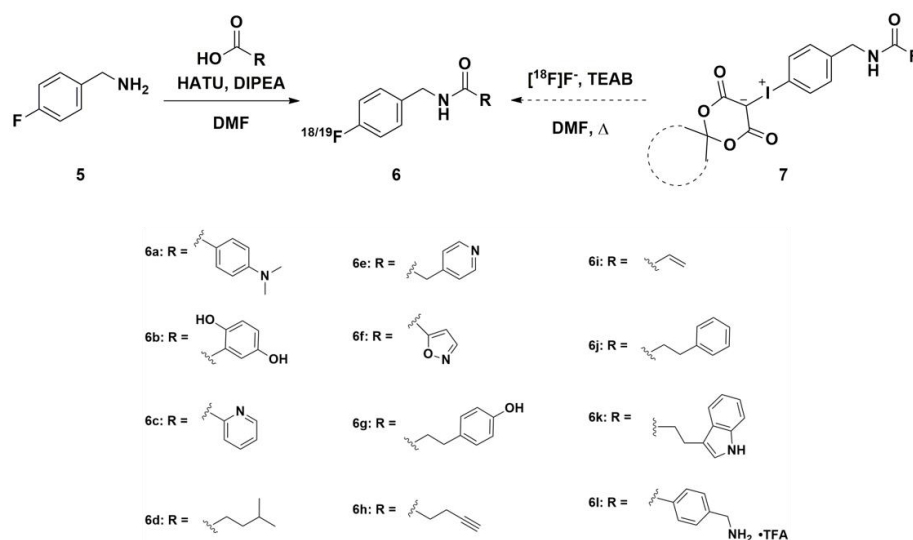
The synthesis of fragment **6l** was slightly altered from scheme 5.2. A competing reactive primary amine within the R group of the carboxylate moiety needed to first be protected as shown in scheme 5.3 to give compound **9** in order to prevent self-coupling. Boc-protected **9** was then coupled to compound **5** in the same fashion as the other class B fragments of this subtype and the Boc group was subsequently cleaved to give fragment **6l** as a TFA salt.

Scheme 5.3. Synthesis of class B fragment **[¹⁹F]6l** through Boc-protection of acid **8** and subsequent deprotection after coupling.
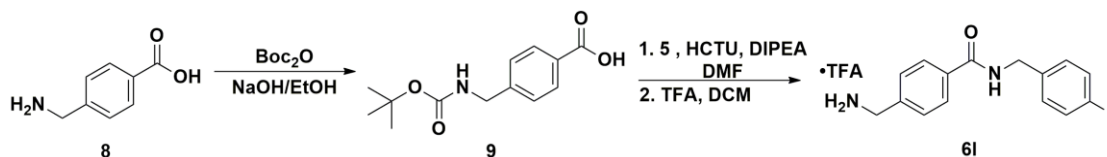
A common method for the conjugation of ¹⁸F-containing moieties to biomolecules is the copper-catalyzed azide-alkyne cycloaddition (CuAAC), where a 1,3-dipolar cycloaddition between an azide and a terminal alkyne takes place in the presence of Cu(I) catalyst to reveal a 1,2,3-triazole.[33] A pivotal publication by Sharpless *et al.* first described the catalysis of this reaction and gave it the widely recognized name of 'click chemistry'.[34] In the context of using this reaction for ¹⁸F radiochemistry, click reactions such as CuAAC are widely applicable to many types of molecules ranging from small molecules to macromolecules, such as oligonucleotides, due to its orthogonal nature.[35] Additional protecting groups are generally not required and this type of reaction, as well as its products, must be insensitive to water and oxygen in order to be ideal for use in biological systems.[36] As such, the second subtype found in class B was designed to be assembled through CuAAC as shown in scheme 5.4. The fluorine-containing azide, 4-fluorobenzyl azide, has been successfully labelled with fluoride-18 via a SCIDY precursor and could then be subsequently reacted with alkynes bearing a diversifying R group to complete the molecule.[35] The ¹⁹F-containing fragments of this subtype were synthesized by reacting commercially available 4-fluorobenzyl bromide precursor (**10**) with NaN₃ to produce 4-fluorobenzyl azide (**11**), which was then clicked to four diversifying alkynes under copper-catalyzed conditions to produce fragments **12a-d**.

Scheme 5.4. Synthesis of subtype 2 of class B fragments **[¹⁹F]12a-d** through CuAAC between compound **11** and terminal alkynes. Corresponding ¹⁸F-labeled fragments may be produced from precursor **13**.
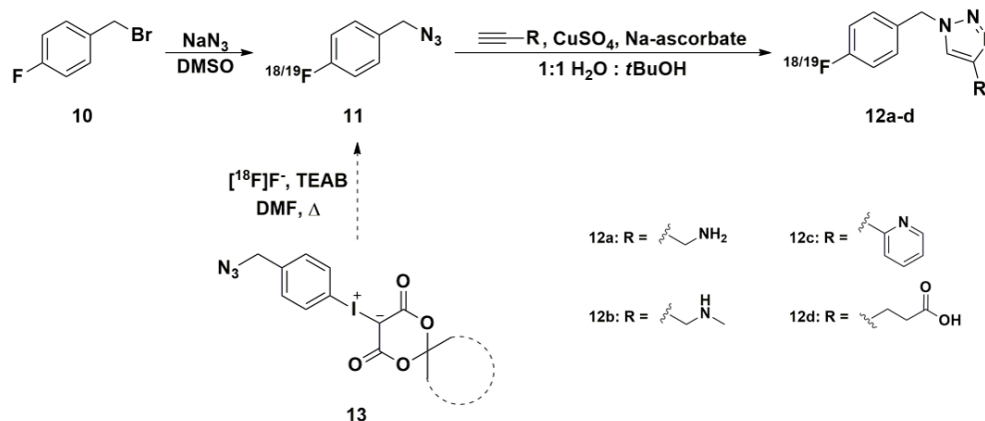
Class C fragments were designed to be radiolabeled through S_N2 nucleophilic aliphatic substitution. Following the requirements for an efficient S_N2 reaction, a suitable alcohol was converted to a tosylate to form a better leaving, which can be subsequently fluorinated with fluoride-18 or fluoride-19. However, the risk of competing elimination reactions occurring under the elevated and basic conditions typically required in radiofluorination reactions is a concern that may limit radioactive product yields.[37] Seven fragments were synthesized or commercially obtained for this class with four belonging to a certain subtype.

Similar to the second subtype found in class B, a subtype in class C was also designed to be assembled through CuAAC. However, since the azide moiety is labelled with fluoride-18/19 through an S_N2 mechanism (Scheme 5.5), this subtype of fragments was stratified into class C of this library. Azide **26** was synthesized as shown in scheme 5.5 from 4-bromophenol **13**, which was first extended to compound **14** using 3-bromo-1-propanol under increased temperatures of 70 ˚C. The aromatic bromine was replaced with an azide for the upcoming click reaction and the primary alcohol on compound **15** was tosylated in preparation for fluorination. Both fluorination and the CuAAC reaction of compound **16** were performed in one-pot where ¹⁹F-fluorination was first carried out using TBAF at temperatures of 100 ˚C. Upon cooling of the reaction mixture, the cycloaddition took

place mediated by CuSO$_4$ and sodium ascorbate, to produce fragments, **22a-d**. Within the entire fluorine-containing fragment library, 62 fragments across classes A-C were synthesized or obtained and prepared for screening against the biological target, GHSR.

Scheme 5.5. Synthesis of a subtype of class C fragments **[^{19}F]17a-d** through one-pot fluorination and CuAAC of azide **16** with a terminal alkyne.
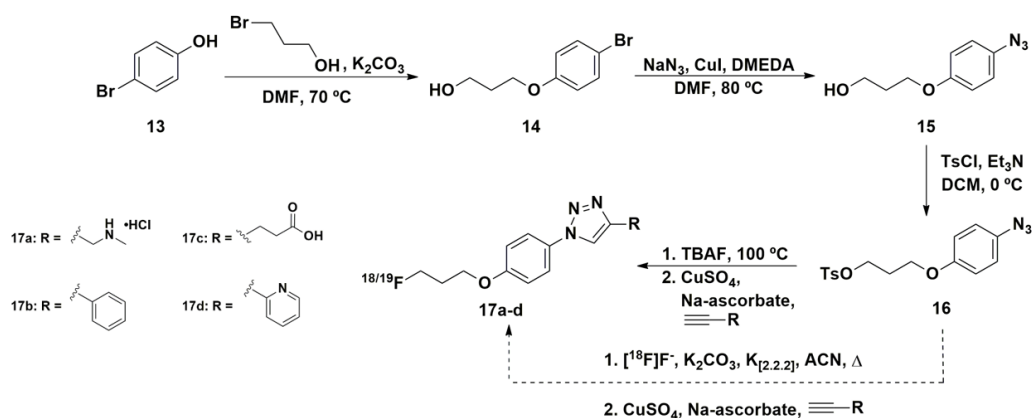
5.2.2 Fragment Screening and Hit Validation

The fluorine-containing fragment library was screened for binding against the GHSR target by means of a cell-based radioligand-displacement binding assay. The assay was performed using HEK293 cells that were transiently transfected with GHSR-eYFP, and human [^{125}I]-ghrelin(1-28) as the radioligand. A ghrelin(1-8) analogue, [Inp[1], Dpr[3](6-FN), 1Nal[4], Thr[8]]ghrelin(1-8) amide (**18**), reported to possess high affinity for the GHSR (IC$_{50}$ = 0.11 nM), was used as a reference to ensure the validity of the assay.[22] The affinity of fragment hits toward the screening target are expected to be quite weak due to their small size. For this reason, it has been well documented that fragment libraries often need to be screened at high concentrations with reports well into the millimolar range.[38] As such, we initially sought to screen fragments at a concentration of 1 mM. Unfortunately, due to the nature of small organic molecules, fragment solubility in an aqueous environment at these concentrations was not achievable for much of the library without large quantities of the organic solvent, DMSO. While DMSO is a relatively well tolerated organic solvent in the presence of cells, it can exhibit cytotoxic effects at high concentrations. A DMSO tolerance experiment showed a significant decrease in cell-bound radioligand in the

presence 3% DMSO or higher, indicating cytotoxicity. However, no significant effect on radioligand detection was observed at concentrations of 1% DMSO or less. Therefore, a final DMSO concentration of up to 1% was permitted in the fragment screen. As a result, the fragment library was screened at a final concentration of 0.5 mM, which was successful for most library members. However, some of the more hydrophobic fragments were unable to meet the DMSO solubility requirements and were, as a result, screened at a lower concentration of 0.05 mM. The degree to which a fragment successfully displaced the ghrelin radioligand is referred to as radioligand inhibition and is expressed as a percentage of a no-fragment-added control (Figure 5.3). Non-specific binding was accounted for by including the reference compound **18** as an additional control, which is known to maximally displace the radioligand at a concentration of 1 µM.[22]
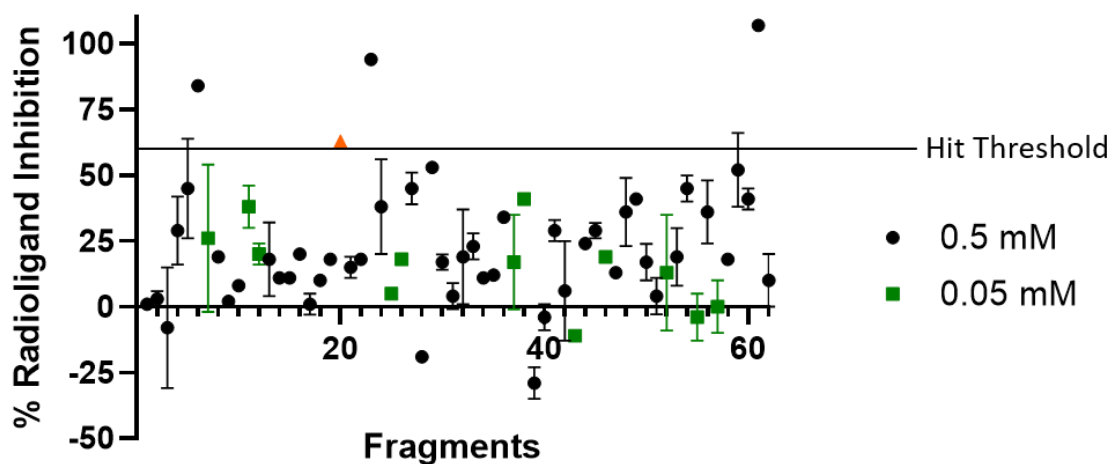
Figure 5.3. Screening the fluorine-containing fragment library against the GHSR via a radioligand-displacement binding assay. Fragments were screened in duplicate either at 0.5 mM (Black closed-circles) or 0.05 mM (Green closed-squares). Hit threshold set to 60% radioligand inhibition. False positive result shown as orange closed-triangle (screened at 0.5 mM).

An inhibition threshold of 60% resulted in the initial identification of 4 fragment hits. However, one hit, shown in figure 5.3 as an orange triangle data-point, displayed insolubility during the screening assay resulting in the observation of a white precipitate

covering the cell pellet. It is possible that the precipitate prevented the radioligand from reaching the binding site of the receptor and was consequently washed away resulting in what appeared to be a hit. False positive results are not uncommon in high concentration screening campaigns; therefore, it is important to acknowledge every abnormal observation. Furthermore, one hit, compound **19**, was included in the library as a biased ligand for the GHSR as it consists of the three *N*-terminal amino acids of the reference compound **18**. The ability for the fragment screening assay to identify this compound as a hit further validates its successful application for screening of this library toward the GHSR.
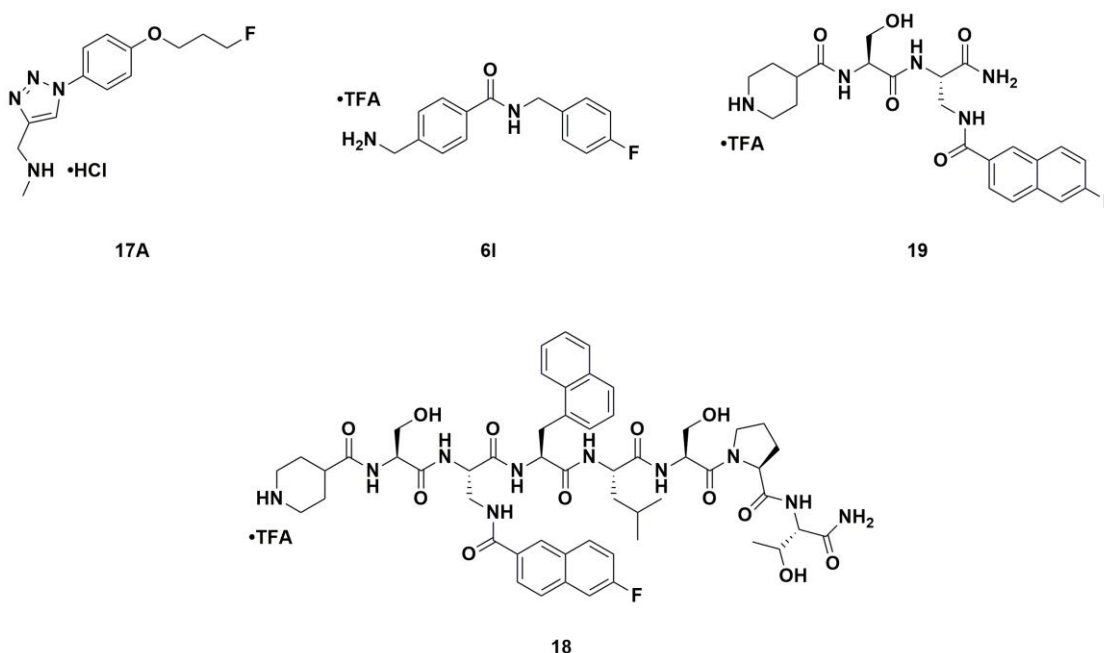
Figure 5.4. Structures of fragment hits **17A** and **6l**, biased ligand **19**, and reference compound **18**.

Therefore, the fragment screened yielded two fragment hits, which corresponds to a hit rate of 3.2% for this library against the GHSR (Figure 5.4). The hit fragments were re-screened in triplicate in at least 6 independent trials to account for any inter-day variability in the sensitivity of the cell-based assay. Compound **17A**, belonging to class C of the fragment library, demonstrated 84 ± 2% radioligand inhibition (n = 8) and compound **6l**, belonging to class B of the fragment library, demonstrated 94 ± 2%

radioligand inhibition (n = 6). Interestingly, both fragment hits possess amino functionality and were screened as salts, which afforded them high solubility in the aqueous assay environment. It has been noted in the literature that the positively charged *N*-terminus of ghrelin participates strongly with the Glu124 residue in the GHSR binding site.[25,39] Therefore, it is possible that these fragments interact with the receptor in a similar manner. However, these two fragments were not the only compounds to bear this functionality in the library; many other fragments included amino groups and were also isolated and screened in the salt form but were not identified as hits. Therefore, other structural characteristics within these hits likely also play a role in their binding mode toward the GHSR. A structure-activity relationship study will need to be performed in the future to elucidate the key binding interactions of these fragment hits with the receptor.

The two fragment hits were then characterized for binding affinity, ligand efficiency, and Ro3 compliance (Table 5.1). Both hits **17A** and **6l** were found to reasonably follow Ro3 guidelines in terms of molecular weight, hydrogen bond donors, and clogP. Only hit **17A** exceeded the stipulated Ro3 limit of hydrogen bond acceptors. The IC_{50} values of **17A** and **6l** were 232 µM and 326 µM, respectively (Figure 5.5), and while these initial binding affinity values are weak relative to known GHSR ligands, they are quite reasonable when compared to other recently identified fragment hits reported in the literature.[3] Ligand efficiency is a commonly reported parameter in drug discovery and is often used as a guiding tool during hit-to-lead optimization.[40] Ligand efficiency (LE) is defined as the Gibbs free energy of binding ($\Delta_B G$) in kcal mol^{-1} divided by the heavy atom count (N), which is expanded in equation 5.1.

$$LE = \frac{-RTln(IC_{50})}{N} \tag{5.1}$$

Equation 5.1 can be simplified into equation 5.2, which effectively summarizes that the logarithmic relationship between binding affinity and the heavy atom count.[41]

$$LE = 1.4\frac{pIC_{50}}{N} \tag{5.2}$$

The ligand efficiency values for hits **17A** and **6l** were 0.27 and 0.26 respectively, which are slightly below the accepted LE value of 0.3, considered to be a suitable starting point

for fragment hit optimization.[40] Further optimization of these fragment hits prior to the fragment elaboration stage may result in higher LE values and increased receptor affinity.

Table 5.1. Characterization of fragment hits **17A** and **6l** for binding affinity (IC$_{50}$), ligand efficiency, and compliance to Ro3 guidelines.

Hit	IC$_{50}$	LE	MW(neutral)	# Hydrogen bond donors	# Hydrogen bond acceptors	cLogP
17A	232 μM	0.27	264.30 g·mol^{-1}	2	5	1.77
6l	326 μM	0.26	258.29 g·mol^{-1}	2	3	1.92
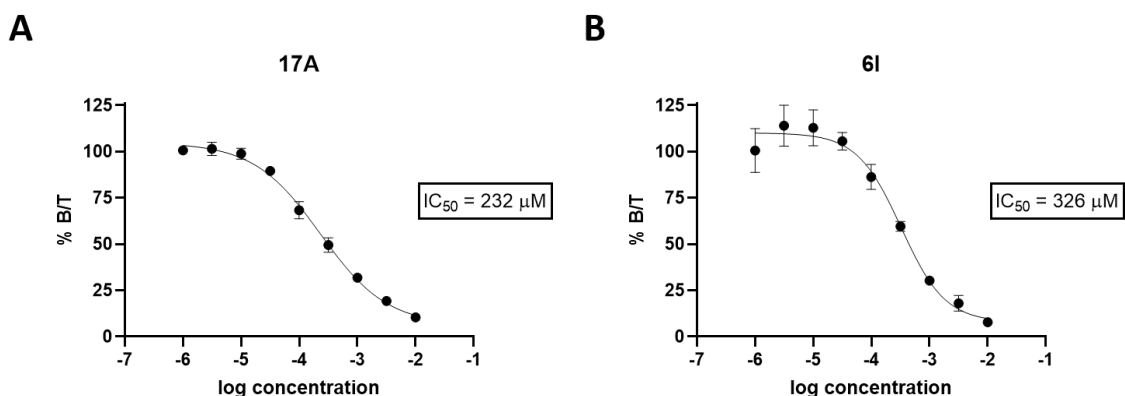
Figure 5.5. IC$_{50}$ curves for fragment hits **17A** (A) and **6l** (B) obtained via competitive radioligand-displacement binding assay in HEK293 GHSR-eYFP cells.

5.3 Conclusions

Fragment-based drug design is now firmly established in the world of drug discovery with four new, targeted drugs discovered by this method and subsequently approved for clinical use. The most noteworthy advantage of the fragment-based methodology is that it allows for a larger proportion of chemical space to be sampled with greater precision, compared to larger molecules involved in a typical HTS campaign. While this technique has been accepted for drug discovery, it has yet to reach the field of molecular imaging. The goal of this project was to apply FBDD towards the direct discovery of ^{18}F-PET imaging agents. A fluorine-containing fragment library of 62 compounds was designed and assembled where each fragment contains fluoride in a position that may be readily

radiolabeled with fluoride-18. While the library developed in this study is relatively small, this focused library is ever growing with goal that more fragments will be added to the fluorine-library catalogue over time.

Each fragment was screened for binding against the GHSR through a radioligand-displacement binding assay. Gratifyingly, two fragment hits were identified as weak GHSR binders from this screening campaign. Hit **17A** was found to bind with an IC_{50} value of 232 µM and hit **6l** was found to bind with an IC_{50} value of 326 µM. Both hits follow Ro3 guidelines and possess similar ligand efficiencies and calculated lipophilicities. They also both possess amino functionality and aromatic moieties, which are structural features known to participate in ligand binding toward the GHSR. A structure-activity relationship (SAR) investigation of each fragment should be carried out to identify and optimize the binding interactions prior to expanding the molecule. This would provide insight into the possible mode of fragment binding and possibly shed light toward the best avenue to pursue for structural expansion. The eventual fragment elaboration step would result in candidate molecules that are inherently fluoride-containing imaging agents where the identical species will then be radiolabeled with fluoride-18 for PET imaging. This work was designed to explore a new chemical technology through the application of fragment-based design, which could ultimately be applied toward any imaging target, not only the GHSR. The resulting candidate molecules that emerge from this research would be the first examples of using a fragment-based approach to directly discover novel molecular imaging agents.

5.4 Experimental

5.4.1 Materials and Methods

All common solvents were obtained from Fisher Scientific. Human [^{125}I]-ghrelin (NEX388010UC) was purchased from Perkin Elmer. All other reagents were purchased from Sigma-Aldrich, Fisher Scientific, or Oakwood Chemicals and were used as received. Analytical UHPLC-MS was performed using a Waters Inc. Acquity UPLC H-class instrument in combination with a Xevo QToF mass spectrometer. A Waters Acquity analytical column (UPLC BEH C18 2.1 x 50 mm, 1.7 µm) was used and the UV

absorbance was detected using a Waters Acquity PDA detector. The solvent system ran gradients of solvent A, 0.1% formic acid in acetonitrile (ACN, Optima grade, Fisher Scientific), and solvent B, 0.1% formic acid in MilliQ water (18.2 mΩ•cm conductivity), at a flow rate of 0.6 mL/min over 3 minutes followed by a wash over 1 minute. Organic reactions were monitored by thin layer chromatography (TLC) using plastic-backed silica gel TLC plates. Flash chromatography was performed using a Biotage® Isolera™ Prime advanced automated flash purification instrument. Biotage SNAP KP-Sil 10 g, 25 g, or 50 g cartridges (50 μm irregular silica) were used with solvent flow rates of 12, 25, or 50 mL/min for each cartridge type respectively along with the gradient solvent system specified. NMR spectra were obtained using an Agilent Mercury VX 400 MHz, Inova 400 MHz, or a Bruker 400 MHz spectrometer. Chemical shifts are referenced to the residual solvent peaks and recorded in parts per million. Mass spectra were determined in positive ion mode using an electrospray ionization (ESI) ion source on a Waters Xevo QToF. Additional experimental information for individual fragment library members including structures, yields, purification conditions, and characterization data is presented in Appendix D.

5.4.2 Fragment Library Synthesis

N-**Succinimidyl 4-fluorobenzoate (2).** CAS: 66134-67-6. 4-Fluorobenzoic acid, **1** (0.207 g, 1.47 mmol) and *N*-hydroxysuccinimide (0.192 g, 1.66 mmol) were dissolved in DMF (10 mL) and stirred for 10 minutes at room temperature. A solution of EDC•HCl (0.281 g, 1.46 mmol) previously dissolved in DMF (10 mL) was added dropwise and the reaction mixture stirred at room temperature for 18 h. The reaction was quenched with water (50 mL) and the product extracted into EtOAc (x3). The organic extracts were washed with brine, dried over $MgSO_4$, and concentrated under reduced pressure. The crude product was purified by automated Isolera flash chromatography using 12-100% EtOAc in hexanes to give **2** as a white powder (0.292 g, 83%). ^{1}H NMR (400 MHz, $CDCl_3$): δ 8.19-8.15 (m, 2H), 7.26-7.17 (m, 2H), 2.91 (s, br 4H). ^{13}C NMR (100 MHz, $CDCl_3$): δ 169.1, 165.6, 133.4, 133.3, 116.4, 116.2, 25.6. HRMS (ESI$^+$): [M+H]$^+$ calculated: 238.0516; [M+H]$^+$ found: 238.0647.

General procedure for compounds 3a-e:

Modified from Bemis and Vu[42], **2** (1 eq.) was dissolved in DCM followed by the addition of the corresponding amine (2 eq.) and triethylamine (9 eq.). After stirring 18 h, the reaction mixture was diluted with H_2O and the product was extracted into DCM (x3). The organic layer was dried over $MgSO_4$ and concentrated under reduced pressure. The crude product was purified by automated Isolera flash chromatography to give the amide products, **3a-e**.

General procedure for compounds 3f-i:

Adjusted from Monnard *et al.*[43], the required amine (2 eq) was dissolved in a 2:1 H_2O : acetone solvent mixture followed by the addition of KH_2PO_4 (1.1 eq.) and **2** (1 eq.). The reaction mixture stirred 18 h and the acetone was then removed under reduced pressure. The product was extracted into DCM (x3), dried over $MgSO_4$, and concentrated under reduced pressure. The crude product was purified by automated Isolera flash chromatography to give the amide products **3f-g** and boc-protected intermediates toward fragments **3h-i**.

General procedure for compounds 3k-l:

Following the procedure by Horatscheck *et al*[44] with minor alterations, compound **2** (1 eq.) was dissolved in a 3:1 H_2O : THF solvent mixture followed by the addition of the corresponding amine (2 eq.) and Na_2CO_3 (3 eq.). The reaction mixture stirred 18 h at room temperature then was quenched with EtOAc and sat. $NaHCO_3$(aq). The aqueous phase was separated, washed twice with EtOAc, and then acidified with 5% (v/v) HCl(aq) until precipitation was observed. The precipitate was extracted into EtOAc (x3) and washed with brine. The organic layer was dried over $MgSO_4$ and concentrated under reduced. The crude product was then purified by automated Isolera flash chromatography to give the desired amide products **3k-l**.

General procedure for compounds 3m-o:

Compound **2** (1 eq.) was dissolved in DMF and the corresponding amine (2 eq.) was added followed by DIPEA (9 eq.). The reaction mixture stirred at room temperature for 18 h and then was diluted with water and extracted into EtOAc (x3). The organic layer was washed with brine, dried over MgSO$_4$, and concentrated under reduced pressure. The crude product was then purified by automated Isolera flash chromatography to give the desired amide products **3n-o** and the boc-protected intermediate toward fragment **3m**.

Boc deprotection for compounds 3h-3j, 3m:

The Boc-protected intermediates were dissolved in EtOAc (5 mL) and the Boc groups were cleaved by adding 4 M HCl in dioxanes (2 mL) dropwise. The reactions stirred 18 h at room temperature then were concentrated under reduced pressure and residual acid was removed with co-evaporation with DCM to reveal the hydrochloride salts **3h-j, 3m**.

4-(Dimethylamino)-*N*-(4-fluorobenzyl)benzamide (6a). CAS: 1181040-77-6. 4-Dimethylaminobenzoyl chloride (0.0510 g, 0.278 mmol) was dissolved in DCM and cooled to 0 ˚C. 4-fluorobenzylamine **5** (80 µL, 0.70 mmol) was added dropwise and the solution stirred at 0 ˚C for 45 min before allowing it to warm to room temperature and stir another 2.5 h. The reaction was quenched with water and extracted into DCM (x3). The organic extracts were washed with brine, dried over MgSO$_4$, and concentrated under reduced pressure. The crude product was purified by automated Isolera flash chromatography using 12-100% EtOAc in hexanes to give **6a** as a white powder (0.063 g, 84%).

General procedure for compounds 6b-f:

The required carboxylic acid (1.5 eq) was dissolved in DMF followed by the addition of **5** (1 eq.), DIPEA (3 eq.), and HATU (1.1 eq.). The reaction mixture stirred 3 h at room temperature prior to being diluted with water and extracted into EtOAc (x3). The organic layer was washed with brine, dried over MgSO$_4$, and concentrated under reduced pressure. The crude product was purified by automated Isolera flash chromatography to give the corresponding amide products **6b-f**.

General procedure for compounds 6g-k:

The required carboxylic acid (1.2 eq.) was dissolved in DMF followed by the addition of **5** (1 eq.), EDC•HCl (1.3 eq.), DMAP (0.2 eq.), and DIPEA (2.5 eq.). The reaction mixture stirred 18 h at room temperature prior to being diluted with water and extracted into EtOAc (x3). The organic layer was washed with brine, dried over MgSO₄, and concentrated under reduced pressure. The crude product was purified by automated Isolera flash chromatography to give the corresponding amide products **6g-k**.

4-(((*tert*-Butoxycarbonyl)amino)methyl)benzoic acid (9). CAS: 33233-67-9. Prepared according to the protocol reported by Madden *et al*[45] from 4-aminomethylbenzoic acid, **8** (0.204 g, 1.35 mmol). Compound **9** was obtained as a white solid (0.218 g, 64%). ^{1}H NMR (400 MHz, CDCl₃): δ 8.03 (d, *J = 8.4 Hz*, 2H), 7.35 (d, *J = 8.4 Hz*, 2H), 4.90 (br s, 1H), 4.36 (d, *J =5.2 Hz*, 2H), 1.43 (s, 9H). ^{13}C NMR (100 MHz, MeOD-*d₄*): δ 168.3, 157.2, 145.1, 129.5, 129.2, 126.6, 78.9, 43.3, 27.3. HRMS (ESI⁺): [M+H]⁺ calculated: 252.1236; [M+H]⁺ found: 252.1922.

4-(Aminomethyl)-*N*-(4-fluorobenzyl)benzamide (6l). Compound **9** (0.134 g, 0.532 mmol) was dissolved in DMF and HCTU (0.890, 2.15 mmol) was added followed by DIPEA (372 µL, 2.13 mmol) and compound **5** (182 µL, 1.59 mmol). The reaction mixture stirred 18 h at room temperature prior to being diluted with water. The resulting beige precipitate was filtered *in vacuo* and purified by automated Isolera flash chromatography (5-40% hexanes in EtOAc) to produce a white powder. The compound was then Boc-deprotected by dissolving in DCM and adding TFA (0.5 mL) slowly dropwise. The mixture stirred at room temperature for 1 h before the solvent and excess TFA were removed under reduced pressure co-evaporating with DCM to reveal the final product, **6l** as a TFA salt (0.184 g, 93%).

4-Fluorobenzyl azide (11). CAS: 159979-96-1. 4-Fluorobenzyl bromide **10** (1.0 mL, 8.02 mmol) was dissolved in anhydrous DMSO followed by the addition of NaN₃ (0.817 g, 12.5 mmol). The reaction mixture stirred 18 h at room temperature and then was cooled to 0 ˚C prior to being quenched with water. The product was extracted into EtOAc (x3) and the organic layer was washed with brine, dried over MgSO₄, and concentrated

under reduced pressure. The crude product was purified by automated Isolera flash chromatography 2-20% EtOAc in hexanes to reveal **11** as a colourless oil (1.27 g, 93%). ^{1}H NMR (400 MHz, CDCl$_3$): δ 7.31-7.28 (m, 2H), 7.10-7.05 (m, 2H), 4.32 (s, 2H). ^{13}C NMR (100 MHz, CDCl$_3$): δ 161.4, 131.2, 130.0, 115.9, 54.0.

General procedure for compounds 12a-c:

Compound **11** (1 eq.) was dissolved in a solution of water and *tert*-butanol (1:1 v/v). The appropriate terminal alkyne (1 eq.), CuSO$_4$•H$_2$O (0.2 eq.), and *L*-ascorbic acid (0.2 eq.) were added and the mixture stirred 18 h at room temperature. The solution was then diluted with sat. EDTA(aq) and extracted with CHCl$_3$. The first organic extract was discarded and 2 M NaOH(aq) was added until a white precipitate formed. The precipitate was extracted into CHCl$_3$ (x3), dried over MgSO$_4$, and concentrated under reduced pressure. The crude product was purified by automated Isolera flash chromatography to give **12a-c**.

3-(1-(4-Fluorobenzyl)-1*H*-1,2,3-triazol-4-yl)propanoic acid (12d). CAS: 1929770-04-6. Compound **11** (0.181 g, 1.20 mmol) was dissolved in a solution of DCM and methanol (1:1 v/v). 4-pentynoic acid (0.242 g, 2.47 mmol), CuI (0.054 g, 0.29 mmol), and triethylamine (0.45 mL, 3.2 mmol) were added and the reaction mixture stirred 18 h at room temperature. The solvent was removed under reduced pressure and the resulting oil was re-suspended in sat. EDTA(aq). The product was extracted into CHCl$_3$ (x3), dried over MgSO$_4$, and concentrated under reduced pressure. The crude product was purified by automated Isolera flash chromatography using 2-20% MeOH in CHCl$_3$ to give **12d** (0.046 g, 15%).

3-(4-Bromophenoxy)propan-1-ol (14). CAS: 67900-64-5. Prepared from compound **13** (3.90 g, 22.5 mmol) according to the protocol reported by Sirion *et al*[46]. The crude product was purified by automated Isolera flash chromatography using 7-60% EtOAc in hexanes to give **14** (4.49 g, 86%). ^{1}H NMR (400 MHz, CDCl$_3$): δ 7.36 (d, *J = 4.8 Hz*, 2H), 6.78 (d, *J = 4.8 Hz*, 2H), 4.08 (t, *J = 6 Hz*, 2H), 3.85 (t, *J = 5.6, 6 Hz*, 2H), 2.06-2.00 (m, 2H), 1.77 (s, br, 1H). ^{13}C NMR (100 MHz, CDCl$_3$): δ 157.9, 132.3, 116.3, 113.0, 65.8, 60.2, 31.9. HRMS (ESI[+]): [M+H][+] calculated: 231.0021; [M+H][+] found: 231.9996.

3-(4-Azidophenoxy)propan-1-ol (15). CAS: 943726-03-2. Prepared from compound **14** (2.45 g, 10.6 mmol) according to the protocol reported by Sirion *et al*[46]. The crude product was purified by automated Isolera flash chromatography using 7-60% EtOAc in hexanes to give **15** (1.82 g, 89%). ^{1}H NMR (400 MHz, CDCl$_3$): δ 6.98-6.90 (m, 4H), 4.11 (t, *J = 6 Hz*, 2H), 3.87 (t, *J = 6, 5.6 Hz*, 2H), 2.07-2.04 (m, 2H), 1.92 (s, br, 1H). ^{13}C NMR (100 MHz, CDCl$_3$): δ 156.2, 132.5, 120.0, 115.7, 66.0, 60.2, 32.0. HRMS (ESI$^+$): [M+H]$^+$ calculated: 194.0930; [M+H]$^+$ found: 194.0964.

3-(4-Azidophenoxy)propyl 4-methylbenzenesulfonate (16). CAS: 2077985-46-5. Compound **15** (1.780, 9.21 mmol) was dissolved in anhydrous DCM and cooled to 0 ˚C. Triethylamine (4.02 mL, 28.8 mmol) and DMAP (0.111 g, 0.908 mmol) were added followed by dropwise addition of *p*-toluenesulfonyl chloride (3.515 g, 18.5 mmol) in DCM. The reaction mixture stirred 3 h at room temperature prior to being quenched with 10% HCl(aq) and extracted into DCM (x3). The organic extracts were washed with brine, dried over MgSO$_4$, and concentrated under reduced pressure. The crude product was purified by automated Isolera flash chromatography using 5-40% EtOAc in hexanes to give **16** (2.98 g, 93%). %). ^{1}H NMR (400 MHz, CDCl$_3$): δ 7.77 (d, *J = 8 Hz*, 1H), 7.28 (d, *J = 8 Hz*, 1H), 6.93 (d, *J = 8.8 Hz*, 1H), 6.77 (d, *J = 8.8 Hz*, 1H), 4.25 (t, *J = 6 Hz*, 2H), 3.94 (t, *J = 6 Hz*, 2H), 2.13 (quintet, *J = 6 Hz*, 2H). ^{13}C NMR (100 MHz, CDCl$_3$): δ 155.8, 144.8, 132.8, 132.6, 129.8, 127.8, 119.9, 115.6, 66.9, 63.5, 28.9, 21.6. HRMS (ESI$^+$): [M+H]$^+$ calculated: 348.1018; [M+H]$^+$ found: 348.1032.

General procedure for compounds 17a-d:

Under a nitrogen atmosphere, compound **16** (1 eq.) was suspended in *t*BuOH. A solution of TBAF (1 M in THF) (2 eq.) was added and the reaction stirred at 100 ˚C for 1 h. The mixture was cooled to room temperature and the appropriate terminal alkyne (2.0 eq.) was added followed by CuSO$_4$•H$_2$O (0.2 eq.), sodium ascorbate (0.3 eq.), and water. The reaction stirred for 18 h and was subsequently diluted with water and extracted into EtOAc (x3). The organic extracts were washed with brine, dried over MgSO$_4$, and concentrated under reduced pressure. The crude products were purified by automated Isolera flash chromatography to give **17a-d**.

5.4.3 Fragment Screen

Fragments were screened for binding toward the GHSR using a competitive radioligand-displacement binding assay human [^{125}I]-ghrelin(1-28) (PerkinElmer Inc., cat. NEX388010UC) as the radioligand. HEK293 cells were transiently transfected with GHSR-eYFP using XtremeGENE^{TM} 9 DNA transfection agent (Sigma-Aldrich, cat. 06365787001) according to the manufacturer's protocol over 48 hours prior to being frozen at 2 million cells per vial in 10% DMSO in FBS. A frozen aliquot of cells were thawed, centrifuged (3,000 rpm, 10 min, room temperature), and the cell pellet was resuspended in binding buffer (25 mM HEPES, 5 mM magnesium chloride, 2.5 mM EDTA, 1 mM calcium chloride, and 0.4% BSA, pH = 7.4). A suspension of cells (100,000 cells per assay tube) were incubated at 37 °C with fragments (in duplicate at a single concentration of either 0.5 mM or 50 µM), or reference compound **18**, and [^{125}I]-ghrelin (15 pM per assay tube) in 1% DMSO and binding buffer for 20 minutes with agitation. The tubes were then centrifuged at 13,000 g for 5 min and unbound [^{125}I]-ghrelin was removed in the supernatant. The cell pellets were then washed with 500 µL of ice-cold TRIS-HCl buffer (50 mM, pH = 7.4) and centrifuged again at 13,000 g for 5 min. The quantity of [^{125}I]-ghrelin bound to the cell membranes was measured by gamma counter. The resulting counts (cpm) from the reference compound were subtracted from the resulting counts from all other samples. The counts from each fragment was then compared to control samples containing only radioligand and cell membranes in binding buffer. A greater than 60% reduction in counts compared to the control was considered a positive result, which identified a fragment hit.

5.4.4 Competitive Radioligand-Displacement Binding Assay

The binding affinity of fragment hits **17A** and **6l** were determined using a similar radioligand-displacement binding assay protocol as that used for the fragment screen. Assays were performed using HEK293 cells transiently transfected with GHSR-eYFP as the receptor source and human [^{125}I]-ghrelin(1-28) (PerkinElmer Inc., cat. NEX388010UC) as the radioligand. In triplicate, a suspension of cells (100,000 cells per assay tube) were incubated at 37 °C with varying concentrations of each fragment (concentrations from 10^{-2} M-10^{-6} M in half-log steps) and [^{125}I]-ghrelin (15 pM per assay

tube) in binding buffer (25 mM HEPES, 5 mM magnesium chloride, 2.5 mM EDTA, 1 mM calcium chloride, and 0.4% BSA, pH = 7.4) for 20 minutes with agitation at 550 rpm. The tubes were then centrifuged at 13,000 g for 5 min and unbound [^{125}I]-ghrelin was removed in the supernatant. The cell pellets were then washed with 500 μL of ice-cold TRIS-HCl buffer (50 mM, pH = 7.4) and centrifuged again at 13,000 g for 5 min. The quantity of [^{125}I]-ghrelin bound to the cell membranes was measured by gamma counter. IC$_{50}$ values were determined by non-linear regression analysis to fit a four-parameter dose-response curve using GraphPad Prism$^{®}$ 6 version 6.0c.

5.5   References

1   C. W. Murray and D. C. Rees, *Nat. Chem.*, 2009, **1**, 187–192.

2   M. Congreve, R. Carr, C. Murray and H. Jhoti, *Drug Discov. Today*, 2003, **8**, 876–877.

3   W. Jahnke, D. A. Erlanson, I. J. P. De Esch, C. N. Johnson, P. N. Mortenson, Y. Ochi and T. Urushima, *J. Med. Chem.*, 2020, **63**, 15494–15507.

4   G. Bollag, J. Tsai, J. Zhang, C. Zhang, P. Ibrahim, K. Nolop and P. Hirth, *Nat. Rev. Drug Discov.*, 2012, **11**, 873–886.

5   S. Cang, C. Iragavarapu, J. Savooji, Y. Song and D. Liu, *J. Hematol. Oncol.*, 2015, **8**, 1–8.

6   W. D. Tap, Z. A. Wainberg, S. P. Anthony, P. N. Ibrahim, C. Zhang, J. H. Healey, B. Chmielowski, A. P. Staddon, A. L. Cohn, G. I. Shapiro, V. L. Keedy, A. S. Singh, I. Puzanov, E. L. Kwak, A. J. Wagner, D. D. Von Hoff, G. J. Weiss, R. K. Ramanathan, J. Zhang, G. Habets, Y. Zhang, E. A. Burton, G. Visor, L. Sanftner, P. Severson, H. Nguyen, M. J. Kim, A. Marimuthu, G. Tsang, R. Shellooe, C. Gee, B. L. West, P. Hirth, K. Nolop, M. van de Rijn, H. H. Hsu, C. Peterfy, P. S. Lin, S. Tong-Starksen and G. Bollag, *N. Engl. J. Med.*, 2015, **373**, 428–437.

7   C. W. Murray, D. R. Newell and P. Angibaud, *Medchemcomm*, 2019, **10**, 1509–1511.

8   A. Lawson, *Curr. Top. Med. Chem.*, 2015, **15**, 2523–2527.

9   E. Szollosi, A. Bobok, L. Kiss, M. Vass, D. Kurk, S. Kolok, A. Visegrady and G. M. Keseru, *Bioorganic Med. Chem.*, 2015, **23**, 3991–3999.

10   S. P. Andrews, G. A. Brown and J. A. Christopher, *ChemMedChem*, 2014, **9**, 256–275.

11   M. Congreve, A. S. Doré, A. Jazayeri and R. Nonoo, in *Multifaceted Roles of Crystallography in Modern Drug Discovery*, Springer Netherlands, 2015, pp. 1–18.

12   G. Yuan, N. G. Gedeon, T. C. Jankins and G. B. Jones, *Expert Opin. Drug Discov.*, 2015, **10**, 63–80.

13   S. Gnanapavan, B. Kola, S. Bustin, D. Morris, P. McGee, P. Fairclough, S. Bhattacharya, R. Carpenter, A. Grossman and M. Korbonits, *J. Clin. Endocrinol. Metab.*, 2002, **87**, 2988–2991.

14   B. Ueberberg, N. Unger, W. Saeger, K. Mann and S. Petersenn, *Horm. Metab. Res.*, 2009, **41**, 814–821.

15   Y. Lv, T. Liang, G. Wang and Z. Li, *Biosci. Rep.*, 2018, **38**, 1–13.

16   T. D. Müller, R. Nogueiras, M. L. Andermann, Z. B. Andrews, S. D. Anker, J. Argente, R. L. Batterham, S. C. Benoit, C. Y. Bowers, F. Broglio, F. F. Casanueva, D. D'Alessio, I. Depoortere, A. Geliebter, E. Ghigo, P. A. Cole, M. Cowley, D. E. Cummings, A. Dagher, S. Diano, S. L. Dickson, C. Diéguez, R. Granata, H. J. Grill, K. Grove, K. M. Habegger, K. Heppner, M. L. Heiman, L. Holsen, B. Holst, A. Inui, J. O. Jansson, H. Kirchner, M. Korbonits, B. Laferrère, C. W. LeRoux, M. Lopez, S. Morin, M. Nakazato, R. Nass, D. Perez-Tilve, P. T. Pfluger, T. W. Schwartz, R. J. Seeley, M. Sleeman, Y. Sun, L. Sussel, J. Tong, M. O. Thorner, A. J. van der Lely, L. H. T. van der Ploeg, J. M. Zigman, M. Kojima, K. Kangawa, R. G. Smith, T. Horvath and M. H. Tschöp, *Mol. Metab.*, 2015, **4**, 437–460.

17   P. L. Jeffery, A. C. Herington and L. K. Chopin, *J. Endocrinol.*, 2002, **172**, R7–R11.

18   F. Lanfranco, M. Baldi, P. Cassoni, M. Bosco, C. Ghé and G. Muccioli, *Vitam. Horm.*, 2007, **77**, 301–324.

19   T. C. Lin and M. Hsiao, *Biochim. Biophys. Acta*, 2017, **1868**, 51–57.

20   M. D. Childs and L. G. Luyt, *Mol. Imaging*, 2020, **19**, 1–15.

21   D. Rosita, M. A. Dewit and L. G. Luyt, *J. Med. Chem.*, 2009, **52**, 2196–2203.

22   C. L. Charron, J. Hou, M. S. McFarland, S. Dhanvantari, M. S. Kovacs and L. G.

Luyt, *J. Med. Chem.*, 2017, **60**, 7256–7266.

23 K. O. Cameron, S. K. Bhattacharya and A. K. Loomis, *J. Med. Chem.*, 2014, **57**, 8671–8691.

24 J. Rudolph, W. P. Esler, S. O'Connor, P. D. G. Coish, P. L. Wickens, M. Brands, D. E. Bierer, B. T. Bloomquist, G. Bondar, L. Chen, C.-Y. Chuang, T. H. Claus, Z. Fathi, W. Fu, U. R. Khire, J. A. Kristie, X.-G. Liu, D. B. Lowe, A. McClure, M. Michels, A. A. Ortiz, P. D. Ramsden, R. W. Schoenleber, T. E. Shelekhin, A. Vakalopoulos, W. Tang, L. Wang, L. Yi, S. J. Gardell, J. N. Livingston, L. J. Sweet and W. H. Bullock, *J. Med. Chem.*, 2007, **50**, 5202–5216.

25 J. Hou, C. L. Charron, M. M. Fowkes and L. G. Luyt, *Eur. J. Med. Chem.*, 2016, **123**, 822–833.

26 G. Ferré, M. Louet, O. Saurel, B. Delort, G. Czaplicki, C. M'Kadmi, M. Damian, P. Renault, S. Cantel, L. Gavara, P. Demange, J. Marie, J. A. Fehrentz, N. Floquet, A. Milon and J. L. Banères, *Proc. Natl. Acad. Sci. U. S. A.*, 2019, **116**, 17525–17530.

27 Y. Shiimura, S. Horita, A. Hamamoto, H. Asada, K. Hirata, M. Tanaka, K. Mori, T. Uemura, T. Kobayashi, S. Iwata and M. Kojima, *Nat. Commun.*, 2020, **11**, 1–9.

28 G. Vaidyanathan and M. R. Zalutsky, *Nat. Protoc.*, 2006, **1**, 1655–1661.

29 X. Deng, J. Rong, L. Wang, N. Vasdev, L. Zhang, L. Josephson and S. H. Liang, *Angew. Chemie - Int. Ed.*, 2019, **58**, 2580–2605.

30 B. H. Rotstein, N. a Stephenson, N. Vasdev and S. H. Liang, *Nat. Commun.*, 2014, **5**, 4365.

31 B. H. Rotstein, L. Wang, R. Y. Liu, J. Patteson, E. E. Kwan, N. Vasdev and S. H. Liang, *Chem. Sci.*, 2016, **7**, 4407–4417.

32 I. Koslowsky, J. Mercer and F. Wuest, *Org. Biomol. Chem.*, 2010, **8**, 4730–4735.

33 J.-P. Meyer, P. Adumeau, J. S. Lewis and B. M. Zeglis, *Bioconjug. Chem.*, 2016, **27**, 2791–2807.

34 V. V Rostovtsev, L. G. Green, V. V Fokin and K. B. Sharpless, *Angew. Chemie - Int. Ed.*, 2002, **41**, 2596–2599.

35 L. Wang, O. Jacobson, D. Avdic, B. H. Rotstein, I. D. Weiss, L. Collier, X. Chen, N. Vasdev and S. H. Liang, *Angew. Chemie - Int. Ed.*, 2015, **54**, 12777–12781.

36   H. C. Kolb, M. G. Finn and K. B. Sharpless, *Angew. Chemie - Int. Ed.*, 2001, **40**, 2004–2021.

37   H. H. Coenen, in *PET Chemistry*, 2007, pp. 15–50.

38   A. Visegrády and G. M. Keserű, *Expert Opin. Drug Discov.*, 2013, **8**, 811–820.

39   B. Holst, T. M. Frimurer, J. Mokrosinski, T. Halkjaer, K. B. Cullberg, C. R. Underwood and T. W. Schwartz, *Mol. Pharmacol.*, 2009, **75**, 44–59.

40   P. Kirsch, A. M. Hartman, A. K. H. Hirsch and M. Empting, *Molecules*, 2019, **24**, 4309.

41   M. D. Shultz, *Bioorg. Med. Chem. Lett.*, 2013, **23**, 5980–5991.

42   EP002388263A1, 2011.

43   F. W. Monnard, T. Heinisch, E. S. Nogueira, T. Schirmer and T. R. Ward, *Chem. Commun.*, 2011, **47**, 8238–8240.

44   A. Horatscheck, S. Wagner, J. Ortwein, B. G. Kim, M. Lisurek, S. Beligny, A. Schütz and J. Rademann, *Angew. Chemie - Int. Ed.*, 2012, **51**, 9441–9447.

45   2010020556, 2010.

46   U. Sirion, H. J. Kim, J. H. Lee, J. W. Seo, B. S. Lee, S. J. Lee, S. J. Oh and D. Y. Chi, *Tetrahedron Lett.*, 2007, **48**, 3953–3957.

Chapter 6

6   Conclusions

Molecular imaging is an interdisciplinary field of study focused on the visualization of biological processes at the molecular and cellular level through minimally invasive modalities. Positron emission tomography (PET) is a highly sensitive imaging modality able to use molecular imaging probes to visualize both normal biological function and disease states. The unparalleled sensitivity and lack of background signal associated with this modality allow molecular imaging probes to be administered at sub-pharmacologic doses, thus significantly reducing the probability of eliciting undesirable side-effects.[1] Targeted molecular imaging incorporates a traceable signalling entity into the structure of a biomarker-targeting molecule, providing the ability to track the physiology of a specific disease state. Fluorine-18 is the most utilized traceable signalling entity due to its favourable half-life, ease of accessibility, and the ever-growing toolbox of synthetic transformations to incorporate it into targeted molecular imaging probes.[2]

The growth hormone secretagogue receptor 1a (GHSR) has been shown to be differentially expressed in multiple types of cancer compared to healthy tissue, making it a potential biomarker for cancer tumour imaging.[3,4] Furthermore, it has shown abnormal expression in cardiac pathology generating interest in imaging the biological processes related to cardiac GHSR.[5–7] In recent years, many ligands have been adopted as the basis for imaging agent development targeting the GHSR.[8] However, few have been successfully labelled with fluoride-18 and even fewer have continued into *in vivo* preclinical animal models. A [^{18}F]G-7039 analogue was developed and assessed preclinically, but unfortunately possessed unfavourable properties including high lipophilicity and relatively weak receptor affinity, resulting in uptake in several off-target tissues.[9] Three quinazolinone derived small molecules have been ^{18}F-labelled with all three probes containing a [^{18}F]fluoroethyl moiety in the same structural position.[10,11] However, when one of these probes was pursued preclinically, it demonstrated evidence of ^{18}F-defluorination indicating potential stability issues of these tracers *in vivo*.[10] Finally, only one ghrelin analogue has been developed and labelled with fluoride-18 with the

primary goal of imaging the GHSR.[12] Unfortunately, insufficient ^{18}F-fluorination of the precursor resulted in poor radiochemical yields of the desired ghrelin(1-8) product. Therefore, there is still an unmet need for ^{18}F-labelled probes for PET imaging of the GHSR.

Chapter 2 addressed the goal of improving ^{18}F-fluorination of bulky, non-activated aromatic prosthetic groups in an effort to access high-affinity ghrelin(1-8) analogues. Attempts to radiolabel the previously developed ghrelin(1-8) analogue, [Inp[1],Dpr[3](^{18}F]6-FN),1Nal[4],Thr[8]]ghrelin(1-8) amide, with fluoride-18 through conventional substitution methods resulted in low radiochemical yields, impractical for use *in vivo*.[12] Therefore, a recently established method using spirocyclic hypervalent iodonium ylide (SCIDY) precursors for ^{18}F-labelling of non-activated aromatic molecules was pursued as an alternative labelling method to improve radiofluorination efficiency.[13] Since aromatic groups appear to be of value for incorporating fluorine into ghrelin(1-8) analogues, an additional peptide bearing a 4'-fluorobiphenyl-4-carboxyl (4'-FBC) group in place of the octanoyl side chain was also investigated in this manner. The application of SCIDY radiochemistry afforded the synthesis of two non-activated aromatic prosthetic groups, [^{18}F]6-fluoro-2-naphthyl ([^{18}F]6-FN) and [^{18}F]4'-FBC in high radiochemical yields, which were subsequently conjugated to the modified ghrelin(1-8) sequence. The improved radiochemical yield of [Inp[1],Dpr[3](^{18}F]6-FN),1Nal[4],Thr[8]]ghrelin(1-8) amide allowed for further *in vitro* evaluation in cell uptake studies as well as initial *in vivo* evaluation through dynamic PET imaging and *ex vivo* biodistribution. Disappointingly, the probe displayed an unfavourable pharmacokinetic profile *in vivo* prompting curiosity into its metabolic stability. Nevertheless, the successful production of two small, ^{18}F-labelled non-activated aromatic prosthetic groups provided synthetic access to two ghrelin-based PET probes and may be applied as imaging moieties for other targeting entities in the future.

The metabolic stability of [Inp[1],Dpr[3](6-FN),1Nal[4],Thr[8]]ghrelin(1-8) amide was explored in chapter 3 through an *in vitro* structure-activity-stability relationship study. First, the stability and metabolite formation of the unlabelled probe in human serum was identified and characterized revealing a metabolic soft-spot between Leu[5] and Ser[6]. Due to the

significant liver uptake of the ^{18}F-labelled probe observed during *in vivo* PET imaging, hepatic stability was also investigated *in vitro* using human liver S9 fraction. Metabolites from this experiment were indicative of degradation from the *C*-terminus of the peptide while also confirming cleavage of the peptide backbone between Leu[5] and Ser[6]. A focused library of ghrelin(1-8) analogues was developed in an effort to improve stability while maintaining the strong binding affinity of this peptide. While substantial structure-activity information exists regarding the *N*-terminal region of ghrelin, little is known regarding the SAR of positions 5 and 6 specifically.[12,14–16] As such, this library also served to provide additional insight into the structural importance of the residues at these positions, while simultaneously investigating stability. The critical nature of *L*-stereochemistry at position 5 was revealed and exploration of the local chemical space at residue 6 as well as the necessity of the hydroxyl group resulted in a new lead candidate. Substitution of Ser[6] with Dpr created a novel ligand with substantial improvement in metabolic stability in both human serum and human liver S9 fraction compared to the parent peptide, and sub-nanomolar GHSR affinity. Future efforts to develop an efficient method to label this peptide with fluoride-18 are required prior to preclinical PET imaging *in vivo*. Still, the identification of this new lead molecule demonstrates the ability to balance desirable ligand properties, such as binding affinity and stability, to produce a more well-rounded candidate molecule.

Due to the success in ^{18}F-labelling of non-activated aromatic prosthetic groups from SCIDY precursors outlined in chapter 2, the attempt to apply this method toward the direct labelling of a quinazolinone-based GHSR ligand was described in chapter 4. A quinazolinone derivative with unprecedented picomolar affinity toward the GHSR was recently reported by Hou et al.[11] Unlike previously described ^{18}F-labelled quinazolinone derivatives, this ligand contains fluorine on a non-activated aromatic ring inaccessible through prosthetic group conjugation. Therefore, a novel synthetic scheme was developed and successfully optimized to access the SCIDY precursor for radiofluorination. Unfortunately, despite numerous attempts, radiofluorination remains an ongoing challenge since the precursor proved to be highly unstable under ^{18}F-labelling reaction conditions. Future endeavours may pursue alternative labelling strategies that use precursors such as boronic acids, boronic esters, or arylstannanes to access the [18]F-

labelled version of this molecule. Both chapters 2 and 4 probed the applicability of SCIDY radiofluorination techniques toward the production of GHSR-targeting PET imaging agents. From this, it appears that SCIDY precursors are highly useful with smaller non-activated aromatic prosthetic groups; but run into substantial challenges with stability in highly complex substrates such as the quinazolinone derivatives. The ligands discussed in this thesis possess the strongest affinities for the GHSR reported to date. Therefore, effective labelling strategies to access these molecules to investigate their utility *in vivo* is of high importance.

While efforts to address challenges in ligand radiolabelling and poor pharmacokinetic profiles of existing ligands are underway, and have been discussed in this thesis, an alternative strategy to imaging agent development is to discover novel targeting entities toward disease biomarkers, such as the GHSR. Drug discovery techniques provide the opportunity to discover new receptor-targeting scaffolds, but few strive to incorporate the signalling source into the targeting entity from inception. Some combinatorial libraries have done this with peptide ligands for ^{18}F-PET by incorporating fluorine-18 prosthetic groups into one-bead-one-compound (OBOC) peptide libraries prior to the screening process.[17,18] Fragment-based drug design (FBDD) is a drug discovery approach that serves to detect new receptor-ligand interactions in small fragment-sized molecules. The small size of fragment library members offer the advantage of being able to screen fewer compounds while still covering a wide scope of chemical space.[19] While fragment-based drug design is well established in the field of drug discovery, it has yet to be applied toward molecular imaging agent development. Chapter 5 explores a novel chemical technology for direct discovery of molecular imaging agents through the application of FBDD, which could ultimately be applied toward any imaging target. A novel fluorine-containing fragment library was designed and assembled where each fragment molecule contains fluorine in a position readily accessible to known ^{18}F-labelling strategies. As a result, receptor-binding molecules would contain the imaging moiety within the targeting entity from the beginning. As a proof-of-concept, this library was screened for binding toward the GHSR resulting in the identification of two fragment hits, which were then validated and found to display high micromolar affinities. More research is required to optimize and elaborate these fragment hits into high-affinity ligands. Such ligands would

represent molecular imaging candidates where imaging was at the forefront of ligand development thereby eliminating post-development re-evaluation to include a signalling entity.

In summary, this thesis highlights the development and optimization of ^{18}F-PET imaging agents targeting the GHSR. The application of SCIDY labelling methods to access bulky, non-activated aromatic prosthetic groups successfully produced two ghrelin-based ^{18}F-PET probes. However, attempts to apply it to a more structurally complex substrate was unsuccessful due to inadequate precursor stability. A poor pharmacokinetic profile of one ghrelin-based probe prompted curiosity into its serum and hepatic metabolic stability. A structure-activity-stability relationship study addressed a metabolic soft-spot while also providing previously unknown insight into the binding interactions at positions 5 and 6 in the peptide sequence. Finally, the conceptual application of FBDD toward the discovery of new ^{18}F-PET imaging agents was put into practice through the development of a fluorine-containing fragment library, which was screened against the GHSR revealing two fragment hits. The application of this technology toward molecular imaging agent discovery could potentially increase the scope of compounds able to effectively target and visualize biomarkers for therapeutic and diagnostic purposes.

6.1 References

1   M. L. James and S. S. Gambhir, *Physiol. Rev.*, 2012, **92**, 897–965.

2   O. Jacobson, D. O. Kiesewetter and X. Chen, *Bioconjug. Chem.*, 2015, **26**, 1–18.

3   C. Lu, M. S. McFarland, R. L. Nesbitt, A. K. Williams, S. Chan, J. Gomez-Lemus, A. M. Autran-Gomez, A. Al-Zahrani, J. L. Chin, J. I. Izawa, L. G. Luyt and J. D. Lewis, *Prostate*, 2012, **72**, 825–833.

4   T. C. Lin and M. Hsiao, *Biochim. Biophys. Acta*, 2017, **1868**, 51–57.

5   A. Beiras-Fernandez, S. Kreth, F. Weis, C. Ledderose, T. Pöttinger, C. Dieguez, A. Beiras and B. Reichart, *Peptides*, 2010, **31**, 2222–2228.

6   Aleksova, Beltrami, Bevilacqua, Padoan, Santon, Biondi, Barbati, Stenner, Gortan Cappellari, Barazzoni, Ziberna, Zwas, Avraham, Agostoni, Not, Livi and Sinagra, *J. Clin. Med.*, 2019, **8**, 1152.

7   T. Tokudome, K. Otani, M. Miyazato and K. Kangawa, *Peptides*, 2019, **111**, 42–

46.

8   M. D. Childs and L. G. Luyt, *Mol. Imaging*, 2020, **19**, 1–15.

9   M. M. Fowkes, T. Lalonde, L. Yu, S. Dhanvantari, M. S. Kovacs and L. G. Luyt, *Eur. J. Med. Chem.*, 2018, **157**, 1500–1511.

10   K. Kawamura, M. Fujinaga, Y. Shimoda, T. Yamasaki, Y. Zhang, A. Hatori, L. Xie, H. Wakizaka, K. Kumata, T. Ohkubo, Y. Kurihara, M. Ogawa, N. Nengaki and M. R. Zhang, *Nucl. Med. Biol.*, 2017, **52**, 49–56.

11   J. Hou, M. S. Kovacs, S. Dhanvantari and L. G. Luyt, *J. Med. Chem.*, 2018, **61**, 1261–1275.

12   C. L. Charron, J. Hou, M. S. McFarland, S. Dhanvantari, M. S. Kovacs and L. G. Luyt, *J. Med. Chem.*, 2017, **60**, 7256–7266.

13   B. H. Rotstein, L. Wang, R. Y. Liu, J. Patteson, E. E. Kwan, N. Vasdev and S. H. Liang, *Chem. Sci.*, 2016, **7**, 4407–4417.

14   M. A. Bednarek, S. D. Feighner, S. S. Pong, K. K. McKee, D. L. Hreniuk, M. V. Silva, V. A. Warren, A. D. Howard, L. H. Y. Van der Ploeg and J. V. Heck, *J. Med. Chem.*, 2000, **43**, 4370–4376.

15   M. Matsumoto, H. Hosoda, Y. Kitajima, N. Morozumi, Y. Minamitake, S. Tanaka, H. Matsuo, M. Kojima, Y. Hayashi and K. Kangawa, *Biochem. Biophys. Res. Commun.*, 2001, **287**, 142–146.

16   M. Van Craenenbroeck, F. Gregoire, P. De Neef, P. Robberecht and J. Perret, *Peptides*, 2004, **25**, 959–965.

17   Y. C. Tang, R. A. Davis, T. Ganguly and J. L. Sutcliffe, *Molecules*, 2019, **24**, 1–16.

18   E. Murrell and L. G. Luyt, *ACS Comb. Sci.*, 2020, **22**, 109–113.

19   C. W. Murray and D. C. Rees, *Nat. Chem.*, 2009, **1**, 187–192.

Appendix A: Additional Data for Chapter 2
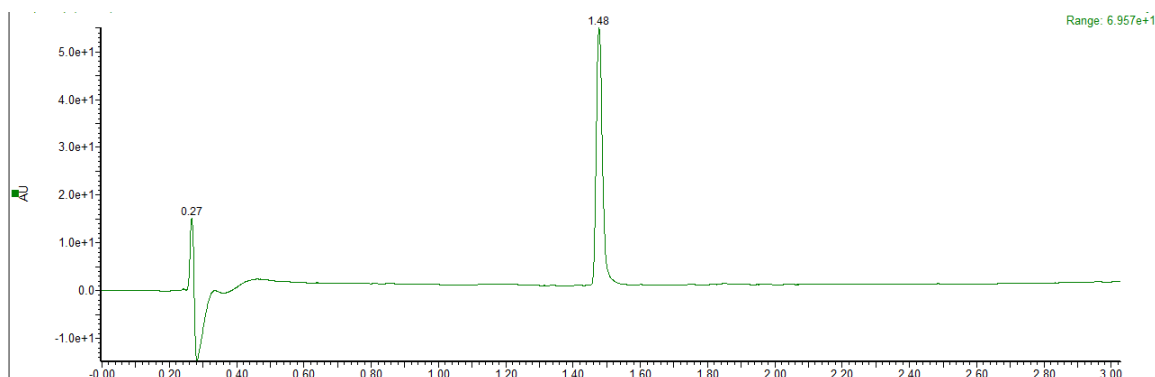
Figure A1. UHPLC of ghrelin(1-8) analogue **1** (5-95% ACN in water).
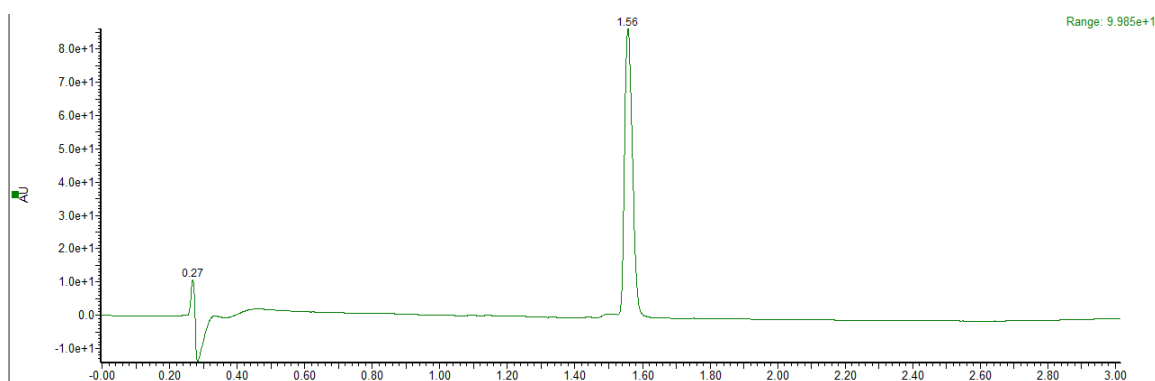
Figure A2. UHPLC of ghrelin(1-8) analogue **2** (5-95% ACN in water).
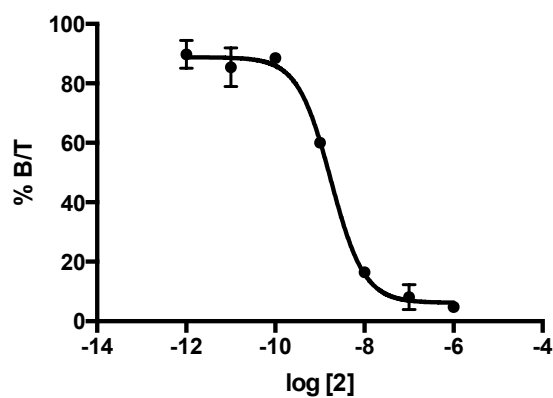
Figure A3. IC$_{50}$ curve for ghrelin(1-8) analogue **2** in HEK293 GHSR$^+$ cells (IC$_{50}$ = 2.23 ± 0.93; n=3).
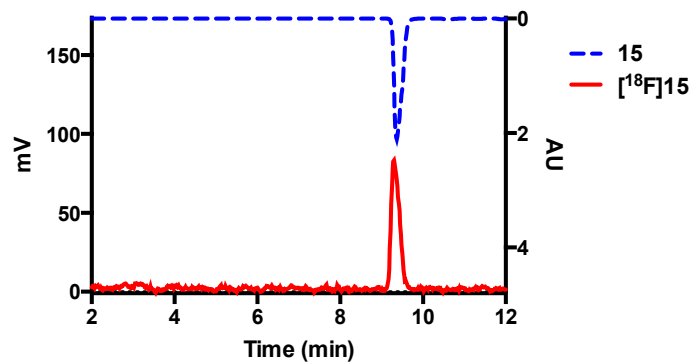
Figure A4. Analytical HPLC trace of **[$^{18/19}$F]15**. Independent injections of the radio-HPLC trace of the radiolabelled product is shown in red (mV) and the UV-HPLC trace of the non-radioactive standard is shown in blue (AU).
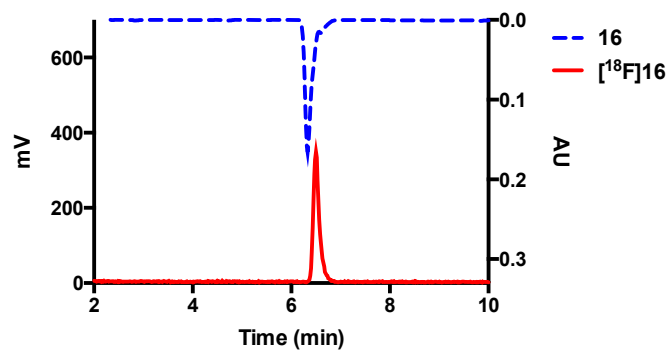
Figure A5. Analytical HPLC trace of **[$^{18/19}$F]16**. Independent injections of the radio-HPLC trace of the radiolabelled product is shown in red (mV) and the UV-HPLC trace of the non-radioactive standard is shown in blue (AU).
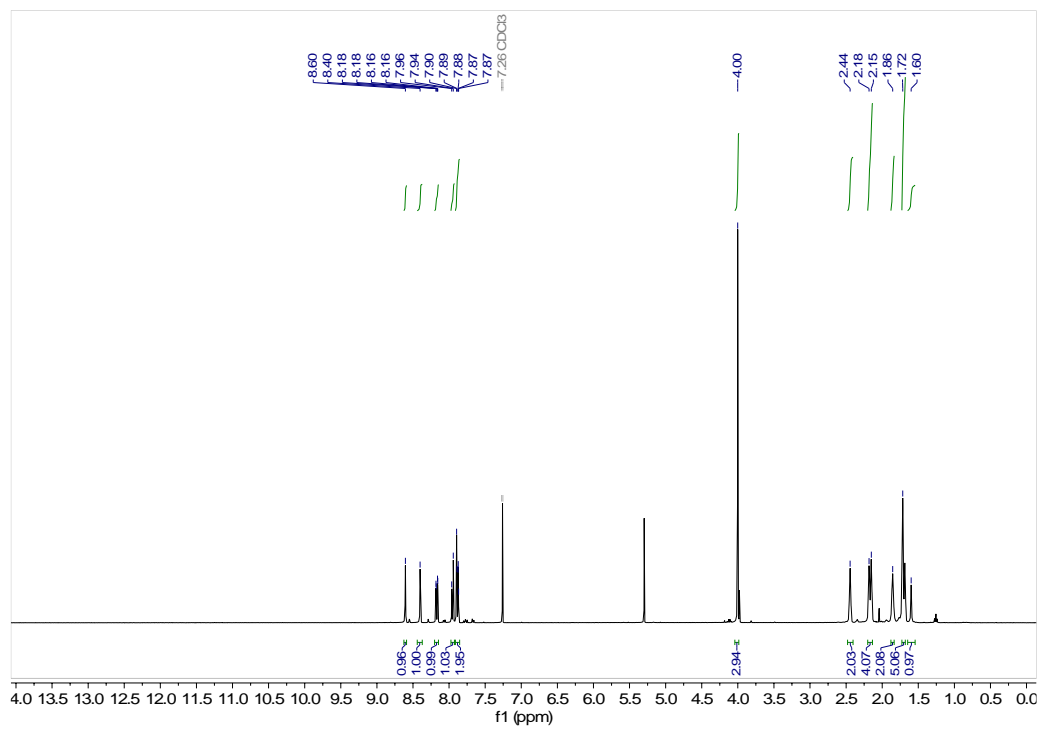
Figure A6. ^{1}H NMR of compound **6** in CDCl$_3$.
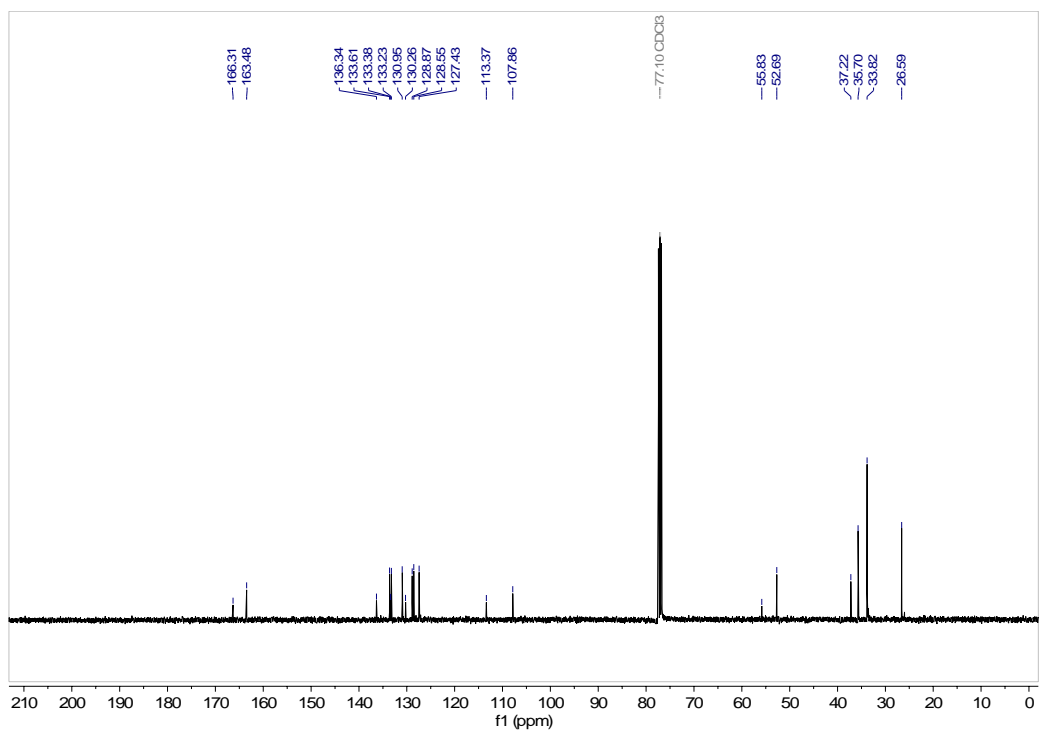
Figure A7. ^{13}C NMR of compound **6** in CDCl$_3$.
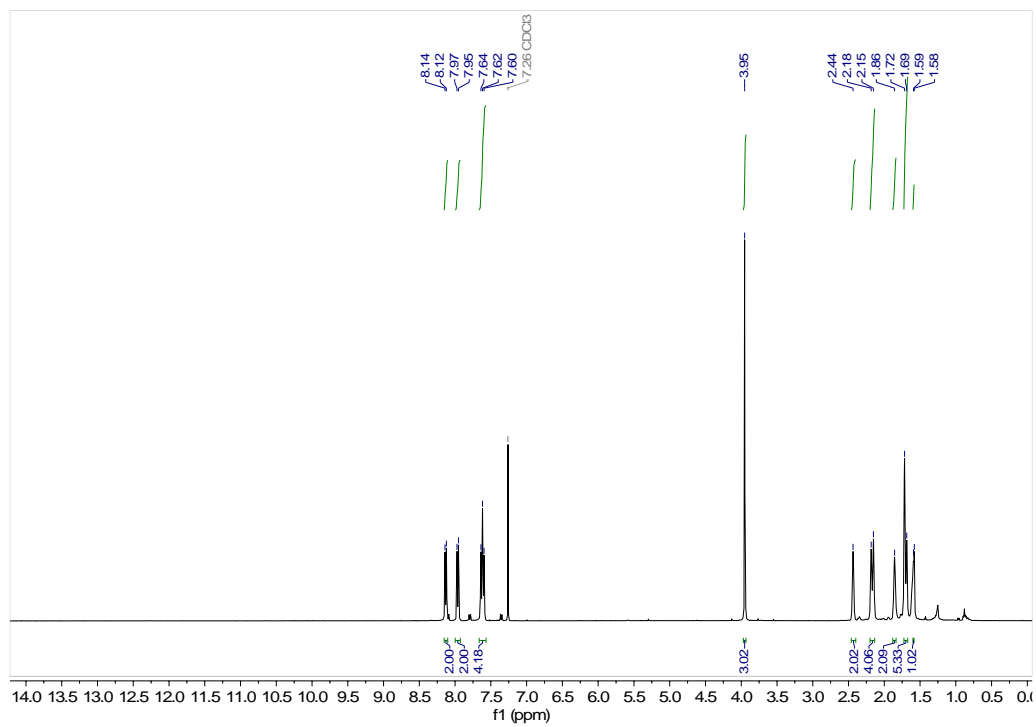
Figure A8. ^{1}H NMR of compound **10** in CDCl$_3$.
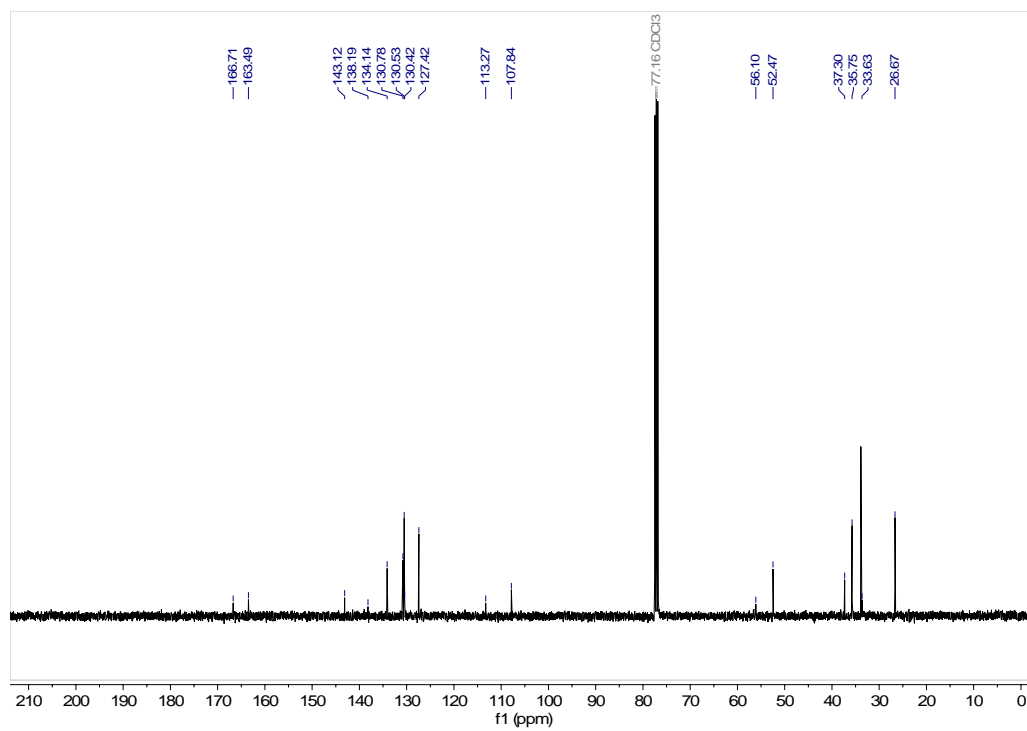
Figure A9. ^{13}C NMR of compound **10** in CDCl$_3$.
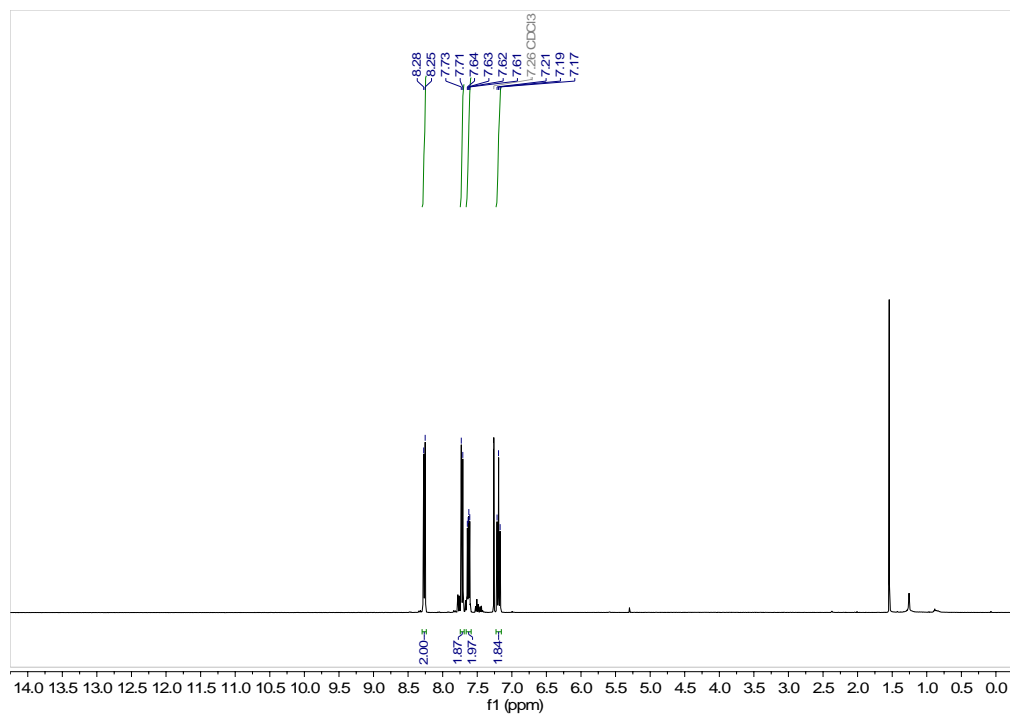
Figure A10. ^{1}H NMR of compound **16** in CDCl$_3$.
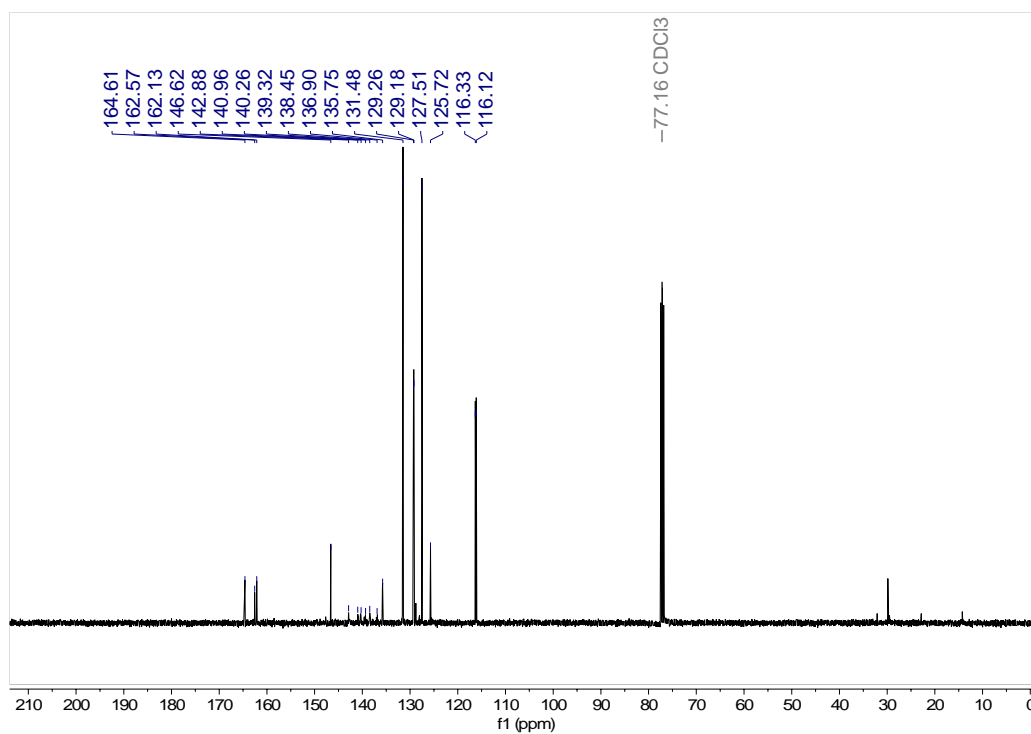
Figure A11. ^{13}C NMR of compound **16** in CDCl$_3$.
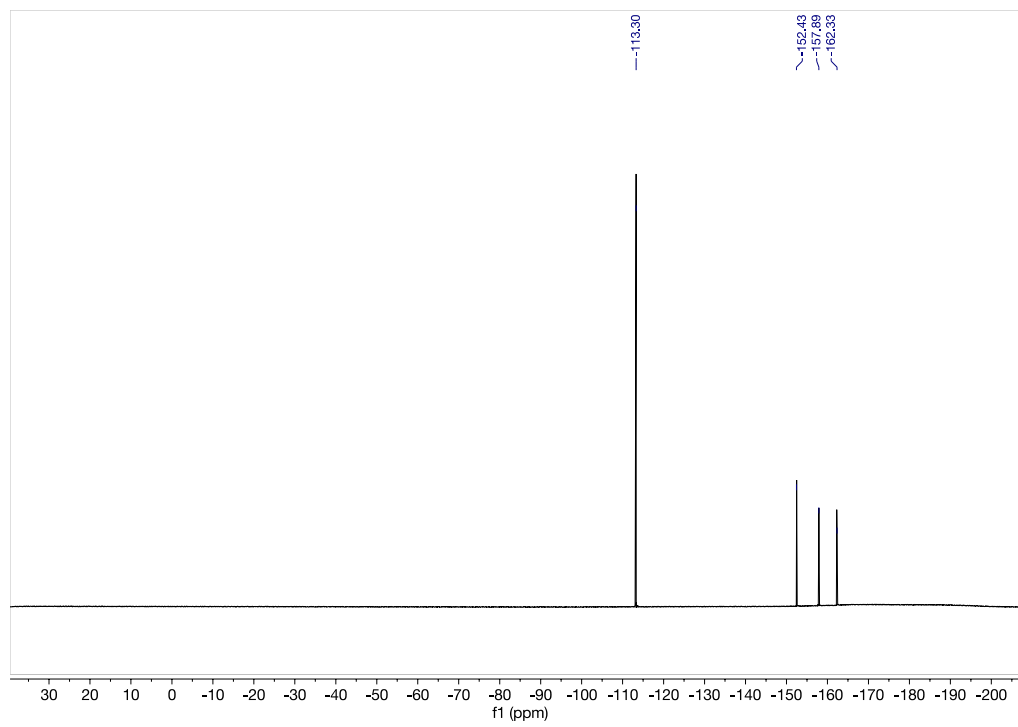
Figure A12. ^{19}F NMR of compound **16** in CDCl$_3$.

Appendix B: Additional Data for Chapter 3
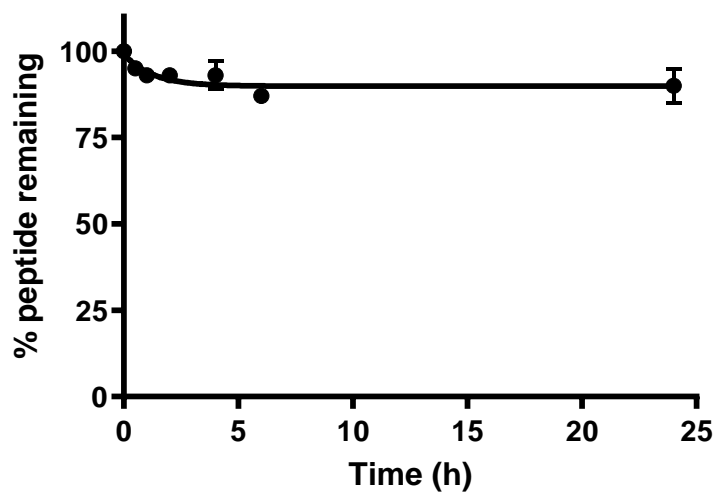
Figure B1. Chemical Stability of peptide **1** in PBS (pH=7.4) at 37 °C over 24 hours.
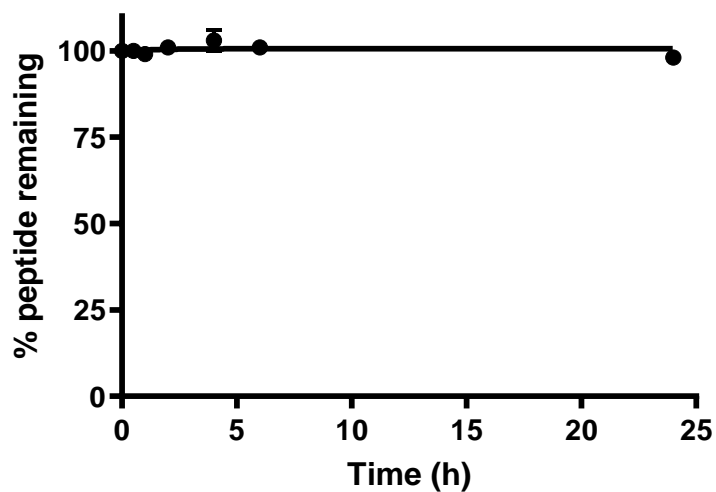
Figure B2. Chemical Stability of peptide **2** in PBS (pH=7.4) at 37 °C over 24 hours.
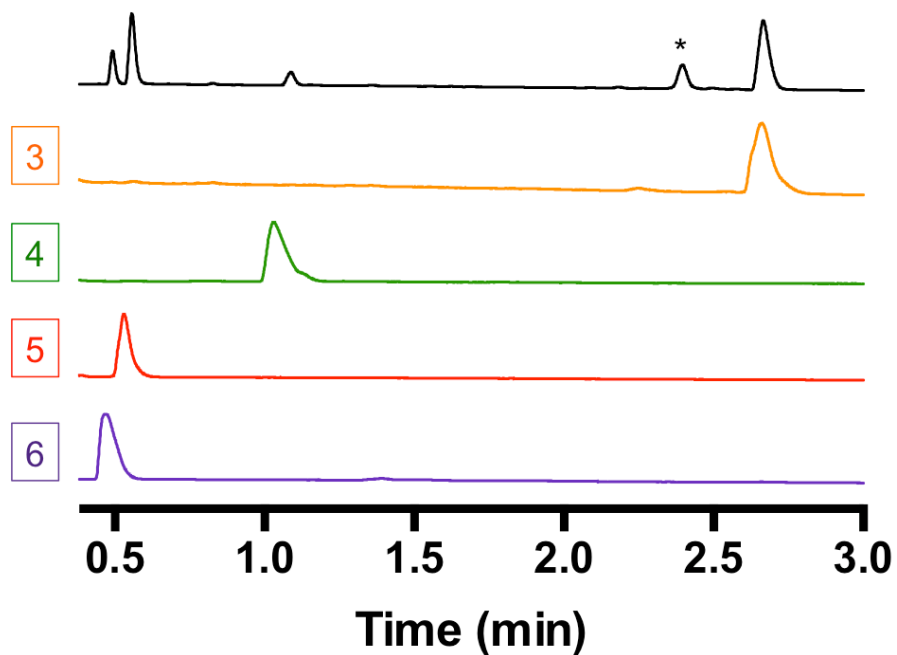
Figure B3. (Top) UHPLC-UV chromatogram for peptide **1** after 24 h incubation in human serum (* indicates parent peptide **1**). Stacked UHPLC-UV chromatograms of independently synthesized metabolites **3-6** are shown to confirm metabolite identities.
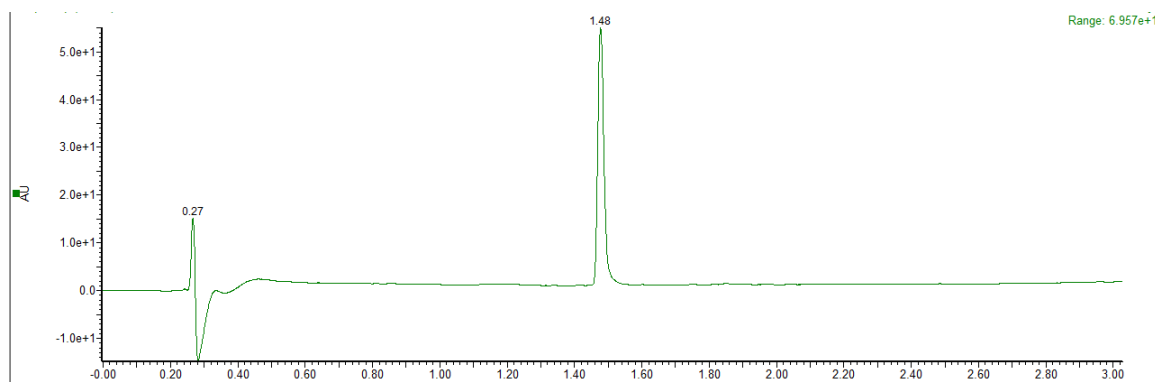
Figure B4. UHPLC of ghrelin(1-8) analogue **1** (5-95% ACN in water).
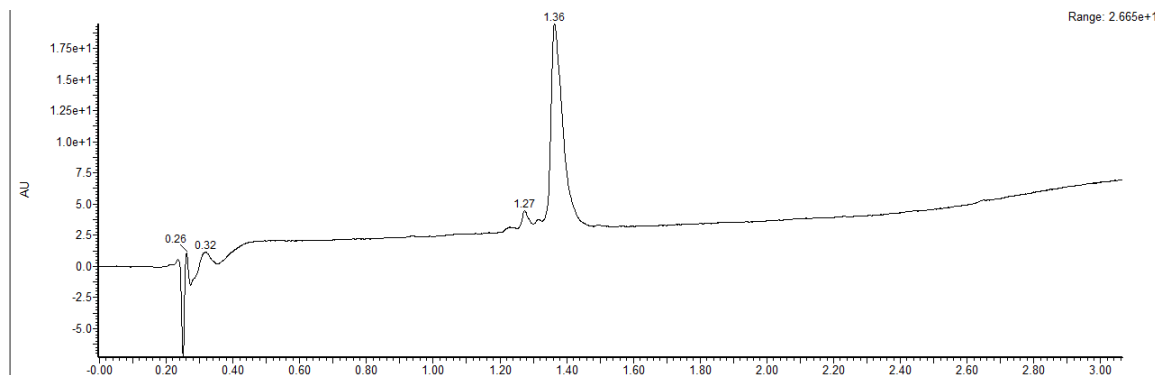
Figure B5. UHPLC of ghrelin(1-8) analogue **2** (10-95% ACN in water).
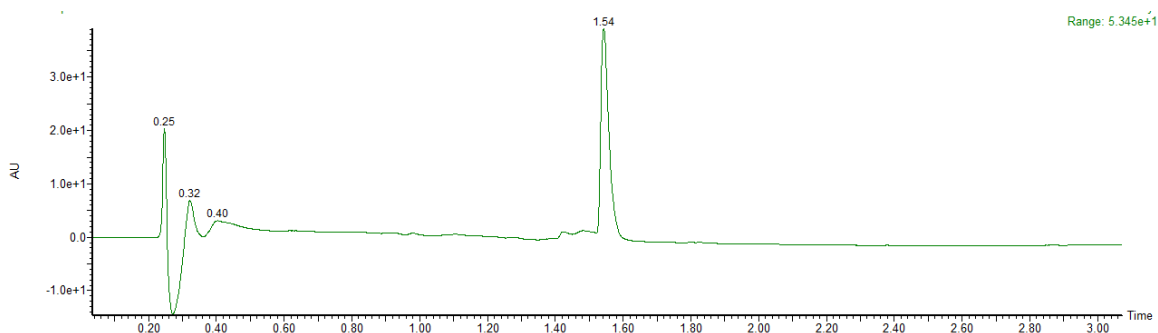
Figure B6. UHPLC of ghrelin(1-8) analogue **3** (20-40% ACN in water).
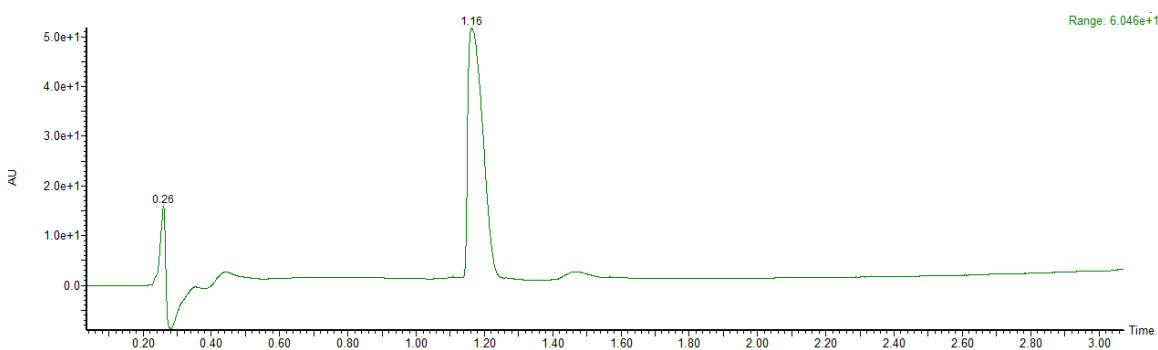
Figure B7. UHPLC of ghrelin(1-8) analogue **4** (5-95% ACN in water).
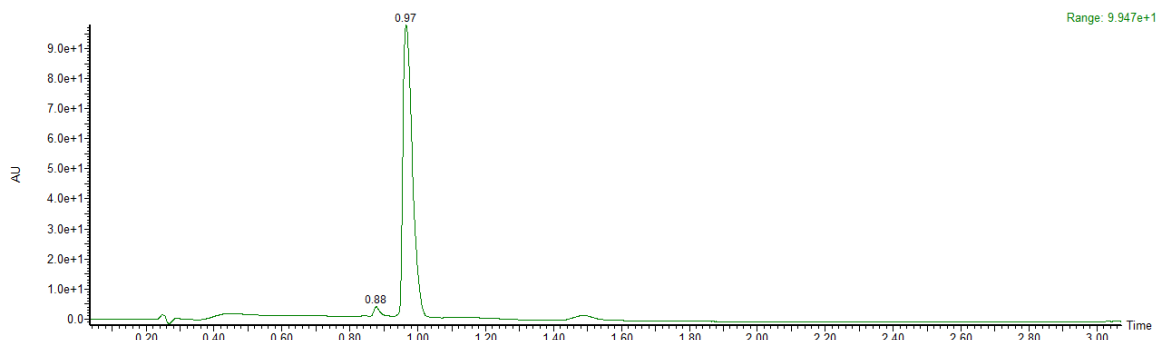
Figure B8. UHPLC of ghrelin(1-8) analogue **5** (5-95% ACN in water).
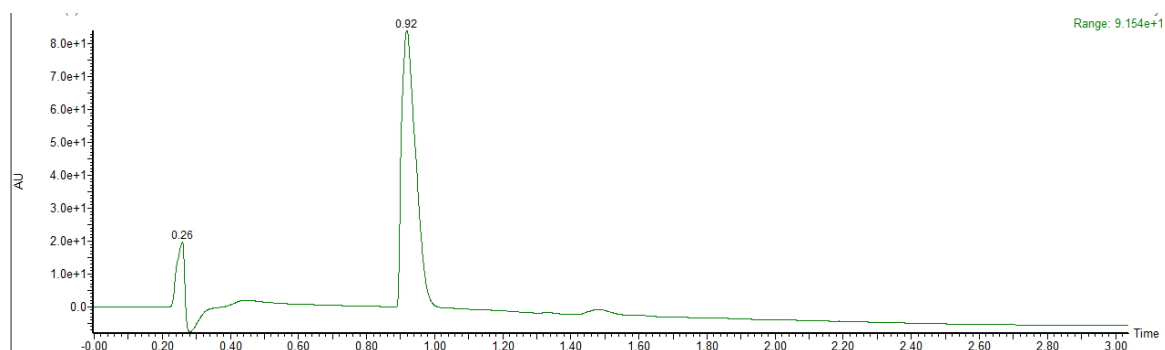
Figure B9. UHPLC of ghrelin(1-8) analogue **6** (5-95% ACN in water).
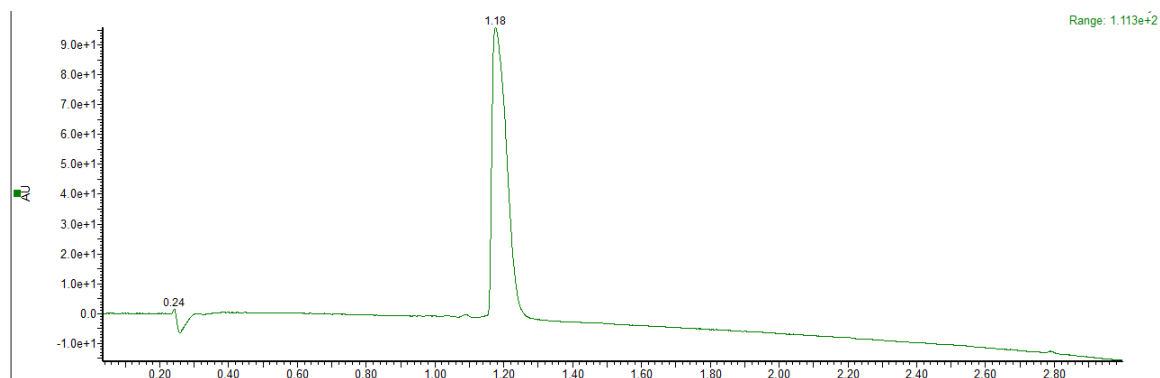
Figure B10. UHPLC of ghrelin(1-8) analogue **9** (20-95% ACN in water).
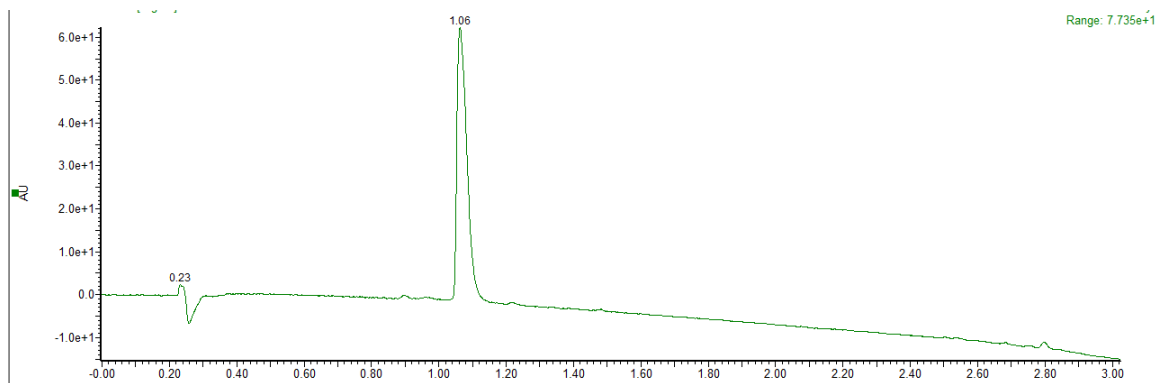
Figure B11. UHPLC of ghrelin(1-8) analogue **10** (20-95% ACN in water).
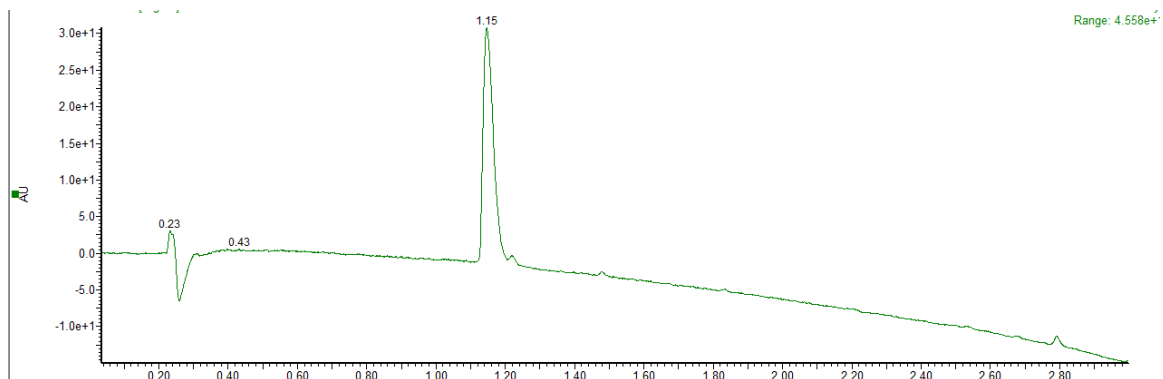
Figure B12. UHPLC of ghrelin(1-8) analogue **11** (20-95% ACN in water).
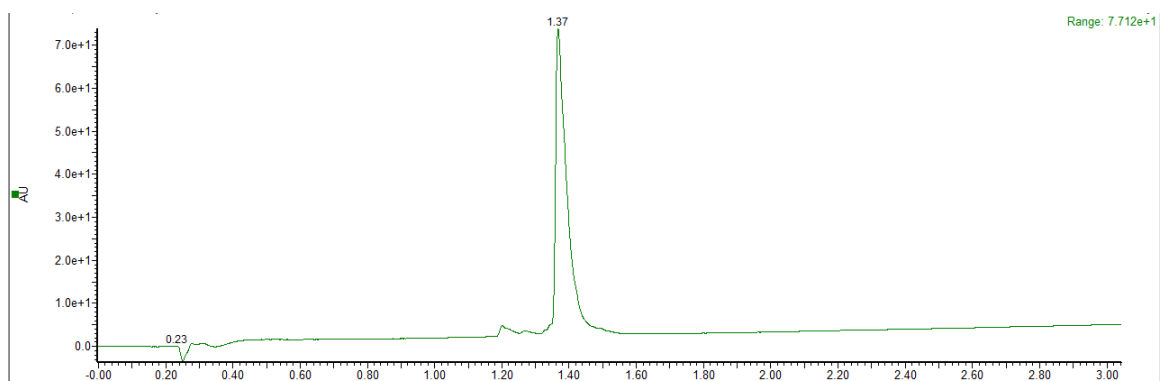
Figure B13. UHPLC of ghrelin(1-8) analogue **12** (10-95% ACN in water).
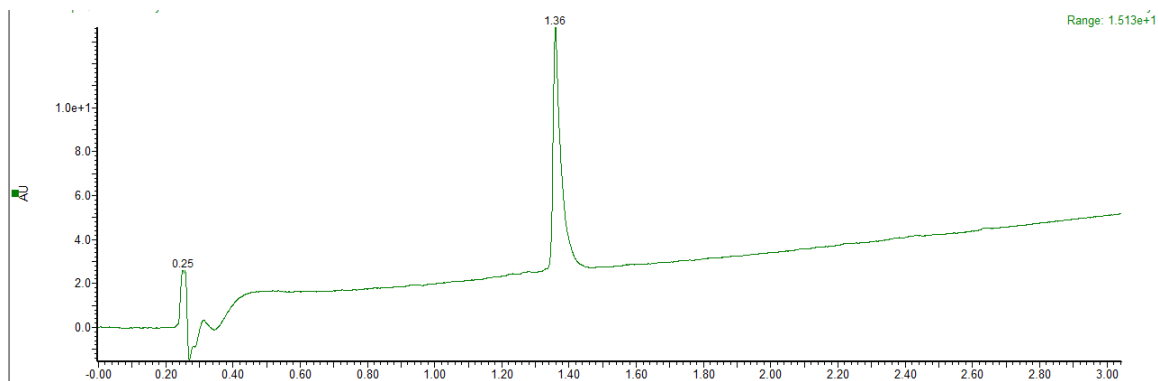
Figure B14. UHPLC of ghrelin(1-8) analogue **13** (10-95% ACN in water).
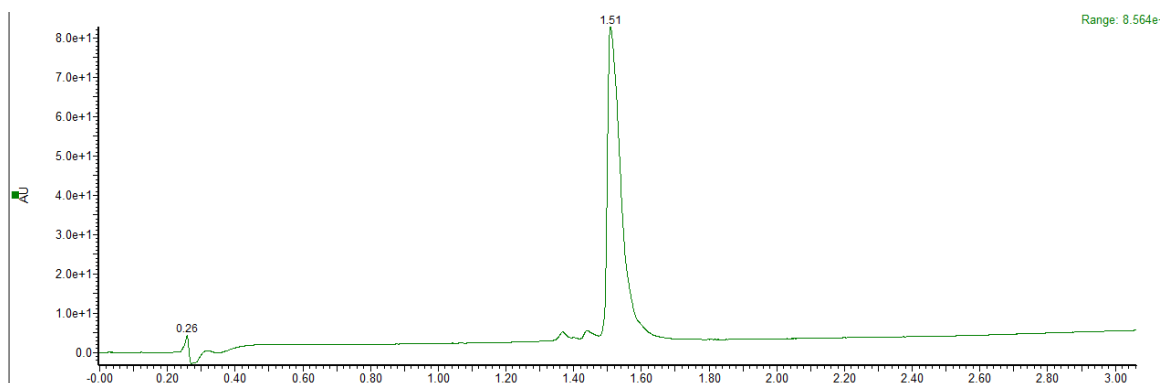
Figure B15. UHPLC of ghrelin(1-8) analogue **14** (10-95% ACN in water).
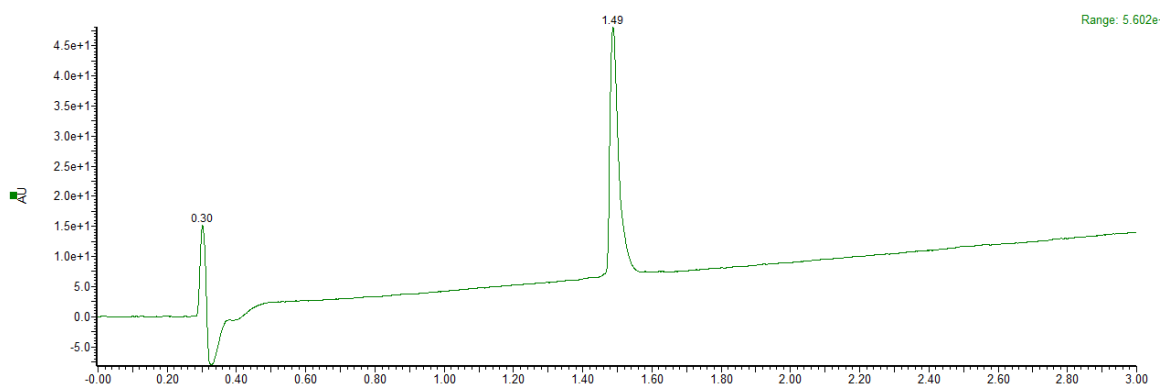
Figure B16. UHPLC of ghrelin(1-8) analogue **15** (10-95% ACN in water).
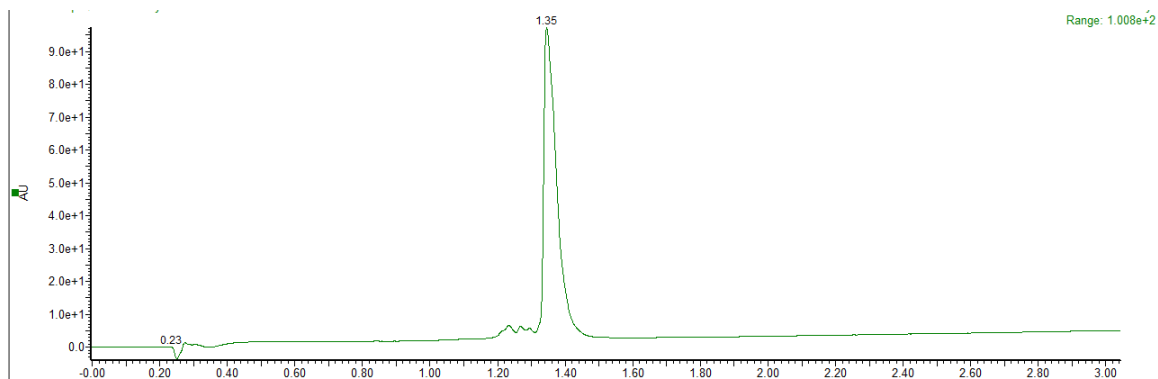
Figure B17. UHPLC of ghrelin(1-8) analogue **16** (10-95% ACN in water).
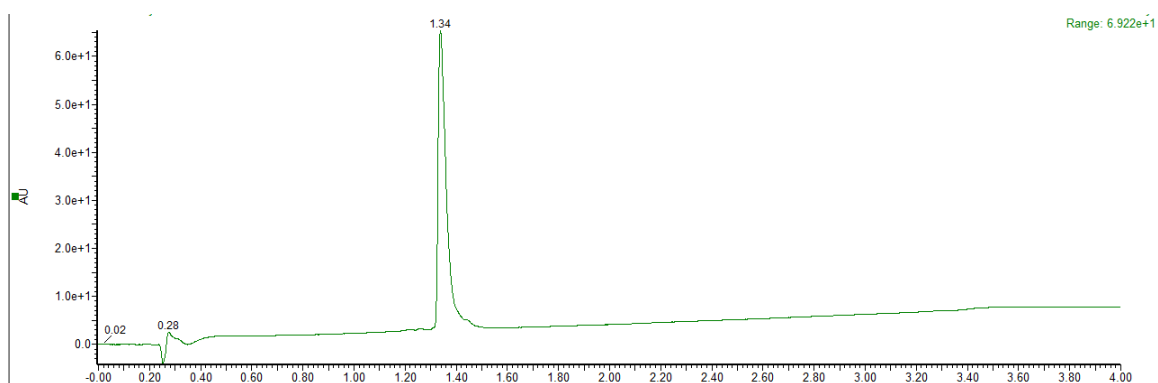
Figure B18. UHPLC of ghrelin(1-8) analogue **17** (10-95% ACN in water).
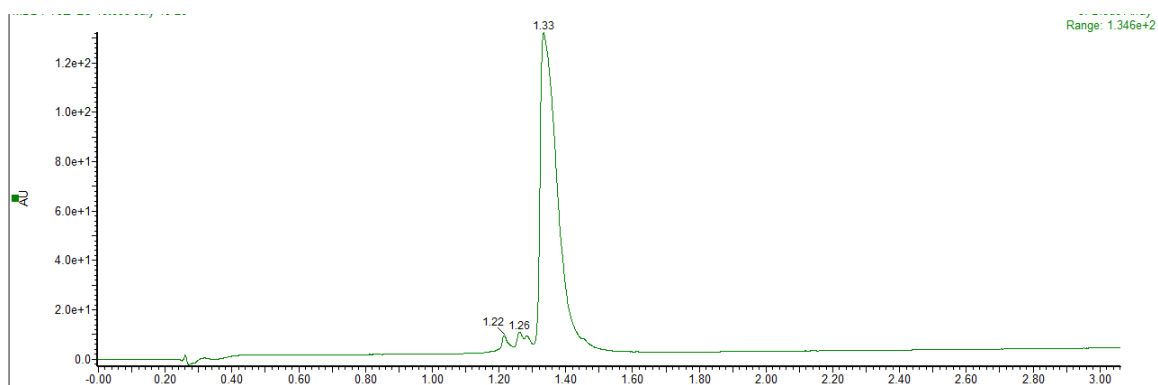
Figure B19. UHPLC of ghrelin(1-8) analogue **18** (10-95% ACN in water).
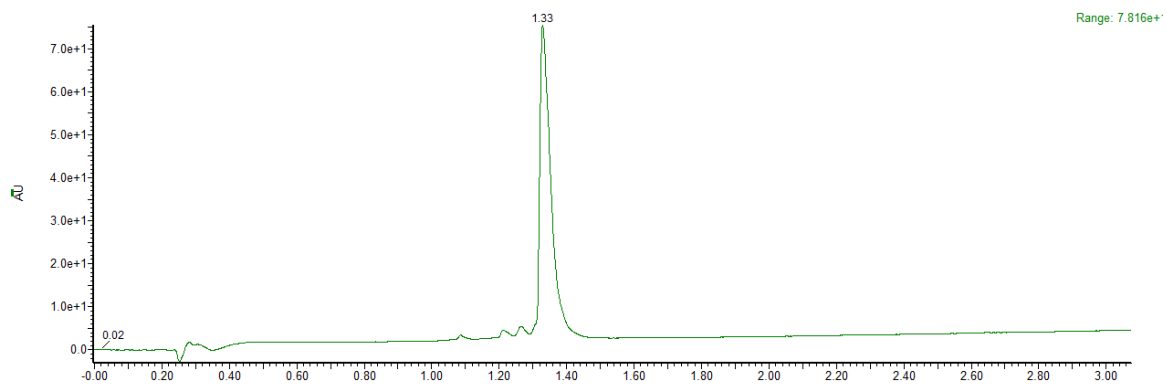
Figure B20. UHPLC of ghrelin(1-8) analogue **19** (10-95% ACN in water).
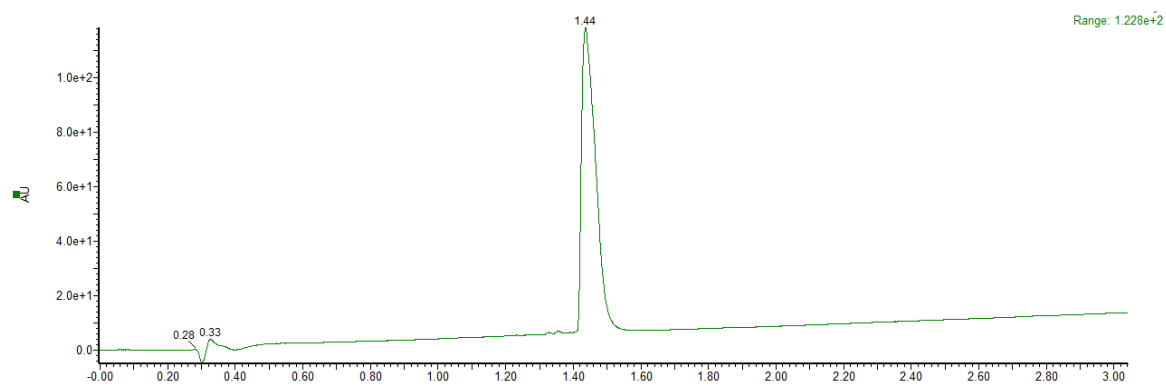
Figure B21. UHPLC of ghrelin(1-8) analogue **20** (10-95% ACN in water).
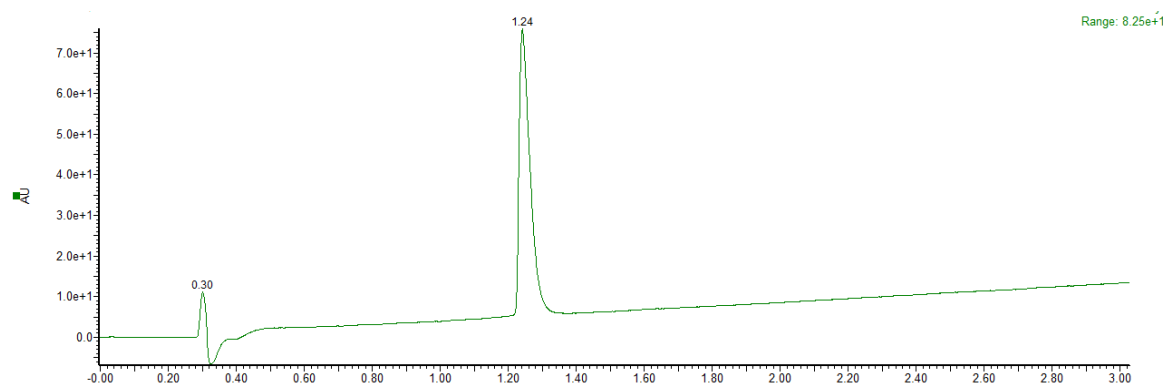
Figure B22. UHPLC of ghrelin(1-8) analogue **21** (10-95% ACN in water).
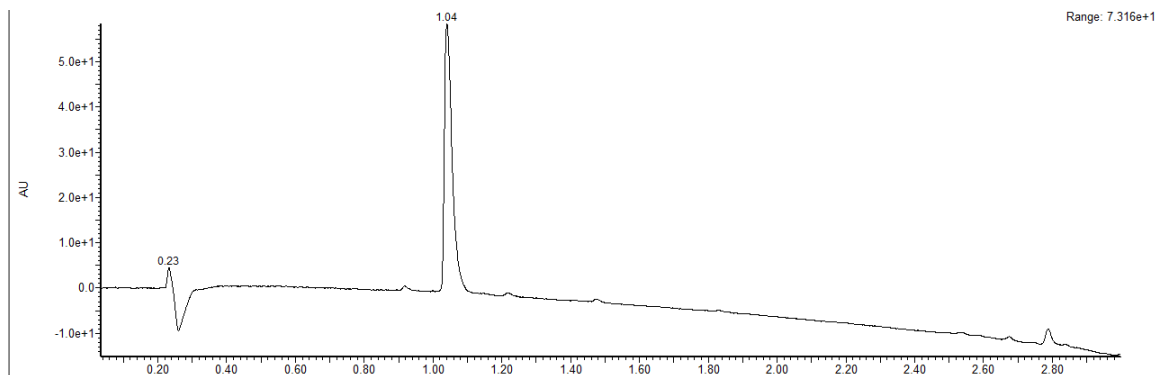
Figure B23. UHPLC of ghrelin(1-8) analogue **22** (20-95% ACN in water).
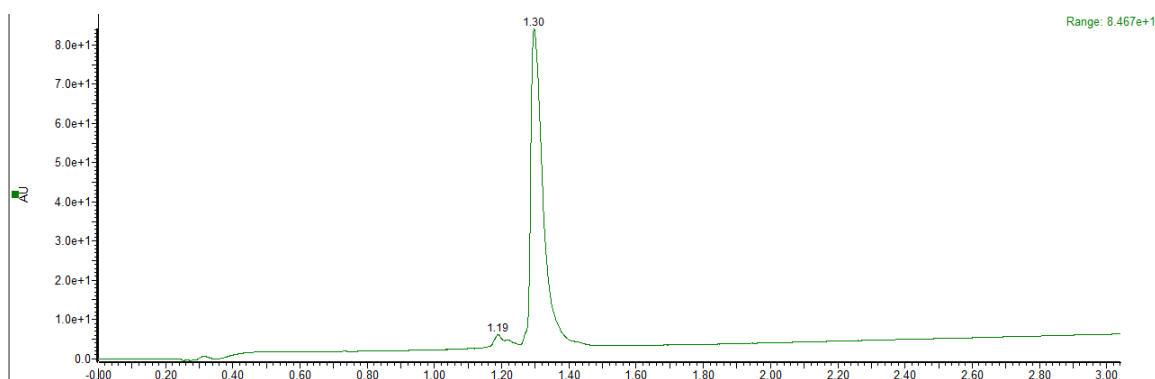
Figure B24. UHPLC of ghrelin(1-8) analogue **23** (10-95% ACN in water).
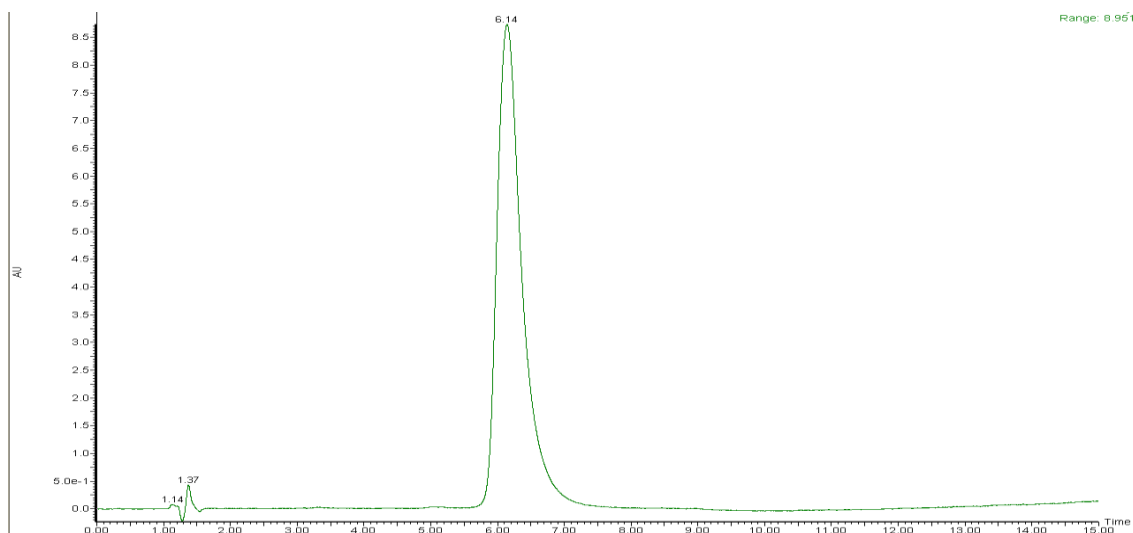
Figure B25. HPLC of ghrelin(1-8) analogue **24** (33-90% ACN in water).
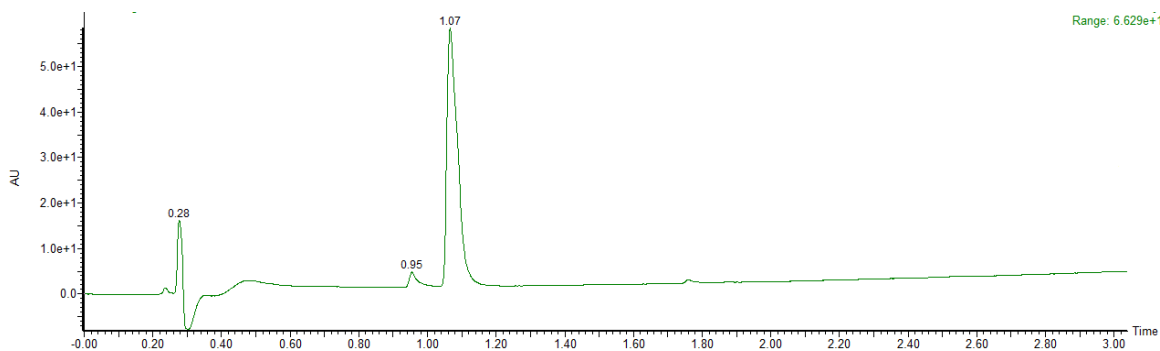
Figure B26. UHPLC of imidazole-1-sulfonyl azide hydrogen sulfate (05-95% ACN in water).
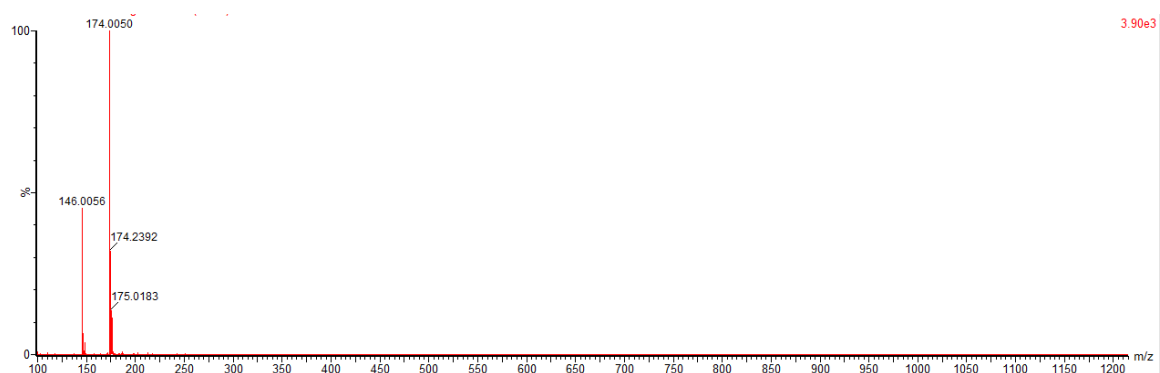
Figure B27. ESI⁺ mass spectrum of imidazole-1-sulfonyl azide hydrogen sulfate.
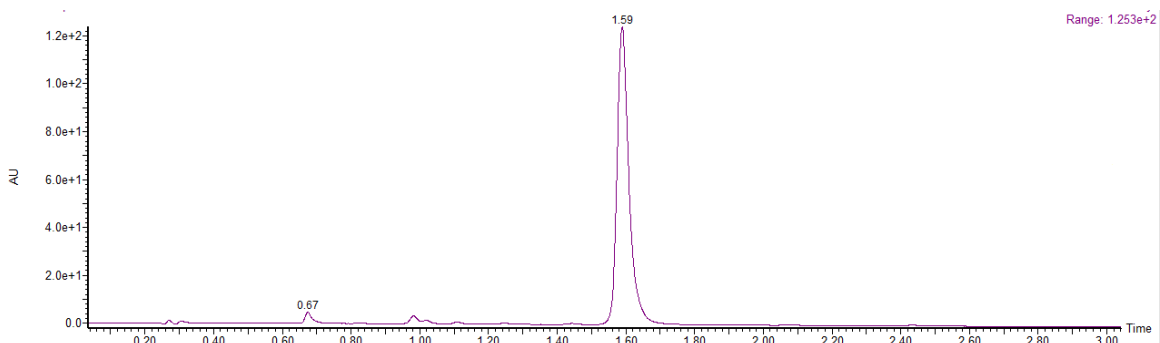
Figure B28. UHPLC of Fmoc-Ala-Leu alkyne (50-75% ACN in water).
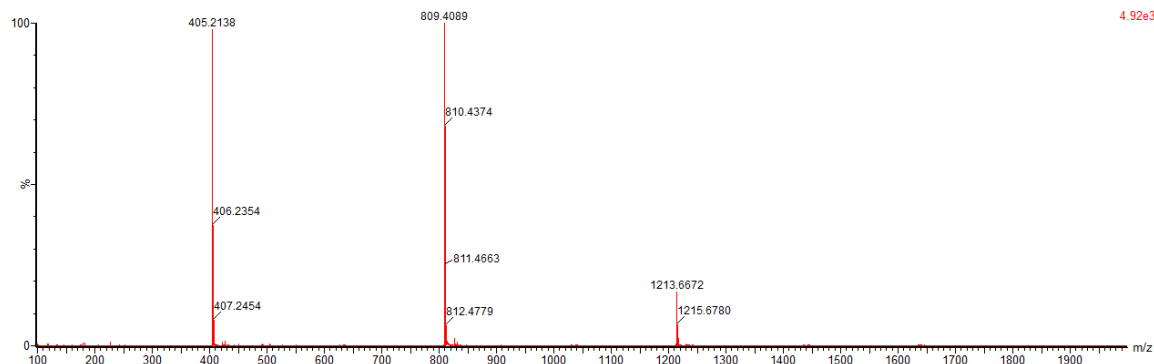
Figure B29. ESI$^+$ mass spectrum of Fmoc-Ala-Leu alkyne.
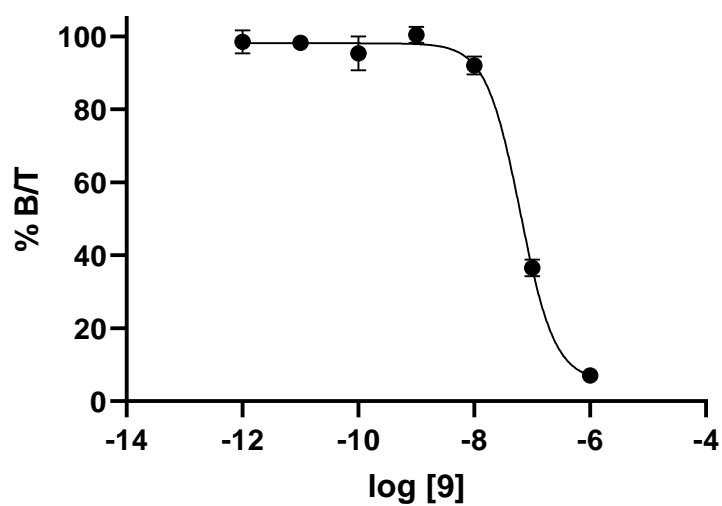
Figure B30. IC$_{50}$ curve for compound **9** in HEK293 GHSR-eYFP cells (n=2).
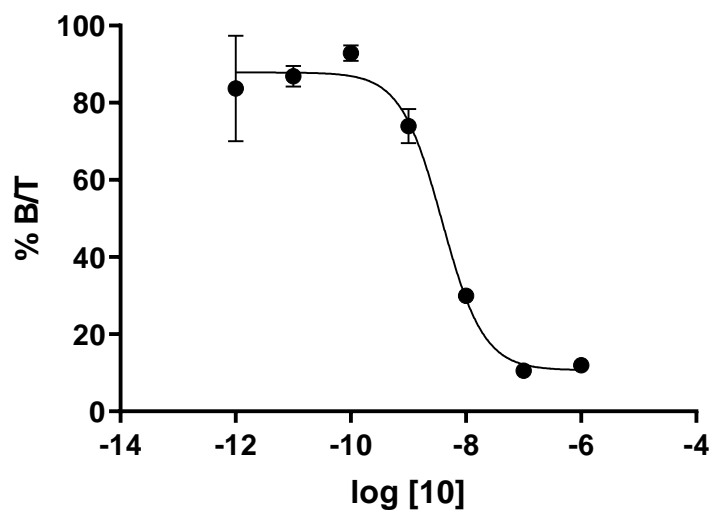
Figure B31. IC$_{50}$ curve for compound **10** in HEK293 GHSR-eYFP cells (n=2).
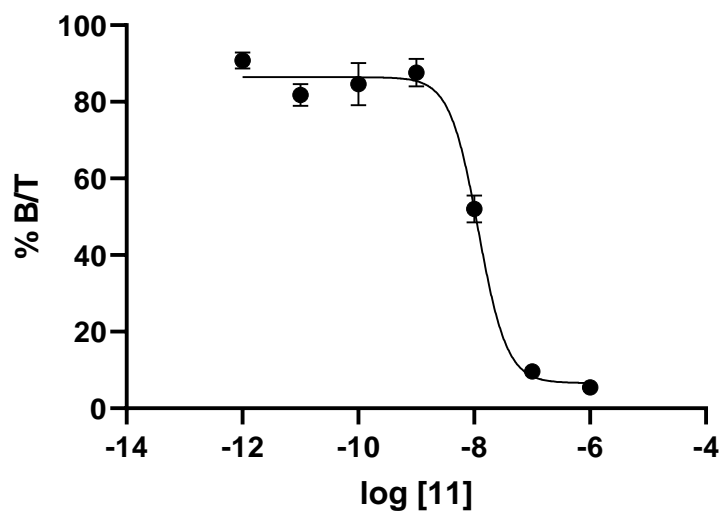
Figure B32. IC$_{50}$ curve for compound **11** in HEK293 GHSR-eYFP cells (n=2).
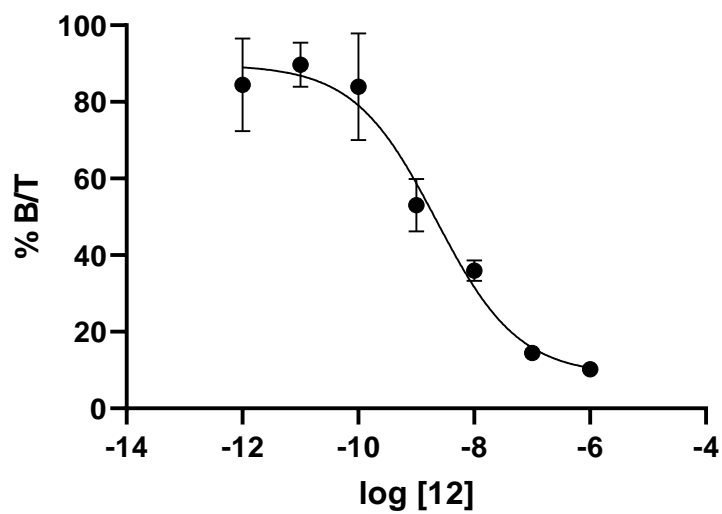
Figure B33. IC$_{50}$ curve for compound **12** in HEK293 GHSR-eYFP cells (n=2).
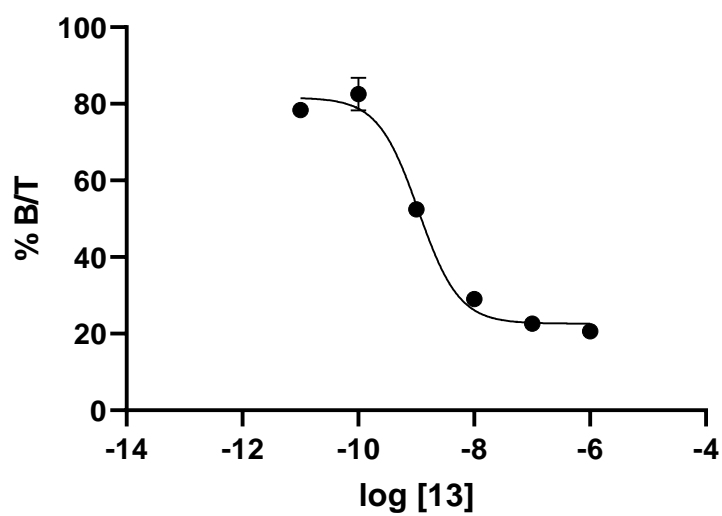
Figure B34. IC$_{50}$ curve for compound **13** in HEK293 GHSR-eYFP cells (n=2).
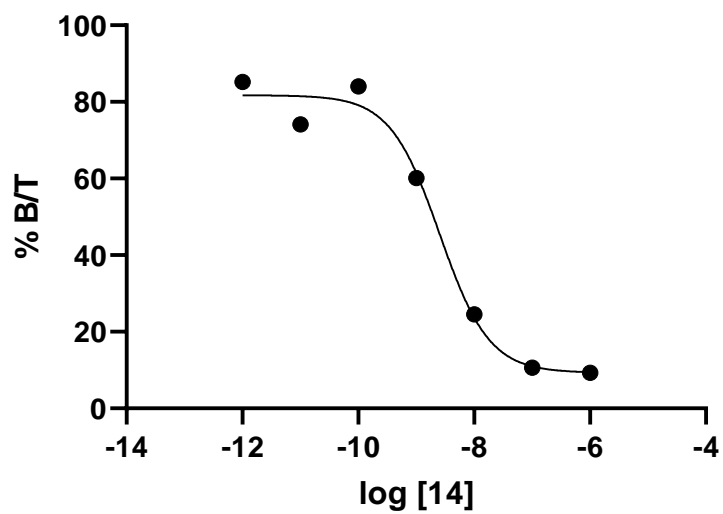
Figure B35. IC$_{50}$ curve for compound **14** in HEK293 GHSR-eYFP cells (n=2).
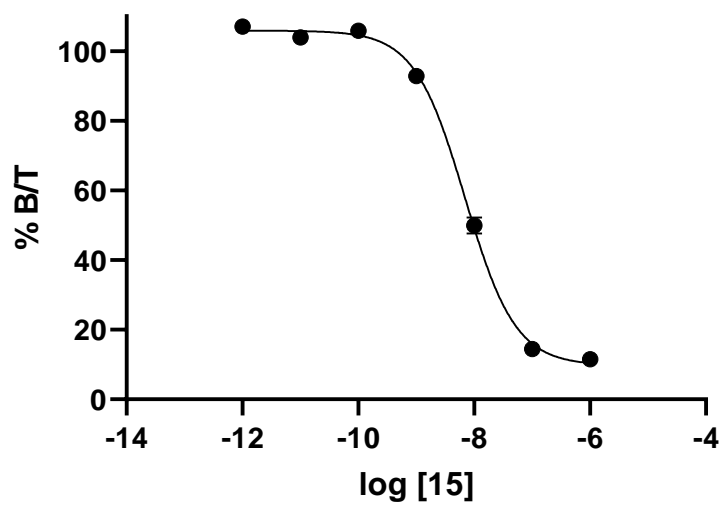
Figure B36. IC$_{50}$ curve for compound **15** in HEK293 GHSR-eYFP cells (n=2).
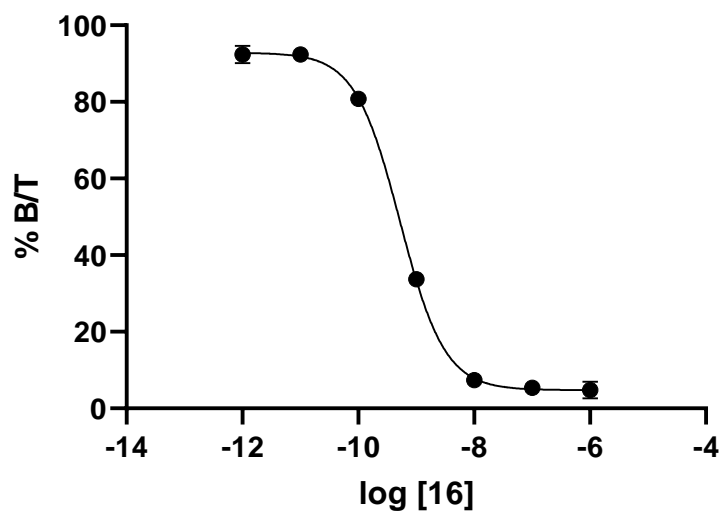
Figure B37. IC$_{50}$ curve for compound **16** in HEK293 GHSR-eYFP cells (n=2).
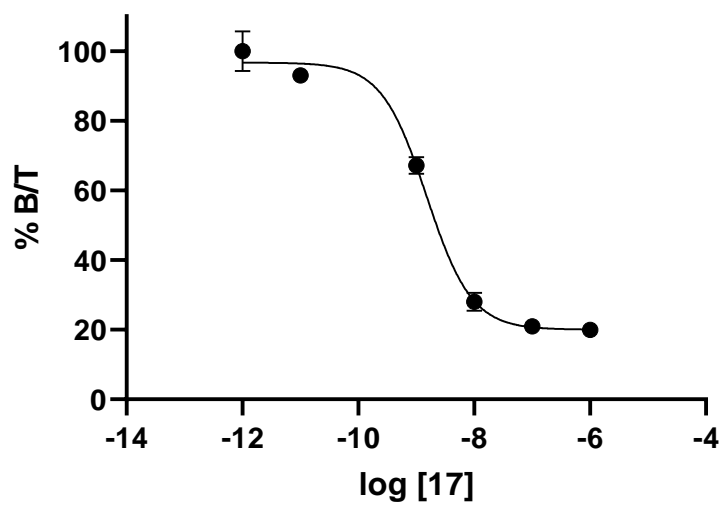
Figure B38. IC$_{50}$ curve for compound **17** in HEK293 GHSR-eYFP cells (n=2).
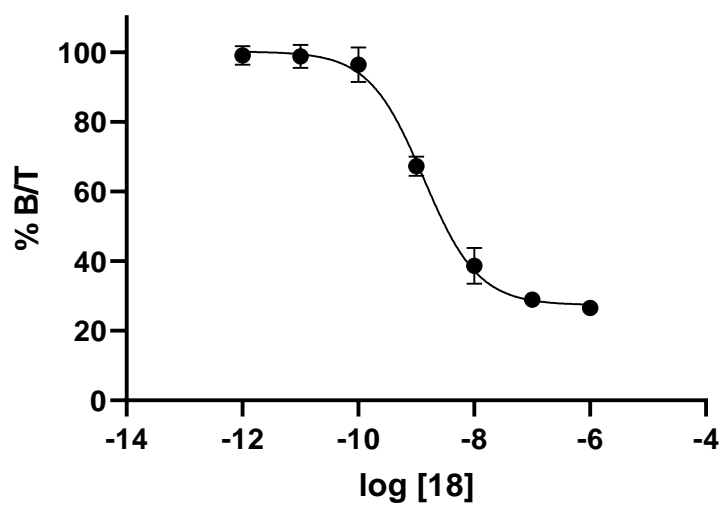
Figure B39. IC$_{50}$ curve for compound **18** in HEK293 GHSR-eYFP cells (n=2).
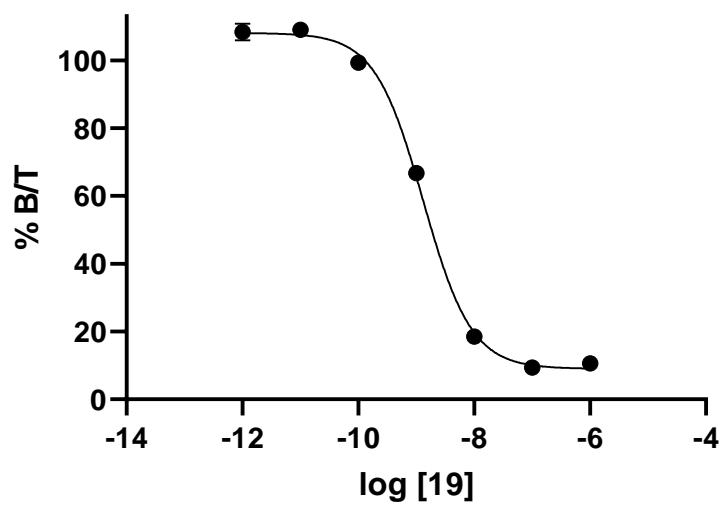
Figure B40. IC$_{50}$ curve for compound **19** in HEK293 GHSR-eYFP cells (n=2).
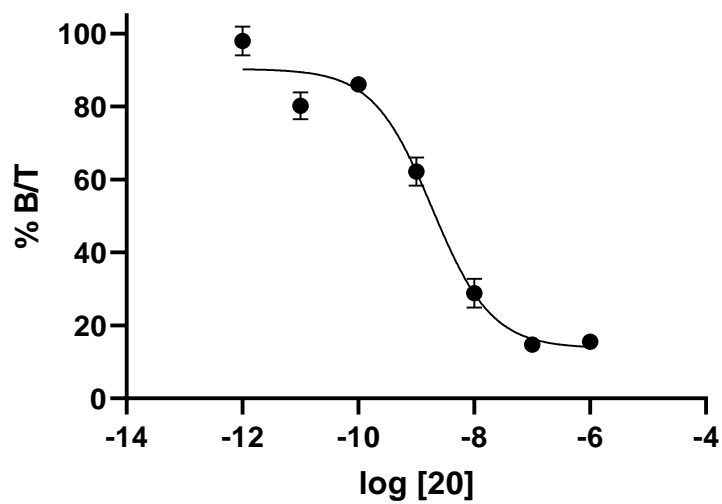
Figure B41. IC$_{50}$ curve for compound **20** in HEK293 GHSR-eYFP cells (n=2).
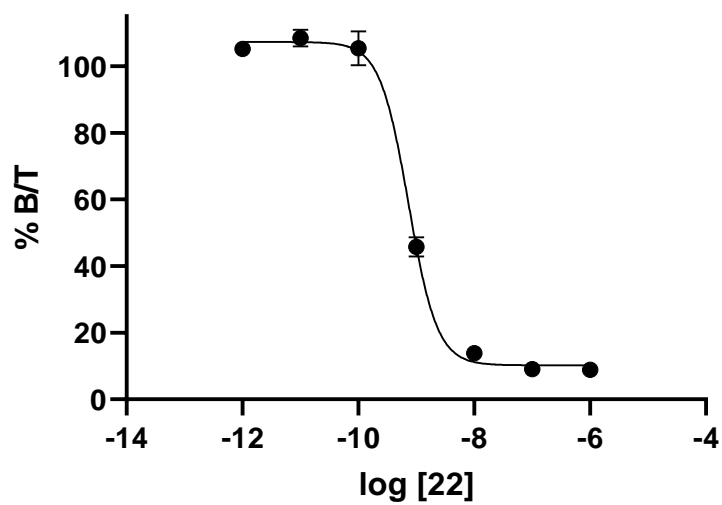
Figure B42. IC$_{50}$ curve for compound **22** in HEK293 GHSR-eYFP cells (n=2).
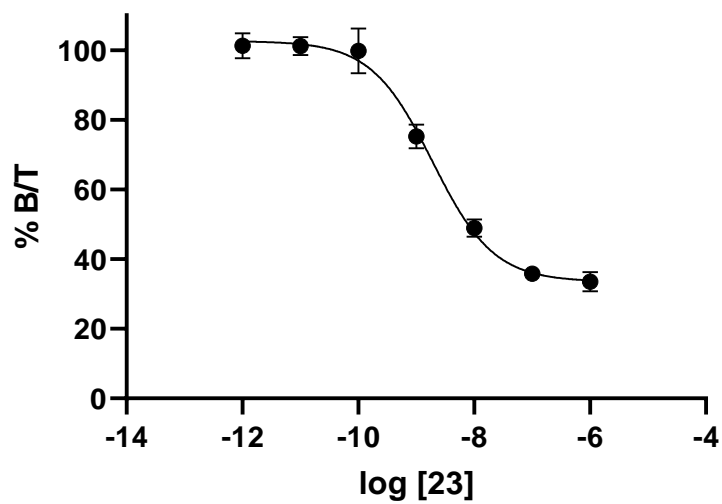
Figure B43. IC$_{50}$ curve for compound **23** in HEK293 GHSR-eYFP cells (n=2).
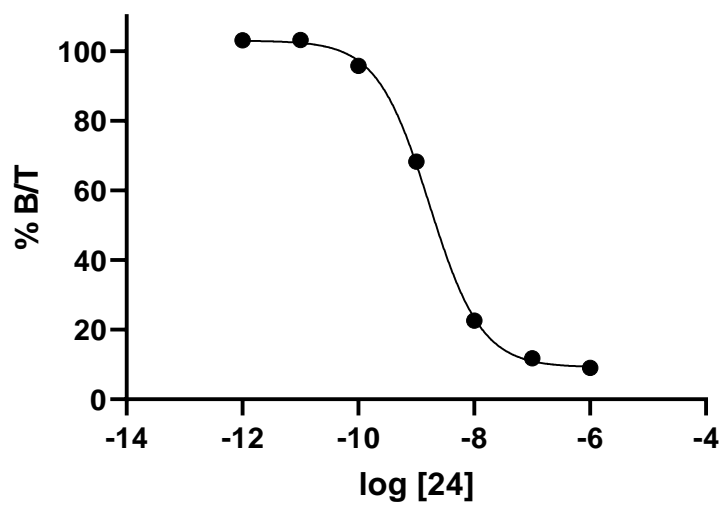
Figure B44. IC$_{50}$ curve for compound **24** in HEK293 GHSR-eYFP cells (n=2).
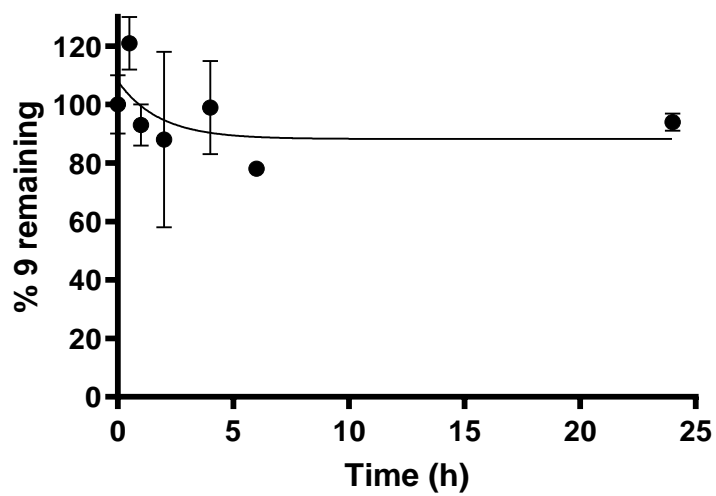
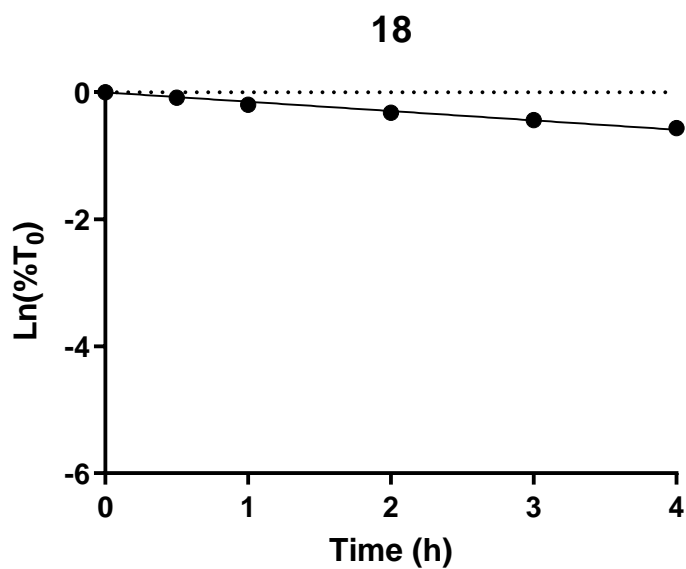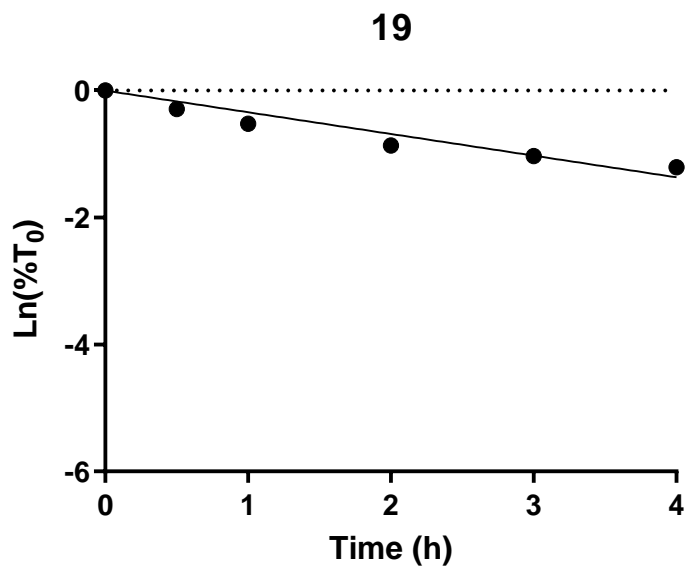**Figure B45.** *In vitro* stability of compound **9** in human serum.
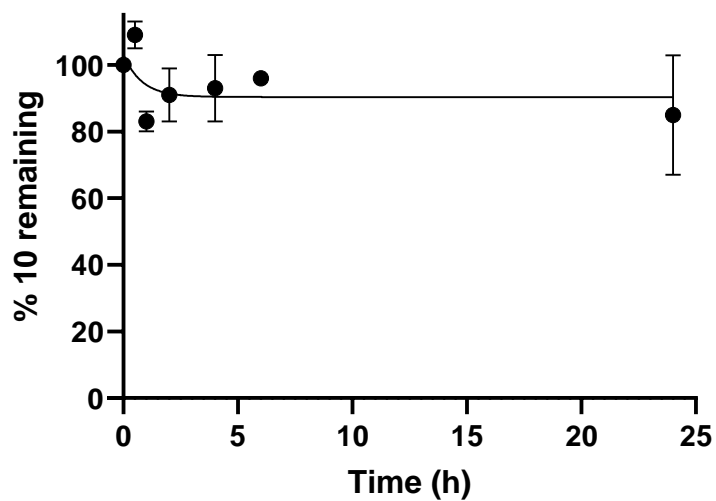
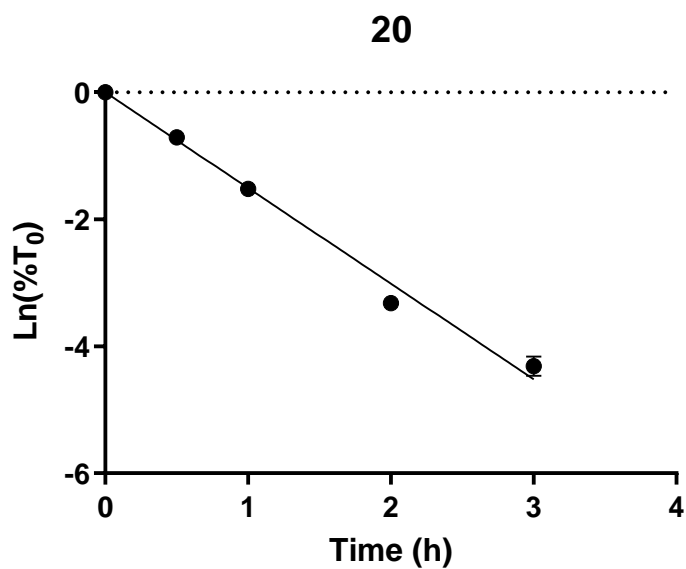**Figure B46.** *In vitro* stability of compound **10** in human serum.
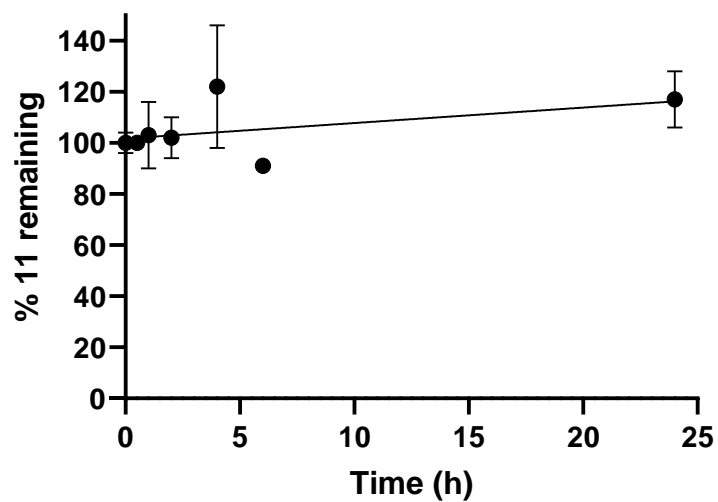
Figure B47. *In vitro* stability of compound **11** in human serum.
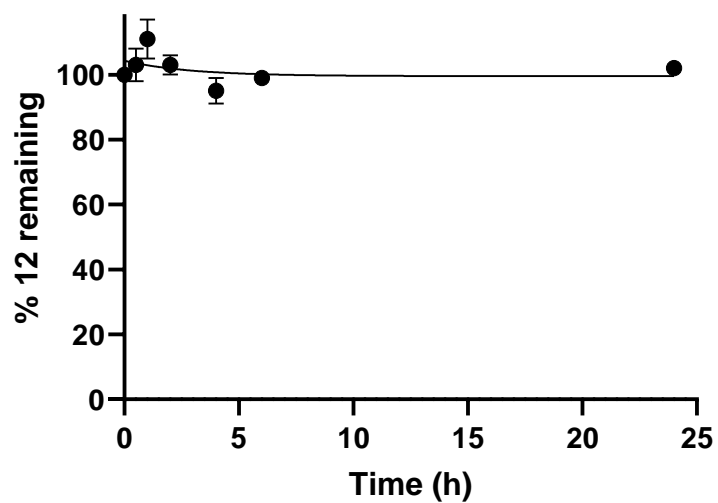
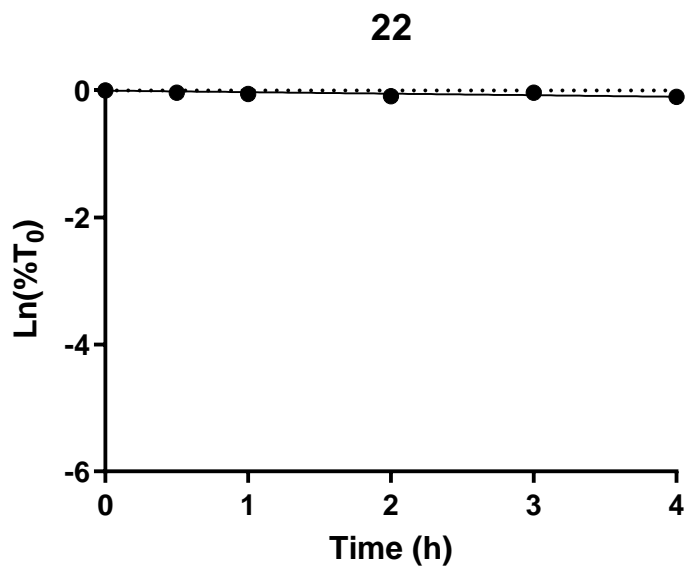**Figure B48.** *In vitro* stability of compound **12** in human serum.
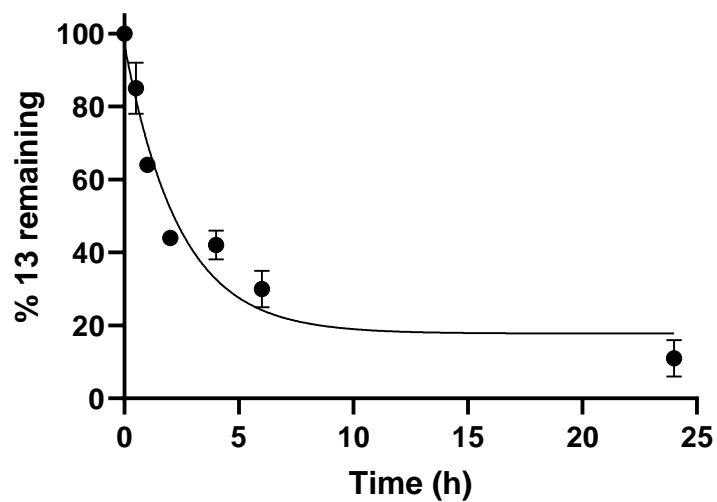
Figure B49. *In vitro* stability of compound **13** in human serum.
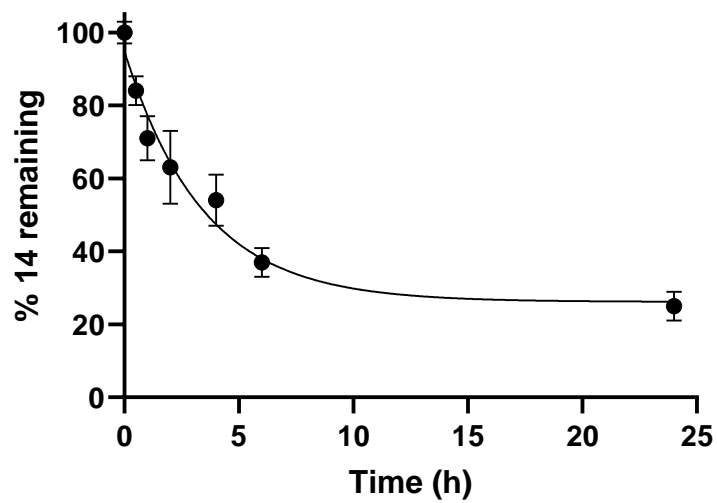
Figure B50. *In vitro* stability of compound **14** in human serum.
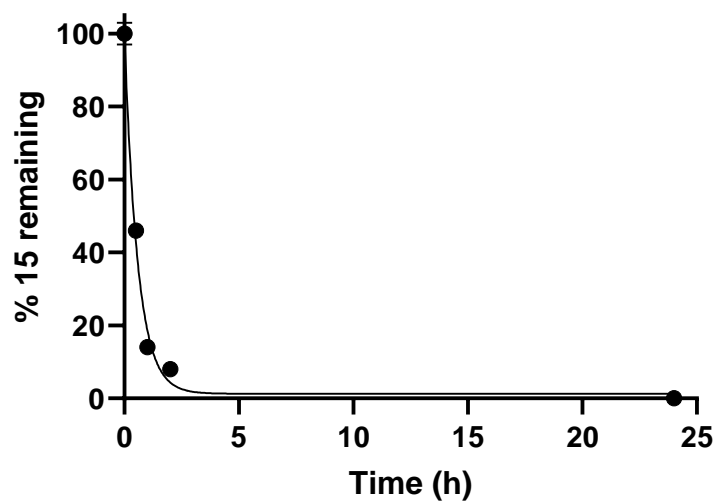
Figure B51. *In vitro* stability of compound **15** in human serum.
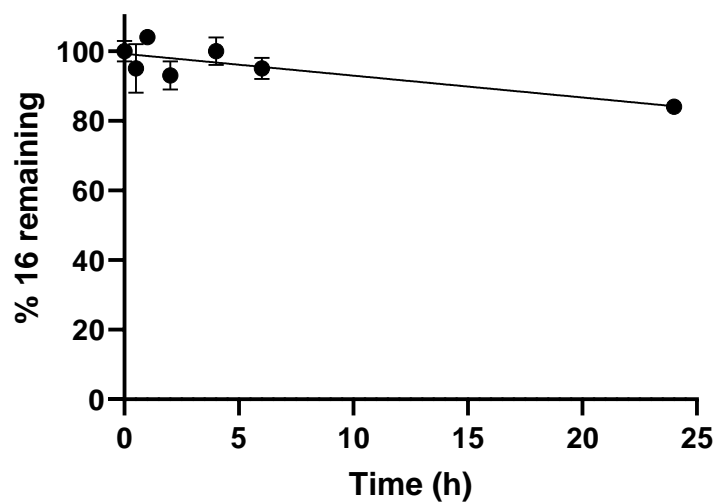
Figure B52. *In vitro* stability of compound **16** in human serum.
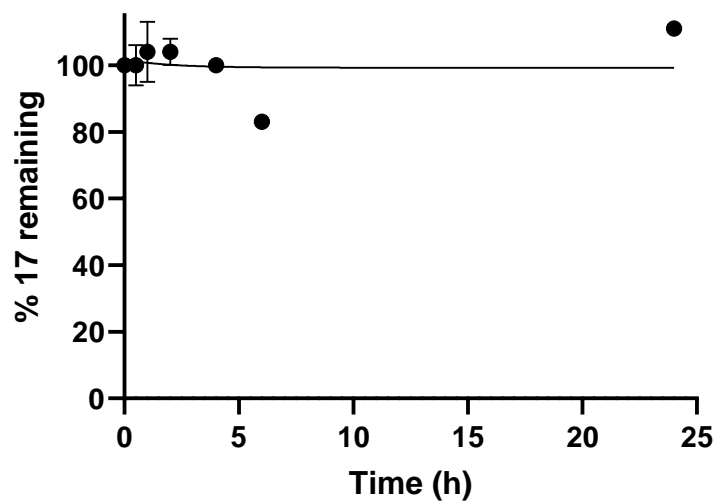
Figure B53. *In vitro* stability of compound **17** in human serum.
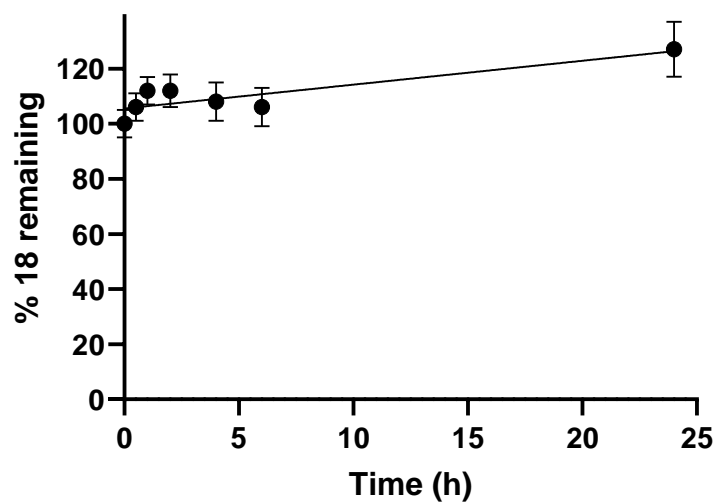
Figure B54. *In vitro* stability of compound **18** in human serum.
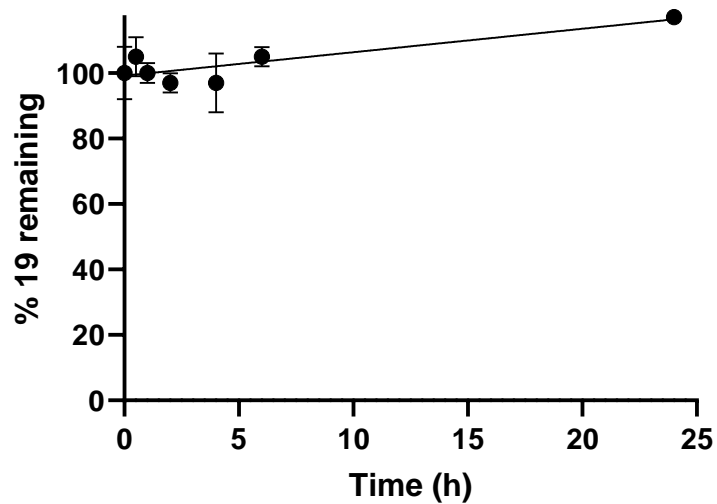
Figure B55. *In vitro* stability of compound **19** in human serum.
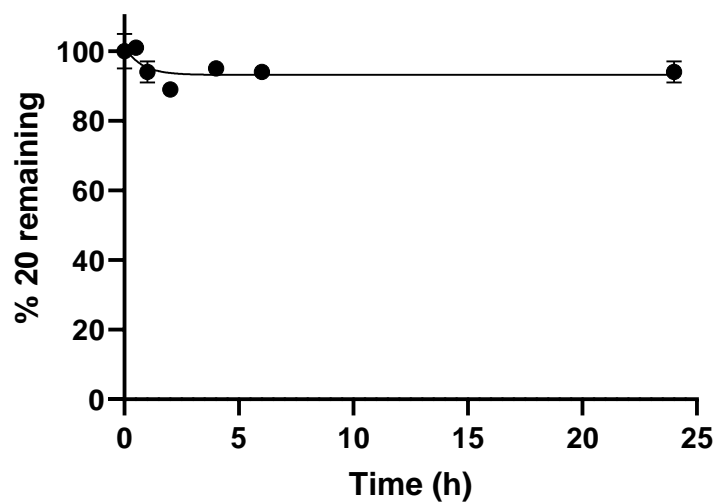
Figure B56. *In vitro* stability of compound **20** in human serum.
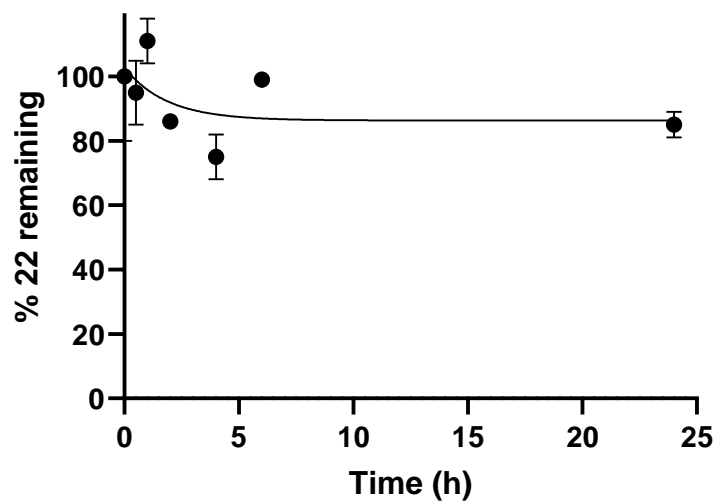
Figure B57. *In vitro* stability of compound **22** in human serum.
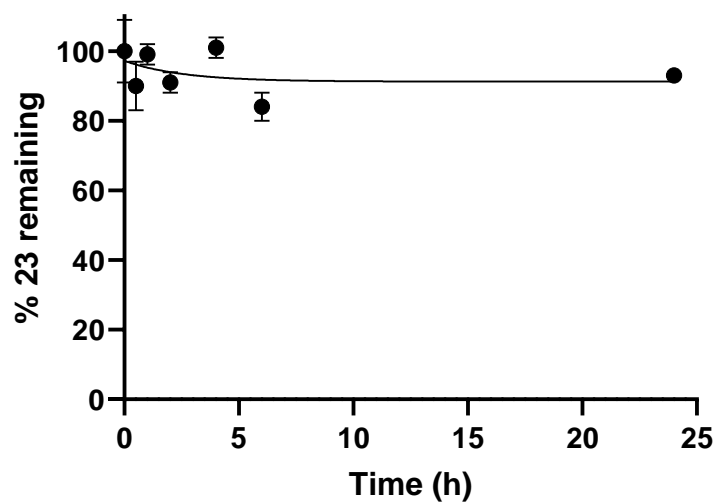
Figure B58. *In vitro* stability of compound **23** in human serum.
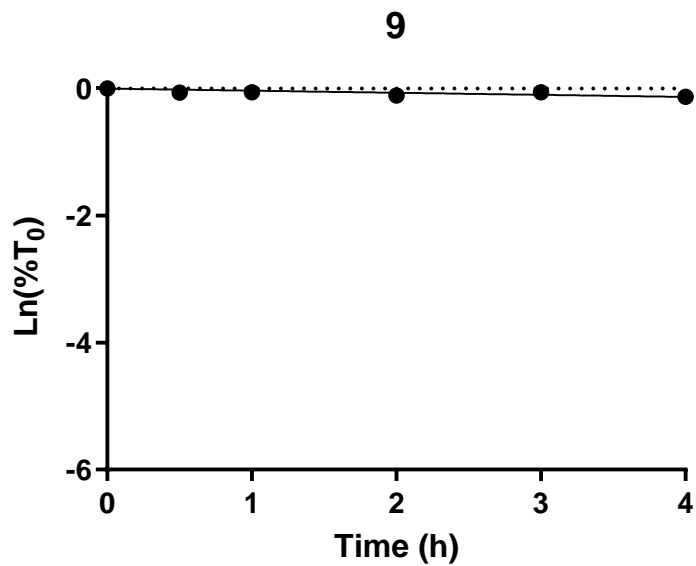
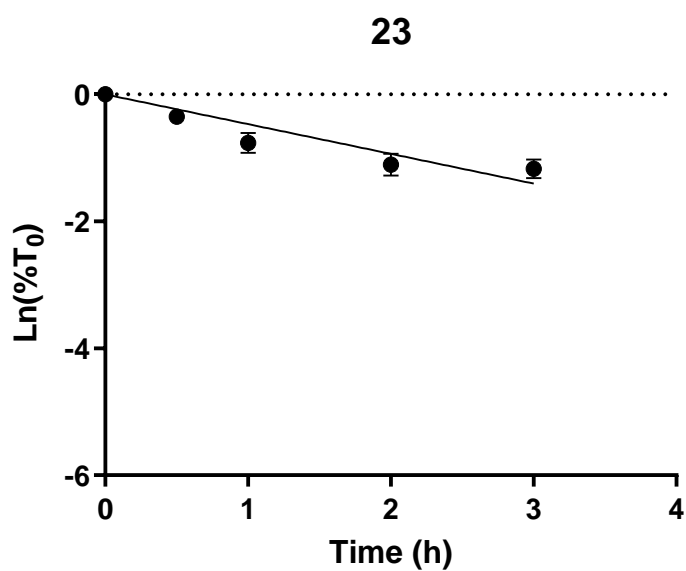**Figure B59.** *In vitro* stability of compound **9** in human liver S9 fraction.
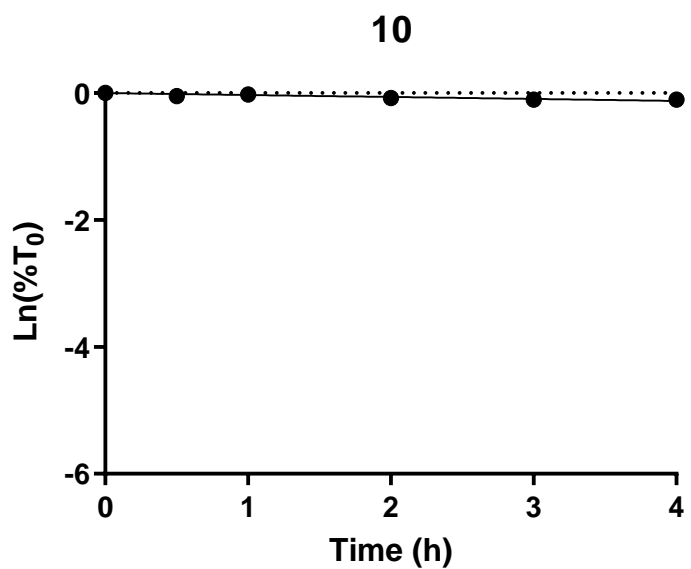
**Figure B60.** *In vitro* stability of compound **10** in human liver S9 fraction.
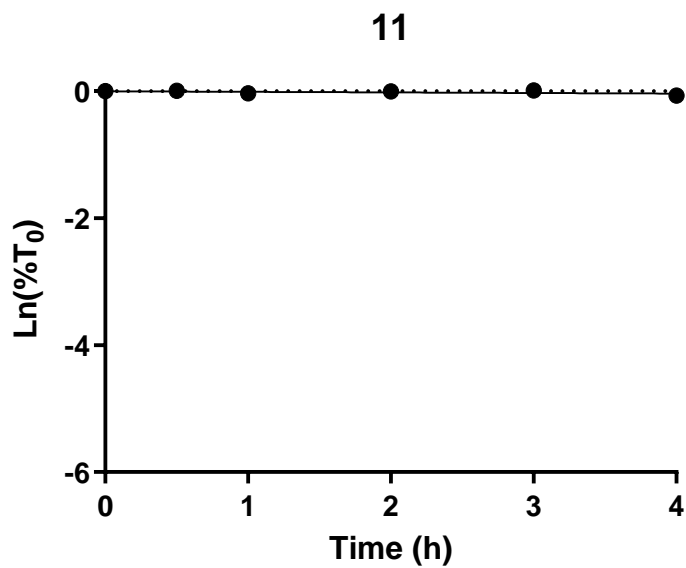
Figure B61. *In vitro* stability of compound **11** in human liver S9 fraction.
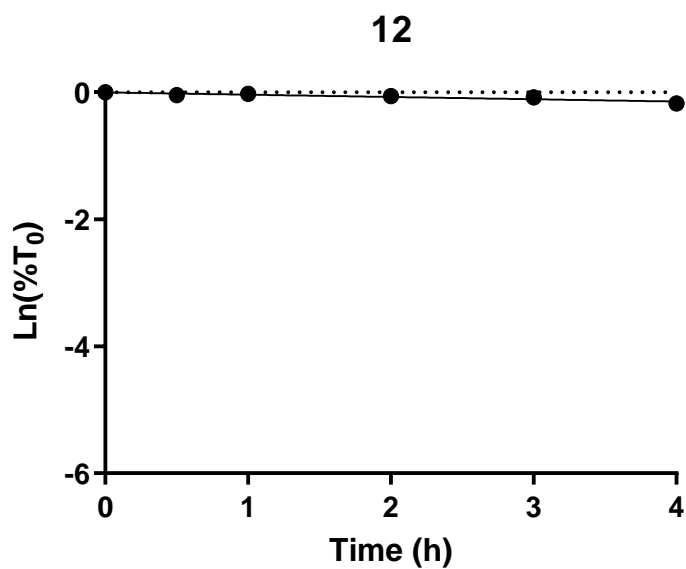
Figure B62. *In vitro* stability of compound **12** in human liver S9 fraction.

13
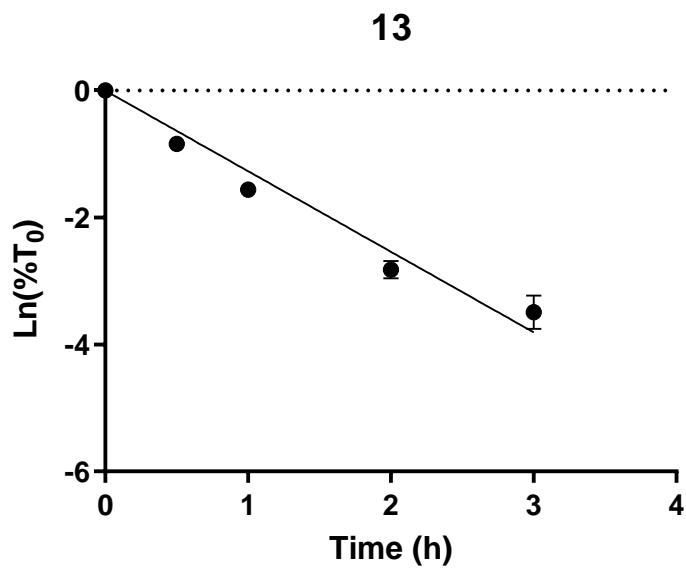
Figure B63. *In vitro* stability of compound **13** in human liver S9 fraction.

14
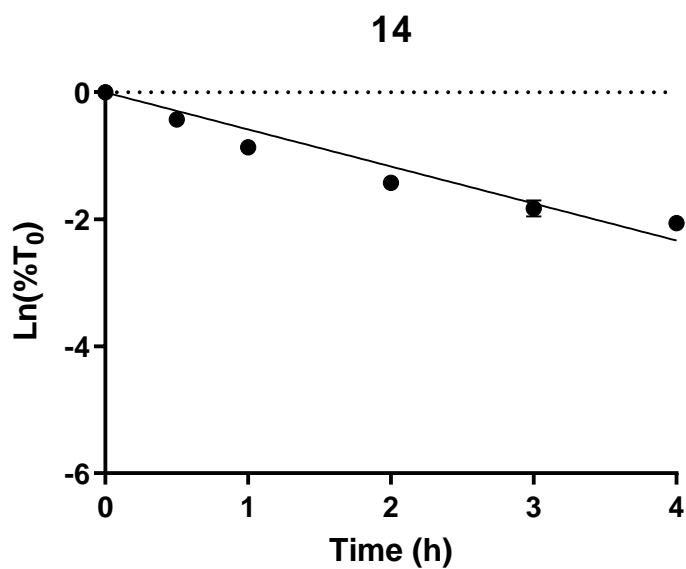
Figure B64. *In vitro* stability of compound **14** in human liver S9 fraction.

15
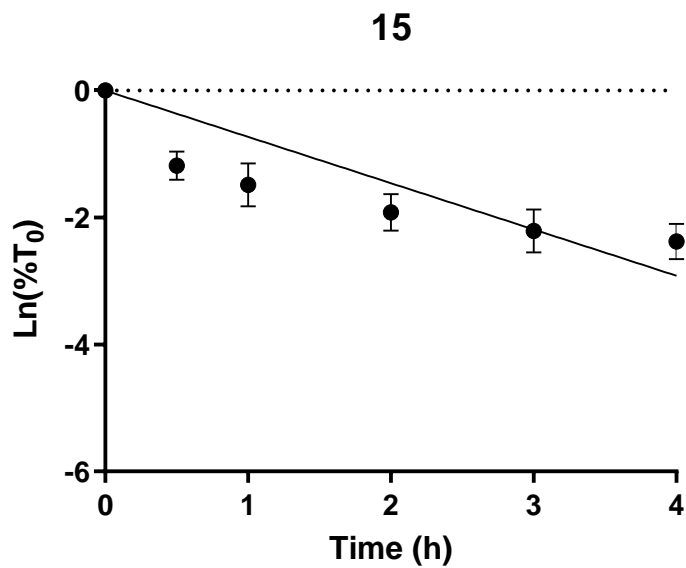
Figure B65. *In vitro* stability of compound **15** in human liver S9 fraction.

16
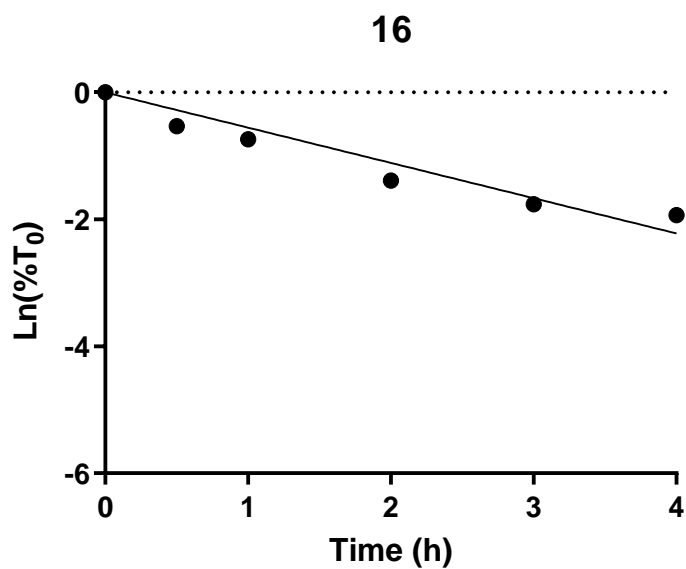
Figure B66. *In vitro* stability of compound **16** in human liver S9 fraction.

17
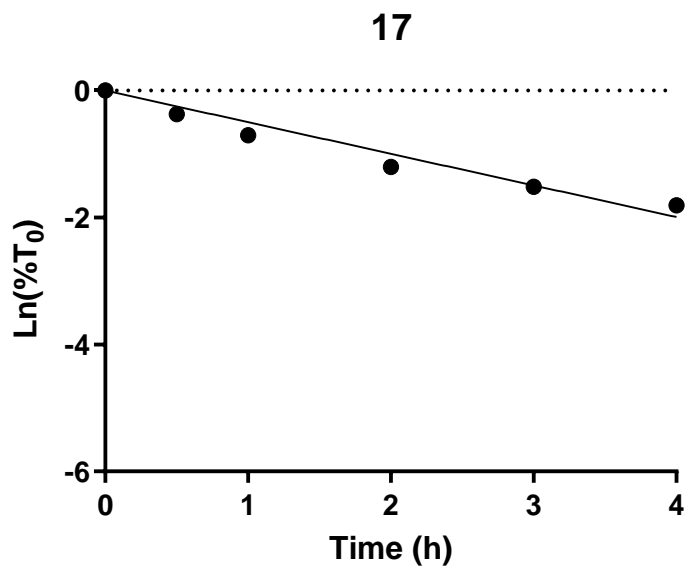
Figure B67. *In vitro* stability of compound **17** in human liver S9 fraction.

18

Figure B68. *In vitro* stability of compound **18** in human liver S9 fraction.

19

Figure B69. *In vitro* stability of compound **19** in human liver S9 fraction.

20

Figure B70. *In vitro* stability of compound **20** in human liver S9 fraction.

22

Figure B71. *In vitro* stability of compound **22** in human liver S9 fraction.

23

Figure B72. *In vitro* stability of compound **23** in human liver S9 fraction.
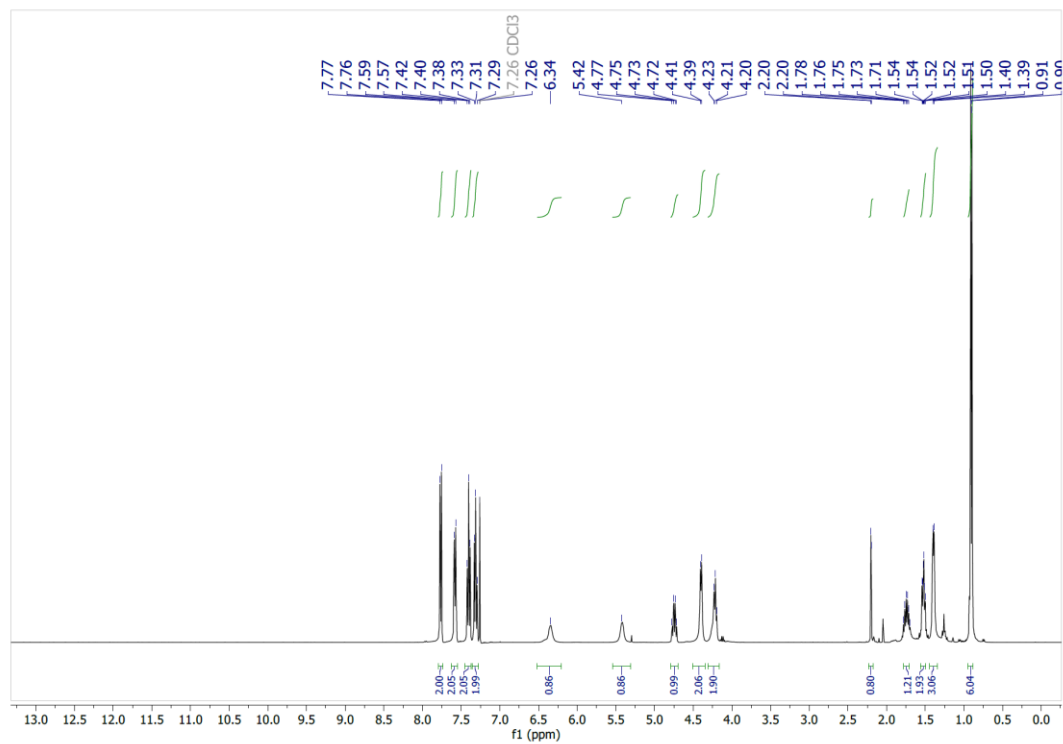
Figure B73. ^{1}H NMR of Fmoc-Ala-Leu alkyne in CDCl$_3$.
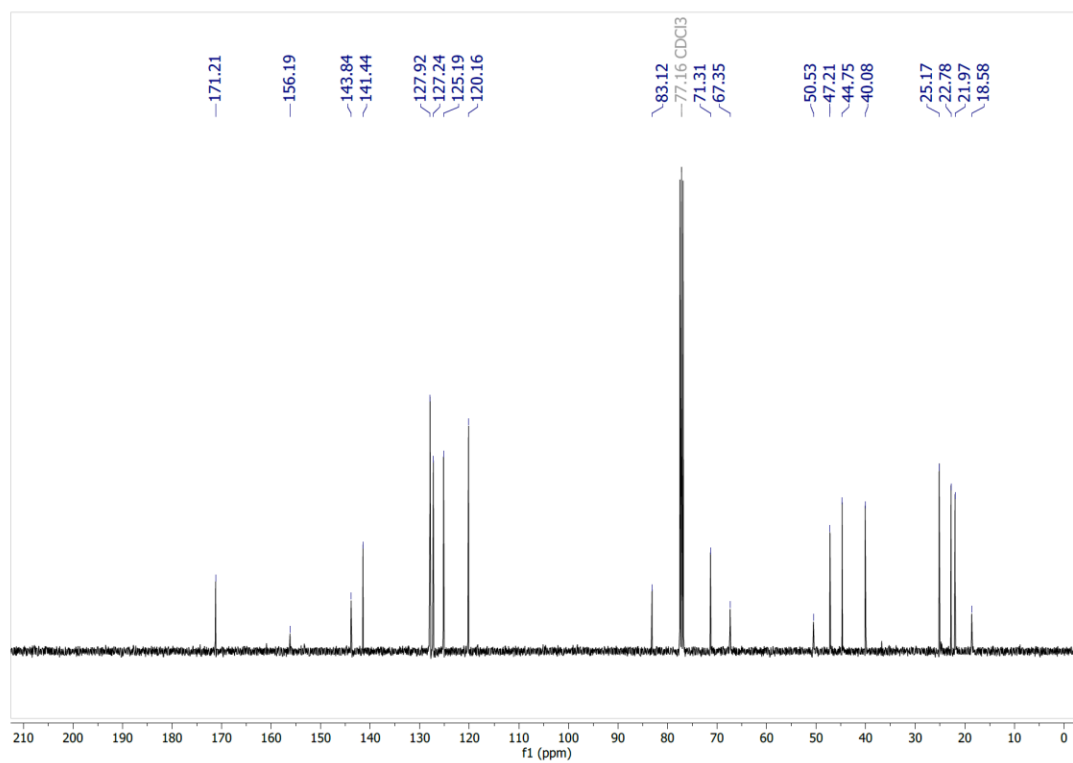
Figure B74. ^{13}C NMR of Fmoc-Ala-Leu alkyne in CDCl$_3$.

Appendix C: Additional Data for Chapter 4
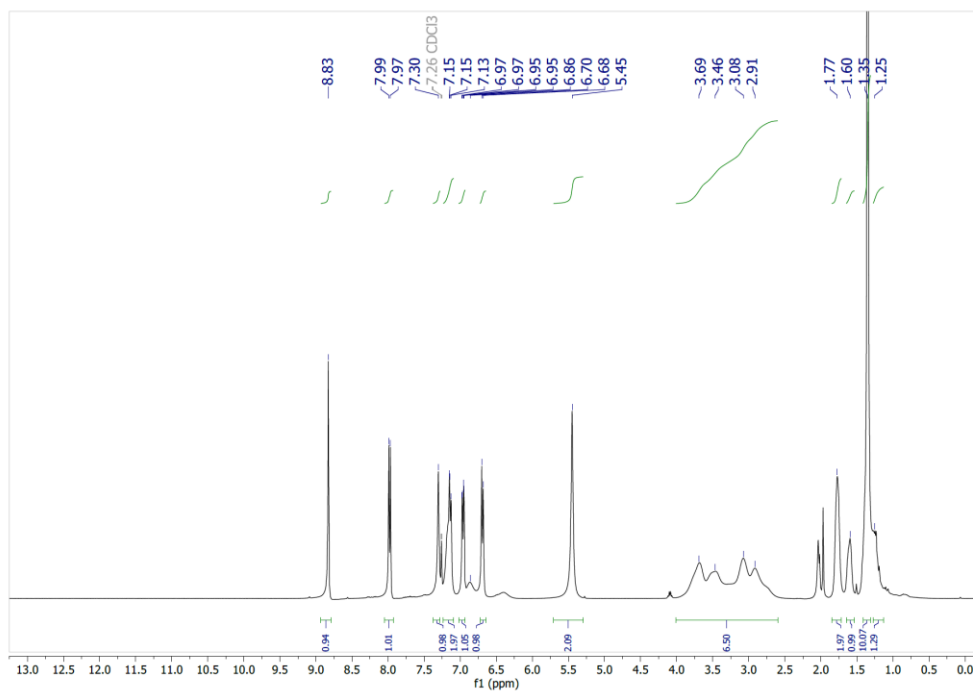
Figure C1. ^{1}H NMR of compound **11** in CDCl$_3$.
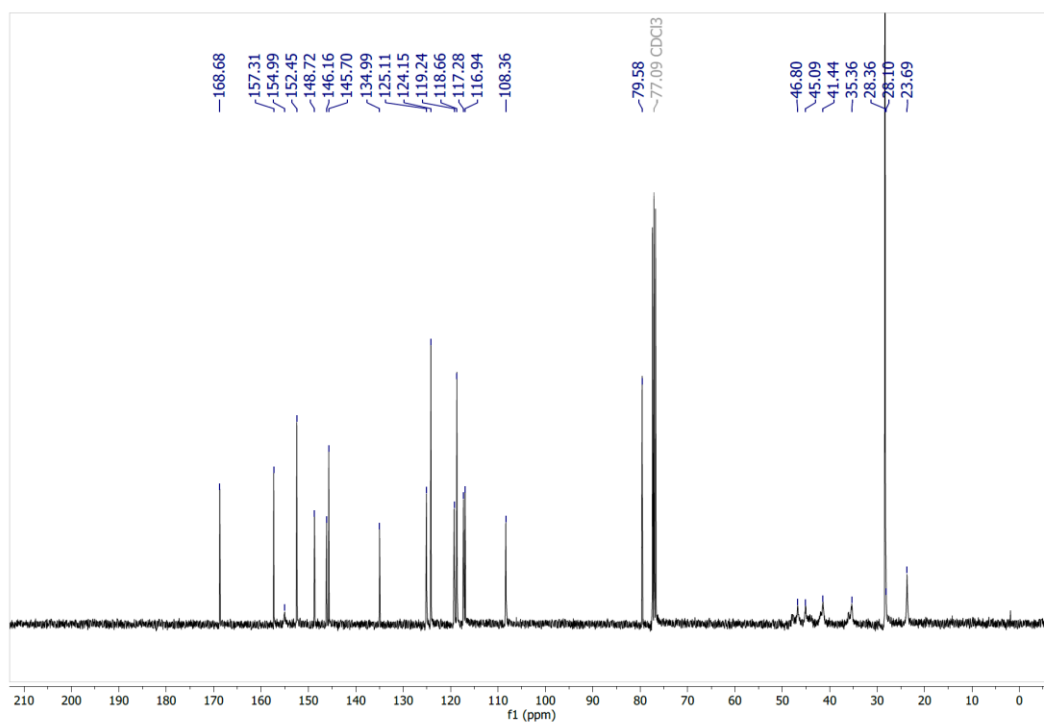
Figure C2. ^{13}C NMR of compound **11** in CDCl$_3$.
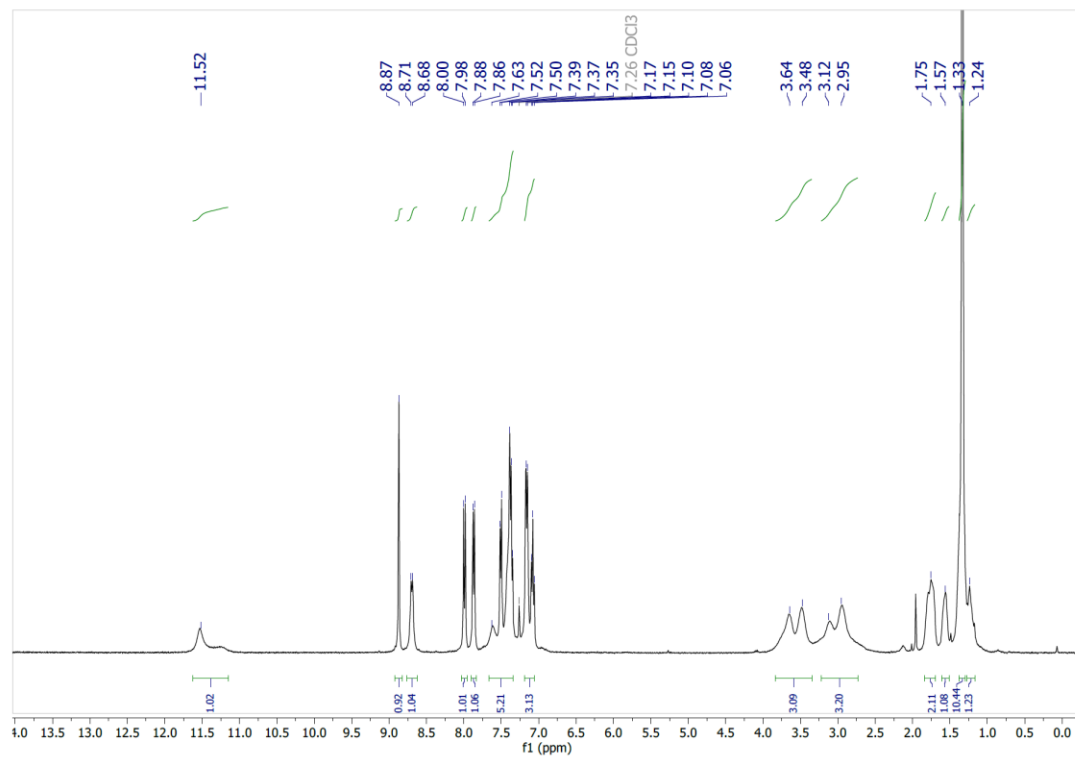
Figure C3. ^{1}H NMR of compound **12** in CDCl$_3$.
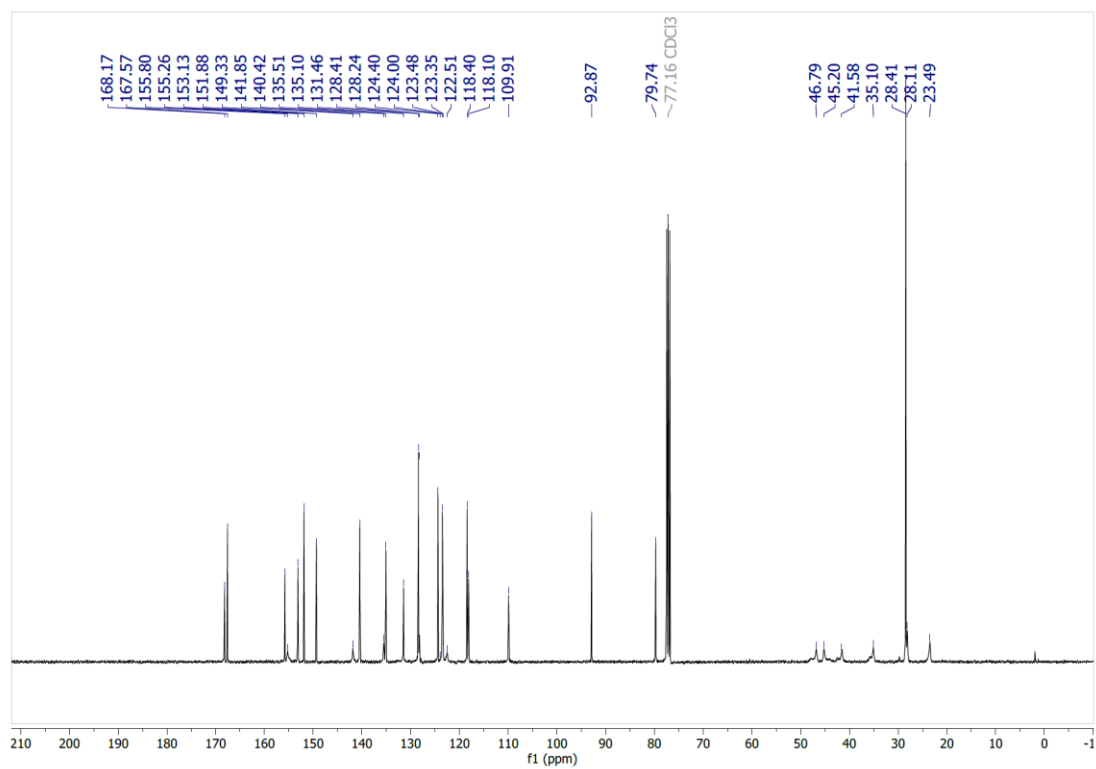
Figure C4. ^{13}C NMR of compound **12** in CDCl$_3$.
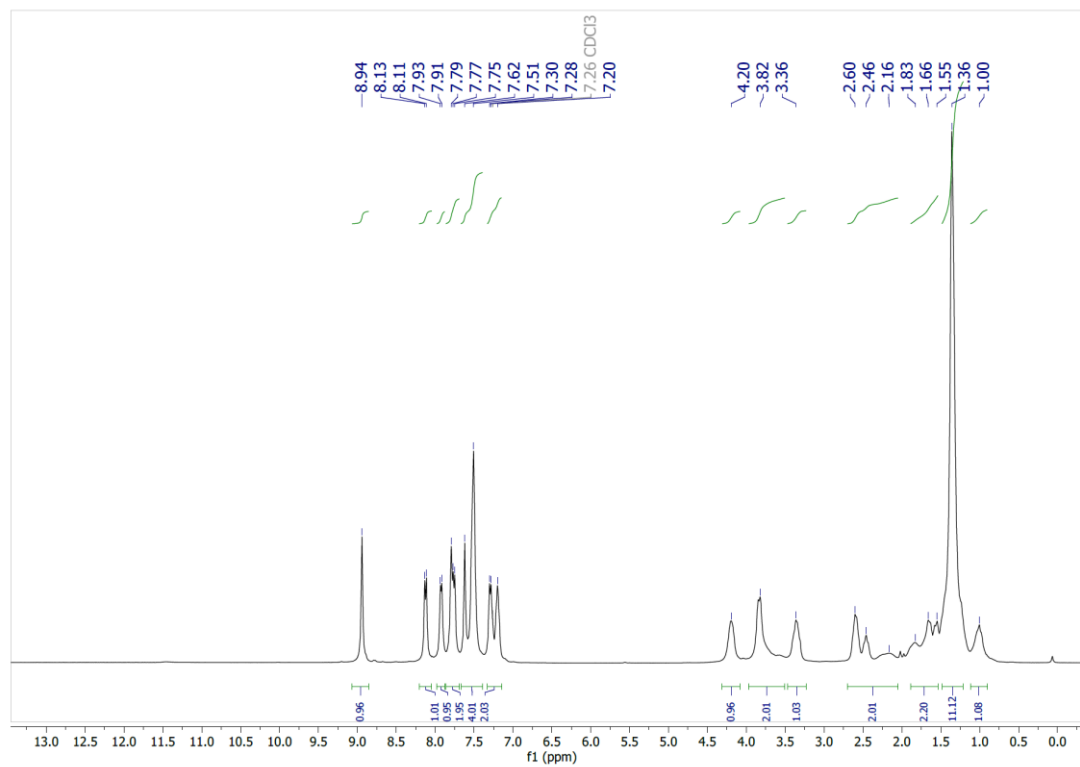
Figure C5. ¹H NMR of compound **8B** in CDCl₃.
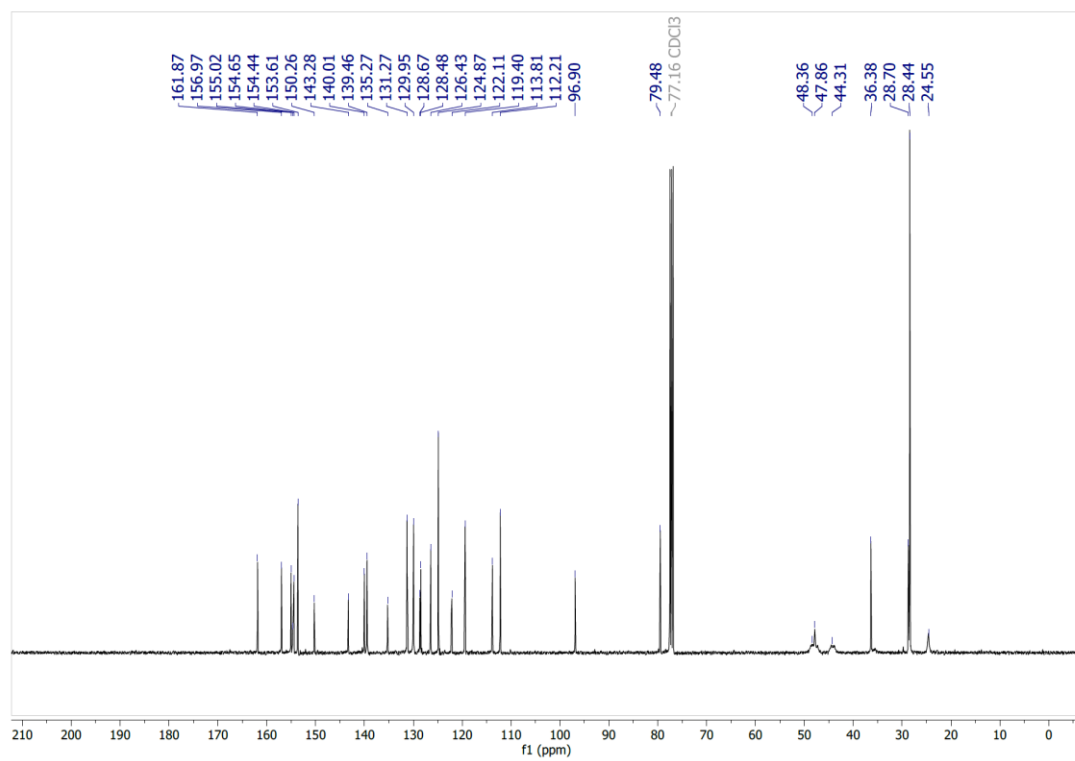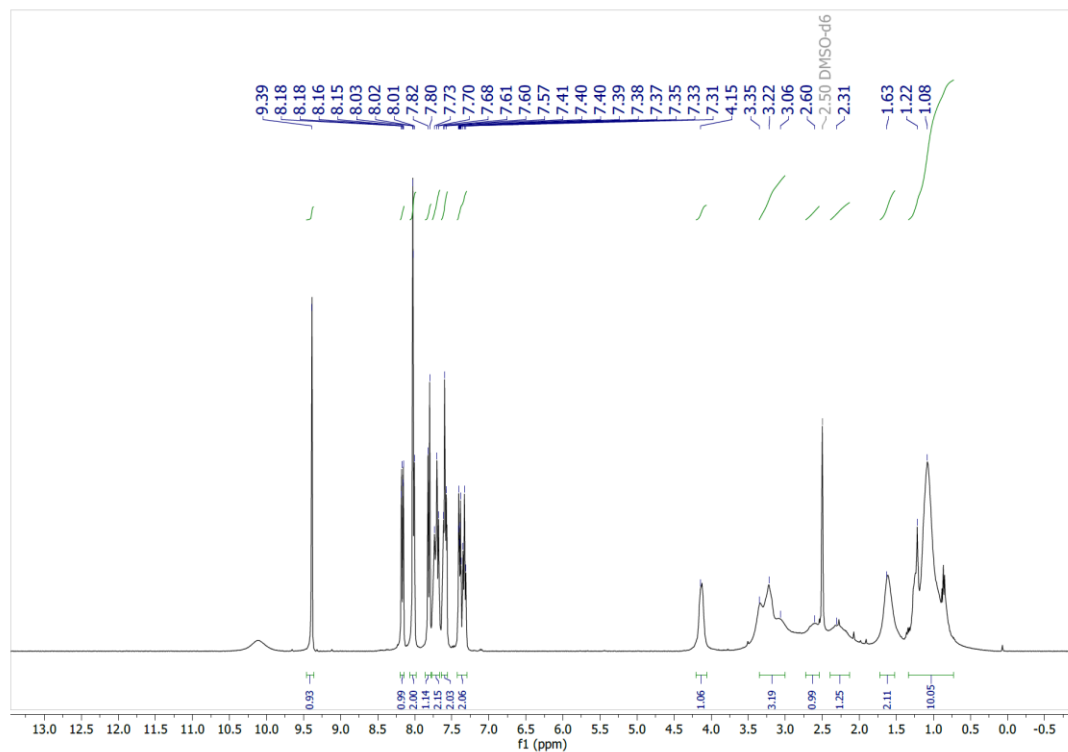

Figure C6. ¹³C NMR of compound **8B** in CDCl₃.

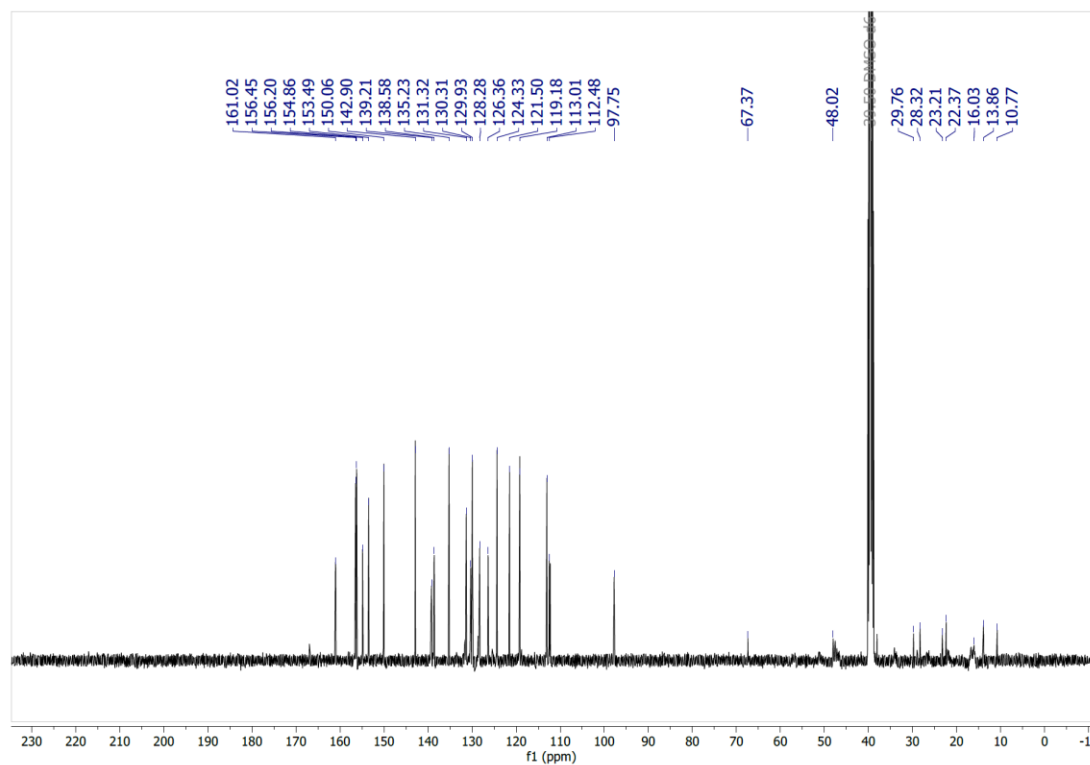**Figure C7.** ^{1}H NMR of compound **13** in DMSO-d6.

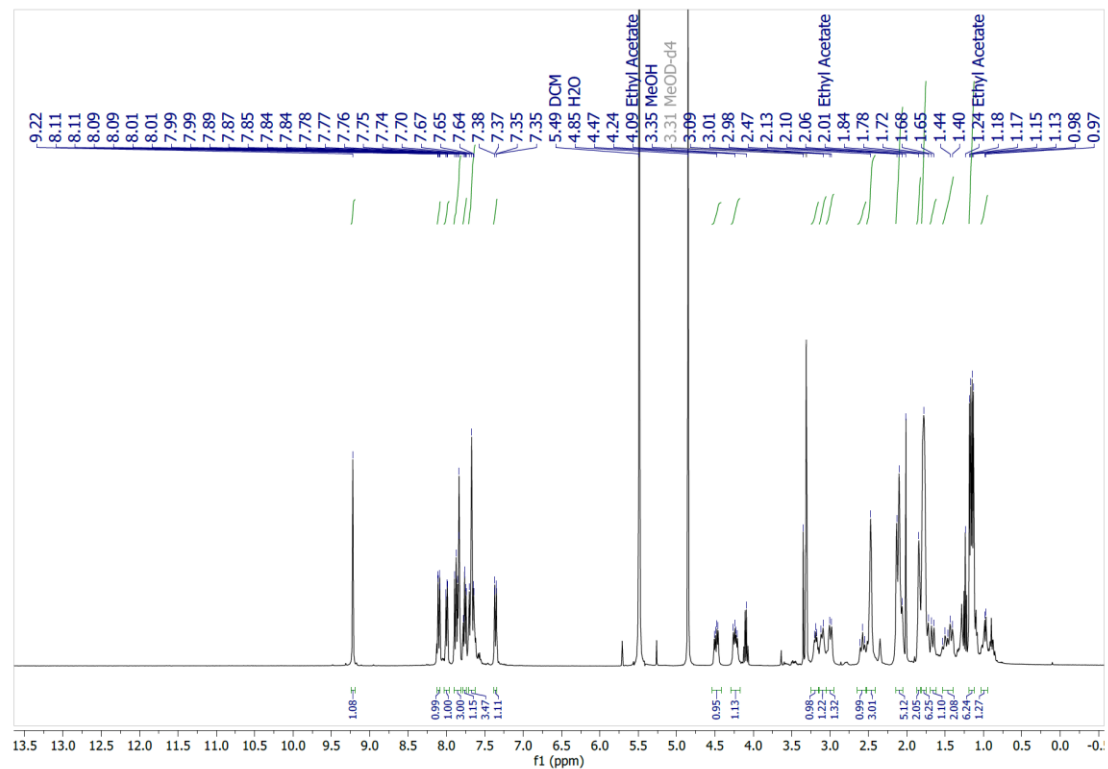**Figure C8.** ^{13}C NMR of compound **13** in DMSO-d6.

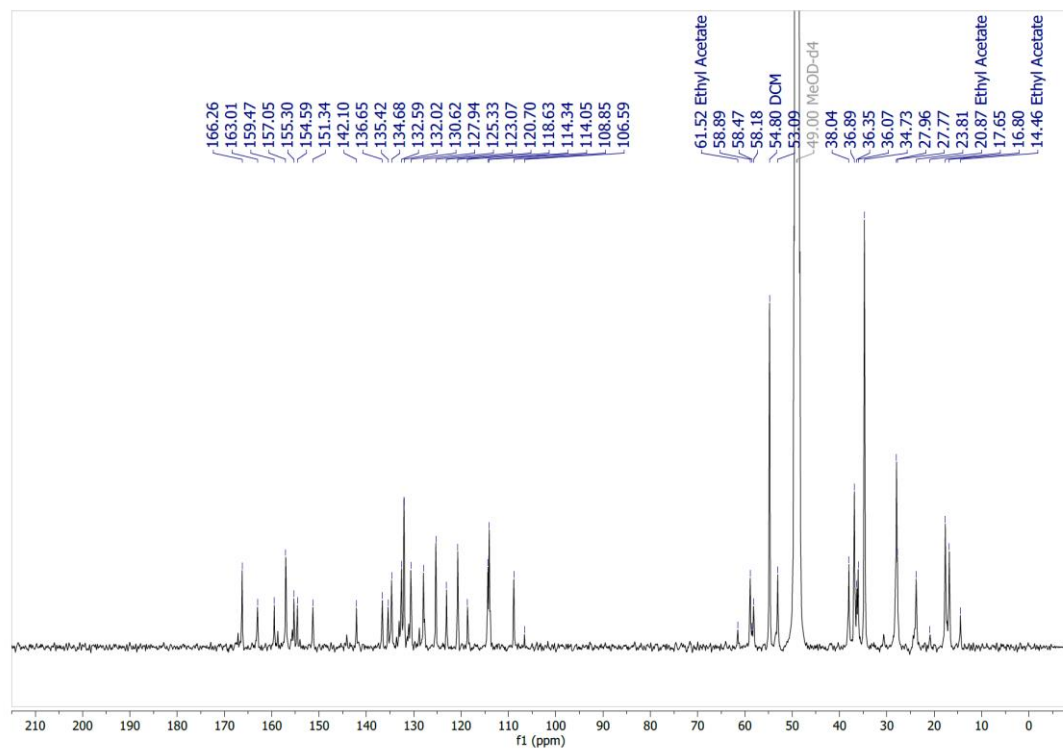**Figure C9.** [^1]H NMR of compound **14** in MeOD-d4.

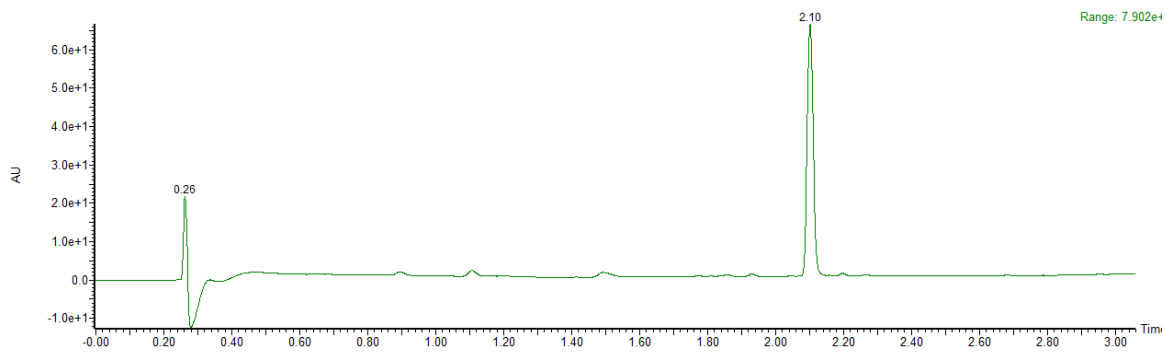**Figure C10.** [^13]C NMR of compound **14** in MeOD-d4.

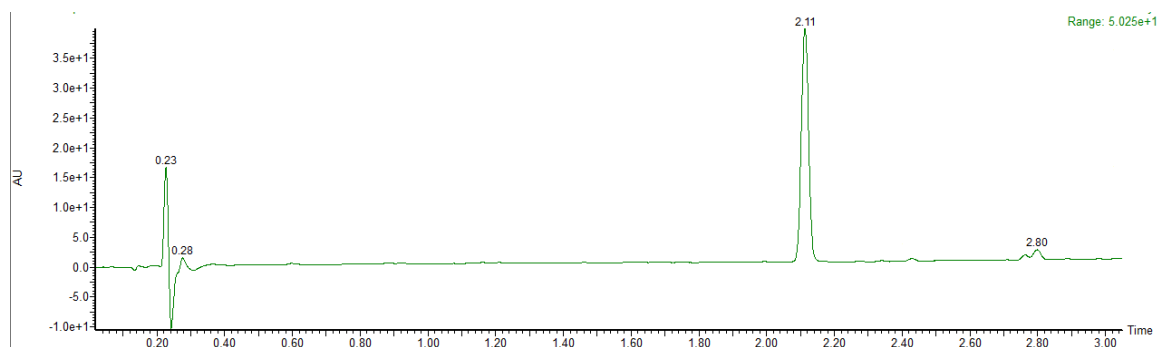**Figure C11.** UHPLC of compound **11** (5-95% ACN in water).

Figure C12. UHPLC of compound **12** (40-95% ACN in water).
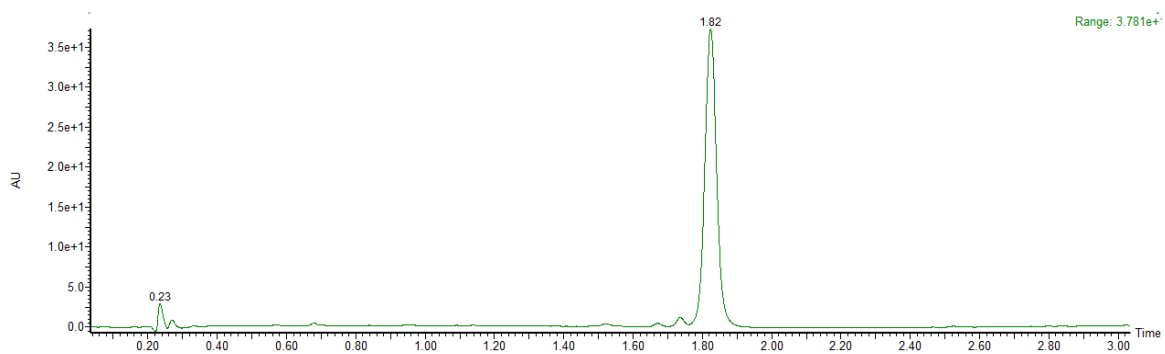

Figure C13. UHPLC of compound **8B** (50-95% ACN in water).
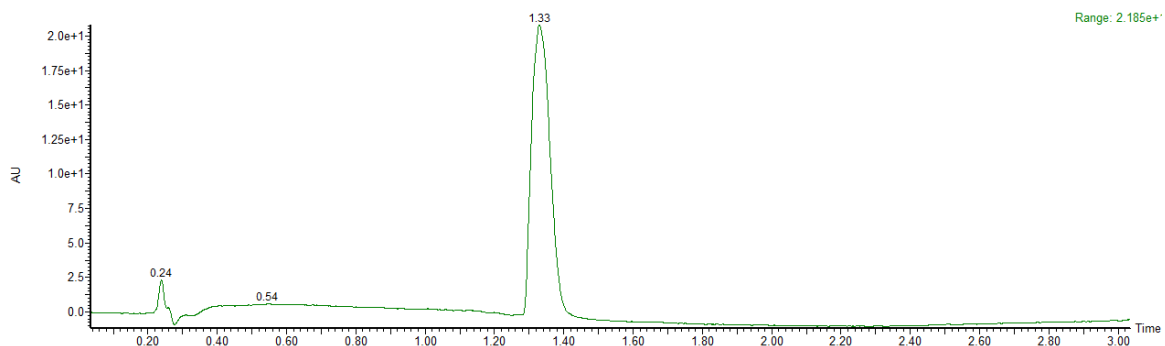
Figure C14. UHPLC of compound **13** (20-95% ACN in water).
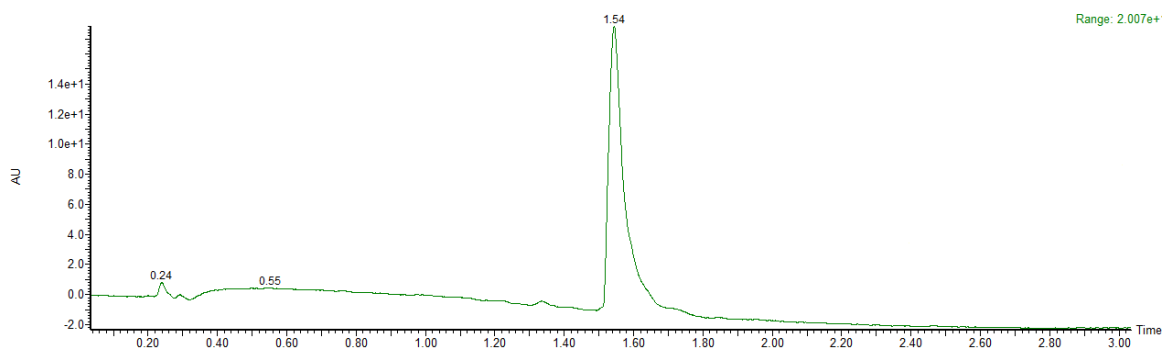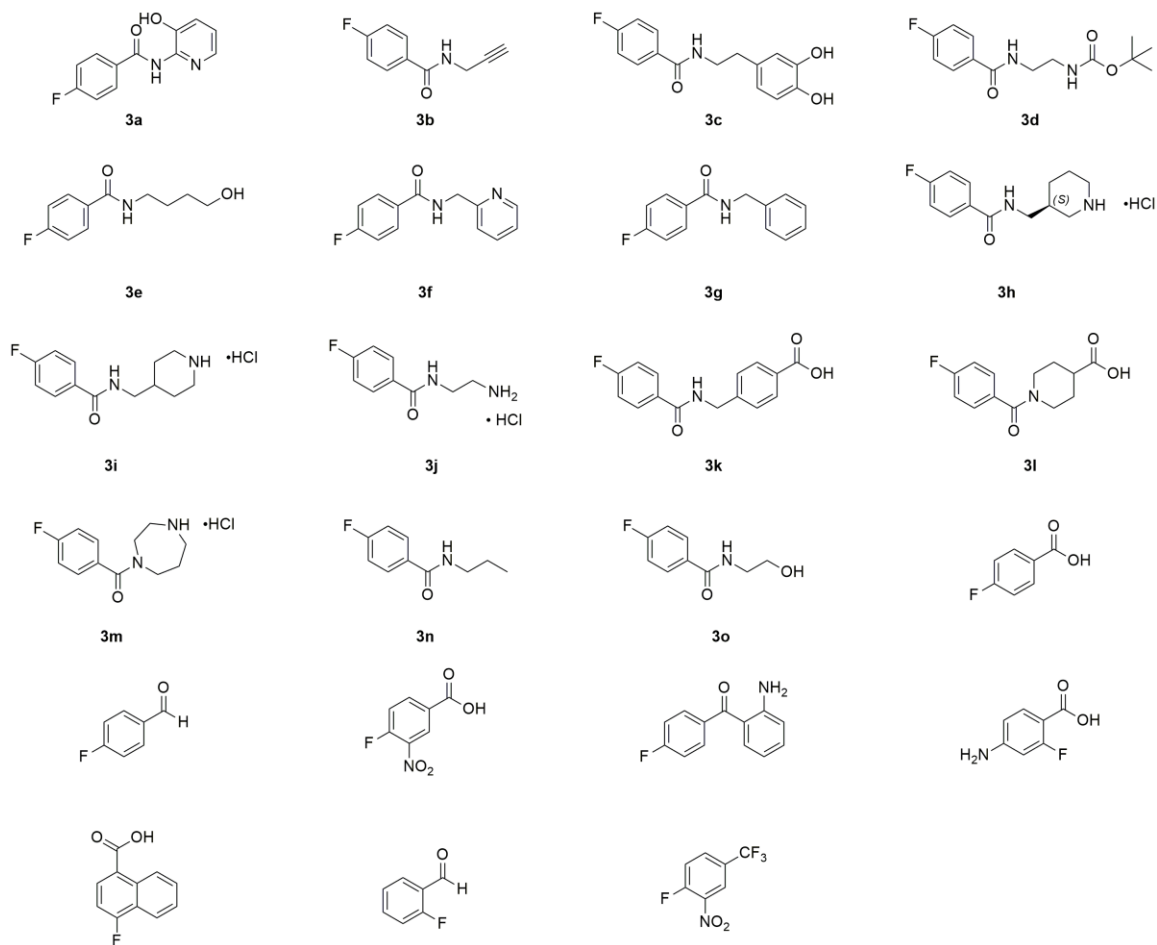

Figure C15. UHPLC of compound **14** (20-95% ACN in water).

Appendix D: Additional Data for Chapter 5

Class A

Figure D1. Structures of fragments in class A.
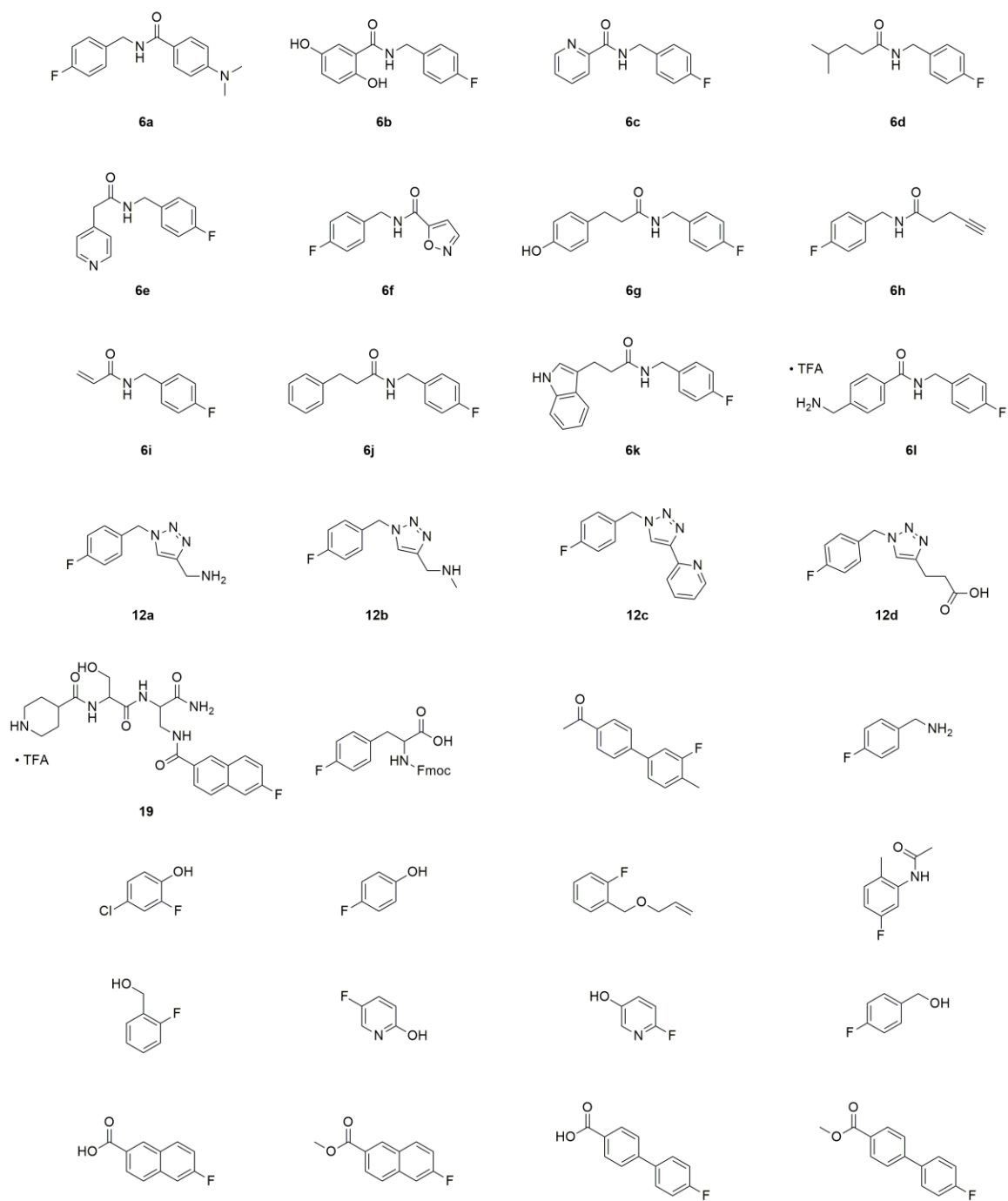
Class B

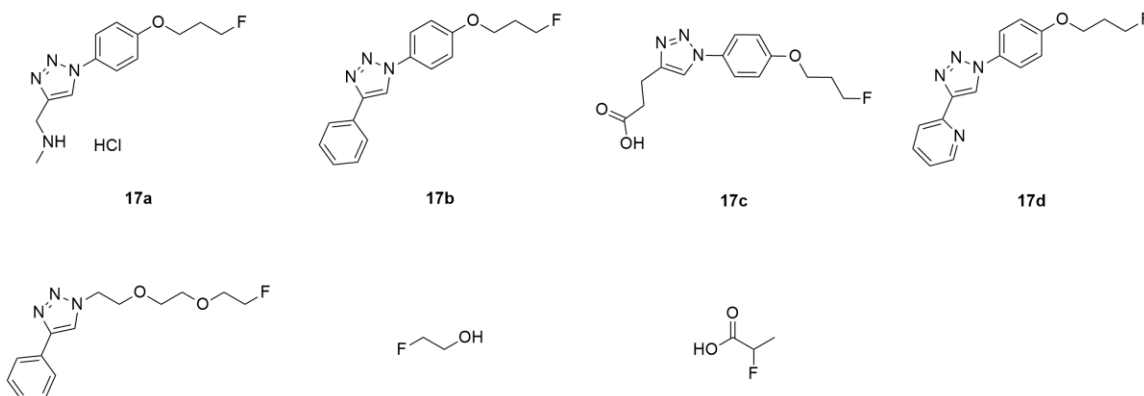**Figure D2.** Structures of fragments in class B.

Class C

Figure D3. Structures of fragments in class C.

4-Fluoro-*N*-(3-hydroxy-2-pyridinyl)benzamide (3a). CAS: 943411-26-5. Purified using 12-100% EtOAc in hexanes to give a white powder (49%). ^{1}H NMR (400 MHz, CDCl$_3$): δ 8.23-8.20 (m, 2H), 7.99 (d, *J* = 5.2 Hz, 1H), 7.39 (d, *J* = 6.4 Hz, 1H), 7.22-7.18 (m, 2H), 6.76-6.72 (m, 1H), 4.63 (s, br, 2H). ^{13}C NMR (100 MHz, CDCl$_3$): δ 167.7, 163.3, 151.3, 145.4, 133.2, 132.9, 129.8, 125.0, 116.2, 114.5. HRMS (ESI$^+$): [M+H]$^+$ calculated: 233.1087; [M+H]$^+$ found: 233.0654.

4-Fluoro-*N*-2-propyn-1-ylbenzamide (3b). CAS: 82225-36-3. Purified using 12-100% EtOAc in hexanes to give a white powder (90%). ^{1}H NMR (400 MHz, CDCl$_3$): δ 7.80-7.78 (m, 2H), 7.12-7.08 (m, 2H), 6.44 (s, br, 1H), 4.23 (dd, *J* = 2.8 Hz, 2.4 Hz, 2H), 2.28 (t, *J* = 2.6 Hz, 1H). ^{13}C NMR (100 MHz, CDCl$_3$): δ 166.2, 163.6, 129.9, 129.3, 115.6, 79.3, 72.04, 29.9. HRMS (ESI$^+$): [M+H]$^+$ calculated: 177.0668; [M+H]$^+$ found: 177.0642.

***N*-(3,4-dihydroxyphenethyl)-4-fluorobenzamide (3c).** CAS: 710292-39-0. Purified using 2-18% MeOH in DCM to give a white powder (91%). ^{1}H NMR (400 MHz, CDCl$_3$): δ 7.69-7.66 (m, 2H), 7.33 (s, br, 1H), 7.09-7.04 (m, 2H), 6.82 (d, *J* = 8 Hz, 1H), 6.75 (s, 1H), 6.60 (dd, *J* = 6Hz, 2Hz, 1H), 6.26 (s, br, 1H), 6.18 (s, 1H), 3.63 (q, *J* = 6.8 Hz, 2H), 2.77 (t, *J* = 6.8 Hz, 2H). ^{13}C NMR (100 MHz, CDCl$_3$): δ 167.6, 163.5, 144.9, 143.4, 130.7, 129.4, 119.7, 115.5, 115.0, 41.6, 34.5. HRMS (ESI$^+$): [M+H]$^+$ calculated: 276.1036; [M+H]$^+$ found: 276.1020.

tert-Butyl (2-(4-fluorobenzamido)ethyl)carbamate (3d). CAS: 260433-18-9. Purified using 12-100% EtOAc in hexanes to give a white powder (96%). ^{1}H NMR (400 MHz, CDCl$_3$): δ 7.85-7.82 (m, 2H), 7.11-7.07 (m, 2H), 4.97, (s, br, 1H), 3.56-3.52 (m, 2H), 3.43-3.39 (m, 2H), 1.42 (s, 9H). ^{13}C NMR (100 MHz, CDCl$_3$): δ 166.6, 163.5, 154.8, 130.3, 129.4, 115.6, 80.2, 42.5, 38.8, 28.3. HRMS (ESI$^+$): [M+H]$^+$ calculated: 283.1458; [M+H]$^+$ found: 283.1490.

4-Fluoro-_N_-(4-hydroxybutyl)benzamide (3e). CAS: 220647-70-1. Purified using 2-20% MeOH in DCM to give a white powder (39%). ^{1}H NMR (400 MHz, CDCl$_3$): δ 7.80-7.76 (m, 2H), 7.11-7.07 (m, 2H), 6.54 (s, br, 1H), 3.73 (m, 2H), 3.50 (q, _J_ = 6.4 Hz, 2H), 1.75-1.66 (m, 5H). ^{13}C NMR (100 MHz, CDCl$_3$): δ 166.5, 163.4, 130.9, 129.2, 115.6, 62.5, 39.9, 29.8, 26.3. HRMS (ESI$^+$): [M+H]$^+$ calculated: 212.1087; [M+H]$^+$ found: 212.1006.

4-Fluoro-_N_-(2-pyridinylmethyl)benzamide (3f). CAS: 326902-23-2. Purified using 2-20% MeOH in DCM to give a white powder (90%). ^{1}H NMR (400 MHz, CDCl$_3$): δ 8.55 (d, _J_ = 4.4 Hz, 1H), 7.91-7.87 (m, 2H), 7.69 (t, _J_ = 7.6, 6 Hz, 1H), 7.64 (s, br, 1H), 7.33 (d, _J_ = 7.6 Hz, 1H), 7.24-7.21 (m, 1H), 7.14-7.10 (m, 2H), 4.74 (d, _J_ = 4.8 Hz, 2H). ^{13}C NMR (100 MHz, CDCl$_3$): δ 166.3, 163.5, 155.9, 149.0, 136.8, 130.6, 129.4, 122.5, 122.2, 115.6, 44.7. HRMS (ESI$^+$): [M+H]$^+$ calculated: 231.0934; [M+H]$^+$ found: 231.0863.

4-Fluoro-_N_-(phenylmethyl)benzamide (3g). CAS: 725-38-2. Purified using 10-80% EtOAc in hexanes to give a white powder (93%). ^{1}H NMR (400 MHz, CDCl$_3$): δ 7.82-7.82 (m, 2H), 7.37-7.30 (m, 5H), 7.12-7.08 (m, 2H), 4.64 (d, _J_ = 5.6 Hz, 2H). ^{13}C NMR (100 MHz, CDCl$_3$): δ 166.3, 164.5, 138.1, 130.6, 129.3, 128.8, 127.9, 127.7, 115.7, 44.2. HRMS (ESI$^+$): [M+H]$^+$ calculated: 230.0981; [M+H]$^+$ found: 230.0951.

_(S)_-4-fluoro-_N_-(piperidin-3-ylmethyl)benzamide hydrochloride (3h). CAS: 1016685-25-8. A colourless oil revealed the hydrochloride salt, **3h** (48%). ^{1}H NMR (400 MHz, D$_2$O): δ 7.73- 7.69 (m, 2H), 7.18-7.13 (m, 2H), 3.38-3.28 (m, 4H), 2.85 (t, _J_ = 12.4 Hz, 1H), 2.70 (t, _J_ = 12.4 Hz, 1H), 2.09-2.03 (m, 1H), 1.93-1.86 (m, 2H), 1.70-1.60 (m, 1H), 1.32-1.21 (m, 1H). ^{13}C NMR (100 MHz, D$_2$O): δ 170.2, 163.5, 129.6, 115.8, 115, 5, 46.8, 44.1, 42.3, 33.9, 25.7, 21.4. HRMS (ESI$^+$): [M+H]$^+$ calculated: 237.1403; [M+H]$^+$ found: 237.1758.

4-Fluoro-*N*-(piperidin-4-ylmethyl)benzamide hydrochloride (3i). CAS: 748078-33-3. A white solid revealed the hydrochloride salt, **3i** (68%). ^{1}H NMR (400 MHz, MeOD-d_4): δ 7.90-7.86 (m, 2H), 7.22-7.18 (m, 2H), 3.42-3.39 (m, 2H), 3.34-3.32 (m, 2H), 3.01-2.95 (m, 2H), 2.01-1.97 (m, 3H), 1.52-1.43 (m, 2H). ^{13}C NMR (100 MHz, D$_2$O): δ 170.0, 163.4, 129.5, 129.4, 115.7, 44.3, 43.7, 33.5, 26.1. HRMS (ESI$^+$): [M+H]$^+$ calculated: 237.1403; [M+H]$^+$ found: 237.1367.

***N*-(2-aminoethyl)-4-fluorobenzamide hydrochloride (3j):** CAS: 94319-99-0. A white solid revealed the hydrochloride salt **3j** (90 %). ^{1}H NMR (400 MHz, MeOD-d_4): δ 7.96-7.92 (m, 2H), 7.23-7.19 (m, 2H), 3.66 (t, *J* = 5.6, 6 Hz, 2H*)*, 3.16 (t, *J* = 6, 5.6 Hz, 2H). ^{13}C NMR (100 MHz, MeOD-d_4): δ 170.4, 163.6, 129.7, 129.2, 115.8, 39.3, 37.3. HRMS (ESI$^+$): [M+H]$^+$ calculated: 183.0934; [M+H]$^+$ found: 183.0970.

4-((4-Fluorobenzamido)methyl)benzoic acid (3k): CAS: 925137-90-2. Reaction time: 2 h. Purified using 12-100% EtOAc in hexanes to give a white powder (83%). ^{1}H NMR (400 MHz, DMSO-d_6): δ 12.87 (s, br, 1H), 9.14 (s, br, 1H), 7.97-7.89 (m, 2H), 7.88 (d, *J* = 8 Hz, 2H), 7.40 (d, *J* = 8.4 Hz, 2H), 7.33-7.28 (m, 2H), 4.52 (d, *J* = 6 Hz, 2H). ^{13}C NMR (100 MHz, DMSO-d_6): δ 167.6, 165.7, 163.2, 145.2, 131.1, 130.4, 129.9, 129.7, 115.7, 43.0. HRMS (ESI$^+$): [M+H]$^+$ calculated: 274.0879; [M+H]$^+$ found: 274.0734.

1-(4-Fluorobenzoyl)piperidine-4-carboxylic acid (3l): CAS: 139679-45-1. Reaction time: 18 h. Purified using 2-20% MeOH in DCM to give a white powder (44%). ^{1}H NMR (400 MHz, MeOD-d_4): δ 7.50-7.66 (m, 2H), 7.24-7.19 (m, 2H) 4.46-4.45 (m, 1H), 3.73-3.71 (m, 1H), 3.16-3.13 (m, 2H), 2.70-2.62 (m, 1H), 2.04-1.92 (m, 2H), 1.70-1.69 (m, 2H). ^{13}C NMR (100 MHz, MeOD-d_4): δ 176.4, 170.2, 162.3, 131.9, 129.0, 115.3, 41.4, 40.4, 28.3. HRMS (ESI$^+$): [M+H]$^+$ calculated: 252.1036; [M+H]$^+$ found: 252.1016.

(1,4-Diazepan-1-yl)(4-fluorophenyl)methanone hydrochloride (3m): CAS: 1269152-18-2. A beige solid revealed the hydrochloride salt, **3m** (12%). ^{1}H NMR (400 MHz, D$_2$O): δ 7.45-7.40 (m, 2H), 7.20-7.15 (m, 2H), 3.91-3.88 (m, 1H), 3.77-3.72 (m, 1H), 3.56 (t, *J* = 6.4, 6 Hz, 2H), 3.42-3.40 (m, 1H), 3.34-3.23 (m, 3H), 2.14 (s, 1H), 2.01-1.99 (m, 2H). ^{13}C NMR (100 MHz, D$_2$O): δ 173.3, 162.3, 130.4, 129.1, 115.9, 48.4, 45.1, 44.5, 42.1, 25.3. HRMS (ESI$^+$): [M+H]$^+$ calculated: 223.1247; [M+H]$^+$ found: 223.1217.

4-Fluoro-*N*-propylbenzamide (3n): CAS: 349129-65-3. Purified using 12-100% EtOAc in hexanes to give a white powder (89%). ^{1}H NMR (400 MHz, CDCl$_3$): δ 7.75-7.71 (m, 2H), 7.09-7.04 (m, 2H), 6.03 (s, br, 1H), 3.37 (q, *J = 6.8, 6, 6.8 Hz*, 2H), 1.61 (sextet, *J =* 7.2 Hz, 2H), 0.95 (t, *J =* 7.6 Hz, 2H). ^{13}C NMR (100 MHz, CDCl$_3$): δ 166.5, 163.4, 131.0, 129.1, 115.6, 41.8, 22.9, 11.4. HRMS (ESI$^+$): [M+H]$^+$ calculated: 182.0981; [M+H]$^+$ found: 182.0951.

4-Fluoro-N-(2-hydroxyethyl)benzamide (3o): CAS: 57728-63-9. Purified using 2-20% MeOH in DCM to give a white powder (94%). ^{1}H NMR (400 MHz, MeOD-*d$_4$*): δ 7.91-7.87 (m, 2H), 7.20-7.16 (m, 2H), 3.70 (t, *J* = 6 Hz, 2H), 3.49 (t, *J* = 6 Hz, 2H). ^{13}C NMR (100 MHz, MeOD-*d$_4$*): δ 167.9, 163.5, 130.6, 129.5, 114.8, 60.2, 42.2. HRMS (ESI$^+$): [M+H]$^+$ calculated: 184.0774; [M+H]$^+$ found: 184.0759.

4-(Dimethylamino)-*N*-(4-fluorobenzyl)benzamide (6a). CAS: 1181040-77-6. ^{1}H NMR (400 MHz, CDCl$_3$): δ 7.69 (d, *J* = 9.2 Hz, 2H), 7.34-7.30 (m, 2H), 7.04-7.00 (m, 2H), 6.66 (d, *J* = 9.2 MHz, 2H), 6.25 (s, br, 1H), 4.60 (d, *J* = 5.6 Hz, 2H), 3.02 (s, 6H). ^{13}C NMR (100 MHz, CDCl$_3$): δ 167.2, 163.3, 152.5, 134.7, 129.5, 128.4, 120.9, 115.6, 111.1, 43.2, 40.1. HRMS (ESI$^+$): [M+H]$^+$ calculated: 273.1403; [M+H]$^+$ found: 273.1404.

N-(4-fluorobenzyl)-2,5-dihydroxybenzamide (6b):** CAS: 1912060-64-0. Purified using 12-100% EtOAc in hexanes to give a white powder (59%). ^{1}H NMR (400 MHz, DMSO-*d$_6$*): δ 11.6 (s, 1H), 9.21 (s, br, 1H), 9.02 (s, 1H), 7.37-7.34 (m, 2H), 7.25-7.23 (m, 1H), 7.18-7.13 (m, 2H), 6.87-6.84 (m, 1H), 6.75-6.72 (m, 1H), 4.45 (d, *J* = 6 Hz, 2H). ^{13}C NMR (100 MHz, DMSO-*d$_6$*): δ 168.8, 160.4, 152.6, 149.8, 135.8, 129.8, 121.8, 118.3, 116.2, 115.6, 113.9, 42.2. HRMS (ESI$^+$): [M+H]$^+$ calculated: 262.0879; [M+H]$^+$ found: 262.0897.

N-(4-fluorobenzyl)picolinamide (6c):** CAS: 803694-10-2. Purified using 12-100% EtOAc in hexanes to give a white powder (76%). ^{1}H NMR (400 MHz, CDCl$_3$): δ 8.53 (d, *J* = 4.8 Hz, 1H), 8.37 (s, br, 1H), 8.23 (d, *J* = 7.6 Hz, 1H), 7.86 (t, *J* = 7.6 Hz, 1H), 7.45-7.42 (m, 1H), 7.35-7.32 (m, 2H), 7.04-7.00 (m, 2H), 4.64 (d, *J* = 2.8 Hz, 2H). ^{13}C NMR (100 MHz, CDCl$_3$): δ 164.2, 160.9, 149.7, 48.1, 137.4, 134.0, 129.5, 126.3, 122.4, 115.6, 42.76. HRMS (ESI$^+$): [M+H]$^+$ calculated: 231.0934; [M+H]$^+$ found: 231.0959.

N-(4-fluorobenzyl)-4-methylpentanamide (6d): CAS: 1624371-59-0. Purified using 12-100% EtOAc in hexanes to give a white powder (98%). ^{1}H NMR (400 MHz, CDCl$_3$): δ 7.26-7.22 (m, 2H), 7.03-6.99 (m, 2H), 5.76 (br s, 1H), 4.40 (d, J = 6 Hz, 2H), 2.23-2.19 (m, 2H), 1.56-1.53 (m, 3H), 0.90 (d, J = 6 Hz, 6H). ^{13}C NMR (100 MHz, CDCl$_3$): δ 173.1, 160.9, 134.3, 129.5, 115.6, 42.8, 34.7, 34.5, 27.8, 22.3. HRMS (ESI$^+$): [M+H]$^+$ calculated: 224.1451; found: 224.1357.

N-(4-fluorobenzyl)-2-(pyridin-4-yl)acetamide (6e): CAS: 1790880-41-9. Purified using 2-20% MeOH in DCM to give a white powder (60%). ^{1}H NMR (400 MHz, CDCl$_3$): δ 8.55-8.54 (m, 2H), 7.22-7.17 (m, 4H), 7.01-6.97 (m, 2H), 5.91 (s, br, 1H), 4.38 (d, J = 5.6 Hz, 2H), 3.56 (s, 2H). ^{13}C NMR (100 MHz, CDCl$_3$): δ 168.9, 160.9, 150.2, 143.7, 133.7, 129.4, 124.7, 115.7, 43.1, 42.8. HRMS (ESI$^+$): [M+H]$^+$ calculated: 245.1090; [M+H]$^+$ found: 245.1073.

N-(4-fluorobenzyl)isoxazole-5-carboxamide (6f): CAS: 1786325-99-2. Purified using 15-100% EtOAc in hexanes to give beige crystals (18%). ^{1}H NMR (400 MHz, CDCl$_3$): δ 8.34 (d, J = 2 Hz, 1H), 7.34-7.31 (m, 2H), 7.07-7.03 (m, 2H), 6.95 (d, J = 1.6 Hz, 1H), 6.88 (s, br, 1H), 4.60 (d, J = 6 Hz, 2H). ^{13}C NMR (100 MHz, CDCl$_3$): δ 163.4, 160.9, 156.7, 150.9, 134.1, 129.3, 114.9, 105.7, 41.9. HRMS (ESI$^+$): [M+H]$^+$ calculated: 221.0726; [M+H]$^+$ found: 221.0722.

N-(4-fluorobenzyl)-3-(4-hydroxyphenyl)propanamide (6g): CAS: none found. Purified by precipitating from DCM. The product was obtained as a fine white powder (61%). ^{1}H NMR (400 MHz, DMSO-d_6): δ 9.17 (s, 1H), 8.29 (t, J = 8 Hz, 1H), 7.14-7.06 (m, 4H), 6.99-6.96 (m, 2H), 6.66-6.63 (m, 2H), 4.21 (d, J = 6 Hz, 2H), 2.72 (t, J = 7.2 Hz, 2H), 2.37 (t, J = 7.2 Hz, 2H). ^{13}C NMR (100 MHz, DMSO-d_6): δ 171.4, 159.8, 155.5, 135.7, 131.2, 129.2, 129.0, 115.0, 114.7, 41.2, 37.4, 30.3. HRMS (ESI$^+$): [M+H]$^+$ calculated: 274. 1243; [M+H]$^+$ found: 274.1154.

N-(4-fluorobenzyl)pent-4-ynamide (6h): CAS: none found. Purified using 12-100% EtOAc in hexanes to give a white crystalline solid (85%). ^{1}H NMR (400 MHz, CDCl$_3$): δ 7.28-7.25 (m, 2H), 7.04-6.99 (m, 2H), 5.94 (s, br, 1H), 4.43 (d, J = 5.6 Hz, 2H), 2.59-2.54 (m, 2H), 2.45-2.42 (m, 2H), 1.99 (t, J = 2.8 Hz, 1H). ^{13}C NMR (100 MHz, CDCl$_3$):

δ 171.0, 161.1, 134.1, 129.7, 115.8, 83.1, 69.6, 43.1, 35.5, 15.1. HRMS (ESI$^+$): [M+H]$^+$ calculated: 206.0981; [M+H]$^+$ found: 206.0985.

***N*-(4-fluorobenzyl)acrylamide (6i):** CAS: 1046471-60-6. Purified using 12-100% EtOAc in hexanes to give a pink crystalline solid (23%). ^{1}H NMR (400 MHz, CDCl$_3$): δ 7.28-7.25 (m, 2H), 7.04-6.99 (m, 2H), 6.33 (dd, *J* = 16.8, 1.2 Hz, 1H), 6.11 (dd, *J* =16.8, 10.4 Hz, 1H), 5.90 (s, br, 1H), 5.68 (dd, *J* = 10.4, 1.6 Hz, 1H), 4.48 (d, *J* = 6 Hz, 2H). ^{13}C NMR (100 MHz, CDCl$_3$): δ 165.3, 161.0, 133.9, 130.5, 129.6, 127.0, 115.7, 42.9. HRMS (ESI$^+$): [M+H]$^+$ calculated: 180.0825; [M+H]$^+$ found: 180.0825.

***N*-(4-fluorobenzyl)-3-phenylpropanamide (6j):** CAS: 392740-97-5. Purified using 12-100% EtOAc in hexanes to give a white solid (69%). ^{1}H NMR (400 MHz, CDCl$_3$): δ 7.29-7.27 (m, 2H), 7.23-7.18 (m, 3H), 7.10-7.06 (m, 2H), 6.98-6.93 (m, 2H), 5.67 (s, br, 1H), 4.34 (d, *J* = 6 Hz, 2H), 2.99 (t, *J* = 7.6 Hz, 2H), 2.51 (t, *J* = 7.6 Hz, 2H). ^{13}C NMR (100 MHz, CDCl$_3$): δ 171.9, 160.9, 140.7, 134.0, 129.4, 129.3, 128.5, 126.3, 115.5, 42.8, 38.5, 31.7. HRMS (ESI$^+$): [M+H]$^+$ calculated: 258.1294; [M+H]$^+$ found: 258.1241.

***N*-(4-fluorobenzyl)-3-(1*H*-indol-3-yl)propanamide (6k):** CAS: 848320-38-7. Purified using 12-100% EtOAc in hexanes to give a white solid (92%). ^{1}H NMR (400 MHz, CDCl$_3$): δ 8.00 (s, br, 1H), 7.60 (d, *J* = 7.6 Hz, 1H), 7.37 (d, *J* = 8 Hz, 1H), 7.22-7.18 (m, 1H), 7.14-7.10 (m, 1H), 7.02-6.97 (m, 3H), 6.94-6.90 (m, 2H), 5.59 (s, br, 1H), 4.31 (d, *J* =5.6 Hz, 2H), 3.15 (t, *J* = 7.2 Hz, 2H), 2.61 (t, *J* = 7.2 Hz, 2H). ^{13}C NMR (100 MHz, CDCl$_3$): δ 172.5, 160.8, 136.3, 134.0, 129.3, 127.1, 122.1, 121.9, 119.4, 118.7, 115.5, 114.8, 111.2, 42.8, 37.5, 21.4. HRMS (ESI$^+$): [M+H]$^+$ calculated: 297.1403; [M+H]$^+$ found: 297.1378.

4-(Aminomethyl)-*N*-(4-fluorobenzyl)benzamide (6l). CAS: none found. ^{1}H NMR (400 MHz, D$_2$O): δ 7.78 (d, *J* = 7.4 Hz, 2H), 7.52 (d, *J* = 7.9 Hz, 2H), 7.34-7.31 (m, 2H), 7.07 (t, *J* = 7.6 Hz, 2H), 4.49 (s, 2H), 4.22 (s, 2H). ^{13}C NMR (100 MHz, D$_2$O): δ 170.1, 160.6, 136.4, 134.2, 133.7, 129.1, 129.0, 127.8, 115.4, 42.9, 42.6. HRMS (ESI$^+$): [M+H]$^+$ calculated: 259.1247; [M+H]$^+$ found: 259.1229.

(1-(4-Fluorobenzyl)-1*H*-1,2,3-triazol-4-yl)methanamine (12a): CAS: 1250599-01-9. Purified using 5-40% hexanes in EtOAc to give a white solid (80%). ^{1}H NMR (400 MHz, MeOD-*d₄*): δ 7.84 (s, 1H), 7.36-7.32 (m, 2H), 7.08-7.04 (m, 2H), 5.53 (s, 2H), 3.89 (s, 2H). ^{13}C NMR (100 MHz, MeOD-*d₄*): δ 161.5, 130.0, 129.3, 126.7, 123.0, 115.4, 52.6, 37.7. HRMS (ESI$^+$): [M+H]$^+$ calculated: 207.1046; [M+H]$^+$ found: 207.1005.

1-(1-(4-Fluorobenzyl)-1*H*-1,2,3-triazol-4-yl)-*N*-methylmethanamine (12b): CAS: 1480464-52-5. Purified using 5-40% MeOH in CHCl₃ to give a white solid (51%). ^{1}H NMR (400 MHz, MeOD-*d₄*): δ 7.36 (s, 1H), 7.23-7.19 (m, 2H), 7.02-6.97 (m, 2H), 5.43 (s, 2H), 3.78 (s, 2H), 2.39 (s, 3H), 1.70 (s, br, 1H). ^{13}C NMR (100 MHz, MeOD-*d₄*): δ 161.5, 147.2, 130.6, 129.9, 121.4, 115.9, 53.3, 46.6, 36.0. HRMS (ESI$^+$): [M+H]$^+$ calculated: 221.1202; [M+H]$^+$ found: 221.1194.

2-(1-(4-Fluorobenzyl)-1*H*-1,2,3-triazol-4-yl)pyridine (12c): CAS: 1133862-82-4. Purified using 5-40% hexanes in EtOAc to give a beige solid (33%). ^{1}H NMR (400 MHz, CDCl₃): δ 8.57-8.55 (m, 1H), 8.21-8.18 (m, 1H), 8.06 (s, 1H), 7.81-7.77 (m, 1H), 7.37-7.33 (m, 2H), 7.26-7.22 (m, 1H), 7.12-7.07 (m, 2H), 5.58 (s, 2H). ^{13}C NMR (100 MHz, CDCl₃): δ 161.7, 150.1, 149.4, 148.9, 136.9, 130.3, 130.1, 122.9, 121.7, 120.2, 116.3, 53.6. HRMS (ESI$^+$): [M+H]$^+$ calculated: 255.1046; [M+H]$^+$ found: 255.1090.

3-(1-(4-Fluorobenzyl)-1*H*-1,2,3-triazol-4-yl)propanoic acid (12d). CAS: 1929770-04-6. ^{1}H NMR (400 MHz, MeOD-*d₄*): δ 7.22 (s, 1H), 7.20-7.16 (m, 2H), 7.00-6.96 (m, 2H), 5.38 (s, 2H), 2.92 (t, *J* = 7.2 Hz, 2H), 2.62 (t, *J* = 7.2 Hz, 2H). ^{13}C NMR (100 MHz, MeOD-*d₄*): δ 174.6, 161.5, 146.9, 131.6, 129.8, 122.0, 115.4, 52.6, 32.9, 20.5. HRMS (ESI$^+$): [M+H]$^+$ calculated: 250.0992; [M+H]$^+$ found: 250.0932.

1-(1-(4-(3-fluoropropoxy)phenyl)-1*H*-1,2,3-triazol-4-yl)-*N*-methylmethanamine hydrochloride (17a): CAS: none found. Purified using 5-40% MeOH in DCM to give a beige solid. The product was then dissolved in EtOAc and precipitated using HCl (4 M in dioxanes) to give the hydrochloride salt **17a** (40%). ^{1}H NMR (400 MHz, MeOD-*d4*): δ 8.53 (s, 1H), 7.76-7.74 (m, 2H), 7.16-7.14 (m, 2H), 4.70 (t, *J* = 5.8 Hz, 1H), 4.58 (t, *J* = 5.8 Hz, 1H), 4.40 (s, 2H), 4.19 (t, J = 6.2 Hz, 2H), 2.23 (pentet, J = 6 Hz, 1H), 2.16 (pentet, J = 6 Hz, 1H). ^{13}C NMR (100 MHz, MeOD-*d4*): δ 161.1, 140.2, 124.5, 123.4,

116.6, 114.0, 82.4, 65.4, 44.3, 33.2, 31.6. HRMS (ESI$^+$): [M+H]$^+$ calculated: 265.1459; [M+H]$^+$ found: 265.1460.

1-(4-(3-Fluoropropoxy)phenyl)-4-phenyl-1*H*-1,2,3-triazole (17b): CAS: 943726-06-5. Purified using 1-5% EtOAc in DCM to give an white solid (61%). ^{1}H NMR (400 MHz, CDCl$_3$): δ 8.13 (s, 1H), 7.94-7.92 (m, 2H), 7.71 (d, *J* = 9.2 Hz, 2H), 7.50-7.46 (m, 2H), 7.41-7.37 (m, 1H), 7.07 (d, *J* = 9.2 Hz, 2H), 4.76 (t, *J* = 6 Hz, 1H), 4.64 (t, *J* = 6 Hz, 1H), 4.20 (t, *J* = 6 Hz, 2H), 2.30-2.18 (m, 2H). ^{13}C NMR (100 MHz, CDCl$_3$): δ 159.0, 148.2, 130.4, 128.9, 128.3, 125.8, 122.2, 117.8, 115.3, 81.3, 64.0, 30.4. HRMS (ESI$^+$): [M+H]$^+$ calculated: 298.1356; [M+H]$^+$ found: 298.1596.

3-(1-(4-(3-fluoropropoxy)phenyl)-1*H*-1,2,3-triazol-4-yl)propanoic acid (17c): CAS: none found. Purified using 4-40% MeOH in DCM to give an off-white solid. The product was then recrystallized from EtOH and water to form a white solid (71%). ^{1}H NMR (400 MHz, CDCl$_3$): δ 7.75 (s, 1H), 7.55-7.54 (m, 2H), 6.97-6.95 (m, 2H), 4.69-4.65 (m, 1H), 4.57-4.54 (m, 1H), 4.11-4.08 (m, 2H), 3.05-3.03 (m, 2H), 2.73-2.71 (m, 2H), 2.20-2.11 (m, 2H), ^{13}C NMR (100 MHz, CDCl$_3$): δ 175.1, 159.1, 142.3, 130.6, 122.2, 120.3, 115.3, 81.4, 64.0, 33.5, 30.4, 20.8. HRMS (ESI$^+$): [M+H]$^+$ calculated: 294.1248; [M+H]$^+$ found: 294.1249.

2-(1-(4-(3-fluoropropoxy)phenyl)-1*H*-1,2,3-triazol-4-yl)pyridine (17d): CAS: none found. Purified using 20-100% EtOAc in hexanes to give an off-white solid (29%). ^{1}H NMR (400 MHz, CDCl$_3$): δ 8.61-8.54 (m, 2H), 8.25 (s, br, 1H), 7.84-7.80 (m, 1H), 7.73-7.70 (m, 2H), 7.27 (s, br, 1H), 7.06-7.02 (m, 2H), 4.73 (t, *J* = 5.7 Hz, 1H), 4.61 (t, *J* = 5.7 Hz, 1H), 4.16 (t, *J* = 6.1 Hz, 2H), 2.24 (pentet, J = 5.9 Hz, 1H), 2.17 (pentet, J = 5.9 Hz, 1H). ^{13}C NMR (100 MHz, CDCl$_3$): δ 159.2, 150.2, 149.5, 148.8, 137.2, 130.7, 123.2, 122.2. 120.6, 120.3, 115.5, 81.5, 64.1, 30.6. HRMS (ESI$^+$): [M+Na]$^+$ calculated: 321.1122; [M+Na]$^+$ found: 321.1133.
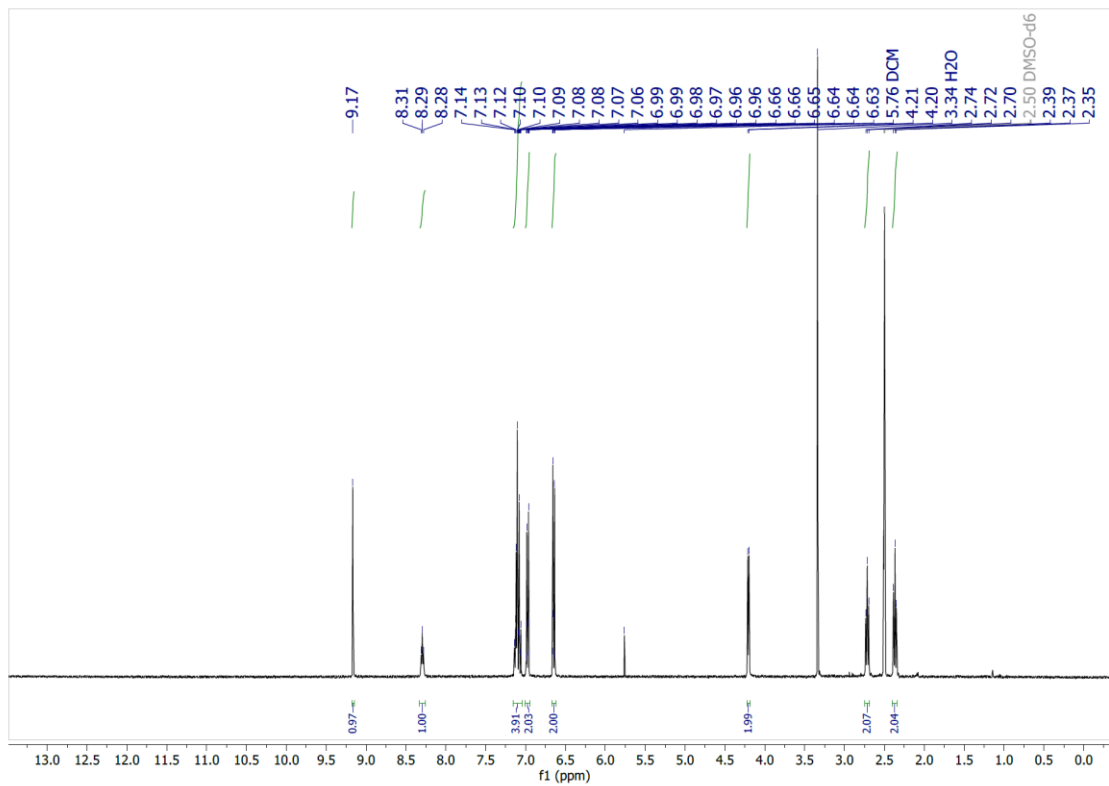
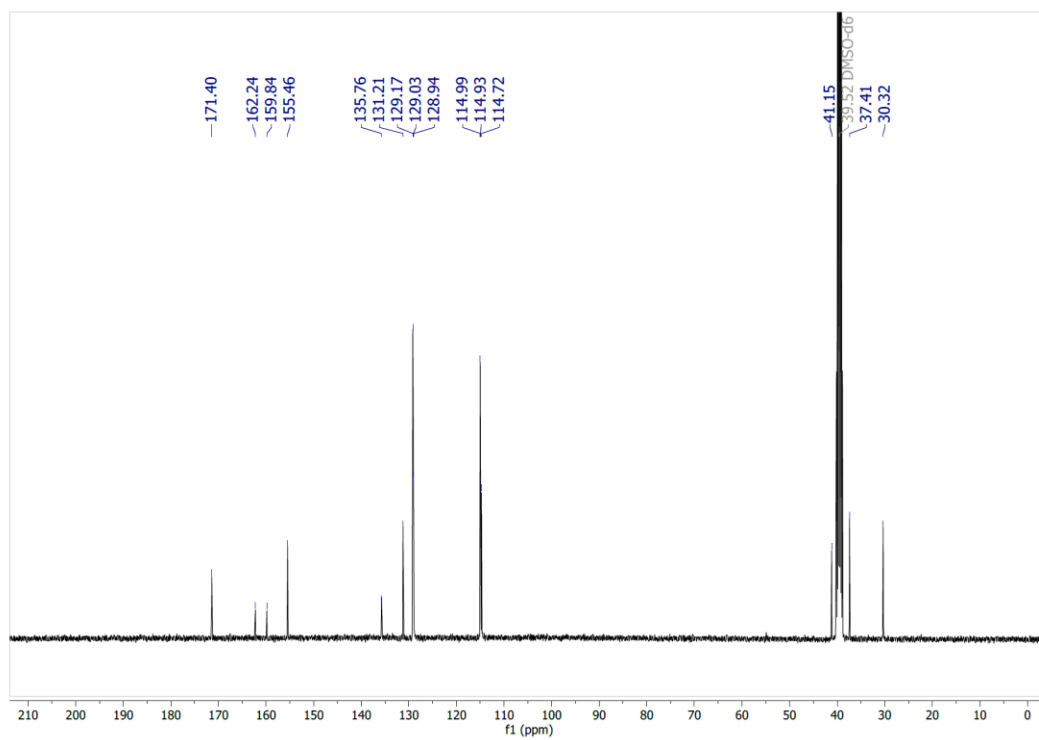**Figure D4.** ^{1}H NMR of fragment **6g** in DMSO-*d6*.

Figure D5. ^{13}C NMR of fragment **6g** in DMSO-*d6*.
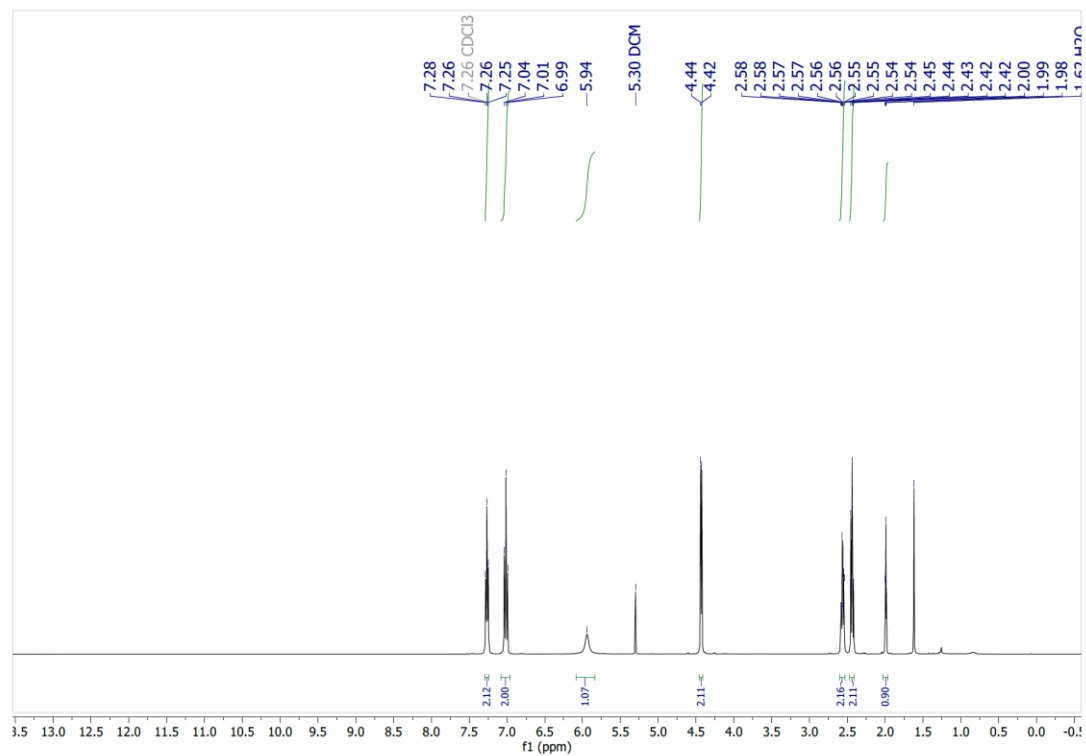
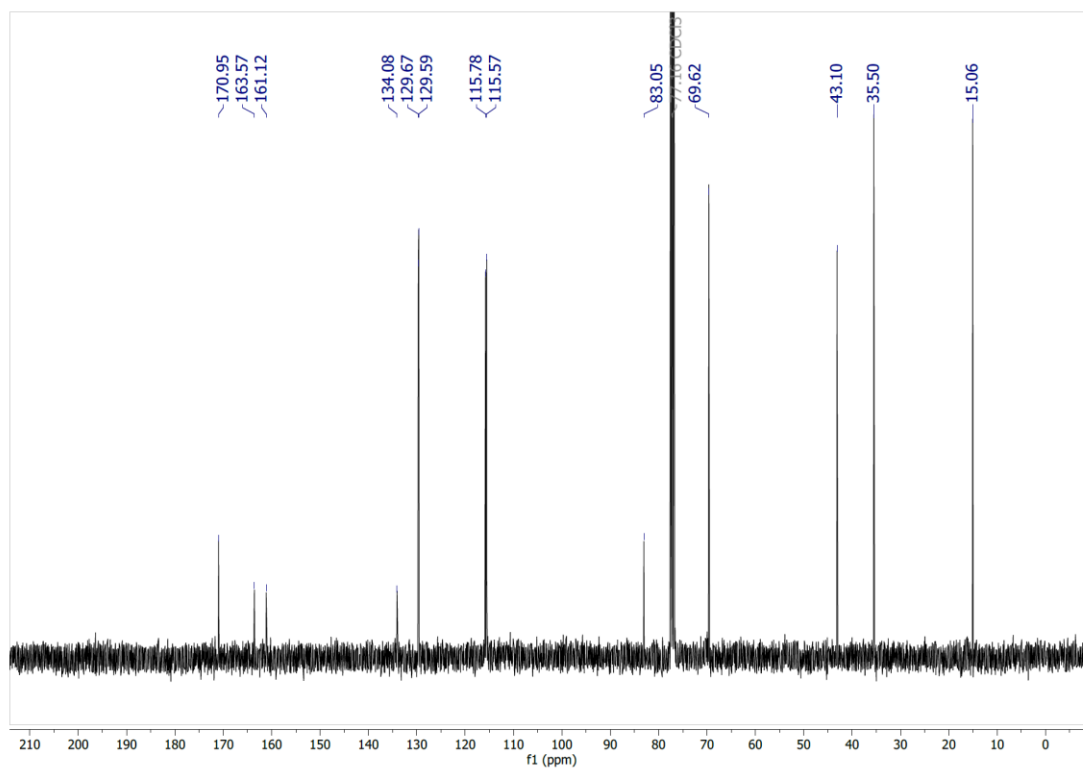**Figure D6.** ^{1}H NMR of fragment **6h** in CDCl$_3$.

Figure D7. ^{13}C NMR of fragment **6h** in CDCl$_3$.
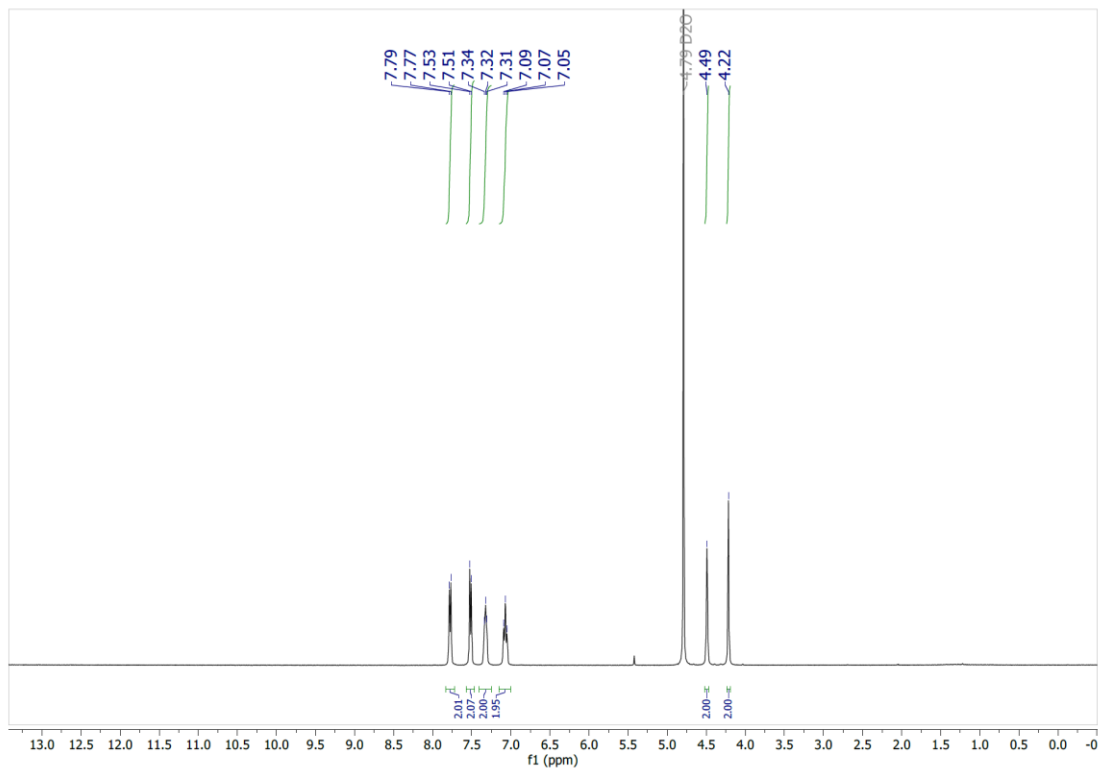
Figure D8. ^{1}H NMR of fragment **6l** in D$_2$O.
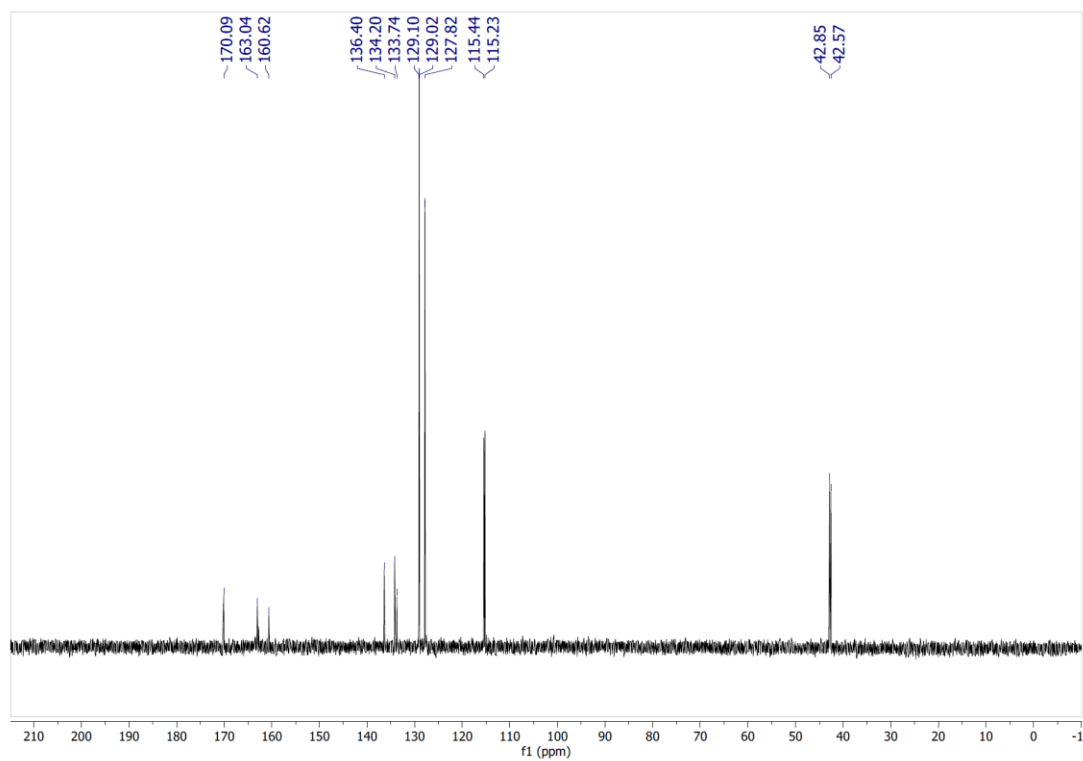
Figure D9. ^{13}C NMR of fragment **6l** in D$_2$O.
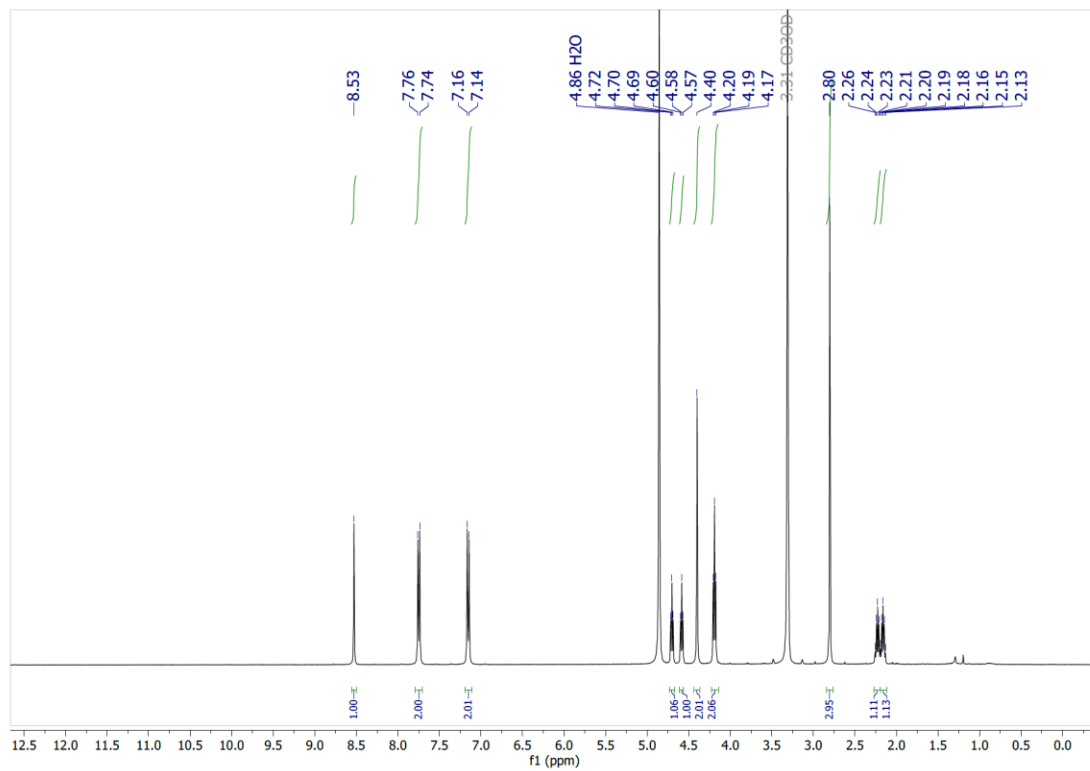
Figure D10. ^{1}H NMR of fragment **17a** in MeOD-*d4*.
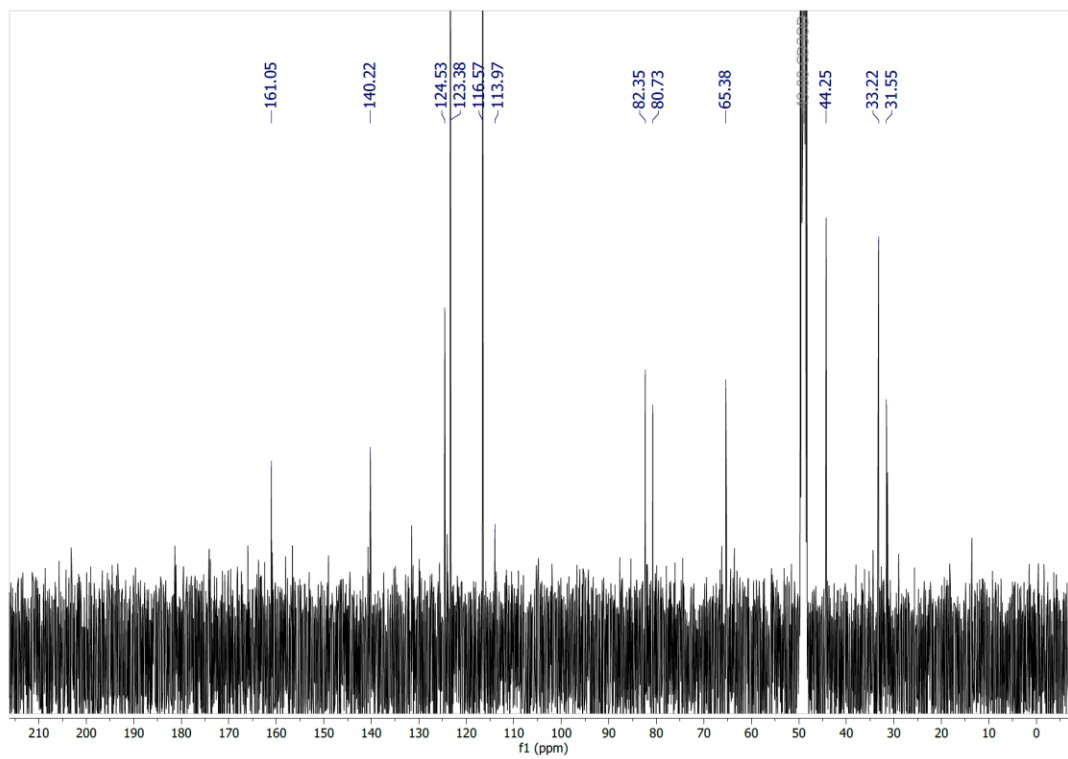

Figure D11. ^{13}C NMR of fragment **17a** in MeOD-*d4*.
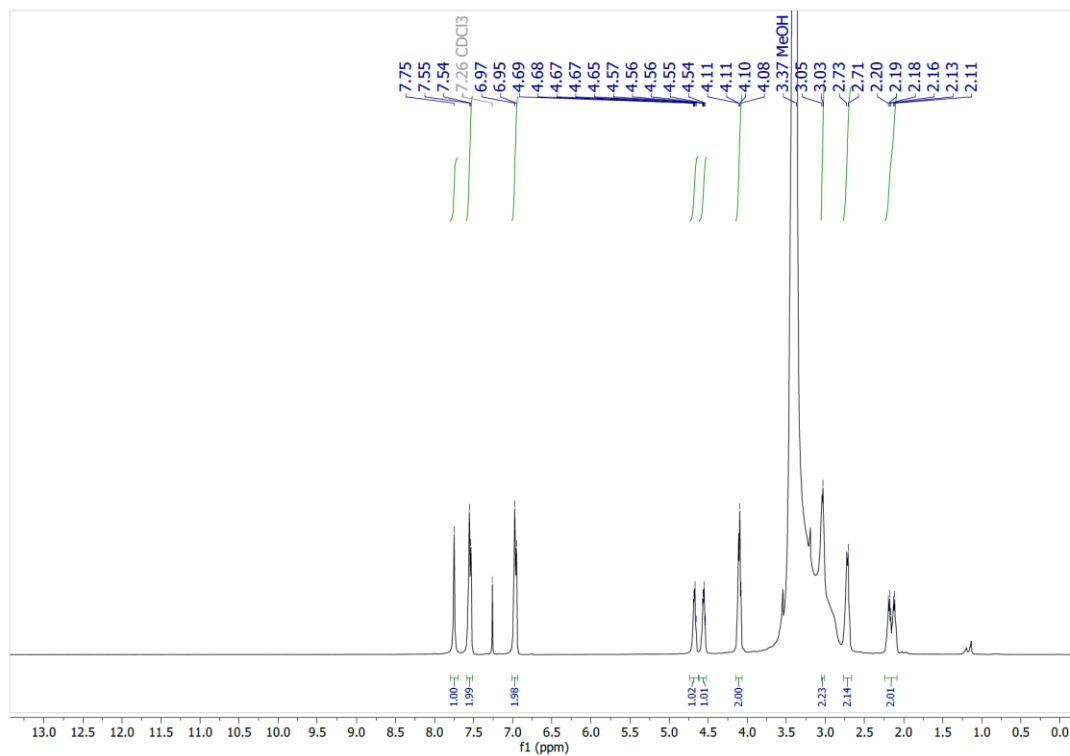
Figure D12. ¹H NMR of fragment **17c** in CDCl₃.
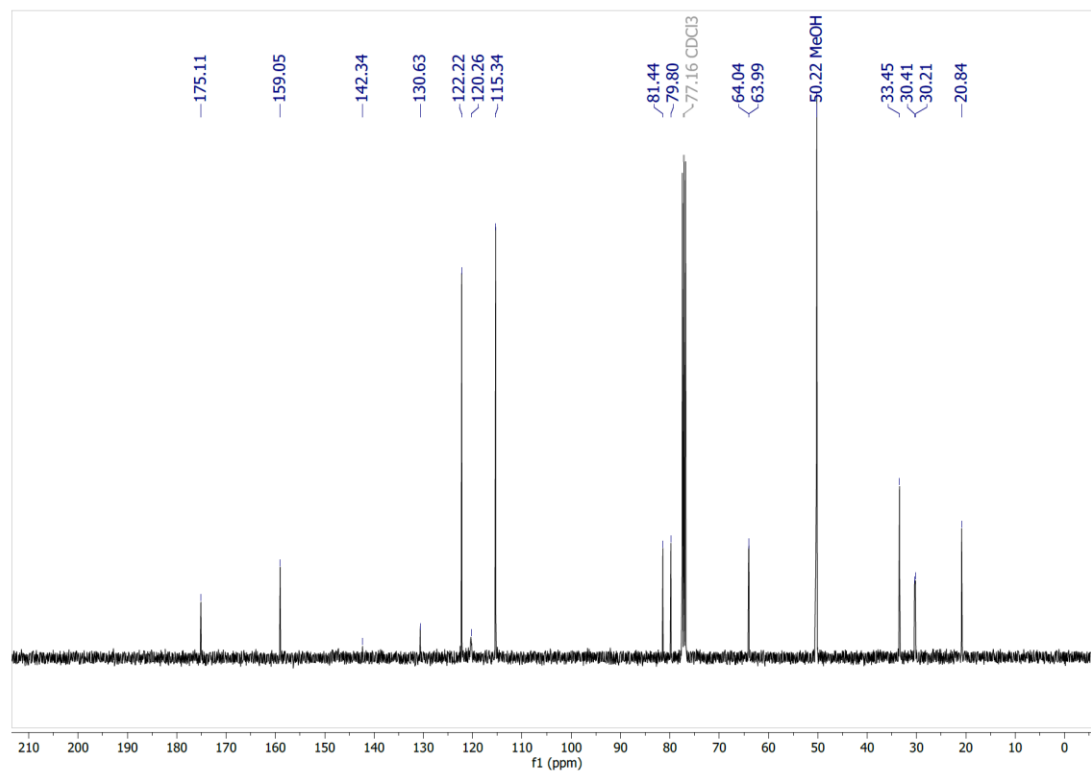

Figure D13. ¹³C NMR of fragment **17c** in CDCl₃.
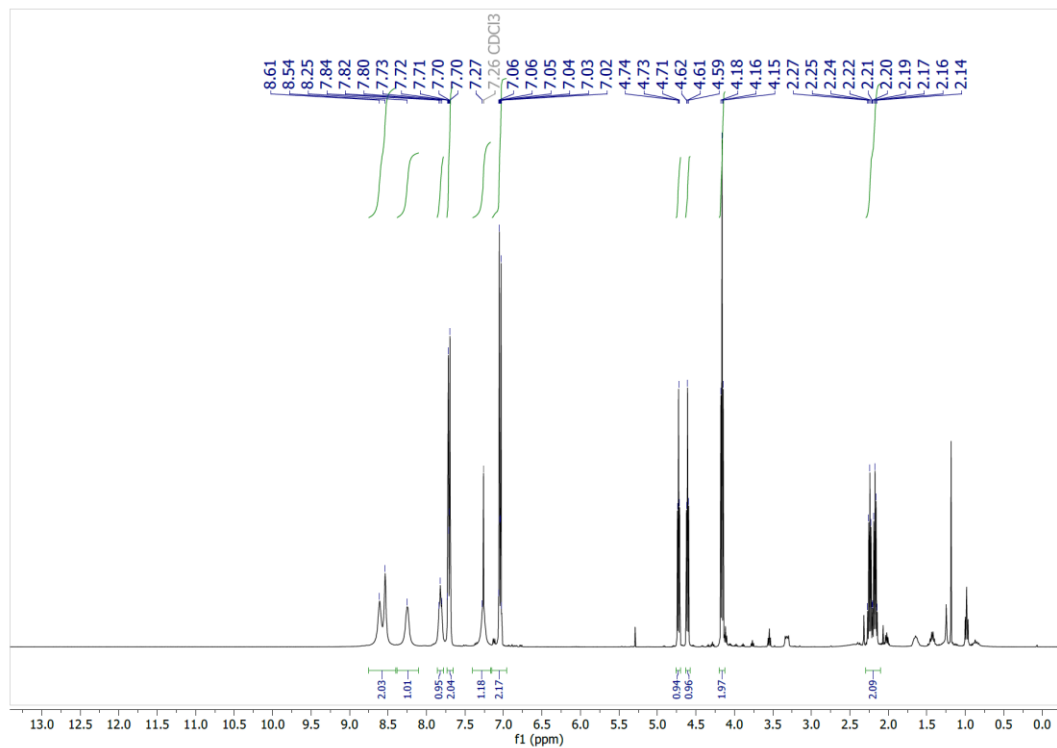
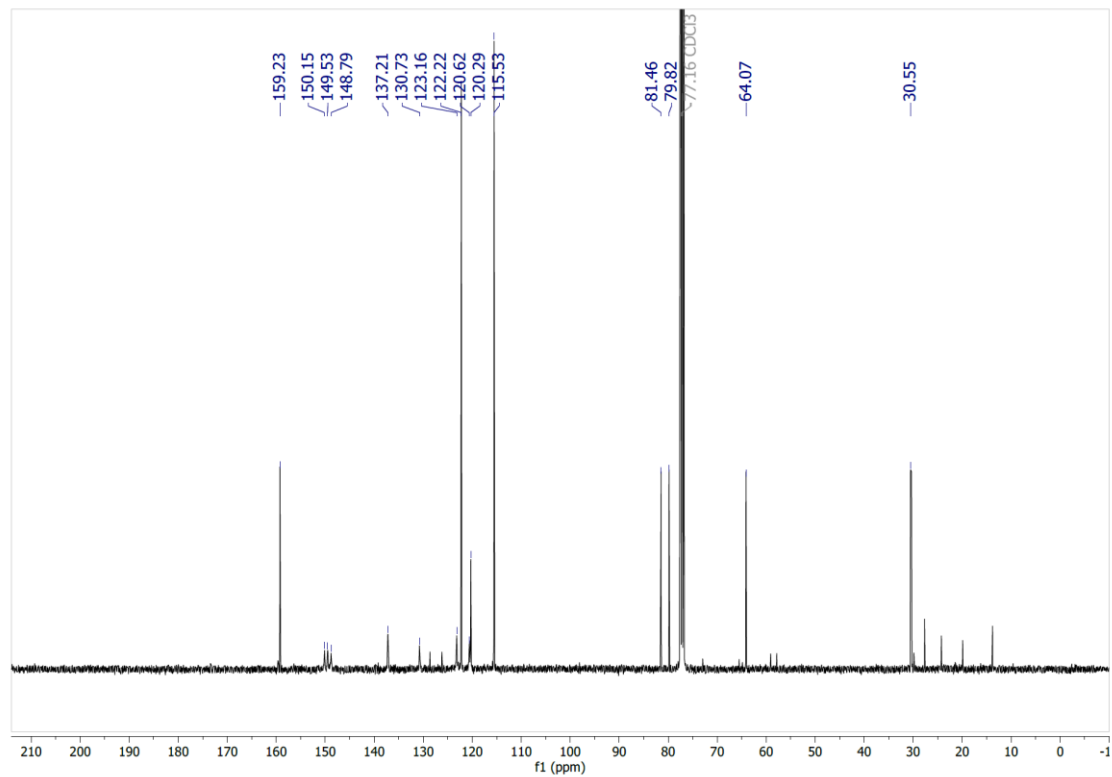**Figure D14.** ¹H NMR of fragment **17d** in CDCl₃.

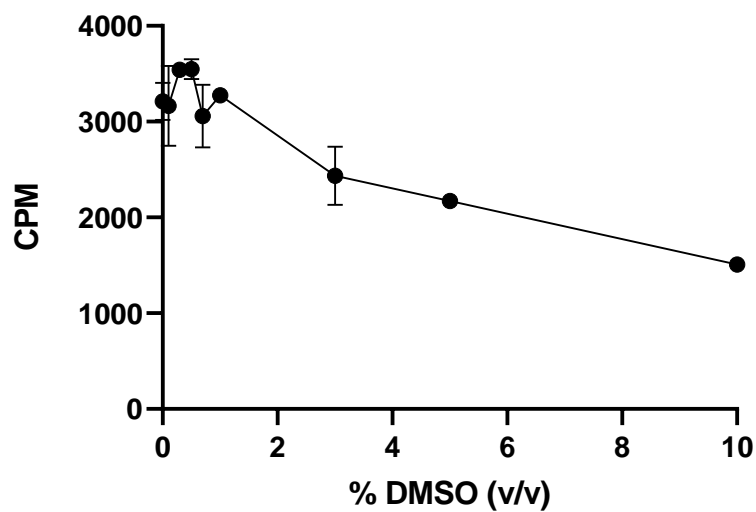

Figure D15. ¹³C NMR of fragment **17d** in CDCl₃.

Figure D16. DMSO tolerance assay in HEK293 GHRS-eYFP cells in presence of radioligand (human $[^{125}I]$-ghrelin(1-28)). CPM = counts per minute.
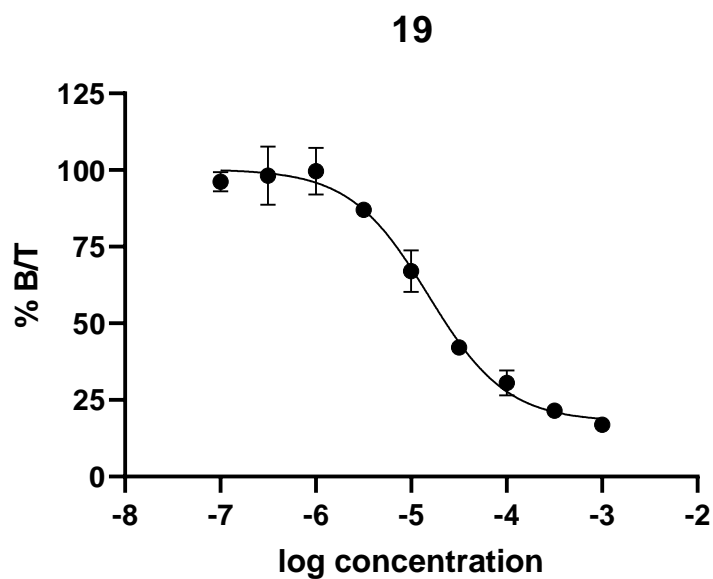
19

Figure D17. IC_{50} curve biased fragment **19** in HEK293 GHSR-eYFP cells (IC_{50}=15.1 µM).

Curriculum Vitae

EDUCATION

Ph.D. Organic Chemistry (Molecular Imaging)   May 2016 – April 2021
University of Western Ontario; London, ON, Canada
Western Certificate in University Teaching and Learning
Research Supervisor: Prof. Dr. Leonard G. Luyt
Thesis: The Development of Fluorine-18 Imaging Agents Targeting the GHSR

B.Sc. Honours Chemistry Co-op   Sept. 2011 – Dec. 2015
University of Guelph; Guelph, ON, Canada
Minor: Mathematical Science
Research Supervisor: Prof. Dr. Adrian Schwan
Thesis: Probing a New Isoindolone Synthesis using SO_2 Extrusion and Diels- Alder Methodologies

ADDITIONAL RESEARCH EXPERIENCE

Nuclear Medicine Research Assistant   May 2015 – Aug. 2015
TRIUMF; Vancouver, BC, Canada
Research Supervisor: Dr. Paul Schaffer
Project Title: Synthesis of the Enantiopure Radiotracer [^{18}F]5-fluoroaminosuberic acid for PET Imaging of Oxidative Stress

Research Assistant   May 2014 – Dec. 2014
University of Guelph; Guelph, ON, Canada
Research Supervisor: Dr. Peter Tremaine
Project Title: Apparent Molar Volumes and Apparent Molar Heat Capacities of Aqueous 2-methylpiperidine Systems

TEACHING EXPERIENCE

Teaching Assistant
University of Western Ontario; London, ON, Canada
- *Resource Room TA*   2017-2020
  - Chem 2223 – Organic Chemistry of Biological Molecules

- *Marking TA*   Winter 2017
  - Chem 3393 – Medicinal Chemistry

- *Laboratory TA*   2016-2017
  - Chem 2213 – Organic Chemistry for Life Sciences
  - Chem 2223 – Organic Chemistry of Biological Molecules

Undergraduate Mentor

University of Western Ontario; London, ON, Canada

- Western Undergraduate Summer Research Internship (Jakob Kaminski)   2020
    - *Stapled Ghrelin(1-20) Analogues for the Targeting of GHSR-1a in Cancer*

- Chem 4491 Undergraduate Thesis Project (Derian Hodgson)   2019-2020
    - *Improving the Metabolic Stability of Ghrelin(1-8) Analogues*

Alternate Instructor

University of Western Ontario; London, ON, Canada

- Chem 2223 – Organic Chemistry of Biological Molecules   Intersession 2019
- Chem 4493 – Chemistry of Biological Macromolecules   Fall 2019

Additional Teaching Training

University of Western Ontario; London, ON

- Advanced Teaching Program (ATP)   Nov. 2020
- Teaching Mentor Program   Winter 2019
- Teaching Assistant Training Program   Sept. 2018
- Future Prof Series Workshops   2016 – 2021

SCHOLARSHIPS

NSERC Postgraduate Scholarship – Doctoral (PGS-D)   2018-2021
QEII Graduate Scholarship in Science and Technology (declined)   2018-2019
QEII Graduate Scholarship in Science and Technology   2017-2018
Western Science Entrance Scholarship   May 2016
QEII Aiming for the Top Government Scholarship   2011-2015
University of Guelph Entrance Scholarship   Sept. 2011

HONOURS AND AWARDS

Molecular Imaging Program Travel Award   2019
Peter J. Guthrie Travel Award, Department of Chemistry, UWO   2019
ISRS 2019 Travel Bursary   2019
Lipson-Baines Award, Department of Chemistry, UWO   2019
Molecular Imaging Program Travel Award   2018
Chemistry Co-op Book Prize, Department of Chemistry, University of Guelph   2015

PUBLICATIONS

- **Childs, M. D.** and Luyt, L. G. A Decade's Progress in the Development of Molecular Imaging Agents Targeting the Growth Hormone Secretagogue Receptor. *Mol. Imaging*. 2020, *19*, 1-15.

PUBLISHED ABSTRACTS

- **Lazarakos, M**; Kovacs, M. S. and Luyt, L. G. Radiofluorination of non-activated aromatic prosthetic groups for efficient synthesis of fluorine-18 labelled ghrelin(1-8) analogues. *J. Label. Compd. Radiopharm.* 2019, 62, S120.

- Yang, H*; Merkens, H; Colovic, M; Jenni, S; **Lazarakos, M**; Rodrigo, I; Miao, Q; Webster, J; Bernard, F; Schaffer, P. "The impact of chirality on oxidative stress imaging with [^{18}F]5-fluoro-aminosuberic acid ([^{18}F]FASu)". *J. Nucl. Med.* 2016, 57:2625.

SUBMITTED MANUSCRIPTS

- LeSarge, J. C; Thibeault, P; Yu, L; **Childs, M. D**; Kovacs, M. S; Ramachandran, R and Luyt, L. G. Peptides for use in positron emission tomography (PET) imaging of protease-activated receptor 2 (PAR2). Submitted to the Journal of Medicinal Chemistry.

MANUSCRIPTS IN PREPARATION

- **Childs, M. D**; Yu, L; Kovacs, M. S. and Luyt, L. G. Radiofluorination of Non-activated Aromatic Prosthetic Groups for Synthesis and Evaluation of ^{18}F-labelled Ghrelin(1-8) Analogues.

- **Childs, M. D**; Chandrabalan, A; Hodgson, D; Ramachandran, R and Luyt, L. G. Investigating the *in vitro* Metabolic Stability of Ghrelin(1-8) Analogues.

- Campana, M. B; Cleverdon, E. R; Curtis, E. R; **Childs, M. D**; Davis, T. R; Morales-Rodriguez, Y; Hehnly, H; Luyt, L. G. and Hougland, J. L. A remarkably specific ligand for ghrelin *O*-acyltransferase reveals a secretory pathway enzyme interaction with extracellular peptides.

ADDITIONAL CONFERENCE ABSTRACTS

- **Childs, M. D**; Yu, L; Hodgson, D; Kovacs, M. S. and Luyt, L. G. Radiofluorination and preliminary *in vivo* evaluation of bulky aromatic side chains in ghrelin(1-8) analogues. Canadian Chemistry Conference and Exhibition 2020. Winnipeg, MB. [Accepted for an oral presentation] – Cancelled due to COVID-19 pandemic.

- **Lazarakos, M**; Yu, L; Kovacs, M. S and Luyt, L. G. Radiosynthesis, *in vitro*, and *in vivo* evaluation of ^{18}F-labelled ghrelin(1-8) analogues for PET imaging of the GHSR-1a. Great Lakes Molecular Imaging Conference. 2019. Holland, MI.

- **Lazarakos, M**; Kovacs, M. S. and Luyt, L. G. Improved Radiofluorination of Ghrelin(1-8) Analogues. 101st Canadian Chemistry Conference and Exhibition. 2018. Edmonton, AB. [Oral Presentation]

- **Lazarakos, M**; Kovacs, M and Luyt, L. New Approaches in Radiolabelling ^{18}F-labelled Ghrelin(1-8) as a Novel PET Imaging Probe. 2nd Cellular and Molecular Imaging Symposium. 2018. London, ON.

- **Lazarakos, M** and Luyt, L. Fragment-based approach towards the discovery of novel cancer imaging agents. 14th Annual Oncology Research & Education Day. 2017. London, ON.